Microfluidic Systems for Continuous Crystallization of Small Organic Molecules

by

Mahmooda Sultana

Bachelors of Science
University of Southern California

Submitted to the Department of Chemical Engineering
in partial fulfillment of the requirements for the degree of

Doctor of Philosophy in Chemical Engineering

at the

MASSACHUSETTS INSTITUTE OF TECHNOLOGY

May 2010
[June 2010]

Author.....
Mahmooda Sultana
Department of Chemical Engineering
May 25, 2010

Certified by.....
Klavs F. Jensen
Warren K. Lewis Professor of Chemical Engineering
Professor of Materials Science and Engineering
Thesis Supervisor

Accepted by.....
William M. Deen
Carbon P. Dubbs Professor of Chemical Engineering
Chairman, Committee for Graduate Students

Microfluidic Systems for Continuous Crystallization of Small Organic Molecules

by
Mahmooda Sultana

Submitted to the Department of Chemical Engineering on May 25th, 2010
in partial fulfillment of the requirements for the degree of
Doctor of Philosophy in Chemical Engineering

Abstract

This thesis presents one of the first demonstrations of continuous crystallization in microfluidic devices, and illustrates their use for various applications related to crystallization of small organic molecules. Crystallization is an important process in a number of industries, including specialty chemicals, food, cosmetics, nutraceuticals and, most importantly, pharmaceuticals. Most small molecule pharmaceuticals are isolated in crystalline form, and more than ninety percent of all pharmaceutical products are formulated in particulate, mainly crystalline form. However, crystallization is not a completely understood process. The sensitivity of the process to synthesis conditions gives rise to serious reproducibility issues. The traditional batch crystallizers suffer from non-uniform process conditions across the reactor, and chaotic, poorly controlled mixing of the reagents, often resulting in polydisperse crystal size distribution and impure polymorphs. This makes it difficult to obtain reliable information on the process kinetics that can be used for scale-up, as well as to study the fundamentals of the process.

Microfluidic systems offer a unique toolset for crystallization because of well-defined laminar flow profiles, enhanced heat and mass transfer, better control over the contact mode of the reagents, and optical access for *in situ* characterization. The better control over the synthesis conditions gives rise to the potential for controlling the crystal size, as well as the polymorphic form. In addition, low consumption of reagents makes it an attractive research tool for expensive pharmaceutical compounds. Some of the advantages of microfluidics have been demonstrated for crystallization in micro-batches, but so far not in continuous devices. Continuous crystallization is difficult to achieve in microchannels as uncontrolled nucleation, crystal growth, agglomeration and sedimentation of crystals easily clog the small channels. The interaction of crystals with channel walls may also contribute to channel plugging in these devices.

This thesis has developed microfluidic devices for continuous crystallization of small organic molecules for the first time. We have decoupled nucleation and growth, the two key steps of crystallization, using reaction engineering principles, and have developed two separate continuous devices, one for each of these two processes. We have used seeded crystallization and reactor design to achieve controlled growth, as well as to suppress secondary nucleation, agglomeration and sedimentation of crystals. In addition, we have eliminated any significant interaction of crystals with channel walls by

controlling the properties of channel surfaces. We have also integrated microscopy and spectroscopy tools with the device for *in-situ* characterization of crystal size and polymorphic form. We have illustrated the use of these devices to extract growth kinetics data for crystals of various shapes, including high aspect ratio systems such as that with acicular or plate-like habits. The reproducibility and control in our devices have allowed us to elucidate the growth mechanism and fundamentals of the growth process for difficult crystal systems. In addition, we have demonstrated that continuous microfluidic devices offer a unique advantage over the current state-of-the art technology to measure the size, size distribution and growth kinetics of high aspect ratio crystal systems more accurately.

Moreover, we have demonstrated the use of microfluidic devices for understanding crystal habit modification in the presence of impurities. We take advantage of the high spatiotemporal resolution of microfluidic devices to study the evolution of crystal habit over time, and to obtain information on the kinetics of habit modification in the presence of different impurities. We have developed an understanding of the habit modification mechanism for alpha glycine in the presence of alpha amino acids. Such information may not only provide insights into impurity-crystal interactions, but also serve as a powerful tool for the design of impurities that can be deliberately added to improve the crystallization process.

Furthermore, we have designed and developed a second microfluidic device for continuous supercritical crystallization for the first time. Using supercritical fluid as an antisolvent, we have demonstrated continuous spontaneous nucleation of acetaminophen. We have shown the ability to produce micron-sized crystals, which may be useful for increasing the bioavailability of drugs with lower solubility, as well as for inhalable and highly potent drugs with stringent size requirements. The developed platform can also be used as a high-throughput device for safely screening crystallization conditions in the supercritical domain. We have demonstrated such use by screening the effects of pressure and various solvents on the habit, size and polymorphic form of acetaminophen crystals.

Thesis Supervisor: Klavs F. Jensen
Title: Department Head, Warren K. Lewis Professor of Chemical Engineering
Professor of Materials Science and Engineering

Acknowledgements

This thesis would not have been possible without the support of my advisor, Professor Klavs Jensen. I sincerely thank him for allowing me to initiate this project from scratch, and to pursue my ideas. I also thank him for his continuous guidance and encouragement throughout the last few years of work. He definitely has been a role model, who inspires his students to always think creatively and work hard, yet is the most supportive and considerate at difficult times. I am thankful to my thesis committee members, Professors Martin Schmidt and Bernhardt Trout for their insightful feedback during the committee meetings. I would like to particularly thank Professor Schmidt for taking the time to read this thesis and providing valuable recommendations. I would also like to thank Professor Alice Gast for her valuable comments and support, and Dr. Brian Johnson at Merck for his insights into crystallization at the early phase of this thesis.

I am thankful to Merck, Bell labs (Alcatel-Lucent) and National Science Foundation for providing funding for this work.

The last few years have been a wonderful learning experience for me, and I thank Klavs, as well as all the past and present members of the Jensen group, for creating such a collaborative environment. I would particularly like to thank Professor Axel Günther for many discussions on microfluidic crystallization that has helped me to formulate my understanding on the subject. I thank Dr. Andrea Aadamo for working with me on developing a sheath flow device in PDMS, as well as for professional mentoring. I am thankful to Professor Michiel Kruetzer for professional guidance and mentoring. I would like to thank Dr. Samuel Marre for his contributions in developing the supercritical microfluidic setup and for collaborating with me to initiate the supercritical crystallization part of this thesis. I am thankful to Dr. Ryan Hartman for working with me on developing the Teflon coating process for PDMS microchannels. Many thanks to Dr. Soubir Basak for fabricating the high pressure devices. Thanks to Ling, Kevin, Victor and Soubir for all the fun times, and for being wonderful officemates, who are always ready to listen to either personal or technical issues/complaints. I would like to thank Vicky for always being there in times of need.

I am thankful to many researchers and staff members outside the Jensen group. I would like to thank Dr. Joseph Gardecki for helping me understand the practical issues with *in situ* Raman Spectroscopy. I would like to thank Dr. Harry Lee for his insights into getting the Raman setup to work. I thank Dr. Scott Speakman at the center for materials science and engineering (CMSE) for his help in obtaining X-ray data for difficult samples, and Patrick Boisvert (CMSE) for his help with imaging the small crystals we produced in the supercritical crystallization process. I thank Mark Belanger at the student machine shop for been very helpful in fabricating customized parts of different setups. I am thankful to Joan Chisholm, one of the sweetest ladies in the world, for always being there for all of us (Jensen group members), for loving us, and for pampering us with candies. I am also thankful to Alina Haverty for always taking care of us, and for listening to our issues.

I would like to thank all my teachers who believed in me and challenged me to do well. I am particularly indebted to Mr. Carlson, Mr. Sims, and Mr. Rivas for guiding me in high school after my family first moved to the United States, Professor Hanna Reisler for taking me under her wings at USC, as well as for her inspiration and guidance. I am thankful to Professor Blankschtein, one of the best teachers I had at MIT, for his support and professional guidance. I am also thankful to Dr. Susane Arney for not only serving as my supervisor at Bell Labs, but also as a mentor since then.

I would like to thank all the wonderful friends I have made at MIT, Shahrooz, Farah, Rubaiyat, Ummul, Labsang, Ling Chao, Patricio and many others. I am thankful to many people outside MIT for the support I have received over the last few years away from home. I am particularly indebted to Dr. Haris Awal for bestowing his fatherly love, Dr. Zaheed Husain for his help and support, and Nasim Jahan for taking care of me in times of need.

I am thankful to my family for the continuous support I have received regarding my education. I would like to thank my mother, Meherun Nesa, for bringing me to this world; my father, Golam Zakaria, for his love and support throughout my life; and my younger brothers, Shuvo and Dipu, for keeping me responsible with the pressure of setting a good example before them. I would like to especially thank my grandmother, Dilara Bari, for all her love. I would like to thank aunt Faizun for her love, and uncles Mahbubul Bari and Azizul Bari for their bits of support. I am thankful to Razib for his help in image analysis of some parts of the presented data on supercritical crystallization. I would like to thank Ashfaque, the most loving, caring and sincere person I have seen in my life. Your disturbingly good and honest nature always sets a high standard for me and makes me want to become a better person. Thank you for always being there for me, and giving a meaning to my life. This work would not have been possible without your unconditional love and support.

Finally, I would like to thank almighty Allah for all his blessings in my life and for instilling the strength and courage in me to keep going through the highs and lows of life.

Table of Contents

List of Figures

List of Tables

1 Introduction

1.1 Crystallization

The process of crystallization is ubiquitous and has been utilized for thousands of years.[1] The main applications of crystals in the 19th century and earlier were as precious stones for their fascinating properties: transparency and color, refractive index and optical dispersion, symmetry and facets.[2] However, with the advent of scientific developments of the 20th century, crystallization has become an important process for numerous modern technologies, for a number of applications such as separation, concentration, purification, and solidification. Crystallization is utilized in the petrochemical industry for separation and purification of solids. It is an important process in the specialty chemicals industry for manufacturing household products and cosmetics. In addition, crystallization finds applications in new areas such as understanding surfactant behavior.[3] It is also utilized in the food industry for controlling stability and texture of food products.[4] Other industries that have applications of crystallization include microelectronics,[5] pigments,[6] and most importantly, pharmaceuticals.[7]

Crystallization finds a variety of applications in the pharmaceutical industry, including isolation and synthesis of Active Pharmaceutical Ingredients (API), co-crystals, excipients, and separation of chiral isomers. More than 90% of all pharmaceutical products, such as tablets, capsules, aerosols, suspensions and suppositories contain the API in particulate, mainly crystalline form,[8, 9] and almost all small molecular weight pharmaceuticals are formulated in particulate, generally crystalline form.[10] This process defines the purity and other solid state properties of the drug such as the crystal habit, size, and polymorphic form, as well as drug product stability and performance. Consequently, reproducibility issues with crystallization process causes a wide range of pharmaceutical formulation problems, such as bioavailability, as well as chemical and physical forms. The most important solid-state and drug delivery characteristics, affected by crystallization, are summarized in Table 1-1. [8]

Table 1-1. Properties affected by crystallization and their relationship with product characteristics.[8]

Solid-state properties	***Effect on products***
Structural	
Crystallinity Polymorphs Solvates Salts Crystal defects	Physical and chemical stability Hygroscopicity Solubility profile and dissolution rate All aspects of processing
Dimensional	
Crystal size distribution Crystal habit Surface structure	Bulk density, agglomeration, rheological properties, compaction Permeability (adsorption) Bioavailability Consistency and uniformity of the dosage form
Chemical	
Impurities	Toxicity
Chiral forms and chiral separation Sterility	Chemical, physical and enantiomeric stability
Mechanical	
Brittle/ductile transitions, fracture stress, indentation hardness, stress/strain relaxation, yield pressure, Young's modulus	Milling and tableting behavior
Electrical	
Electrostatic charge distribution	Agglomeration and flow properties

Crystallization is defined as a phase change in which a solid product with short and long range order with atoms or molecules in a fixed lattice arrangement is obtained from

a solution. It is a deceptively complex process and the final outcome of this process results from the interplay of solution thermodynamics and kinetics, as well as other factors such as mass and heat transfer, fluid dynamics, and molecular recognition phenomena. The lack of understanding of crystallization processes and the various underlying phenomena lead to unwanted or previously unknown nucleation events that threaten the development of a pharmaceutical product. Dunitz and Bernstein have provided examples of such incidents, demonstrating the poor control present in crystallization practices.[11] One of the challenges associated with crystallization is its sensitivity to the process parameters. The sudden appearance of a new crystalline structure, different from the existing form of the HIV drug, Ritonavir, illustrates the sensitivity of the crystallization process to synthesis conditions.[12]

1.1.1 Polymorphism

Polymorphism is one of the most important concepts in organic crystallization: it controls the quality and properties of the final product, and at the same time, increases the complexity of the crystallization process by many folds. Most of the pharmaceutical compounds are polymorphic; which means, they can exist in multiple crystalline phases that have different arrangements or conformations of the molecules. Different polymorphs of a substance may exhibit different physical, thermodynamic, spectroscopic, kinetic, surface, mechanical, packing, and rheological properties.[13] The difference in these properties may often manifest into a difference in bioavailability and pharmaceutical efficacy. According to Storey et al., 51% of all small organic molecules display true polymorphism and more than 87% displays multiple solid forms if solvates are included.[14] Structural differences between the crystalline lattices of polymorphs may originate in three ways, namely packing polymorphism when molecules pack into different three-dimensional structures, conformational polymorphism when confirmationally flexible molecules can fold into different shapes that pack differently, and configurational polymorphism when molecules of different isomers or combinations thereof, pack differently.[7, 13, 15] Figure 1-1 presents an example of conformational polymorphism and an example of packing polymorphism, distinguishing the difference between them.

A molecule may also have pseudopolymorphic solid forms, namely, solvates, where crystalline solid adducts contain solvent molecules within the crystal structure, and hydrates, where the solvent molecule inside the crystal structure is water.[15]

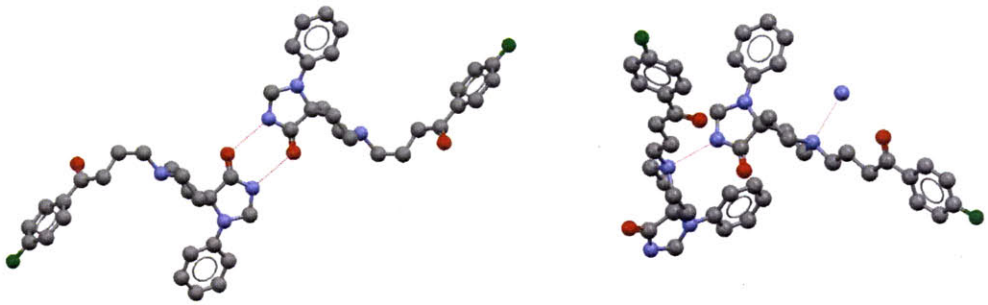

Spiperone, Polymorph I

Spiperone, Polymorph II

Conformational Polymorphism

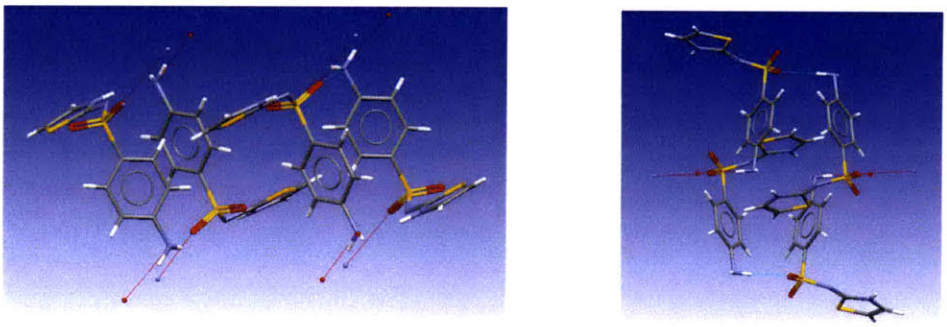

Sulfathiazole, Form II

Sulfathiazole, Form IV

Packing Polymorphism

Figure 1-1. Conformational polymorphism observed in Spiperone crystals: form I,[16] and form II;[17] packing polymorphism observed in Sulfathiazole crystals: form II, and form IV.[18]

1.1.2 Crystal Size Distribution (CSD)

The CSD and polymorphism are the two most important characteristics of crystals that determine the product quality, and are used as the most widely applied quality test for a crystalline product. The efficiency of any process for production of crystals relies on the size, shape and size distribution, as they affect downstream operations such as filtration, drying and formulation.[19] It is important to control the CSD of a pharmaceutical product and achieve as narrow a distribution as possible because a broad size distribution may lead to variation in bioavailability. The CSD obtained during crystallization is influenced by many processes, including rates of nucleation and growth, agglomeration, coalescence, attrition, and breakage.

1.1.3 Role of Supersaturation

Supersaturation is the driving force for crystallization, and is directly related to the chemical potential difference between the old and new phases.

$$\sigma = \frac{(\mu_{old} - \mu_{new})}{k_B T} = \frac{\Delta\mu}{k_B T} \tag{1.1}$$

where μ_{old} is the chemical potential of the solution phase, and μ_{new} is the chemical potential of the crystalline phase. Physically, $\Delta\mu$ represents the gain in free energy per molecule associated with the passage of the old phase to the new phase with lower Gibbs free energy.[20] In terms of measurable quantities, supersaturation can be defined as a function of the activity coefficient, or concentration of some crystallizing species, *i*.[21]

$$\sigma = \ln\left(\frac{a_i}{a_{i,e}}\right) \approx \ln\left(\frac{C_i}{C_{i,s}}\right) \tag{1.2}$$

where a_i is the activity of solute *i*, $a_{i,e}$ is the activity at which the solute and the condensate are in phase equilibrium. C_i is the actual concentration of *i* and $C_{i,s}$ is the solubility limit of *i*.[22] A supersaturated solution, although in a thermally equilibrium state, is not at a thermodynamically equilibrium state. Concentration fluctuations in the solution cause the solute molecules to form clusters. On a microscopic level, a dynamic situation exists where clusters, in the form of dimers, trimers, tetramers, and longer chains, are continuously formed and broken up. Eventually, when the cluster size reaches a critical number, a stable nucleus is born.[23] Among the many factors that affect crystal

nucleation and growth kinetics, supersaturation is the primary factor, directly influencing the number, size, habit, polymorphic form and the structure of the final products.

1.1.4 Modes of Crystallization

Supersaturation can be achieved in a number of ways: by cooling solution, by evaporating solvent, by adding an antisolvent, by changing the pH, by chemical reaction, or by a combination of the above.

a) Cooling: The solubility of a solute is a function of temperature, usually decreasing as the temperature is lowered. It is the most widely used method for generating supersaturation. This type of temperature-dependent solubility data is often used in industry to determine the cooling profile in the crystallizer.[24, 25]

b) Evaporation: If the solvent is evaporated, either by heating the solution to its boiling point, or by convective mass transport, or by vacuum suction, the solute concentration is increased, generating supersaturation.

c) Addition of antisolvent: Adding an antisolvent, in which the solute solubility is low, to a solvent, in which the solute solubility is high, generate supersaturation since the solute solubility in the final solvent composition becomes lower than the initial solubility in the solvent. The degree of supersaturation that can be achieved with this technique depends on the difference in solute solubility in the solvent and the antisolvent.

d) Changing pH: The solubility of a solute can also depend on the pH of the solution. In those cases, the pH can be modulated to decrease the solubility and generate supersaturation.

e) Chemical reaction: A chemical reaction can be used to decrease the solubility of the dissolved solute, creating supersaturation. For example, reactive species such as ions that participate in the precipitation of the solute can be added for this purpose.

Figure 1-2 depicts the generation of supersaturation by cooling (a) and by antisolvent addition (b). Lowering the temperature by ΔT, or by changing the solvent composition to 20-weight percent antisolvent, the solubility decreases to C_{eq}, and thus, a supersaturation of $\ln(C_0/C_{eq})$ is obtained for the solution.

a)

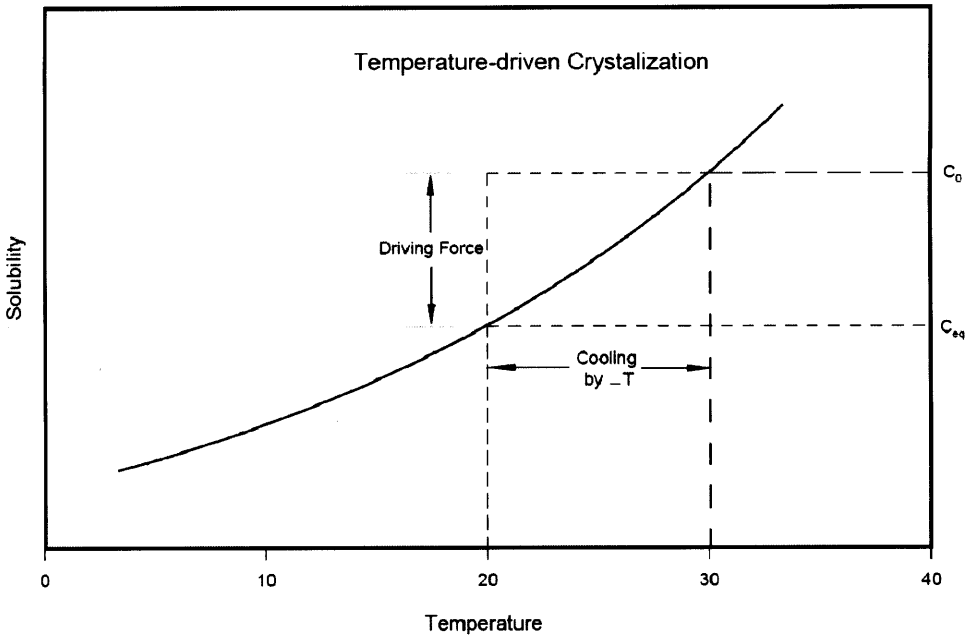

b)

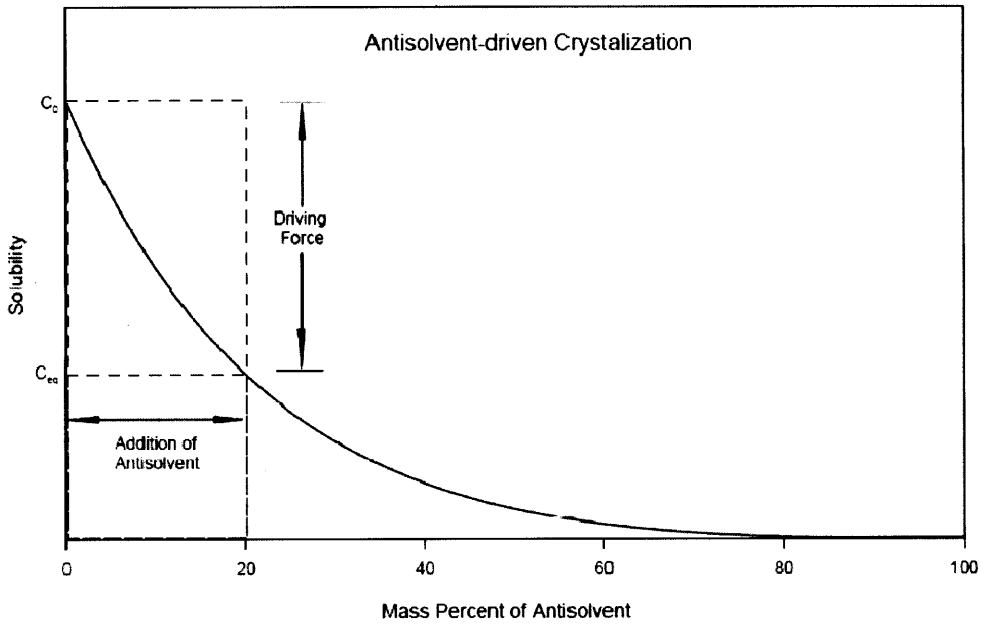

Figure 1-2. Supersaturation generation by cooling and antisolvent addition. a) Lowering the temperature by ΔT decreases the solubility from C_0 to C_{eq}, creating a driving force, C_{eq}/ C_0. b) Similarly, increasing the antisolvent mass percent decreases the solubility from C_0 to C_{eq}, and creates a driving force, C_{eq}/ C_0.

1.1.5 Phase Diagram of a Solution

Figure 1-3 depicts the phase diagram of a chemical system. The solubility curve is the saturation concentration plotted against a process parameter such as temperature, solvent composition, or pH. The metastable limit is the point where nucleation is first observed. The area below the solubility limit is the undersaturated zone and the area above the metastable limit is the supersaturated or labile zone. The area bounded by the solubility limit and the metastable limit is the metastable zone, and the width of this area is called Metastable Zone Width (MSZW). Although the solubility limit is a thermodynamic parameter, the metastable limit, and thus MSZW are kinetic parameters that depend on various operating conditions such as the rate of supersaturation generation,[23] reactor volume,[26] mixing speed,[27] and presence of impurities[28, 29]. Spontaneous nucleation only occurs in the labile zone and hence, MSZW is a measure of how difficult it is to nucleate a solute system. On the other hand, growth occurs as long as the system is above the solubility limit. Crystals dissolve when the system is below the solubility limit.[30]

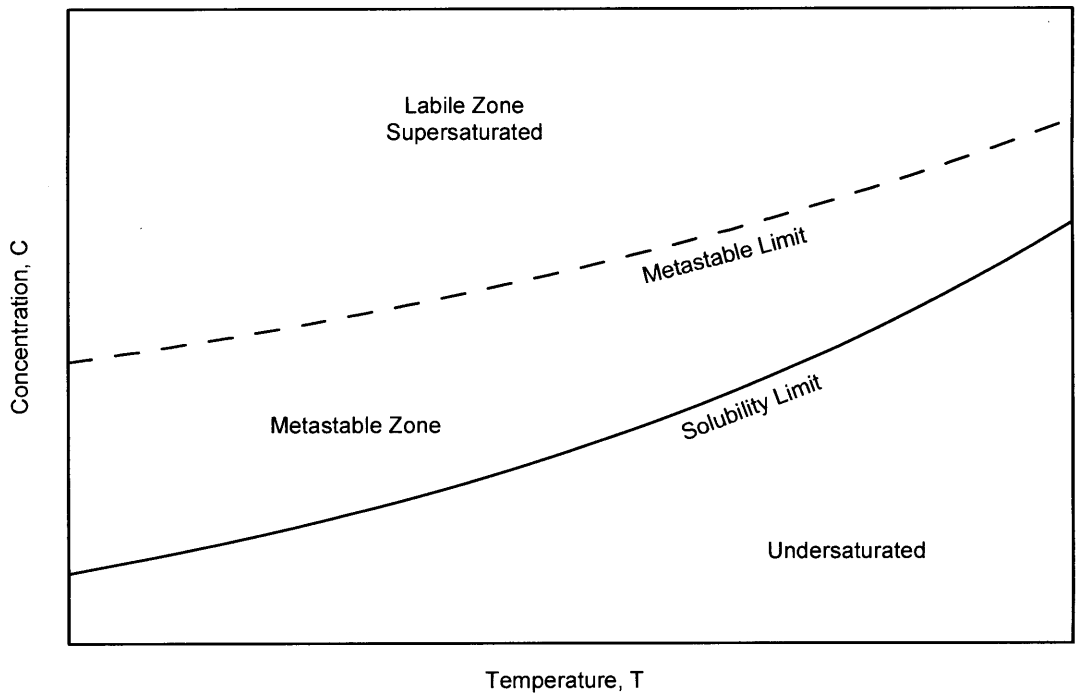

Figure 1-3. Typical phase diagram of a chemical system. The solid line represents the solubility limit and the dashed line represents the metastable limit. The region above the metastable limit is called the labile zone, the region bounded by the metastable limit and the solubility limit is called the metastable zone, and the region below the solubility limit is called the undersaturated zone.

1.2 Crystallization: the Two Step Process

Crystallization is considered as a two step process. The first step is nucleation, the birth of a stable crystal nucleus and the formation of a new solid phase. Nucleation is followed by crystal growth in the second step.

1.2.1 Nucleation

The rate and the mechanism of crystal formation, can be affected by supersaturation, rate of supersaturation generation and desupersaturation, diffusivity, temperature, impurities, and the reactivity of surfaces towards nucleation.[15] Nucleation can be either primary, which occurs in the absence of any crystal surface, or secondary, which requires the presence of a crystal surface in order to generate further nuclei. Primary nucleation can be either homogeneous nucleation, when the nuclei or pre-nucleation clusters form without being in contact with no phases or molecular species other than the old phase, or

heterogeneous nucleation, when nucleation or pre-nucleation cluster formation takes place while being in contact with other phases or molecular species.[31, 32]

Homogeneous Nucleation

The most well developed theory for homogenous nucleation is the capillary or classical theory of nucleation. It dates back to the work of Gibbs,[33] Volmer,[34] and others.[32, 35] The classical nucleation theory proposes successive addition of solute units to form the critical cluster. The free energy of a nucleus of critical size, l, at some supersaturation, σ, is given by the balance of the energy gained by the volume of the new phase, V_l, and the energy lost to form the surface area associated with the new phase, A_l.

$$\Delta G = -\frac{V_l}{\upsilon_{solute}} k_B T \sigma + A_l \gamma \qquad (1.3)$$

where υ_{solute} is the molecular volume of the solute and γ is the interfacial tension between the new phase and the solution. Consequently, the free energy, ΔG, increases with the cluster size, l, until a maximum is reached at l^*, which marks the nucleation event. As the new phase grows larger than l^*, the free energy decreases without bound. Figure 1-4 plots the free energies for alpha glycine using classical nucleation theory.

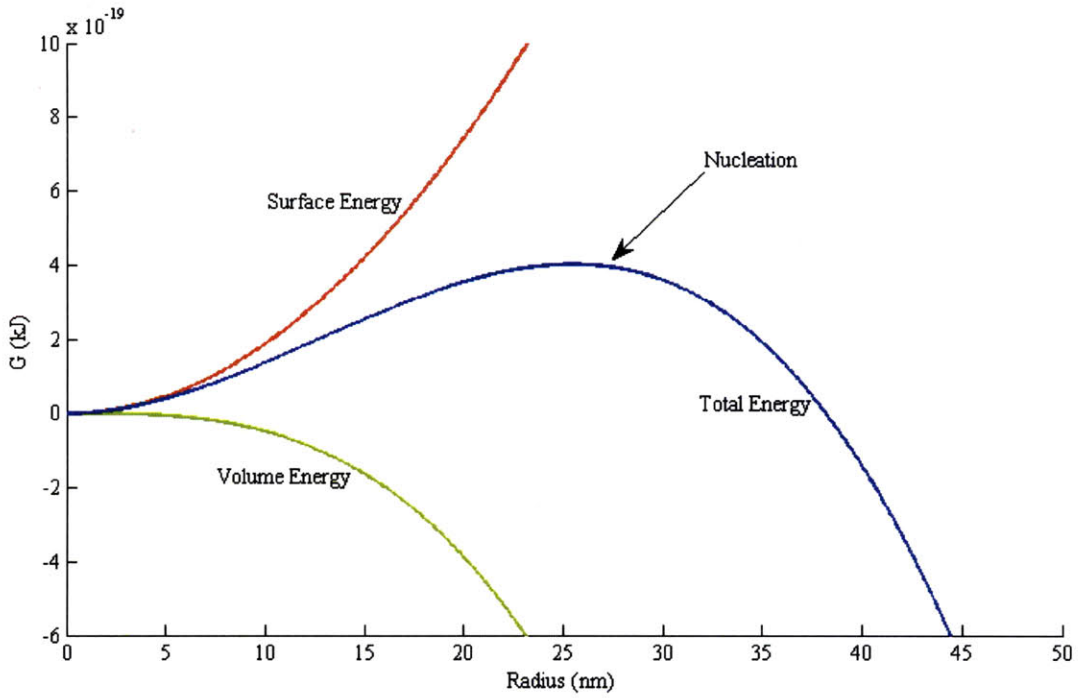

Figure 1-4. Energetics of alpha glycine at T=20°C and σ = 0.2.

Nucleation is a probabilistic event, with the chances for occurrence depending on the free energy barrier relative to $k_B T$. As the supersaturation increases, the free energy barrier, as well as the critical size, l^*, decreases, resulting in faster nucleation. Due to the activated nature of the nucleation process, the rate of homogeneous nucleation can be expressed classically in the form of the Arrhenius equation:

$$J = K_J \exp\left[-\frac{B_J \gamma^3}{T^3 \sigma^2}\right] \tag{1.4}$$

where J is the number of nuclei formed per unit of time per unit of volume. Equation 1.4 summarizes the effects of supersaturation, temperature, and interfacial tension on the nucleation rate. At lower supersaturation, the interfacial tension dominates and there is insufficient free energy to create a new surface. As supersaturation increases, the nucleation rate increases exponentially, eventually reaching a maximum. The nucleation theory predicts the transition behavior from the metastable zone to the labile zone fairly accurately.

However, the classical nucleation theory is limited by the assumptions it requires.[27] The most critical assumption in this theory is the capillary approximation, in which the small critical clusters of the new phase is assumed to represent macroscopic regions. This assumption becomes questionable for nuclei that may contain only tens of molecules. In addition, the macroscopic values of the interfacial tension used in the classical model, which is for an infinite planar surface, may not be an adequate representation of the actual interfacial tension of the new phase, particularly at the critical size.[36] Moreover, it is assumed in the classical nucleation theory that the Gibbs free energy due to the addition of a new species to the nucleus depends only on the nucleus size. However, the free energy may also depend on the configuration and the site of attachment of the new species. The assumption of equilibrium between the critical nucleus and the surrounding is also unrealistic for small critical nuclei, since the exchange of species between the two phases even at equilibrium is associated with fluctuations comparable with the nuclei size.[27]

Heterogeneous Nucleation

The nucleation process is usually enhanced by the presence of impurity particles, ions or foreign surfaces. In industrial crystallizers, nucleation is mostly heterogeneous, with concomitant secondary nucleation. This is because the foreign surface lowers the nucleation energy barrier. The wetting properties of the foreign substance and their atomic packing arrangement are known to affect the heterogeneous nucleation. The Gibbs free energy of the critical nucleus that forms through the heterogeneous, ΔG_{het}, is expressed as:

$$\Delta G_{c,het} = f\Delta G_{c,\text{hom}} \tag{1.5}$$

$$f = \frac{(2+\cos\theta)(1-\cos\theta)^2}{4} \tag{1.6}$$

where ΔG_{hom} is the Gibbs free energy of the critical nucleus in the homogeneous process, f is a geometric correction factor, and θ is the contact angle ($0 \leq \theta \leq 180$). If the foreign surface is not flat, which is the case of nano-sized foreign particles, the size of the foreign material also has to be taken into account. If the contact angle is 180°, as in the case of nonwetting situation, then f is 1, representing homogeneous nucleation. If the contact

angle is between 0 and 180°, then f is smaller than 1 and the nucleation energy barrier is reduced.[37]

Secondary nucleation can also occur by a number of different mechanisms, originating either from the parent crystal, or from the loosely ordered solute molecules near the crystal surface. Initial breeding occurs when the tiny crystallites, loosely bound to the preexisting crystals, act as nucleation sites. When dendritic crystals fragment and serve as nucleation sites, the process is called needle breeding. Microabrasion of crystals at high stirring speeds can also produce fragments that act as nucleation sites, which is called collision or attrition breeding.[38]

Induction Time

In the case of unseeded crystallization, the kinetics of nucleation can be measured with the induction time, defined as the time elapsed between the creation of supersaturation and the formation of the new phase. Induction time is a function of the solution temperature and supersaturation.[38] The induction period, t_{ind} is generally considered to be made of three parts: a relaxation time, t_r, for the system to reach a quasi-steady state distribution of molecular clusters; nucleation time, t_n; and the time a stable nucleus needs to grow to a detectable size, t_g.[35]

$$t_{ind} = t_r + t_n + t_g \tag{1.7}$$

1.2.2 Crystal Growth

Following nucleation, crystal growth occurs through a 2-dimensional molecular self-assembling, where the solute molecules from the supersaturated solution are added to the solid phase. Solute molecules migrate from the bulk solution to the crystal surface, adsorb, diffuse around the surface to find a suitable site, and are finally integrated into the crystal lattice. When the mass transfer is not limiting, surface integration is the rate limiting step of crystal growth. Crystal growth is known to take place in a layer-by-layer fashion with the linear growth velocity of a facet defined in a direction normal to it. Fig 1-5 illustrates the Kossel model, demonstrating the different sites for adsorption of growth units: terrace, step and kink.[39] Since a growth unit is attached to three surfaces in a kink site, it is the most energetically favorable. As growth units are added to a kink site,

the kink moves along a step and eventually a full layer on a facet is completed. Thus, the linear growth rate, v, of the face can be expressed in terms of the step velocity, v_0, the step height, h, and the interstep spacing, y_0:

$$v = {}^{v_0 h}\!/_{y_0} \tag{1.8}$$

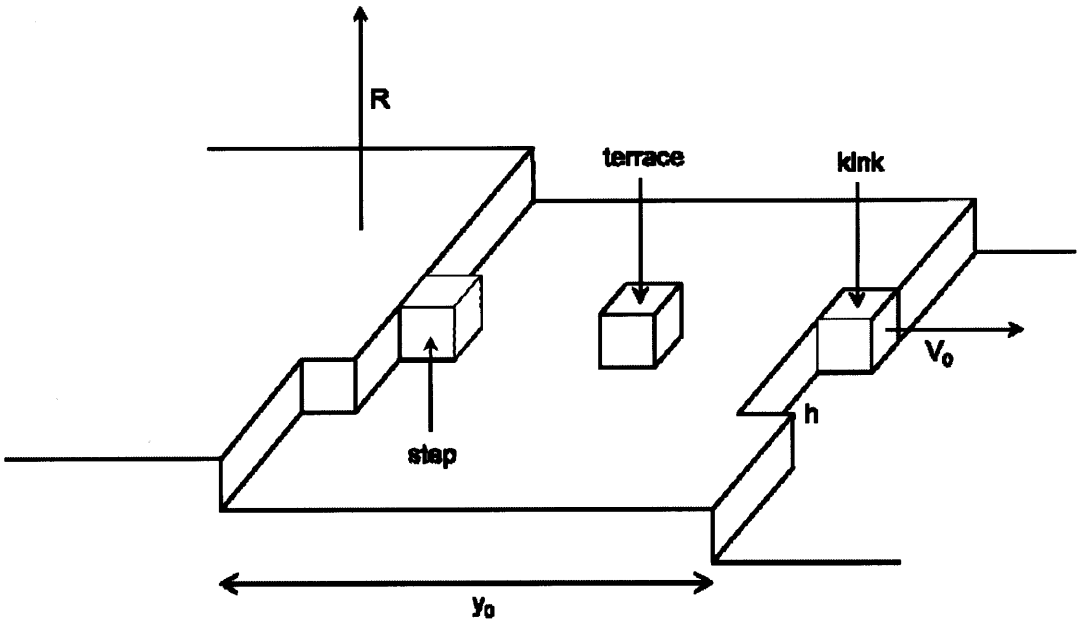

Figure 1-5. Kossel model: schematic of the topographic features on a growing crystal face, illustrating growth units at terrace, step, and kink sites.

The different theories on the different growth mechanisms have been thoroughly reviewed by O'Hara and Reid,[39] and Stickland-constable.[40] They can be classified into three main categories: continuous growth mechanism, birth and spread mechanism, and screw dislocation mechanism. Gilmer and Bennema have shown with computer simulations that for a simple Kossel model, the mechanism of crystal growth is determined by the surface entropy factor, α,[41] which can be approximated as:

$$\alpha = \xi\left(\frac{\Delta H_f}{RT} - \ln x_s\right) \tag{1.9}$$

In equation 1.9, ξ is the anisotropic factor, ΔH_f is the heat of fusion, and x_s is the solubility. The anisotropic factor describes the intermolecular interactions in the crystal surface and can be approximated as:

$$\xi = {E_{slice}}/{E_{cr}}, \tag{1.10}$$

where E_{slice} is the horizontal bond energy between two adjacent blocks, and E_{cr} is the total crystallization or lattice energy.[42] It has been proposed that when α is less than 3, the interface is rough, and growth occurs through continuous or normal mechanism. When α is between 3 and 4, the interface is better defined and growth may occur with surface nucleation methods. As α increases above 4, the interface becomes smoother and growth at low supersaturation occurs at the steps generated by defects.[43, 44]

Rough Surface Mechanism

In the case of a rough interface, there are many kink sites on the crystal surface. Thus, addition of growth units into the crystal lattice occurs easily and continuously. In this case, a continuous growth equation has been suggested:

$$G = k_R \sigma \tag{1.11}$$

In equation 1.11, G is the growth rate, k_R is the rate constant, and σ is the supersaturation as defined previously.

Surface Nucleation Mechanism

In the case of a smoother interface, $3 \leq \alpha \leq 4$, the growth occurs through the formation of a 2-D nucleus on the crystal surface and its subsequent spread to complete the layer. The nucleus is conceived of growing at a finite rate, independent of size, by the incorporation of growth units at the steps. Three types of surface nucleation mechanism have been widely used: mononuclear model, polynuclear model, birth and spread model. Mononuclear model depicts layer-by-layer growth, where only one nucleus exists at a time and the next nucleus forms only after the completion of the previous layer. In this case, the growth rate is expressed by equation 1.12

$$G = k_{MN} \sigma^{1/2} \exp\left(-\frac{g\gamma_E^{\ 2}}{3(k_B T)^2 \sigma} \right), \tag{1.12}$$

where k_{MN} is the rate constant of growth, γ_E is the edge surface tension, g is a shape factor and the exponential term represents the activation energy required for the formation of a critical 2-D nuclei. For circular nuclei, g equals to pi. Polynuclear model is the other extreme configuration of surface nucleation mechanism. In this case, multiple nuclei can exist on the same surface at a time and the rate is limited by the spread of the layer instead of nuclei formation. Hence, the completion of a layer occurs mostly through the formation of nuclei. The growth rate for polynuclear model is expressed as:

$$G = k_{PN}\sigma^{-3/2}\exp\left(-\frac{g\gamma_E^{\ 2}}{3(k_BT)^2\sigma}\right) \tag{1.13}$$

where k_{PN} is the rate constant of growth.

In between the two extreme cases, is the birth and spread model, also known as the nuclei-above-nuclei model. In this case, it is assumed that nuclei can possibly form on incomplete layers and grow at constant step advancement, independent of each other. The rate limiting process in this case is the formation of nuclei. The growth rate for birth and spread model can be expressed as:

$$G = k_{BS}\sigma^{5/6}\exp\left(-\frac{g\gamma_E^{\ 2}}{3(k_BT)^2\sigma}\right), \tag{1.14}$$

where k_{BS} is the rate constant of this model. This model fails to account for the observed growth rates at very low supersaturation, where the driving force necessary for surface nucleation is not achieved.[40] Surface nucleation models exhibit a strong dependency of growth on supersaturation since the time elapsing between two nucleation events decreases rapidly with an increase in supersaturation.[45]

Screw Dislocation Mechanism

At higher α value, the intermolecular interaction in the plane of the interface is enhanced, resulting in a much smoother surface to grow on. In this case, the crystal growth may occur mostly through the steps. BCF (Barton-Cabrera-Frank) theory proposes a mechanism in which steps are self-perpetrating. Once a screw dislocation has formed, that provides a way for the continuous growth of the steps, similar to a spiral staircase. Surface diffusion is assumed to be the rate limiting step in this mechanism and the growth rate is expressed as:

$$G = k_1 \sigma^2 \tanh\left(k_2/\sigma\right) \tag{1.13}$$

where k_1 and k_2 are constants. However, when the supersaturation, σ, is much greater than k_2, the growth rate assumes a linear relationship with supersaturation, similar to rough mechanism.

$$G = k_3 \sigma \tag{1.14}$$

where $k_3=k_1k_2$. On the other hand, when σ is much smaller than k_2, the growth rate assumes a parabolic relationship with supersaturation.

$$G = k_1 \sigma^2 \tag{1.15}$$

Crystal growth rates may vary in a number of ways, making it difficult to interpret the growth kinetics data. Two main phenomena that can cause such variation are distinguished as size dependent growth and growth rate dispersion. Apart from mass transfer limited case, size dependent growth can also result from the Gibbs-Thomson effect for small crystals, less than a few micrometers, with a decreasing growth rate for decreased crystal size,[46] as well as from size dependent integration kinetics. Dislocation density within a crystal may increase as a function of size, due to higher mechanical stress and increased incorporation of impurity atoms.[31, 46] In addition, there has been substantial experimental evidence that even when exposed to identical process conditions, different crystals of a given material and size may grow at different rates, simply because they experience different random fluctuations in defect density.[31]

1.3 Current State of Crystallization Process

Even though crystallization of inorganic compounds from solution has been studied in great detail over the years, crystallization of organic compounds, especially pharmaceuticals and other biomolecules, remain a "low tech area",[8] and more of an art rather than science.[47] However, it is imperative to understand the underlying physicochemical processes and the fundamentals of crystallization in order to design an optimal and efficient process.

1.3.1 Limitations of Batch Crystallizers

Conventionally, crystallization is usually achieved in batch mode in stirred tank reactors or flasks for both production, and research and development. Such syntheses often involve heterogeneous spatial and temporal distributions of process parameters,[47] such as temperature, important in temperature-driven crystallization, and concentration, important in evaporation-driven crystallization as well as in antisolvent-driven crystallization. Traditional batch processes also suffer from poorly controlled mixing of the reagents, important in precipitation and antisolvent-driven crystallization.[48] Crystallization process, on the other hand, is very sensitive to the process parameters and even minute changes in conditions, such as supersaturation, temperature impurity or cooling rate, can produce significant changes in the crystal properties, particularly crystal size, size distribution, shape, purity and defect structure.[8, 49, 50] These effects give rise to major batch-to-batch variation problems, leading to inconsistency of the final properties. In addition, variation across batch reactors may result in mixtures of polymorphic forms,[48] also affecting the reproducibility of solid state properties, including the product stability and kinetics.[8] Consequently, it becomes more challenging to obtain understanding of the fundamentals of the crystallization process for an organic system and obtain accurate kinetics data that can be used for scale-ups.

Moreover, the product from batch crystallization often has wide size distribution due to nonuniform temperature and process conditions across the reactor. Consequently, a number of downstream processing such as drying, milling, granulation, compression and filtration are required to fine-tune the final properties of product crystals,[51] decreasing the cost-efficiency of the process. Furthermore, downstream processes may induce polymorphic transformation.[52] This has been a major problem in the pharmaceutical industry as the properties of the drugs greatly vary from polymorphs to polymorphs. Downstream processing can also lead to various degree of disorder in the form of crystal defects and amorphous regions, giving further rise to reproducibility issues.

The limitations of batch crystallizers necessitate a better platform with superior control over process conditions, for elucidating on the fundamentals of the process. The need for advanced drug delivery systems, including nano- and micro-crystals, controlled release formulations, and reduction of manufacturing cost and complexity, calls for the

development of continuous, one-step crystallization that allows for precise control over the polymorphic form, crystal size, and other crystal properties.[8]

Continuous flow chemical reactors overcome some of the drawbacks of stirred-flask synthesis. Continuous crystallizers have the built-in flexibility for controlling the process parameters that influence crystal size distribution, and other solid state properties.[48] In particular, plug flow reactors ensure spatial homogeneity of concentration and temperature, and thus have the potential to provide great control over the crystallization process with uniform nucleation and crystal growth across reactor channels.

1.4 Motivation: Microreactors for Organic Crystallization

1.4.1 Microfluidic Systems

Scientific and commercial interests in microfluidic systems for chemical and particle synthesis,[53-55] analysis,[56, 57] cell handling,[58] kinetic studies,[59, 60] rapid parameter screening,[61] and reaction optimization[62] has greatly increased since its early development in the 1990s.[63-66] Microfluidic systems are miniaturized devices with dimensions in the range of 1 to 1000 micrometer, and volumes in the range of nanoliter to microliter. Scaling down to such small dimensions offers low Reynolds number and thus, well-defined laminar flow profiles. The small length scale in microfluidic devices also allows for enhanced heat and mass transfer, and thus better control over the process parameters, such as the temperature, and concentration. [63, 64, 67, 68] In addition, the advent of cutting-edge fabrication technologies enables the realization of complex device designs that can precisely control the contact mode of the reagents. Consequently, microfluidic devices have the potential to produce crystals with a narrower size distribution, eliminating subsequent downstream processing steps.[35, 48] In addition, microfluidic systems decrease waste, provide safety advantages, and require only minute amounts of reactants, which is most important when dealing with expensive materials such as pharmaceutical drugs.

Microfluidic devices can be easily integrated to process analytical tools and detection systems.[67] Microscopy and spectroscopy tools, such as UV,[60] IR,[59] Raman,[69] and Fluorescence[70] have been demonstrated as *in situ* monitoring tools with microfluidic

devices. This can be particularly important for crystallization of small organic molecules as the post-processing steps necessary for some of the offline characterization techniques, including SEM, TEM and X-ray, may induce polymorphic transition and crystal agglomeration, resulting in inaccurate information about the actual product made in the reactor. Thus, the *in situ* detection, along with superior control over synthesis conditions, can enable microfluidic devices to provide some fundamental insights into the processes involved in crystallization: nucleation and growth. This may reduce the time and effort invested in process development, which can be an expensive sector in the pharmaceutical industry. Furthermore, a microfluidic device for continuous crystallization may serve as a research tool to understand the challenges associated with the operation of continuous crystallizers, the desirable mode of operation.

Finally, microfluidic platforms have the potential to be used as a production tool for drugs that are needed in smaller quantities such as inhalable aerosols and highly potent cancer drugs. The ability to parallelize microchannels and scale them out, instead of scaling up, maintains the advantages of small dimension, yet enables this technology to increase the yield significantly. Recent research has demonstrated the feasibility of scaling out microfluidic syntheses to larger amounts of production.[71-73]

1.4.2 Microfluidic Systems for Crystallization

Several studies have demonstrated the use of microfluidic devices for continuous synthesis of inorganic,[54, 74-76] polymeric,[77-80] oxide,[81, 82] and metallic particles.[83, 84] For small organic molecules, however, most of the works so far have involved batch crystallization platforms, and there has not been a significant advancement in using microfluidic systems for continuous crystallization. Hansen and Quake have demonstrated the use of microfluidic devices for generating various conditions for protein crystallization.[85, 86] Using free interface diffusion, they have crystallized a number of protein molecules, including lysozyme, thaumatin, xylanase and glucose isomerase, at different crystallization conditions. Ismagilov and coworkers have demonstrated another technique of utilizing microfluidics to generate a variety of conditions of pH, precipitant, and protein concentration in nL-volume droplets and then using the droplets as individual batch reactors for protein crystallization.[87-89] Since then a number of studies have been

performed in the last few years with some variations of the two aforementioned studies. Kenis and coworkers have used a microfluidic device for evaporation-based batch crystallization of protein molecules, lysozyme and thaumatin.[90] He et al. have also used batch microfluidic platforms for evaporation-driven crystallization of glycine.[91] Laval et al. have used microfluidics to generate nL-volume droplets on chip and then used the droplets as individual micro batches for inorganic crystallization, specifically potassium nitrate.[92] Dombrowski et al. used droplet based microfluidics to confine and limit solute amounts in each droplet, which were then used as microbatches, mainly targeting the formation of single crystals in each droplet.[93]

All of the above-mentioned studies have used microfluidics as a high throughput screening device for batch crystallization, similar to 96-well plates, mostly for large organic molecules such as proteins. However, a microfluidics platform for continuous crystallization of small organic molecule that can exploit the discussed promises to their full potential, has not been demonstrated so far, and thus, serves as the motivation for this thesis.

1.5 Thesis Objectives and Layout

This thesis presents microfluidic devices for continuous crystallization and *in situ* detection of small organic molecules, and demonstrates the use of these devices for various applications related to crystallization. Chapter 2 describes the challenges associated with realizing continuous crystallization of organic molecules in microchannels. We develop an understanding of the reasons behind channel clogging, one of the most important challenges in this project, for organic systems. We also discuss various device issues related to particle synthesis, particularly crystallization, and our approaches towards resolving them. Chapter 3 presents a microfluidic device for continuous seeded crystallization. Glycine, the simplest amino acid, is used as the model system in this study. It has three polymorphs, each with a distinct habit and a distinct set of properties, translating to a different set of challenges. The presented microfluidic device for seeded crystallization is applied to each of these three polymorphic forms, demonstrating the versatility of the technique. We integrate a Raman Spectroscopy tool

for *in situ* detection of the polymorphic form. Microscopy tools are used to perform *in situ* characterization of crystal size and size distribution, which is subsequently used to extract the growth kinetics of different crystal facets of the three forms. Chapter 4 demonstrates the use of the developed microfluidic platform for additive screening through crystal habit modification studies. The centrosymmetric alpha form of glycine is used as the model system in this part of the thesis. In addition, we use the information obtained from habit modification studies to gain insights into the mechanism of the process. Chapter 5 presents a microfluidic device for continuous supercritical antisolvent crystallization of small organic molecules. We use acetaminophen as the representative model system for pharmaceutical active ingredients in this part of the thesis, and demonstrate the formation of micron-sized crystals. We also demonstrate that the crystal habit for this system can be tuned by the selection of appropriate solvents. Chapter 6 concludes the thesis with a summary of the technology developed in this work, scale-out considerations and some potential directions for future work.

The continuous microfluidic platform developed in this thesis presents a research tool for gaining fundamental insights into the elusive process of crystallization, including nucleation and growth. The devices can be potentially used for the production of low yield systems such as highly potent cancer drugs and inhalable aerosols, which also have stringent requirements over size and size distribution that are difficult to meet in batch systems. In addition, the developed microfluidic devices can be used as a research tool to facilitate the understanding of the challenges associated with continuous manufacturing of pharmaceuticals – thus being a step towards continuous manufacturing itself.

1.6 List of Variables

σ	supersaturation
μ_{old}	chemical potential of the solution phase
μ_{new}	chemical potential of the crystalline phase
$\Delta\mu$	free energy difference between the old and the new phase per molecule
a_i	activity of solute *i*
$a_{i,e}$	activity at which the solute and the condensate are in phase equilibrium
C_i	concentration of species *i*
$C_{i,s}$	solubility limit of species *i*
ΔG	Gibbs free energy difference
V_l	volume of liquid phase
A_l	surface area associated with the newly formed liquid phase
k_B	Boltzmann constant
T	temperature
v_{solute}	molecular volume of the solute
γ	interfacial tension between the new phase and the solution
J	number of nuclei formed per unit of time per unit of volume
ΔG_{het}	Gibbs free energy change in heterogeneous crystallization
ΔG_{hom}	Gibbs free energy change in homogeneous crystallization process
f	geometric correction factor
θ	contact angle ($0 \leq \theta \leq 180$)
t_{ind}	induction period
t_r	relaxation time required to reach a quasi-steady state distribution of molecular clusters
t_n	nucleation time
t_g	time required for a stable nucleus to grow to a detectable size
v	linear growth rate
v_0	step velocity
h	step height
y_0	interstep spacing

α	surface entropy factor
ξ	anisotropic factor
ΔH_f	heat of fusion
x_s	solubility
E_{slice}	horizontal bond energy between two adjacent crystal blocks
E_{cr}	total crystallization or lattice energy
k_R	rate constant of rough growth mechanism
k_{MN}	rate constant of mononuclear growth model
g	shape factor
γ_E	edge surface tension
k_{PN}	rate constant of polynuclear model
k_{BS}	rate constant of birth and spread model
k_{SN}	rate constant of surface nucleation
k_1, k_2, k_3	constants in BCF model

1.7 References

[1] D. T. J. Hurle, *Handbook of Crystal Growth, Vol. 1*, North-Holland, New York, **1993**.

[2] F. D. Adams, *The Birth and Development of Geological Sciences*, Dover, New York, **1954**.

[3] N. L. Abbott, New horizons for surfactant science in chemical engineering. *Aiche Journal,* **2001**, *47*(12), 2634-2639.

[4] R. W. Hartel, Crystallization in foods. in *Handbook of Industrial Crystallization,* 2nd ed. (Ed.: A. S. Myerson), Butterworth-Heinemann, **2002**, pp. 287-304.

[5] S. A. Middlebrooks, & J. B. Rawlings, Model predictive control of Si1-xGex thin film chemical-vapor deposition. *Ieee Transactions on Semiconductor Manufacturing,* **2007**, *20*(2), 114-125.

[6] K. H. W. Herbst, *Industrial organic pigments: production, properties, applications*, 3rd ed., Wiley-VCH Verlag GmbH & Co. KGaA, Weinheim, **2004**.

[7] R. Hilfiker, *Polymorphism in the Pharmaceutical Industry*, WILEY-VCH Verlag GmbH & Co. KGaA, Weinheim, Germany, **2006**.

[8] B. Y. Shekunov, & P. York, Crystallization processes in pharmaceutical technology and drug delivery design. *Journal of Crystal Growth,* **2000**, *211*(1-4), 122-136.

[9] C. Valder, & D. Merrifield, *SmithKline Beecham R&D News,* **1996**, *32*, 1.

[10] C. R. Gardner, O. Almarsson, H. M. Chen, S. Morissette, M. Peterson, Z. Zhang, S. Wang, A. Lemmo, J. Gonzalez-Zugasti, J. Monagle, J. Marchionna, S. Ellis, C. McNulty, A. Johnson, D. Levinson, & M. Cima, Application of high throughput technologies to drug substance and drug product development. *Computers & Chemical Engineering,* **2004**, *28*(6-7), 943-953.

[11] J. D. Dunitz, & J. Bernstein, Disappearing polymorphs. *Accounts of Chemical Research,* **1995**, *28*(4), 193-200.

[12] G. G. Z. Zhang, D. Law, E. A. Schmitt, & Y. H. Qiu, Phase transformation considerations during process development and manufacture of solid oral dosage forms. *Advanced Drug Delivery Reviews,* **2004**, *56*(3), 371-390.

[13] J. Bernstein, *Polymorphism in Molecular Crystals*, Clarendon Press, Oxford University Press, New York, **2002**.

[14] R. Storey, R. Docherty, P. Higginson, C. Dallman, C. Gilmore, G. Barr, & W. Dong, Automation of solid form screening procedures in the pharmaceutical industry - how to avoid the bottlenecks. *Crystallography Reviews,* **2004**, *10*(1), 45-56.

[15] S. R. Vippagunta, H. G. Brittain, & D. J. W. Grant, Crystalline solids. *Advanced Drug Delivery Reviews,* **2001**, *48*(1), 3-26.

[16] M. H. J. Koch, Crystal and molecular-structure of 8-[3-(para-fluorobenzoyl)propyl]-1-phenyl-1,3,8-triazaspiro[4,5]decan-4- one, $C_{23}H_{26}N_3O_2F$. *Acta Crystallographica,* **1973**, *B 29*, 379-382.

[17] M. Azibi, M. Draguetbrughmans, R. Bouche, B. Tinant, G. Germain, J. P. Declercq, & M. Vanmeerssche, Conformational study of 2 polymorphs of spiperone - possible consequences on the interpretation of pharmacological activity. *Journal of Pharmaceutical Sciences,* **1983**, *72*(3), 232-235.

[18] N. Blagden, R. J. Davey, H. F. Lieberman, L. Williams, R. Payne, R. Roberts, R. Rowe, & R. Docherty, Crystal chemistry and solvent effects in polymorphic systems - Sulfathiazole. *Journal of the Chemical Society-Faraday Transactions,* **1998**, *94*(8), 1035-1044.

[19] K. A. Berglund, Analysis and measurement of crystallization utilizing the population balance. in *Handbook of Industrial Crystallization* (Ed.: A. S. Myerson), Butterworth-Heinemann, **2002**, pp. 101-113.

[20] D. Kashchiev, *Nucleation: basic theory with applications*, Butterworth Heinemann, Oxford, **2000**.

[21] J. G. R. J. Dayey, *From molecules to crystallizers*, Oxford University Press, U.K., **2000**.

[22] O. Sohnel, & J. Garside, *Precipitation, Basic Principles and Industrial Application*, Butterworth-Heinesmann, Oxford, **1992**.

[23] R. M. Ginde, & A. S. Myerson, Effect of impurities on cluster growth and nucleation. *Journal of Crystal Growth,* **1993**, *126*(2-3), 216-222.

[24] A. G. Jones, & J. W. Mullin, Programmed cooling crystallization of potassium sulfate solutions. *Chemical Engineering Science,* **1974**, *29*(1), 105-118.

[25] J. W. Mullin, & J. Nyvlt, Programmed cooling of batch crystallizers. *Chemical Engineering Science,* **1971**, *26*(3), 369-377.

[26] Y. J. Yi, & A. S. Myerson, Laboratory scale batch crystallization and the role of vessel size. *Chemical Engineering Research & Design,* **2006**, *84*(A8), 721-728.

[27] J. Nyvlt, O. Sohnel, M. Matuchova, & M. Broul, *The Kinetics of Industrial Crystallization*, Elsevier, Amsterdam, **1985**.

[28] A. S. Myerson, & S. M. Jang, A comparison of binding-energy and metastable zone width for adipic acid with various additives. *Journal of Crystal Growth,* **1995**, *156*(4), 459-466.

[29] K. Sangwal, & E. Mielniczek-Brzoska, Effect of impurities on metastable zone width for the growth of ammonium oxalate monohydrate crystals from aqueous solutions. *Journal of Crystal Growth,* **2004**, *267*(3-4), 662-675.

[30] A. D. Randolph, & M. A. Larson, *Theory of Particulate Processes*, Academic Press, Inc., **1988**.

[31] J. Garside, A. Mersmann, & J. Nyvlt, *Measurement of Crystal Growth and Nucleation Rates*, 2nd ed., Institution of Chemical Engineers (IChemE), Rugby, UK, **2002**.

[32] I. V. Markov, *Crystal Growth for Beginners: Fundamentals of Nucleation, Crystal Growth and Epitaxy*, World Scientific Publishing Co. Pte. Ltd. , London, **1998**.

[33] J. W. Gibbs, On the equilibrium of heterogeneous substances. in *Collected works*, Longmans, Green and Co. , New York, **1928**.

[34] M. Volmer, & A. Weber, Germ-formation in oversaturated figures. *Zeitschrift Fur Physikalische Chemie--Stochiometrie Und Verwandtschaftslehre,* **1926**, *119*(3/4), 277-301.

[35] J. W. Mullin, *Crystallization*, Butterworth-Heinemann, Oxford, **2001**.

[36] D. W. Oxtoby, Nucleation of first-order phase transitions. *Accounts of Chemical Research,* **1998**, *31*(2), 91-97.

[37] A. Mersmann, *Crystallization Technology Handbook*, 2nd ed., Marcel Dekker, Inc., New York, **2001**.
[38] A. S. Myerson, & R. Ginde, Crystals, crystal growth, and nucleation. in *Handbook of Industrial Crystallization* (Ed.: A. S. Myerson), Butterworth-Heinemann, **2002**, pp. 33-65.
[39] M. Ohara, & R. C. Reid, *Modelling Crystal Growth Rates from Solution*, Englewood Cliffs, Prentice-Hall, New Jersey, **1973**.
[40] R. F. Strickland-Constable, *Kinetics and Mechanisms of Crystallization*, Academic Press, London, **1968**.
[41] G. H. Gilmer, & P. Bennema, Computer simulation of crystal surface-structure and growth kinetics. *Journal of Crystal Growth,* **1972**, *13*(MAY), 148-153.
[42] R. J. Davey, & J. Garside, *From Molecules to Crystallizers*, Oxford University Press, U.K., **2000**.
[43] J. R. Bourne, & R. J. Davey, Role of solvent-solute interactions in determining crystal-growth mechanisms from solution .2. growth kinetics of hexamethylene tetramine. *Journal of Crystal Growth,* **1976**, *36*(2), 287-296.
[44] N. R.-H. L. Li, Growth kinetics and mechanim of glycine crystals. *Journal of Crystal Growth,* **1992**, *121*, 33-38.
[45] A. Mersmann, A. Eble, & C. Heyer, Crystal Growth. in *Crystallizaiton Technology Handbook*, 2nd ed. (Ed.: A. Mersmann), Marcel Dekker, Inc., New York, **2001**, pp. 81-143.
[46] J. Garside, & R. J. Davey, Secondary contact nucleation - kinetics, growth and scale-up. *Chemical Engineering Communications,* **1980**, *4*(4-5), 393-424.
[47] A. Behr, V. A. Brehme, C. L. J. Ewers, H. Gron, T. Kimmel, S. Kuppers, & I. Symietz, New developments in chemical engineering for the production of drug substances. *Engineering in Life Sciences,* **2004**, *4*(1), 15-24.
[48] M. J. Mollan, & M. Lodaya, Continuous processing in pharmaceutical manufacturing. *American Pharmaceutical Review,* **2004**(July/August).
[49] I. Ludlambrown, & P. York, The crystalline modification of succinic acid by variations in crystallization conditions. *Journal of Physics D-Applied Physics,* **1993**, *26*(8B), B60-B65.
[50] B. Y. Shekunov, D. J. W. Grant, R. J. Latham, & J. N. Sherwood, In situ optical interferometric studies of the growth and dissolution behavior of paracetamol (acetaminophen) crystals .3. Influence of growth in the presence of p-acetoxyacetanilide. *Journal of Physical Chemistry B,* **1997**, *101*(44), 9107-9112.
[51] H. Gron, P. Mougin, A. Thomas, G. White, D. Wilkinson, R. B. Hammond, X. J. Lai, & K. J. Roberts, Dynamic in-process examination of particle size and crystallographic form under defined conditions of reactant supersaturation as associated with the batch crystallization of monosodium glutamate from aqueous solution. *Industrial & Engineering Chemistry Research,* **2003**, *42*(20), 4888-4898.
[52] M. L. Maccalman, K. J. Roberts, C. Kerr, & B. Hendriksen, Online processing of pharmaceutical materials using in-situ x-ray diffraction. *Journal of Applied Crystallography,* **1995**, *28*, 620-622.
[53] M. Brivio, W. Verboom, & D. N. Reinhoudt, Miniaturized continuous flow reaction vessels: influence on chemical reactions. *Lab on a Chip,* **2006**, *6*(3), 329-344.

[54] S. A. Khan, A. Gunther, M. A. Schmidt, & K. F. Jensen, Microfluidic synthesis of colloidal silica. *Langmuir,* **2004**, *20*(20), 8604-8611.
[55] S. Marre, & K. F. Jensen, Synthesis of micro and nanostructures in microfluidic systems. *Chemical Society Reviews,* **2010**, *39*(3), 1183-1202.
[56] R. Herzig-Marx, K. T. Queeney, R. J. Jackman, M. A. Schmidt, & K. F. Jensen, Infrared spectroscopy for chemically specific sensing in silicon-based microreactors. *Analytical Chemistry,* **2004**, *76*(21), 6476-6483.
[57] R. Herzig-Marx, K. T. Queeney, R. J. Jackman, M. A. Schmidt, & K. F. Jensen, Integration of multiple internal reflection (MIR) infrared spectroscopy with silicon-based chemical microreactors. *Abstracts of Papers of the American Chemical Society,* **2002**, *223*, U196-U196.
[58] J. El-Ali, P. K. Sorger, & K. F. Jensen, Cells on chips. *Nature,* **2006**, *442*(7101), 403-411.
[59] T. M. Floyd, M. A. Schmidt, & K. F. Jensen, Silicon micromixers with infrared detection for studies of liquid-phase reactions. *Industrial & Engineering Chemistry Research,* **2005**, *44*(8), 2351-2358.
[60] R. J. Jackman, T. M. Floyd, R. Ghodssi, M. A. Schmidt, & K. F. Jensen, Microfluidic systems with on-line UV detection fabricated in photodefinable epoxy. *Journal of Micromechanics and Microengineering,* **2001**, *11*(3), 263-269.
[61] E. R. Murphy, J. R. Martinelli, N. Zaborenko, S. L. Buchwald, & K. F. Jensen, Accelerating reactions with microreactors at elevated temperatures and pressures: Profiling aminocarbonylation reactions. *Angewandte Chemie-International Edition,* **2007**, *46*(10), 1734-1737.
[62] D. M. Ratner, E. R. Murphy, M. Jhunjhunwala, D. A. Snyder, K. F. Jensen, & P. H. Seeberger, Microreactor-based reaction optimization in organic chemistry glycosylation as a challenge. *Chemical Communications,* **2005**(5), 578-580.
[63] H. V. Ehrfeld W, Lowe H, *Microreactors: New Technology for Modern Chemistry*, Wiley-VCH, Weinheim, **2000**.
[64] K. F. Jensen, Microchemical systems: Status, challenges, and opportunities. *Aiche Journal,* **1999**, *45*(10), 2051-2054.
[65] A. Manz, D. J. Harrison, E. M. J. Verpoorte, J. C. Fettinger, H. Ludi, & H. M. Widmer, Miniaturization of chemical-analysis systems - a look into next century technology or just a fashionable craze. *Chimia,* **1991**, *45*(4), 103-105.
[66] R. F. Service, Miniaturization puts chemical plants where you want them. *Science,* **1998**, *282*(5388), 400-400.
[67] K. F. Jensen, Microreaction engineering - is small better? *Chemical Engineering Science,* **2001**, *56*(2), 293-303.
[68] A. J. deMello, Control and detection of chemical reactions in microfluidic systems. *Nature,* **2006**, *442*(7101), 394-402.
[69] P. D. I. Fletcher, S. J. Haswell, & X. L. Zhang, Monitoring of chemical reactions within microreactors using an inverted Raman microscopic spectrometer. *Electrophoresis,* **2003**, *24*(18), 3239-3245.
[70] E. Destandau, J. P. Lefevre, A. C. F. Eddine, S. Desportes, M. C. Jullien, R. Hierle, I. Leray, B. Valeur, & J. A. Delaire, A novel microfluidic flow-injection analysis device with fluorescence detection for cation sensing. Application to potassium. *Analytical and Bioanalytical Chemistry,* **2007**, *387*(8), 2627-2632.

[71] N. de Mas, A. Guenther, T. Kraus, M. A. Schmidt, & K. F. Jensen, Scaled-out multilayer gas-liquid microreactor with integrated velocimetry sensors. *Ind. Eng. Chem. Res.*, **2005**, *44*(24), 8997 - 9013.

[72] N. de Mas, A. Guenther, M. A. Schmidt, & K. F. Jensen, Microfabricated multiphase reactors for the selective direct fluorination of aromatics. *Industrial & Engineering Chemistry Research,* **2003**, *42*(4), 698-710.

[73] N. de Mas, A. Guenther, M. A. Schmidt, & K. F. Jensen, Scalable microfabricated reactors for direct fluorination reactions. *Proceedings of IEEE Transducers, Boston,* **2003**.

[74] S. Marre, J. Park, J. Rempel, J. Guan, M. G. Bawendi, & K. F. Jensen, Supercritical continuous-microflow synthesis of narrow size distribution quantum dots. *Advanced Materials,* **2008**, *20*(24), 4830-4834.

[75] B. K. H. Yen, A. Gunther, M. A. Schmidt, K. F. Jensen, & M. G. Bawendi, A microfabricated gas-liquid segmented flow reactor for high-temperature synthesis: The case of CdSe quantum dots. *Angewandte Chemie-International Edition,* **2005**, *44*(34), 5447-5451.

[76] S. A. Khan, & K. F. Jensen, Microfluidic synthesis of titania shells on colloidal silica. *Advanced Materials,* **2007**, *19*(18), 2556-2560.

[77] D. Dendukuri, T. A. Hatton, & P. S. Doyle, Synthesis and self-assembly of amphiphilic polymeric microparticles. *Langmuir,* **2007**, *23*(8), 4669-4674.

[78] D. Dendukuri, K. Tsoi, T. A. Hatton, & P. S. Doyle, Controlled synthesis of nonspherical microparticles using microfluidics. *Langmuir,* **2005**, *21*(6), 2113-2116.

[79] R. Karnik, F. Gu, P. Basto, C. Cannizzaro, L. Dean, W. Kyei-Manu, R. Langer, & O. C. Farokhzad, Microfluidic platform for controlled synthesis of polymeric nanoparticles. *Nano Letters,* **2008**, *8*(9), 2906-2912.

[80] C. A. Serra, & Z. Q. Chang, Microfluidic-assisted synthesis of polymer particles. *Chemical Engineering & Technology,* **2008**, *31*(8), 1099-1115.

[81] A. Abou-Hassan, O. Sandre, S. Neveu, & V. Cabuil, Synthesis of Goethite by Separation of the Nucleation and Growth Processes of Ferrihydrite Nanoparticles Using Microfluidics. *Angewandte Chemie-International Edition,* **2009**, *48*(13), 2342-2345.

[82] K. Sue, K. Kimura, & K. Arai, Hydrothermal synthesis of ZnO nanocrystals using microreactor. *Materials Letters,* **2004**, *58*(25), 3229-3231.

[83] J. M. Kohler, L. Abahmane, J. Wagner, J. Albert, & G. Mayer, Preparation of metal nanoparticles with varied composition for catalytical applications in microreactors. *Chemical Engineering Science,* **2008**, *63*(20), 5048-5055.

[84] J. Wagner, & J. M. Kohler, Continuous synthesis of gold nanoparticles in a microreactor. *Nano Letters,* **2005**, *5*(4), 685-691.

[85] C. L. Hansen, E. Skordalakes, J. M. Berger, & S. R. Quake, A robust and scalable microfluidic metering method that allows protein crystal growth by free interface diffusion. *Proceedings of the National Academy of Sciences of the United States of America,* **2002**, *99*(26), 16531-16536.

[86] C. L. Hansen, S. Classen, J. M. Berger, & S. R. Quake, A microfluidic device for kinetic optimization of protein crystallization and in situ structure determination. *Journal of the American Chemical Society,* **2006**, *128*(10), 3142-3143.

[87] B. Zheng, J. D. Tice, L. S. Roach, & R. F. Ismagilov, A droplet-based, composite PDMS/glass capillary microfluidic system for evaluating protein crystallization conditions by microbatch and vapor-diffusion methods with on-chip X-ray diffraction. *Angewandte Chemie-International Edition,* **2004**, *43*(19), 2508-2511.

[88] C. J. Gerdts, V. Tereshko, M. K. Yadav, I. Dementieva, F. Collart, A. Joachimiak, R. C. Stevens, P. Kuhn, A. Kossiakoff, & R. F. Ismagilov, Time-controlled microfluidic seeding in nL-volume droplets to separate nucleation and growth stages of protein crystallization. *Angewandte Chemie-International Edition,* **2006**, *45*(48), 8156-8160.

[89] L. Li, W. B. Du, & R. F. Ismagilov, Multiparameter Screening on SlipChip Used for Nanoliter Protein Crystallization Combining Free Interface Diffusion and Microbatch Methods. *Journal of the American Chemical Society*, *132*(1), 112-119.

[90] S. Talreja, D. Y. Kim, A. Y. Mirarefi, C. F. Zukoski, & P. J. A. Kenis, Screening and optimization of protein crystallization conditions through gradual evaporation using a novel crystallization platform. *Journal of Applied Crystallography,* **2005**, *38*(6), 988-995.

[91] G. W. He, V. Bhamidi, S. R. Wilson, R. B. H. Tan, P. J. A. Kenis, & C. F. Zukoski, Direct growth of gamma-glycine from neutral aqueous solutions by slow, evaporation-driven crystallization. *Crystal Growth & Design,* **2006**, *6*(8), 1746-1749.

[92] P. Laval, A. Crombez, & J. B. Salmon, Microfluidic Droplet Method for Nucleation Kinetics Measurements. *Langmuir,* **2009**, *25*(3), 1836-1841.

[93] R. D. Dombrowski, J. D. Litster, N. J. Wagner, & Y. He, Crystallization of alpha-lactose monohydrate in a drop-based microfluidic crystallizer. *Chemical Engineering Science,* **2007**, *62*(17), 4802-4810.

2 Microfluidics for Continuous Crystallization

This chapter explores the scope of microfluidic devices for continuous crystallization of small organic molecules. Microfluidic devices have been widely used for particle synthesis over the last few years, mostly for inorganic, polymeric and metallic particles of various materials and functionalities.[1-9] The application of microfluidics for organic molecules, however, have mostly been limited as a high throughput tool for protein crystallization and have focused on droplet based methods where droplets are used as microbatches.[10-15] One of the main challenges of continuous crystallization in microchannels is channel clogging,[5] resulting from a number of factors. We deal with this issue of clogging extensively in this chapter and develop an understanding of the mechanism of channel clogging for organic solids. In addition, we attempt to develop an understanding of the important factors in the nucleation of small organic molecules with regards to microfluidic systems.

First, we describe the selection of crystallization methodology and device material. We discuss the requirements for continuous crystallization and how that impacts the choice of operating conditions. We then present the various device issues related to particle synthesis, particularly crystallization, and the approaches we take to address them. We find interesting nucleation behavior of other materials at the operating conditions, which can influence the nucleation of the solute of interest. In addition, we discuss channel clogging that often results from nucleation, particularly for organic molecules. We find that a number of factors contribute to the ultimate channel clogging, including interactions of solids with channel surfaces, leading to solid deposition on walls; interactions of crystals with each other to create large units, leading to sedimentation; and high density of crystals and high driving force that result from spontaneous nucleation of organic materials. We also discuss the inherent nucleation behavior of these systems that amplifies the abovementioned issues. In order to address solid-channel surface interactions, we control surface properties of microchannel surfaces; we discuss surface modification techniques to minimize such interaction. In order to address the difficulty of

handling high crystal density, we use sheath flow reactor and discuss how that impacts the crystallization process. Finally, we discuss how all the insights learned in this chapter is used in realizing continuous crystallization in microchannels, which is demonstrated in subsequent chapters.

2.1 Design Criteria

2.1.1 Mode of Crystallization

In general, nucleation of organic molecules are known to be slower than that for inorganic systems.[16] This poses a problem for microfluidic devices that usually have a short residence time. As briefly discussed in chapter 1, the driving force for crystallization is supersaturation, which can be generated by modulating a number of parameters, including temperature, solvent composition, pH, and concentration through solvent evaporation. The mode of crystallization is chosen here using the induction time. If it is assumed that the induction time, t_{ind}, as discussed in chapter 1, is dominated by the nucleation time, t_n, then the induction time can be considered to be inversely proportional to the rate of nucleation, J.[17]

$$t_{ind} \propto J^{-1} = K_J \exp\left[-\frac{B_J \gamma^3}{T^3 \sigma^2}\right] \qquad 2\text{-}1$$

and

$$\ln t_{ind} = C_1 + C_2 \sigma^{-2} \qquad 2\text{-}2$$

If t_{ind} is dominated by t_g, the time required for growth of nuclei to a detectable size, then the induction time can be considered to be inversely proportional to the growth rate, G. In this case, either $t_{ind} \propto \sigma^{-1}$, $t_{ind} \propto \sigma^{-2}$, or $lnt_{ind} \propto \sigma^{-1}$ results, depending on the growth mechanism.[18] Therefore, t_{ind} is a strong function of supersaturation in all cases, decreasing with an increase in supersaturation. Although temperature modulation is the most widely used crystallization technique,[19, 20] the supersaturation achieved in this method typically results in an induction time of hours for organic molecules, depending on the temperature difference, ΔT, and the rate of cooling. The typical residence time in microfluidic devices ranges from a fraction of a second to tens of minutes, making it

difficult to perform temperature modulated crystallization. The solvent composition, on the other hand, affects the solubility much more strongly, as illustrated in Figure 2-1. A much higher supersaturation can be achieved with antisolvent addition, reducing the induction time to seconds, and making crystallization feasible in microfluidic devices. Consequently, antisolvent addition has been used as the supersaturation generation method in the current study.

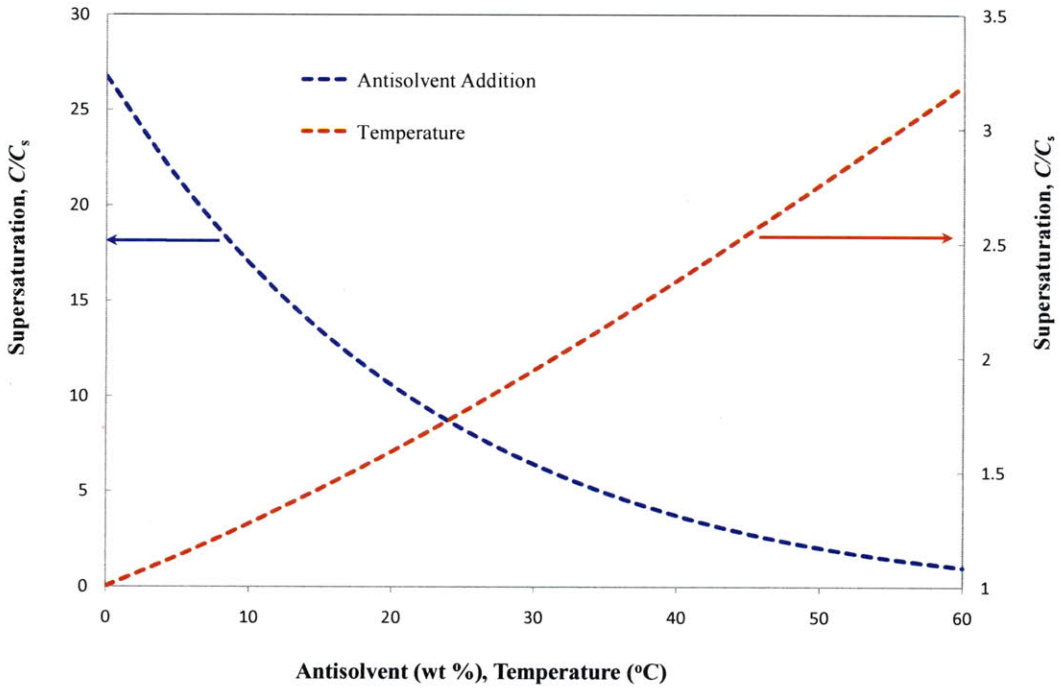

Figure 2-1. Supersaturation that can be generated by either antisolvent addition (e.g. using ethanol as the antisolvent and water as the solvent), or cooling for alpha-glycine, demonstrating that the solubility can be much more sensitive to the solvent composition than temperature.

2.1.2 Mixing

Mixing is an important issue in antisolvent crystallization, where the nucleation kinetics is fast.[21] Lack of rapid mixing may affect the properties of the crystal products such as the particle size distribution, morphology and purity. To minimize such effects, the mixing characteristic time has to be shorter than the induction time.[22]

In microchannels, the low Reynolds number naturally allows mixing to occur only through molecular diffusion and the characteristic mixing time, t_M, is expressed in terms of the characteristic diffusion length, L and the diffusion coefficient, D.

$$t_M = L^2/D \qquad 2\text{-}3$$

Various methods for enhancing mixing in microchannels have been demonstrated,[23] most of which require complicated fabrication process. Parallel lamination is used in this work for enhancing mixing since it can be easily fabricated. The idea is to split the inlet streams into multiple sub-streams and join them into one laminae so as to increase the contact surface between the reagents, and decrease the characteristic diffusion length, L.[24]

2.1.3 Material Selection

Microfluidic devices have been made of glass, silicon, metals, ceramics, soft polymers and even hard polymers for a variety of applications, including chemical synthesis, chemical analysis, cell handling, catalyst testing, particle synthesis, biomedical diagnostics, drug discovery and energy.[25-27] Various fabrication techniques have been used for the different device materials, including cleanroom microfabrication,[28] micromachining,[29] soft lithography techniques such as casting,[30, 31] hot embossing, mechanical machining, micro-electro discharge machining,[32] and laser ablation. The advantages and disadvantages of the different materials with respect to crystallization are summarized in Table 2-1, and the feature size that can be achieved with the various fabrication technologies is summarized in Figure 2-1. Silicon is one of the most chemically resistant device materials. The fabrication processes and techniques for silicon devices are very well developed due to the computer chip manufacturing industry. However, silicon fabrication is usually expensive, complicated and requires cutting-edge equipment. In addition, silicon devices are not optically transparent. Integration of *in situ* detection tools with microfluidic devices, and thus optical access, is imperative for studying the fundamentals of crystallization as discussed in chapter 1. Glass devices, on the other hand, are chemically resistant, as well as optically transparent. The high thermal stability and hardness also makes glass a desirable material in a broad range of applications.[33] However, glass is an amorphous solid and some of the precision

technologies used for fabricating silicon devices, such as anisotropic etching, cannot be used for glass. The geometry, depth and width, of microchannels fabricated in glass is limited by the etching technique.[34] As a result, the fabrication of glass devices is not particularly easy for realizing interesting designs.

The hard polymers can be fabricated using mechanical machining techniques, rapid prototyping techniques such as hot embossing, and laser ablation. Many of these materials such as polymethylmethacrylate (PMMA) and TOPAS (a cyclic olefin copolymer) are optically transparent. Although simple designs are easy to achieve in hard polymers, more intricate features are often quite challenging to realize with some of the fabrication techniques for hard polymers. In addition, the most common material used in hot embossing techniques, PMMA,[34] is not compatible with alcohols, one of the most commonly used solvent classes in antisolvent crystallization. For many of the hard polymers, such as TOPAS, the accuracy of intricate features is often compromised and sealing of the microchannels becomes an issue, since the fabrication techniques for these materials are not very well developed yet.

The soft polymers can be used to fabricate microfluidic devices with soft lithography techniques such as casting, a molding technique that uses chemical processes to harden the polymer. Polydimethylsiloxane (PDMS) is the most widely used material for this technique.[33] Although PDMS is not chemically compatible with many organic solvents or at aggressive conditions,[35] it works fine with a number of solvents that are commonly used for crystallization. Moreover, due to the deformability of PDMS, intricate designs and small features required for fast mixing in antisolvent-based crystallization, can be achieved with high precision.[36] The smooth surface of the elastomer also ensures hermetic seal of the microchannels.[33] Furthermore, its transparency in the visible spectrum allows for integration of *in situ* characterization tools necessary in crystallization. The polymer devices can also be mass produced at a low cost and time.[34] This is advantageous for a sensitive process like crystallization because a new device can be used for each experiment, ensuring that no reminiscent nuclei from past experiment will influence the subsequent experiments. Consequently, PDMS is chosen for the low pressure studies presented in this chapter, as well as in chapter 3 and 4.

Table 2-1. The advantages and disadvantages of typical device materials for crystallization applications

Materials	*Fabrication Method*	*Mixing Criteria*	*Cost*	*Optical Access*	*Ease of Fabrication*
Glass	Photolithography	Difficult	High	Excellent	Hard
Silicon	Photolithography	Easy	High	Poor	Moderate
Hard Polymers	Machining, Hot embossing, Laser ablation	Moderate	Low	Good	Easy
Soft Polymers (PDMS)	Soft Lithography	Easy	Low	Good	Easy

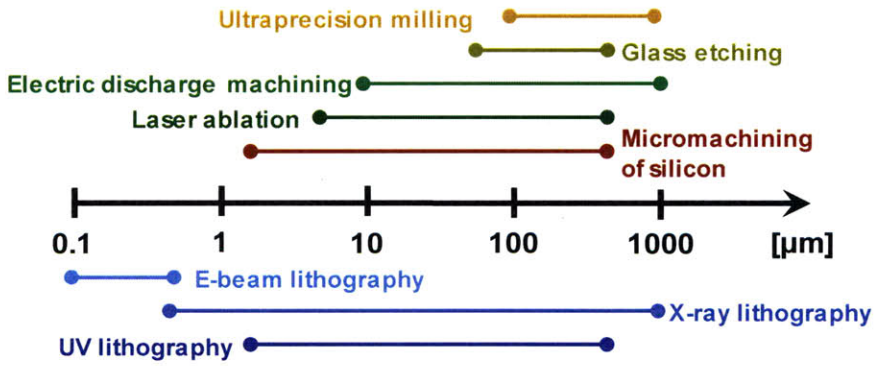

Figure 2-2. Typical dimensions achieved with various fabrication technologies.[26]

2.2 Experimental

2.2.1 Microfluidic Devices: Design and Fabrication

Microfluidic devices used in most of this work were designed to have microchannels that were 30-300 μm wide and approximately 200-250 μm deep. Three different reactor designs, as presented in Figure 2-3, were used for different parts of this study. Design 1 has a long residence time, with an approximate channel length of 1.6 m, and 3 inlets: one for solution, one for antisolvent and the third inlet for introducing gas. Design 2 also has a long residence time with an approximate channel length of 2.3 m, but it has a separate mixing region and no inlets for gas introduction. Design 3 has a short residence time with an approximate channel length of 4.3 cm.

Microfluidic devices were fabricated in PDMS by using standard soft-lithographic techniques.[31] Tight control of structure width and height, as well as its capability to accurately make high aspect ratio features makes SU-8, a negative photoresist, the ideal choice for fabricating the microchannels in PDMS.[30, 37] Hence, microchannels on silicon masters were fabricated with SU-8 (Microchem Corporation). Two layers of 100-150 μm thick SU-8 films were spun on 100 mm diameter silicon wafers (Silicon Quest International). Standard photolithography was used to define negative images of the microfluidic channels, and finally the wafers were developed using SU-8 Developer (Microchem Corporation). The details of the fabrication process can be found in the appendix.

After fabricating the masters, they were silanized in a vacuum chamber with (tridecafluoro-1,1,2,2-tetrahydrooctyl)-1-trichlorosilane (Gelest, Inc.) for at least two hours in order to minimize or eliminate stiction of SU-8 features with molds. PDMS was prepared by mixing Sylgard 184 and its activator (Dow Corning) in a 10 to 1 weight ratio. The mixture was degassed, casted onto the master wafer and cured at 80°C for 2 hours. After reticulation, the devices were peeled off the mold, cut, and inlets and outlets were punched with a 5/64" leather punch. Each device was cleaned, surface activated with a Harrick PDC-32G oxygen plasma chamber for 35 seconds, and finally covalently bonded to a precleaned glass slide, which was also exposed to oxygen plasma for 90 seconds prior to bonding. PEEK tubing (IDEX Health & Science) was inserted in the inlets and

outlets, and glued in place with 5-min epoxy (Devcon). The outer surface of the device was activated with oxygen plasma for 45 seconds prior to gluing the tubes in order to increase the adhesion. The epoxy was finally cured at room temperature for 24 hours or at 80°C for a few hours.

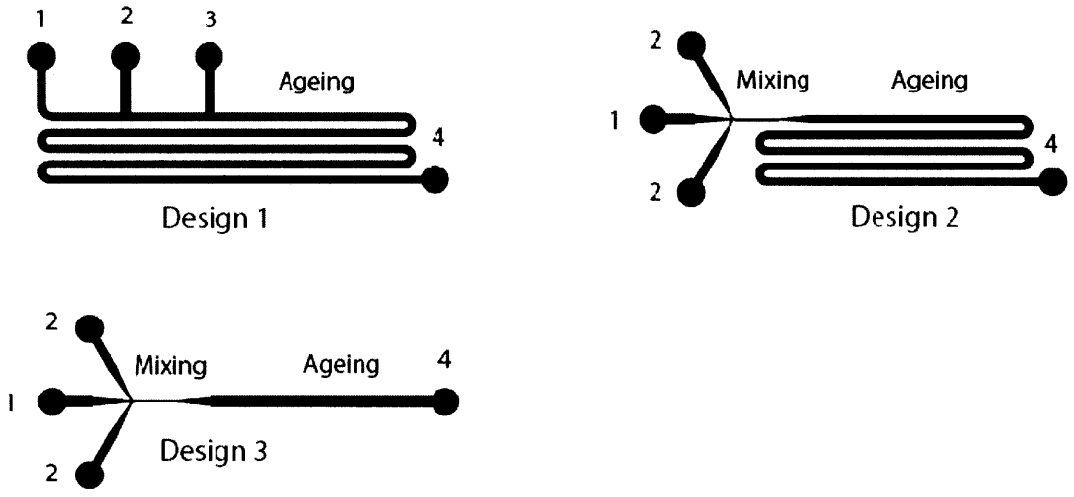

Figure 2-3. Schematics of the different microfluidic devices used in this work: design 1 and 2 have long residence times; whereas design 3 has a short residence time. Design 2 and 3 have a separate mixing zone. In all the designs, "1", "2", and "3" denotes inlet for introducing solution, antisolvent and gas, respectively. "4" denotes the outlet.

2.2.2 Experimental Setup

Syringe pumps (Harvard Apparatus) were used to deliver the fluids into the microchannels with a constant flow mode. Teflon tubing and PEEK fittings (Upchurch Scientific) were used to interface the microfluidic devices with the syringe pumps. Filtered air was used as the gas phase in the multiphase experiment.

A transmission microscope with 5X (numerical aperture 0.12), 10X (0.3), and 20X (0.5) air objectives was used for imaging and a sensitive full frame CCD camera (PCO Sensicam double shot QE) was used for capturing digital images at a rate of up to 10 frames per second.

2.2.3 Crystallization Setup

Two different organic materials: glycine (Sigma-Aldrich), and lovastatin (Sigma-Aldrich) were used for continuous crystallization experiments, each with distinct properties. The molecular structure of glycine and lovastatin are presented in Figure 2-4. Glycine, the simple amino acid, is a common pharmaceutical excipient,[38] and was used as one of the model systems for easier nucleation. It exists in a zwitterionic form in the solid state, with a nonzero zeta potential on its solid facets. For glycine crystallization, water and ethanol were used as the solvent and antisolvent, respectively. Lovastatin, an anti-cholesterol drug, that is known to have very fast kinetics,[39] was used as the second model system. Methanol was used as the solvent and water as the antisolvent for this system. Spectroscopy grade water was purchased from VWR and the rest of the solvents were purchased from Sigma-Aldrich. Further experimental details are provided in the discussion sections of the respective studies.

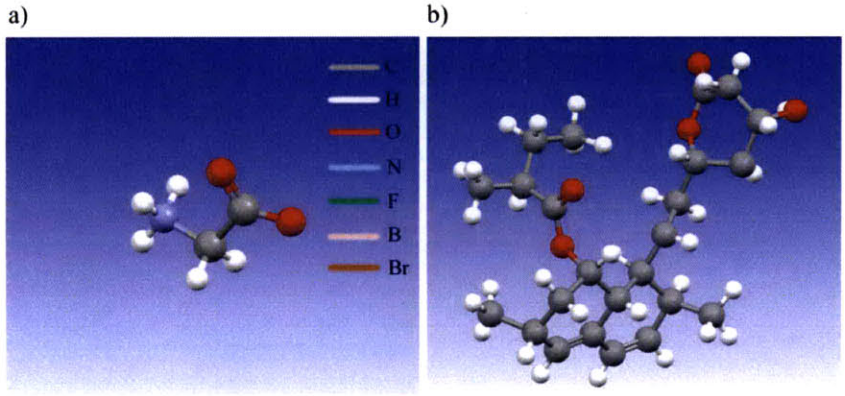

Figure 2-4. The molecular structure of the model systems used in this work: a) glycine, and b) lovastatin.

2.3 Results and Discussion

The main focus of this chapter is to understand the challenges associated with continuous homogeneous nucleation in microfluidic devices. *In situ* microscopy tools, along with the controlled manner of crystallization possible in microfluidic devices, allows one to visualize and study the different physical and chemical processes that

contributes to making continuous crystallization challenging. In the next few sections, we discuss challenges that arise from device issues, as well as challenges that arise from the inherent nature of crystallization. We also discuss the approaches we took to address those challenges.

2.3.1 Segmented Flow vs. Single-Phase Flow

In this section, we describe the effects of multiphase flow on crystallization. Segmented flow has been used extensively in microfluidic devices for particle synthesis applications over the last few years. Ismagilov and coworkers have used multiphase flow, aqueous droplets encapsulated by fluoro-carbon based carrier fluid, for the generation of compartmentalized microbatches for protein crystallization.[14, 40] Salmon and coworkers have also used aqueous droplets encapsulated by fluorinated oil to compartmentalize microbatches for inorganic, as well as organic crystallization.[41] Khan et al. and Yen et al., on the other hand, used gas liquid segmented flow to enhance mixing and reduce Taylor dispersion present in single phase flows.[3, 8]

In this study, glycine crystallization was carried out with devices of design 1. The design consisted of 300 μm by 250 μm channels, with a large pressure drop channel for the gas inlet. 40-100% saturated aqueous solution was used as the crystallizing solution, 70-100% aqueous ethanol was used as the antisolvent, and filtered air was used as the dispersed phase. The flow rate of the liquids was varied between 5-10 $\mu l \cdot min^{-1}$ so as to achieve different supersaturation, S.

$$S = C / C_s \qquad 2\text{-}4$$

where C is the solute concentration and C_s is the solute solubility at the same conditions. The gas flow rate was set equal to the total liquid flow rate. It was found that nucleation always occurred first at the interface of the dispersed and continuous phase for S greater than 1.75. As the nucleation theory suggests, interface lowers the Gibbs free energy for heterogeneous nucleation (equation 1.5 and 1.6) and makes it easier for nucleation to occur.[42] In addition, the interface served as a place for the crystals to congregate, which brought the individual crystals close together, increasing interactions through electrostatic, van der Waals and H-bonding. Subsequently, the crystals agglomerated, and, in many cases, coalesced in an uncontrolled manner, ultimately clogging the channels. With an

increase in the supersaturation, nucleation rate also increased, with crystals appearing at the interface, as well as in the liquid phase. In this case, the crystals that nucleated in the liquid phase also accumulated at the interface of the dispersed and continuous phases over time, and followed the same behavior of growth through agglomeration and coalescence, leading to channel clogging, but at a faster rate due to higher density of crystals. Figure 2-5a illustrates the gas liquid segmented flow achieved in PDMS microchannels, and Figure 2-5b presents a series of images demonstrating early phase of nucleation at the interface followed by their uncontrolled growth.

Subramaniam et al. observed similar congregation of latex particles at gas liquid interface, which then assembled around the bubbles in layers due to their surface charge.[43, 44] Using this phenomenon, they were able to make bubbles covered with jammed colloidal shells, which they termed "colloidal armour". However, there was no repulsive surface charge in the case of organic crystals, but only attractive forces that resulted in their agglomeration. Moreover, the crystals that nucleated at the interface of the dispersed and continuous phases grew mostly to be polycrystals, as shown in Figure 2-5c. Thus, multiphase flow provided an interface that served as a site for uncontrolled growth of organic crystals, making it difficult to study homogenous nucleation or growth at conditions typically experienced in a crystallizer. Consequently, the rest of the studies in this thesis were carried out with single phase flow.

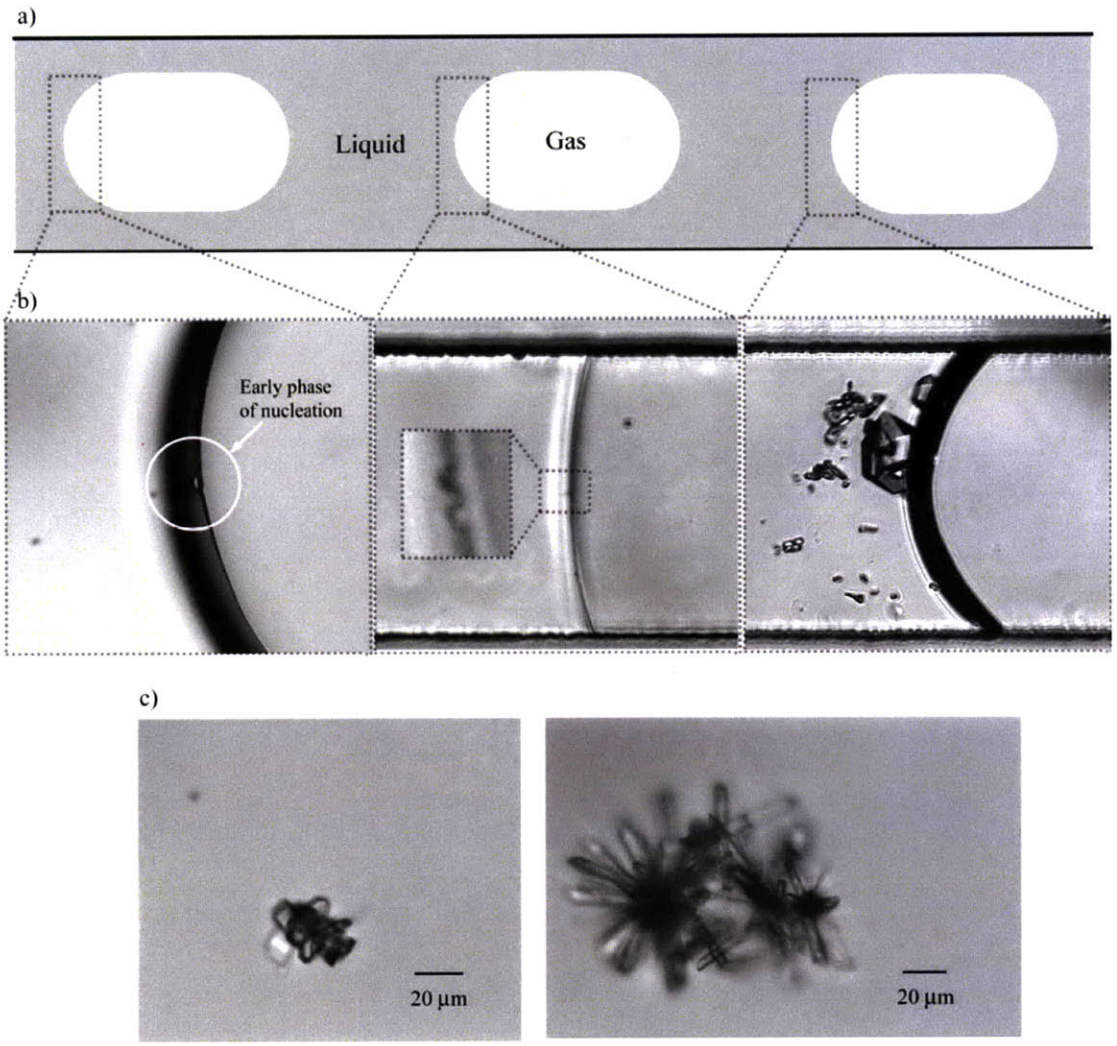

Figure 2-5. The effects of segmented flow on crystallization of organic molecules. a) Schematics of gas liquid segmented flow in PDMS microchannels, with gas as the dispersed phase and liquid as the continuous phase. b) The interface of the two phases serves as a site for heterogeneous nucleation. The series of images demonstrate how the crystals nucleate, as well as congregate at the interface. Subsequently, they agglomerate and coalesce, growing at an uncontrolled manner. d) Crystals that grow at the interface are mostly polycrystals. The microchannels in all the images are 300 µm wide and 250 µm deep.

2.3.2 Bubble Nucleation

Crystallization based on antisolvent addition requires at least two solvents with quite different solubility of the crystallizing solute. Often times, the two solvents may have different solubility for other compounds, even gases, such as oxygen and nitrogen. When the difference is high enough, bubbles may nucleate as the solvents are mixed, in a way very similar to nucleating solids with antisolvent addition. In this study, the solvents used for glycine crystallization, water and ethanol, were found to have sufficient difference in gas solubility so as to nucleate bubbles at the interface where the two solvents meet in the microchannel. Figure 2-6a illustrates such bubble formation in the middle of a microchannel where water and ethanol of equal flow rates were mixed. This type of bubble nucleation was undesirable because the bubbles then presented a site for heterogeneous nucleation, and uncontrolled growth of organic molecules, as discussed in the previous section.

Simple degassing schemes such as purging with helium were inadequate in preventing bubble nucleation. Consequently, we designed and fabricated an online degassing chamber for degassing the solvent and antisolvent. The degassing chamber consisted of thin-walled semi-permeable Teflon tubes (Teflon® AF, Biogeneral Inc., San Diego, CA) and was sealed with an o-ring. Vacuum was applied to the chamber and the gases flowed out due to the pressure difference. Figure 2-6b is a schematic of the degassing chamber and Figure 2-6c is an image of the actual device. The length of the Teflon tubes was calculated using the maximum gas solubility differences, the solvent flow rates and the gas flow rate across the tube wall. The gas flow rate across the tube wall, Q, is expressed as:

$$Q = pA\,\Delta P/h \qquad 2\text{-}5$$

where p is the gas permeability, A is the surface area, h is the thickness of the Teflon tubes, and ΔP is the pressure difference across the tube wall. The solubility of oxygen and nitrogen in water and ethanol, as well as their permeability in Teflon A, are given in Table 2-1. The solubility is presented as Ostwald coefficient, L, as a function of gas volume, V_{gas}, and solvent volume, $V_{solvent}$ at different solvent compositions.

$$L = {}^{V_{gas}}\!/_{V_{solvent}} \qquad 2\text{-}6$$

The length of the tubes was designed to be twice the calculated value in order to ensure sufficient degassing of the solvents. Figure 2-6d demonstrates that adequate degassing was achieved so as to completely eliminate bubble nucleation. The advantage of this degassing chamber is that it can easily be integrated to microfluidic systems for inline degassing. In addition, multiple lines can be added for degassing multiple solvents simultaneously with the same chamber.

Similar phenomenon, namely bubble nucleation, must also occur in the case of antisolvent addition crystallization performed in batch crystallizers. Those bubbles can subsequently affect the nucleation behavior as well, as discussed earlier, albeit to a lesser extent than in microchannels. However, this issue is often neither addressed, nor recognized, in crystallization studies. We were able to recognize this problem and eliminate it in this study because of the *in situ* visualization of process dynamics, possible in microfluidic devices.

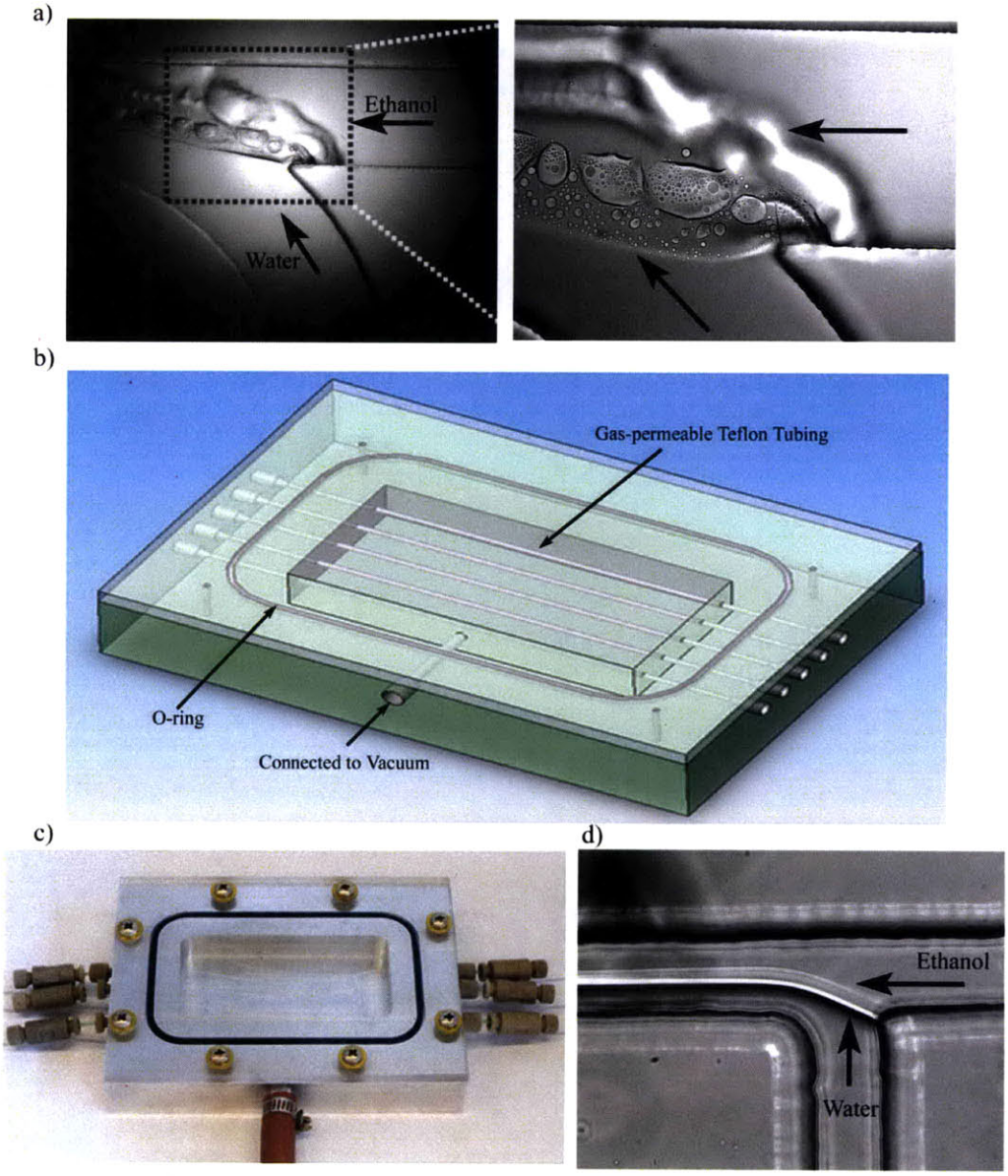

Figure 2-6. Bubble nucleation as a result of gas solubility difference in the solvent and antisolvent used for crystallization. a) Bubbles nucleate at the interface, where water, the solvent, and ethanol, the antisolvent, streams meet in the microchannel. b) Schematic of the online degassing chamber used to degas the solvents inline. c) An image of the assembled degassing chamber. d) Bubble nucleation is successfully prevented by the inline degassing chamber at the interface of water and ethanol streams. The microchannels are 300 μm wide and 250 μm deep in all the images. The arrows represent the flow direction.

Table 2-2. The permeability and Ostwald solubility coefficient of gases[3]

	Oxygen	*Nitrogen*
Permeability in Teflon AF $(cm^2\text{-}cm/(cm\text{-}Hg\text{-}s\text{-}cm^2))$[1]	9.9×10^{-4}	4.9×10^{-4}
Solubility in Water[2], L_w	0.035	0.018
Solubility in Ethanol[2], L_E	0.244	0.151

[1] Taken from biologeneral Inc.'s website.[45]

[2] Data taken from literature.[46, 47]

[3] The solubility data were taken at 20°C, and atmospheric pressure.

2.3.3 Impurities in PDMS Microchannels

The difference in solubilizing abilities of the solvent and antisolvent can give rise to other interesting issues. For example, we observed the formation of inclusions, upon mixing of solvent and antisolvent, in microchannels made of PDMS for long residence time reactors, design 1 and design 2. When using devices of design 1 that had a channel width, depth and length of 300 μm, 250 μm, and 1.6 m, respectively, inclusions started forming, first in half of the microchannel width within ten seconds of residence time, and then across the entire channel width within a residence time of 2 minutes. Figure 2-7 presents a schematic of the inclusion formation in the microchannel for an equal flow rate of the solvent and antisolvent. Figure 2-7a illustrates the first appearance of inclusions at t_0, and Figure 2-7b illustrates the inclusion formation at a later residence time t_1 across the channel width. Figure 2-7c and 2-7d are the actual images of the channels at t_0 and t_1, respectively. When using devices of design 2 that had similar dimensions as design 1 and a mixing channel of 50 μm width, the inclusions took longer to appear. Once they appeared, they seemed more uniform across the channel, as in Figure 2-7d.

We found that the inclusions are formed due to unreacted monomers and oligomers in the PDMS matrix. PDMS is known to have non-cross-linked monomers and oligomers in

its matrix that migrate to the surface, with the flux depending on a number of factors, including the temperature.[48, 49] It is also known that a treated PDMS surface recovers its native hydrophobicity over time, through a number of proposed mechanisms, most important of which is the diffusion of free species to the surface from the bulk through a cracked or porous layer.[50, 51] The semi-structural formula of PDMS is presented in Figure 2-8.[34] In our study, the free monomers and oligomers are extracted in ethanol, the antisolvent in our case, over time. These species have lower solubility in water, the solvent in our case, which causes them to phase separate and form inclusions. This is why the inclusions were initially observed in half of the channel that mostly contained ethanol. As the two solvent streams mixed over time, the inclusions became more uniform across the channel. In case of design 2, the narrow channel enabled fast mixing, within a second. In this case, the extraction of oligomers in the mixed solvent was lower and a few minutes of residence time was required to extract enough oligomers for inclusion formation.

Understanding the inclusion formation process and being able to eliminate it is of paramount importance, as PDMS has been widely used for particle synthesis applications. In such studies, the oligomer impurities, as well as the small inclusions formed by them at certain solvent compositions, may affect the nucleation process. The effect of impurities on particle synthesis is well established. Liu and Botsaris have shown that nucleation, growth, and particle size can be directly correlated to the impurity concentration.[52] In addition, it is readily acknowledged that inclusions extraneous to the precipitating system promote phase transformation, particularly condensation and crystallization.[53]

With the *in situ* microscopy tools, we were able to understand the inclusion formation process in PDMS microchannels. These unreacted monomers and oligomers can be easily removed by cleaning the devices thoroughly with suitable organic solvents. We cleaned our devices with a triethylamine wash that swelled the devices and extracted out the unreacted species, followed by an acetone and ethanol wash. With this simple procedure, we were able to successfully eliminate the impurities, as well as inclusion formation.

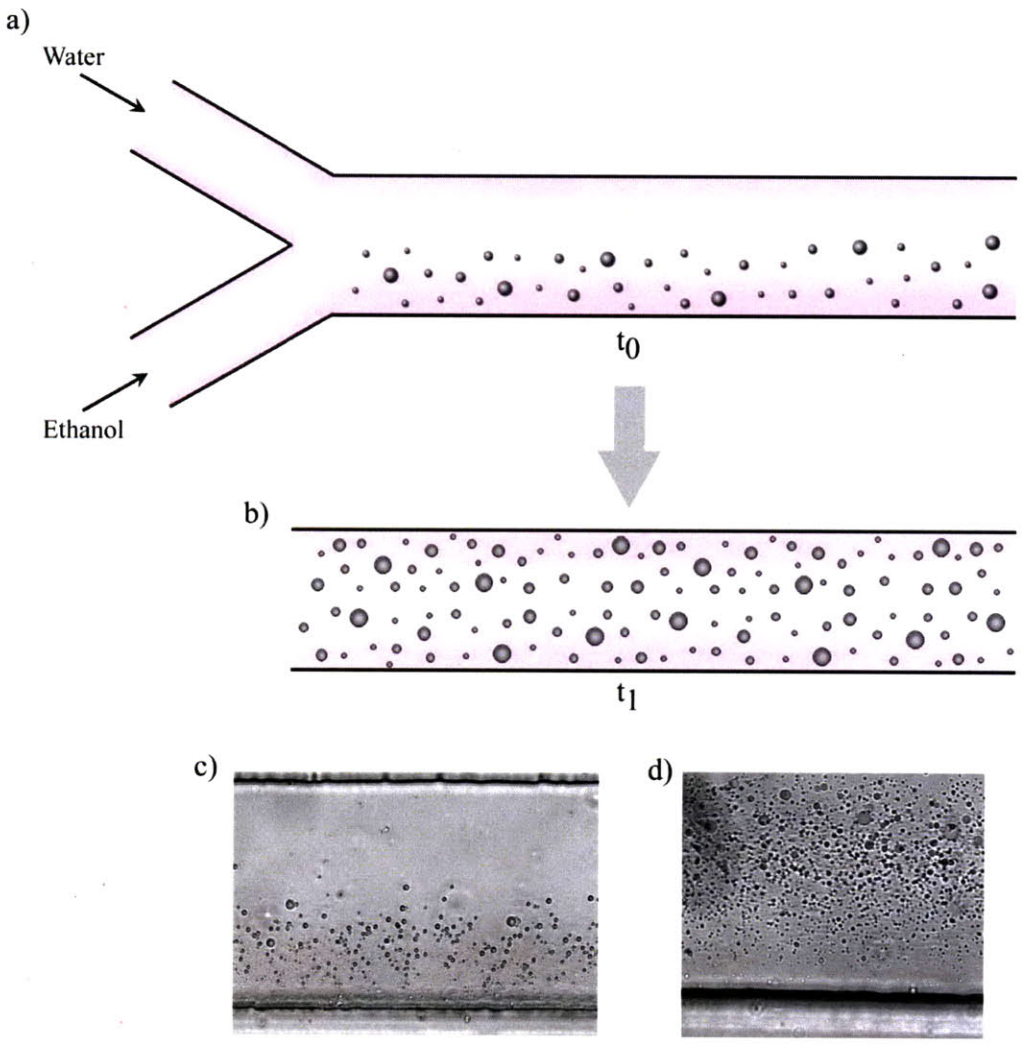

Figure 2-7. Inclusion formation in PDMS microchannels as the solvent and antisolvent are introduced. a) Schematics of inclusions first appearing in half of the channel that contain mostly ethanol, at an earlier time, t_0. b) Schematics of inclusions appearing across the channel at a later time, t_1. c-d) Actual images of the microchannels with inclusions at t_0 and t_1, respectively. The channels are 300 μm wide and 250 μm deep.

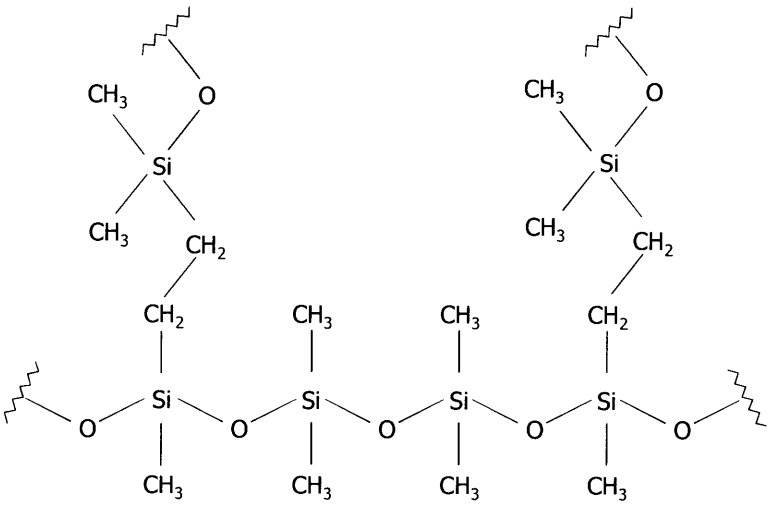

Figure 2-8. Structure of cross-linked PDMS.[34]

2.3.4 Particulate Impurity Control in Microchannels

The sealed microfluidic channels offer a superior control over particulate impurity compared to batch reactors, which can be important in particle synthesis, particularly in crystallization of organic molecules. The effect of particulate impurity in crystallization has been demonstrated in many studies, as reviewed by Turnbull et al.[53] Yi et al. have also shown that primary nucleation occurs faster in a larger batch reactor than a smaller one, due to the fact that a larger volume has higher probability of containing a particulate impurity than a smaller one.[54] In this section, we discuss the particle control achieved in microchannels because of the sealed system, as well as the minute volume used in each experiment.

For this part of the study, we used lovastatin, an anti-cholesterol drug, as the model pharmaceutical. Nucleation process is known to have an energy barrier, as discussed in chapter 1, and the energy barrier increases with the size and the complexity of the molecule. This is because as the molecule becomes larger and more complex, the more difficult it becomes for molecules to come together in the right orientation to form the nuclei or grow.[55] As seen in Figure 2-4b, lovastatin is a complex molecule, yet it is known to have fast nucleation kinetics.[21, 39] Thus, the nucleation process of lovastatin

most likely occurs through heterogeneous mechanism, and that makes it a good model system to use for investigating particulate impurity control.

We found that the nucleation behavior of lovastatin was sensitive to the fluid mechanics and often nucleated at sharp turns present in the long residence time reactors, namely design 1 and design 2. However, such nucleation behavior was quite sporadic and not very reproducible. Consequently, we designed a spiral reactor with a long residence time, but with no sharp turn, as shown in Figure 2-9. The channel width was 50 μm in the mixing region and 300 μm in rest of the reactor. The channel depth and length were approximately 250 μm and 3 m, respectively, resulting in a residence time of 3 to 30 minutes. The solubility data of lovastatin in methanol water system was taken from Merck & Co. (Table 2-3). The induction time data was taken from the literature.[39, 56] We designed the mixing laminae so as to achieve complete mixing before the calculated nucleation time. The characteristic time of mixing, t_M, was approximately 40 ms. We used 25 to 100% saturated methanol solutions as the solvent and 80 to 100 wt % water in methanol as the antisolvent.

Mahajan et al. studied lovastatin nucleation from methanol-water system using a grid mixer and reported that the induction time ranges from 70 ms to 10 s for supersaturation values, (C/C_s), between 2 to 8.7. In our studies, we initially started with a supersaturation of 2 and varied the concentration and flow rates (between 2 to 30 $\mu l \cdot min^{-1}$) to achieve a supersaturation as high as 12. However, we were not able to achieve nucleation within the residence time of our microreactor. As the supersaturation was increased, we observed oiling out, a common phenomenon for complex organic molecules at very high supersaturation.[57] Yet, no nucleation was achieved except at the outlet, which was in contact with air.

The lack of nucleation observed in this study most probably results from an increased metastable zone width achieved in sealed microfluidic devices. That means nucleation is more difficult to achieve in these devices than in larger systems, particularly for large and complex molecules. This presents an opportunity to control nucleation of organic systems in microchannels, and a wider scope for operating in the metastable zone for growth only conditions. We study crystallization in the metastable zone using exactly this

characteristic of microchannels in chapter 3 and 4, and demonstrate how this can be used to our advantage for studying growth processes.

For nucleation studies, we use a simpler molecule such as glycine, which is easier to nucleate in the absence of particulate impurities, and is used in the remaining parts of this chapter.

Table 2-3. The solubility of lovastatin in methanol-water system at 20°C

Methanol (vol%)	*Water (vol%)*	*Solubility mg/ml*[1]
100	0	22
80	20	7
60	40	0.9
0	100	5.8×10^{-4}

[1] Data taken from Merck & Co.

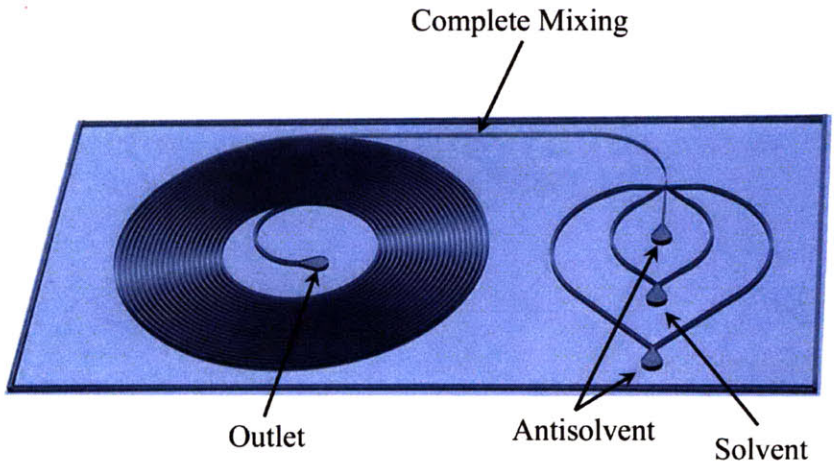

Figure 2-9. Spiral reactor for lovastatin crystallization. The reactor has a long residence time without any sharp turns. The microchannels are 300 μm wide and 250 μm deep. The total reactor length is 3 m. The reactor also achieves fast mixing with a mixing laminae.

2.3.5 Homogeneous Nucleation

Glycine was used as the model system for studying homogeneous nucleation because the simple structure makes the nucleation process easier than more complex molecules. It has three polymorphic forms at atmospheric pressure: alpha, beta and gamma.[58-61] At regular conditions and neutral pH, without the presence of any impurity or additive, the alpha,[62] or the beta form[63] crystallizes spontaneously from solution, and hence, are of significance in this study. The alpha form is the metastable form,[64, 65] and usually crystallizes as centrosymmetric bipyramids in a monoclinic space group ($P2_1$) at comparatively lower supersaturation.[66-68] The beta form is the unstable form, and usually crystallizes as noncentrosymmetric, high aspect ratio habits such as needles in a monoclinic space group ($P2_1/n$), at higher supersaturation.[69, 70]

We used single phase flow in devices of design 3 that have a short residence time, between 3 and 30 seconds, depending on the operating flow rates. Design 3 also has a 30 μm wide mixing channel that results in a characteristic mixing time of 45 ms. We used 70 to 100 weight % aqueous ethanol as the antisolvent and spectroscopy grade water as the solvent. We used a new device for each experiment in order to eliminate any influence of prior experiments. We also cleaned and dried all the fittings and tubing used, prior to each experiment. Glycine solubility data for water-ethanol system were taken from the literature, and correlated as a function of ethanol weight percent, x.[71-74]

$$C_s = -2.618 + 2.264\times10^{-2}\,x + 23.17\exp^{\left(-4.06\times10^{-2}\,x\right)} \qquad 2\text{-}7$$

We systematically varied the supersaturation by varying the composition of the antisolvent, concentration of the solute (20 to 100% saturation), as well as the flow rate ratio of the solvent and antisolvent streams (1 to 3). We observed spontaneous homogeneous nucleation within the short residence time of our reactor for a supersaturation, (C/C_s), greater than 1.9. We observed the formation of mostly needle-like crystals, as presented in Figure 2-10a, corresponding to the habit of the beta form, earlier in the channel at shorter residence time. However, bipyramidal habits, corresponding to the alpha form, started to appear within 3-5 seconds of residence time, as seen in Figure 2-10b. This can occur because of the interplay of thermodynamics and nucleation kinetics of the two polymorphic forms. Ostwald's rule of stages predicts that the less stable form

would appear first.[75] In addition, the solubility of less stable forms (e.g. beta glycine) is higher than that of more stable forms (e.g. alpha glycine).[76] Consequently, when a solution reaches saturation with respect to the less stable form due to its nucleation, the system is still supersaturated with respect to the more stable form and can give rise to further nucleation (of the more stable form), which is exactly what we observed in our experiments.

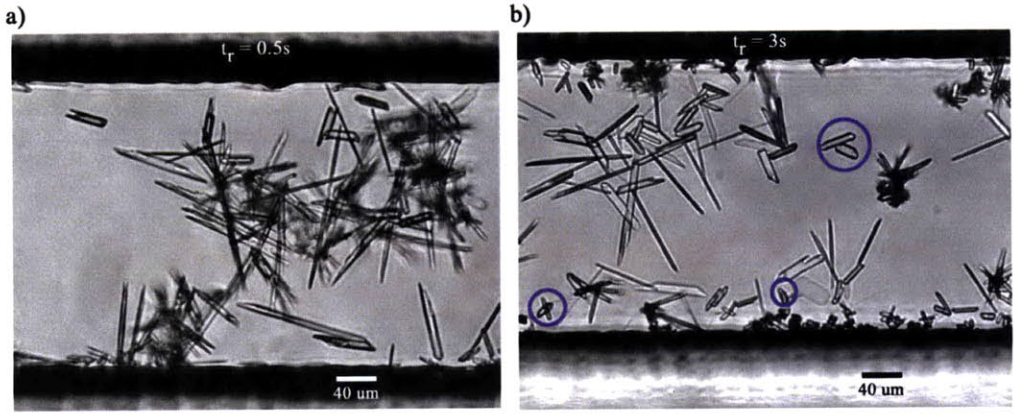

Figure 2-10. Glycine crystallization at a supersaturation of 1.95. a) Needles crystallized initially, at a residence time of 0.5 s, corresponding to the beta form. a) Smaller and more regular shaped alpha form appeared at a longer residence time, with the image corresponding to a residence time of 3 s.

However, it was not possible to operate the device continuously as the reactor was ultimately clogged. It was observed that the clogging time was shorter with a higher supersaturation ratio, as expected, since more material crystallized due to higher potential. Clogging, for glycine crystallization, was not prevented, even at the minimal supersaturation of 1.9 that gave rise to nucleation. When the supersaturation was lowered below 1.9, nucleation was not achieved within the residence time of our device. Therefore, developing an understanding of the clogging mechanism is essential for realizing a microfluidic platform for continuous homogeneous nucleation.

2.3.6 Channel Clogging

It is readily acknowledged that one of the major challenges of achieving homogeneous nucleation in microchannels is channel clogging,[5] which is the topic of discussion in this

section and the next two sections. There have been numerous studies on clogging mechanisms of porous materials, both of pore network as a whole,[77, 78] and of single pores.[79] Although, most of the work focuses mainly on clogging at the pore opening, which would correspond to the channel entrance or junction in the case of microfluidics, many of the proposed mechanisms may apply to clogging inside the microchannels as well. Some of the suggested mechanisms that may be applicable to microfluidic channels are particle deposition by inertial impaction, interception, Brownian diffusion or sedimentation, as well as jamming by hydrodynamic focusing.[80, 81] These mechanisms are mostly discussed in the context of stable colloidal dispersions of polymeric particles, with a charged surface, such as latex and polystyrene. For organic crystals, however, additional mechanisms may play an important role.

In our studies, we found that channel clogging primarily occurred as a result of two main factors: a) interaction of crystals with channel surfaces, and b) high number density of crystals. We discuss these two issues in the next two sections. Positive interaction of crystals with channel surfaces leads to increased solid deposition on the channel wall. In order to address this issue, we used surface modification techniques to control the properties of channel surfaces and minimize such interactions. We discuss these surface modification techniques in the next section. In the subsequent section, we discuss the challenge posed by the high density of crystals that result from spontaneous homogeneous nucleation of small organic molecules.

2.3.7 Towards Understanding Interactions between Crystals and Channel Surfaces

Crystals may interact with the reactor surface through various mechanisms, resulting in deposition on reactor walls, growth of which may ultimately clog the channels. Crystals, in the glycine and lovastatin studies, were found to participate in electrostatic interactions, possibly H-bonding, as well as hydrophobic-hydrophobic interactions. Glycine, that is known to have both positive and negative charges on the crystal facets, was found to interact with glass surface, as illustrated in Figure 2-11a. This may result from electrostatic interaction and/or H-bonding with the hydroxyl groups on glass. Figure 2-11b shows lovastatin crystals that have mostly hydrophobic groups in the largest faces,

interacting with PDMS surface, a hydrophobic material, possibly through hydrophobic interactions. Figure 2-11c shows mass of solid glycine depositing on PDMS channels that have been made hydrophilic through plasma ashing. The solid mass, then, grow on to block the channel, as illustrated in Figure 2-11d. Other studies have also reported that minimizing particle-to-wall interactions under flow reduces clot formation or channel constriction.[82, 83] In order to address the crystal-channel surface interactions, we modified the channel surface with a number of methods in an attempt to control the surface properties. We discuss these modification techniques in the following sections.

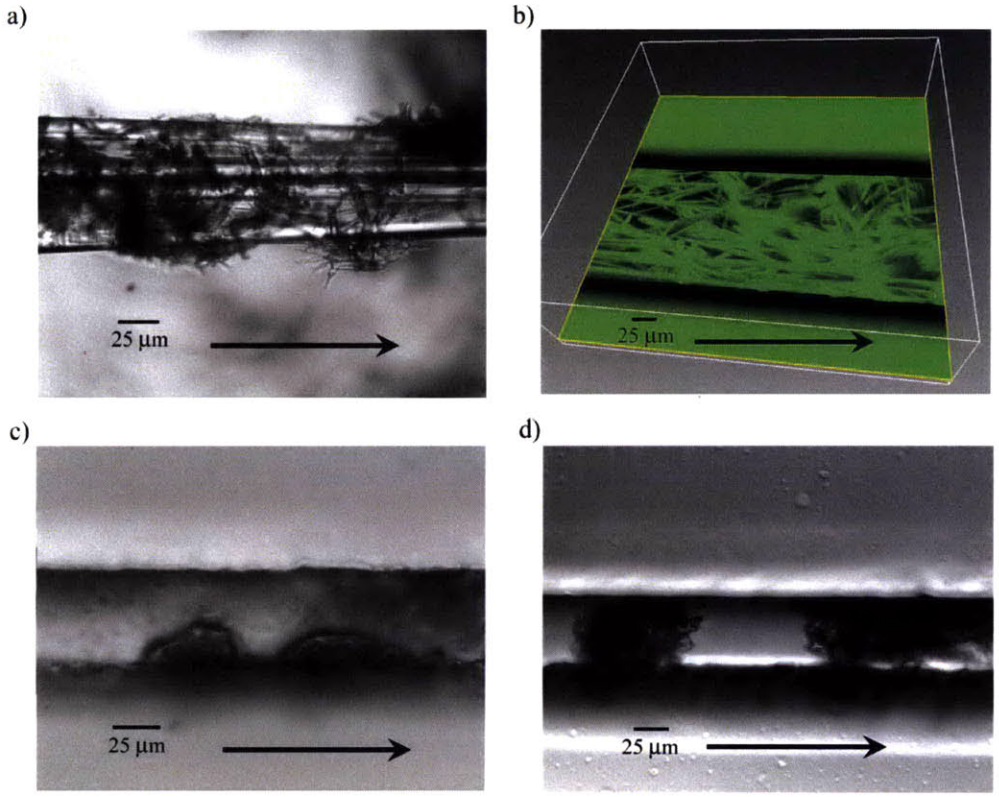

Figure 2-11. Interaction of crystals with surfaces. a) Glycine crystals, which have charged facets, attach to the glass surface, possibly through electrostatic interaction. b) Lovastatin crystals, which have mostly hydrophobic groups, interact and adhere to PDMS surface, possibly through hydrophobic interactions. c-d) Glycine solids deposit on modified PDMS surface that has been made hydrophilic and grow on to constrict the channel. The arrows represent the flow direction.

The surface properties can have a significant impact on the deposition of particles that may lead to channel clogging,[80] particularly in microchannels where the surface to volume ratio is much higher than in typical batch reactors. Therefore, it is imperative to be able to control the surface properties and minimize the interactions of solids with channel surfaces. We use glycine for most of the studies in this thesis, chapters 2 to 4, and hence, focus on the specific interactions of glycine with surfaces. However, we use the insights obtained here to design continuous systems for other materials in chapter 5. As discussed in the previous section, glycine interacts the most with hydrophilic, charged surfaces such as glass and hydrophilic PDMS. Therefore, it is desirable to use hydrophobic surfaces for glycine crystallization. Although PDMS is inherently hydrophobic, with a contact angle of 105, oxygen plasma used to seal the channels with a glass slide, imparts hydroxyl groups to PDMS, and in the process makes it hydrophilic. As discussed in an earlier section, the uncrosslinked oligomers usually migrate to the surface, turning PDMS hydrophobic over time. However, when the uncrosslinked species are removed for a better environment for particle synthesis, the recovery of its native hydrophobicity is much slower. We used a Ramé-Hart automated goniometer with automatic dispenser to track the receding contact angle of a plasma-ashed PDMS over time. The contact angle, θ, is expressed by the Young's equation:

$$\cos\theta = \frac{\gamma_s - \gamma_{ls}}{\gamma_l} \qquad 2\text{-}8$$

where γ_s is the surface energy of the solid sample, γ_l is the surface energy of liquid droplet, deionized water in this case, and γ_{ls} is the interfacial tension between the solid and the liquid.[84] The contact angle of plasma ashed PDMS was found to change over time, as demonstrated in Figure 2-12. The dynamic surface properties of PDMS over the first week of ashing translate into inconsistent interactions between solids and channel surfaces, and require a long wait period for experiments. Therefore, it is desirable to obtain a more stable hydrophobic surface for PDMS.

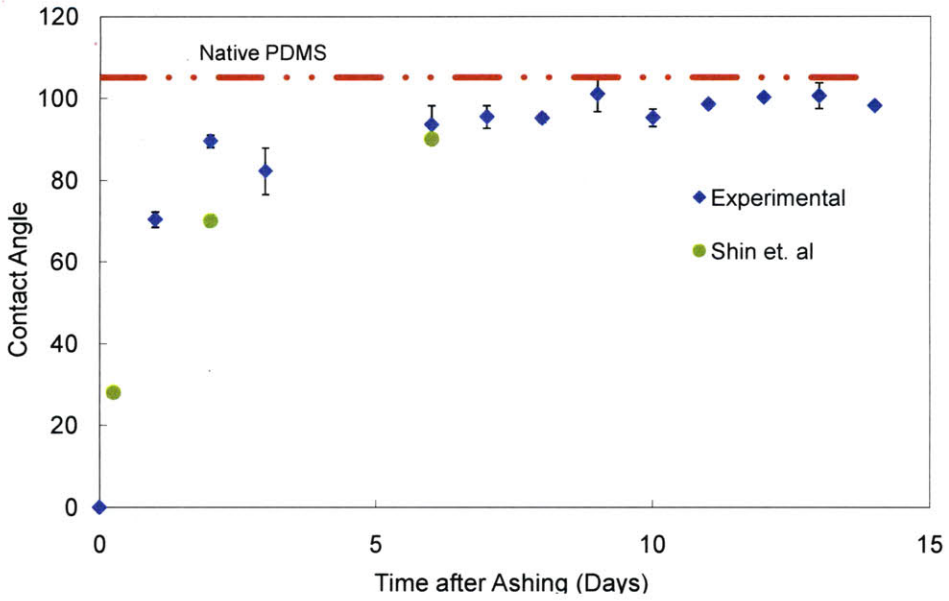

Figure 2-12. The dynamic surface property of plasma ashed PDMS. The advancing angle of PDMS over time shows that it takes a long time for the clean PDMS to recover its native hydrophobicity. The dynamic behaviour is compared with literature.[85]

There have been quite a few studies on surface modification techniques for both PDMS and glass, including exposure to energy such as oxygen plasma, UV light etc., covalent modification such as radiation induced graft polymerization, silanization etc., and physical deposition of other materials, though most of them were focused on small pieces, and not on sealed microchannels.[85-90] Here, we looked into two methods: silanization and physical deposition with Teflon AF for sealed microchannels. To make the glass surface hydrophobic, on the other hand, we simply spin-coated a 20-30 μm layer of PDMS.

We used a long-established silanization technique to modify the PDMS surface.[87, 91, 92] We used tri-alkoxy silanes, for which reaction involves four steps, as presented in Figure 2-13. First, the three labile groups are hydrolyzed, followed by condensation to form oligomers. The oligomers then form hydrogen bond with the hydroxyl groups of the substrate. Finally, covalent bonds are formed between the substrate and the oligomers. We used two silane compounds with different hydrophobicity: octyltrimethoxysilane (Gelest, Inc.), and (helptadecafluoro-1,1,2,2-tetrahydrodecyl)trimethoxysilane. Small amounts of silane (0.2 – 5 weight %) were mixed in a solvent, either ethanol or

isopropanol, and were flown through PDMS reactors for 10 to 35 minutes. PDMS was ashed with oxygen plasma, quickly packaged, and silane solution was introduced immediately, followed by a long solvent wash. The channels were then dried with nitrogen and baked in the oven at 120°C for one hour. Small pieces of PDMS were simultaneously processed at identical conditions and were used for surface characterization. The silane concentration, ashing time of PDMS, wait period for silane introduction (from the time of ashing), exposure time, solvent and baking temperature were optimized. The optimized parameters are given in Table 2-4. Successful surface treatment was confirmed by measuring the advancing contact angle, θ_a, and the receding contact angle, θ_r, with water droplet according to sessile drop method (Table 2-5).[93] The advancing contact angle achieved for the two silanes were 104.8 ± 1.0 and 110.5 ± 1.4, similar to the expected values. The contact angle of the modified PDMS remained stable over time.

Table 2-4. Optimized values of the different parameters for silane modification of PDMS

Parameter	***Optimized Value***
Solvent	Ethanol
Silane Concentration	1.0 weight %
Ashing time	1.5 min
Wait period	20 min
Exposure time	5 min
Baking temperature	120°C

Table 2-5. Contact angle (CA) achieved for modified PDMS surfaces with different silanes.

Silane Compound	θ_a	θ_r	*Expected CA*
PDMS-methyl-term-silane	104.8 ± 1.0	69.2 ± 6.7	105
PDMS-fluorosilane	110.5 ± 1.4	90.3 ± 6.5	115
Unmodified PDMS[1]	70.4 ± 2.0	-	-

[1] Unmodified PDMS was ashed with oxygen plasma for same time as the modified surfaces

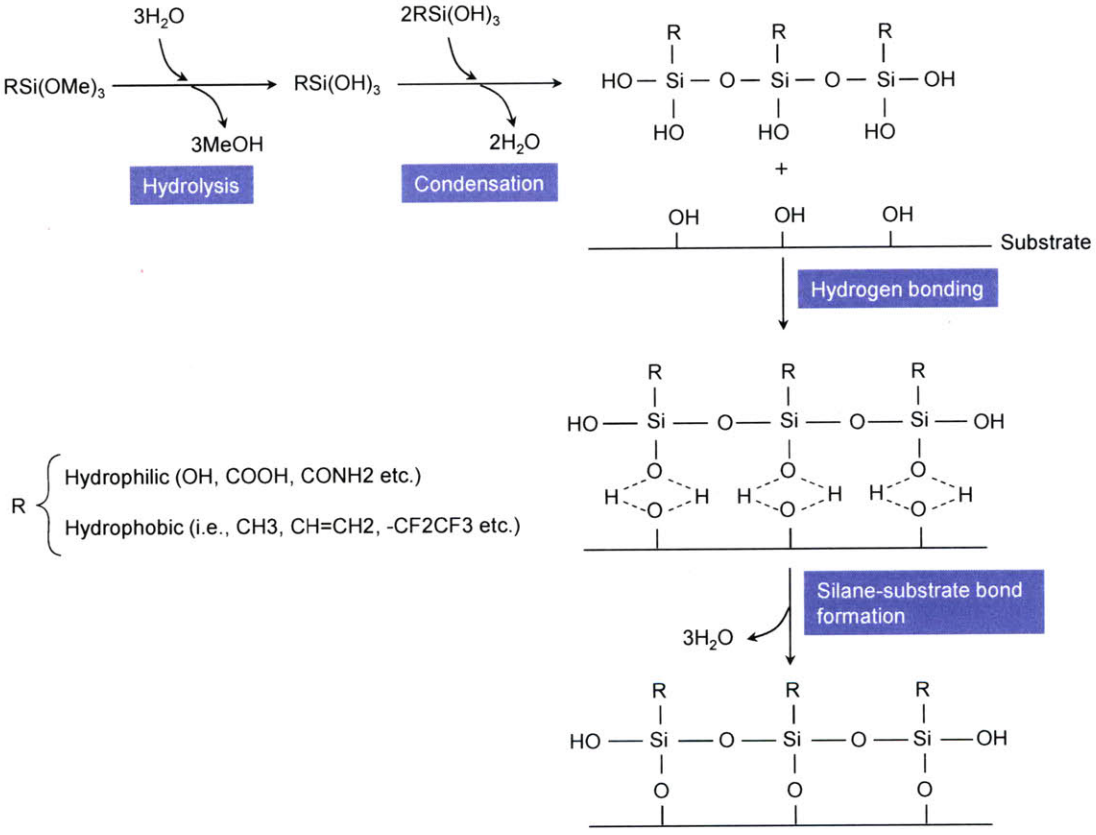

Figure 2-13. Mechanism of surface modification with silanes.

After the successful modification of PDMS microchannels, they were used for crystallization applications. We found an interesting phenomenon on the modified surfaces when the solvent and antisolvent were flown. We observed the formation of self-

assembled structures, first at the interface of the solvent and the antisolvent, and in half of the channel width consisting of mostly organic solvent and a small amount of aqueous solution, as shown in Figure 2-14a, and then across the channel at a later residence time. The locations where the structures formed were similar to where impurity inclusions formed (as discussed earlier); the only difference was that the inclusions were flowing and the polymeric structures were stationary, probably because part of the structure was covalently bonded to PDMS surface. The self-assembled structure formation was not observed when only ethanol or only water was flown into the channels, but when they were co-flown side by side. Authors, who have studied the self-assembly of silane molecules on PDMS, have claimed that silane forms a monolayer through the surface modification method.[87, 90, 91] However, we believe that silane molecules form multilayered structures with one end bonded to the surface and the other end forming fluffy structures that can undergo reorganization at unfavorable conditions. If pure ethanol was flown over these polymeric structures, they underwent a second reorganization to go back to the original state to some extent and disappeared partially.

We found that this type of polymerization had a profound effect on crystallization. When glycine crystallization was run in the modified channel, it was found that heterogeneous nucleation occurred selectively in locations where polymerization was observed. For example, Figure 2-14c shows selective crystallization of thousands of small crystals on the surface of half of the channel width, where polymeric structures appeared (corresponding to Figure 2-14b). These crystals, then, grew to block the channels.

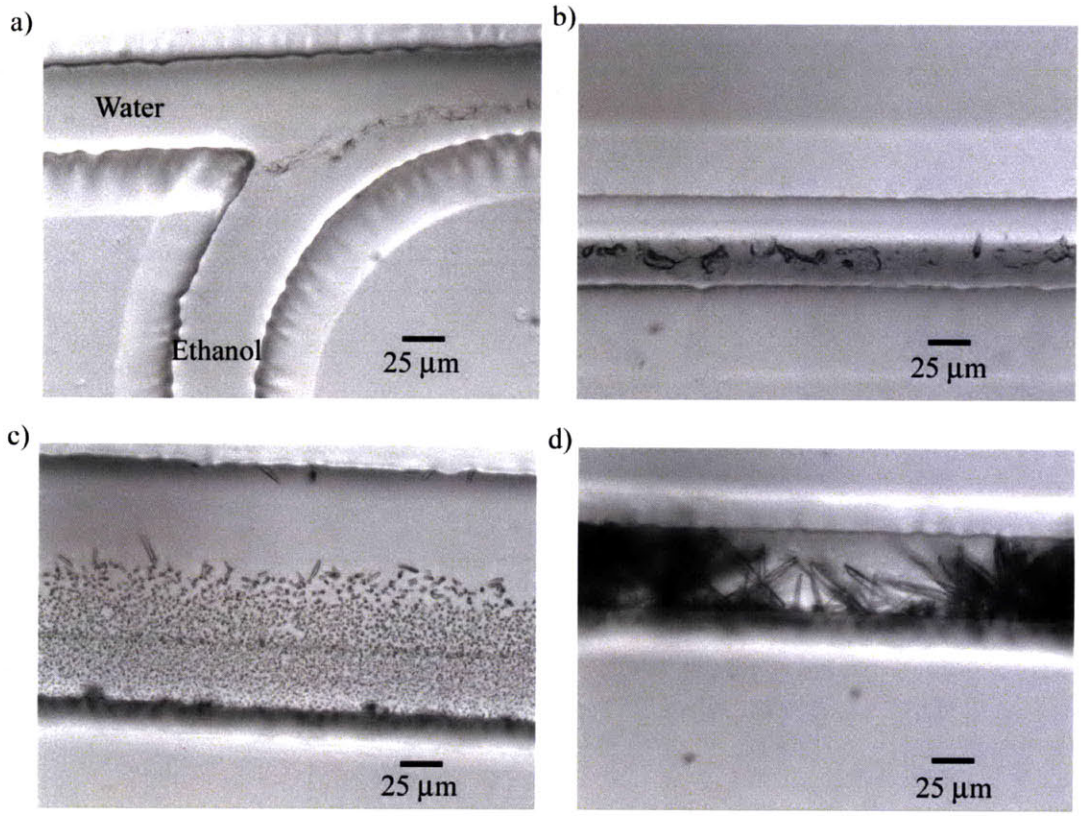

Figure 2-14. Polymerization of silane molecules. a) The silane molecules, used to modify PDMS surface, forms multilayered structures that can go through self assembly as water and ethanol are co-flown side by side. The polymerization appears first at the interface of the water and ethanol stream. b) Polymerization in half of the channel, containing mostly ethanol and some water, appears at a later residence time. c) The polymeric structures induce crystallization. Thousands of small crystals nucleate in half of the channel width where polymeric structures form. d) The stationary crystals then grow on to clog the channels.

Coating surfaces physically with Teflon AF was used as the second method for preparing fluoropolymer modified, stable PDMS surface. Poly(tetrafluoroethylene-*co*-2,2-bis-trisfluoromethyl-4,5-difluoro-1,3-dioxole) or Teflon AF was chosen as the coating material for its optical transparency, as well as increased surface stability. We used liquid Teflon AF and annular type multiphase flow to enable the coating.[*] First, microchannels of homogeneous surfaces were fabricated. Glass slides were spin-coated with liquid PDMS at 2500 rpm to give a thin coating (~20 μm), cured and bonded to

[**] This work was performed in collaboration with Dr. Ryan Hartman, at the time a postdoctoral associate in Professor Jensen's group.

clean PDMS devices. Fabricated devices were, then, injected with 60μL fluoropolymer solvent (FC-75 manufactured by 3M). As soon as the liquid Teflon reached the microchannel, nitrogen gas was used to drive the liquid through the channel, which created an annular flow. This type of flow allowed for controlled evaporation of fluoropolymer solvent, bringing about polymer deposition on microchannel walls. The coating conformed more or less to the channel geometry, except for sharp edges. Nitrogen was flown through the microchannels for two hours in order to evaporate most of the solvent before transferring the device to an oven at 120°C, above the boiling point of the solvent, and baked for four hours while continuing to flow nitrogen in order to ensure complete solvent removal. It was found that prolonged gas flow resulted in a thin and smooth coating on channel surfaces. Finally, the oven temperature was increased to 170°C, above the glass transition temperature of the fluoropolymer, and held for an hour in order to ensure adhesion of the film to channel surfaces. The process was repeated twice to ensure uniform coating of the surfaces.

Successful treatment was confirmed by characterizing the microchannel surfaces with spectroscopy and microscopy techniques. A separate PDMS piece was processed simultaneously with analogous procedure and used for contact angle measurements. A Kratos Axis Ultra Imaging X-ray Photoelectron Spectroscopy tool (manufactured by Kratos Analytical in Manchester, UK) was used with aluminum Kα monochromatic source to investigate surface chemistry. High resolution spectra for C, O, and F were obtained with 20 eV and analyzed with CasaXps (Casa Software Inc.). The spectrum of the fluoropolymer was calibrated by matching the fluorine peak to that of reference organic fluoropolymer. Peaks were also fitted to C1s spectra by using the peak information of reference organic fluoropolymers as a guide.[94] Figure 2-15a compares the surface chemistry of the modified PDMS with native PDMS, and confirms the presence of Teflon fluoropolymer on the surface. The carbon chemistry of the modified and unmodified PDMS surface is presented in Figures 2-15b and 2-15c, respectively. Peak fitting of C1s spectra of the modified surface indicates the presence of at least four types of carbon, which correspond very well with the known structure of coated fluoropolymer, presented in Figure 2-15d.

Optical microscopy and an environmental scanning electron microscopy (SEM) were used to visualize the coating and to obtain an estimate for the coating thickness, respectively. A cryo-microtome was used to cut the PDMS microchannel in order to preserve the film. Figures 2-16a and 2-16b present optical microscopy images of coated and native PDMS. Since the optical microscopy obtained a 2-dimensional projection of the channel, SEM was used to look at the channel cross section in order to obtain a more accurate representation of the coating thickness. The film thickness was found to be approximately 600 nm. SEM images also showed a smooth surface of the coated film (Figure 2-16c).

Since roughness plays an important role in crystallization, as demonstrated with silane-modified PDMS surfaces, the surface topology and roughness of the microchannels were imaged with atomic force microscopy (AFM). Figures 2-16d and 2-16e present the surface topology of a modified and native PDMS microchannel, respectively. The lines seen in the native microchannel surface represents 2-20 nm deep trenches that propagated from SU-8 master. The appearance of trenches was reproducible between various master wafers, and most probably resulted from the processing of SU-8 films. The Teflon AF coating covered the trenches smoothly, as seen in the AFM image. The root mean square roughness of the modified PDMS was found to be 1.5 nm, in the same order of magnitude as the roughness of native PDMS (0.7 nm) when selecting an area without any trenches.

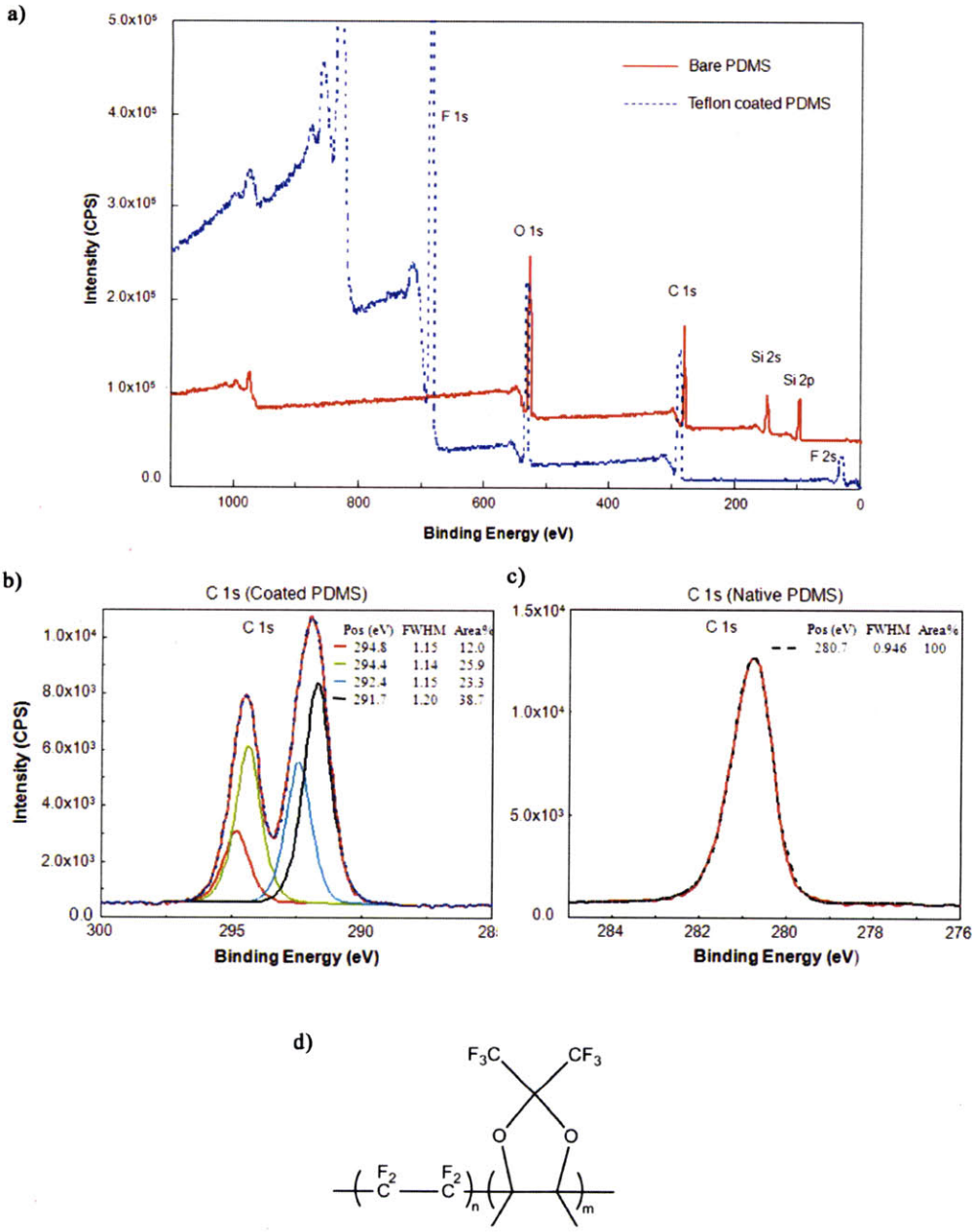

Figure 2-15. X-ray photoelectron spectroscopy (XPS) of the modified PDMS, revealing Teflon coating. a) A comparison of the XPS spectrum of the modified and native PDMS confirms additional fluorine peaks resulting from the coating process. b) The carbon chemistry of the modified surface, indicating the presence of at least four types of carbon. c) The carbon chemistry of native PDMS, indicating the presence of only one type of carbon. d) The structure of the fluoropolymer used in the coating process, representing 4 types of carbon chemistry.

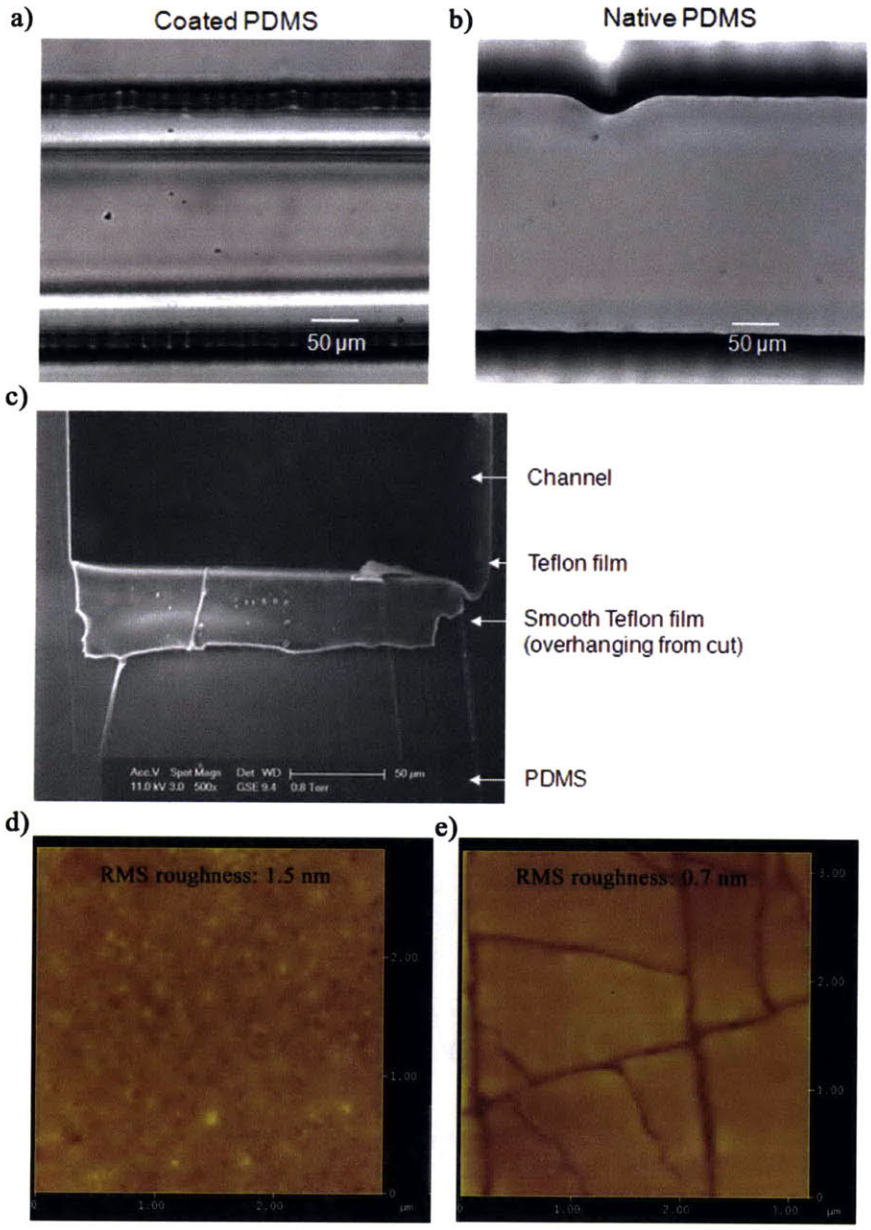

Figure 2-16. Microscopy of Teflon coated PDMS. a-b) Optical microscopy images of coated and native PDMS microchannel. c) SEM image of the coated microchannel, revealing ~600 nm thick layers of Teflon. The overhanging film, resulting from the microtome cut shows a smooth surface of the coating. d-e) The surface of the modified and native PDMS microchannel imaged with AFM. The root mean square (RMS) roughness of the modified PDMS surface is comparable to the native PDMS surface.

Teflon coating not only provides a stable surface to PDMS, but also has the potential to make superhydrophobic surfaces. There has been a lot of interest in fabricating superhydrophic surfaces because of its self-cleaning properties.[95] For crystallization, nonwetting surface can eliminate heterogeneous nucleation, as discussed in Chapter 1. Hence, the wettability of the coated surface was characterized with contact angle measurements. The surface was found to be nonwettable to water as illustrated Figure 2-17. When 5 μl deionized water was dropped on the surface, the advancing and receding contact angles were found to be 121.4 ±1.4.

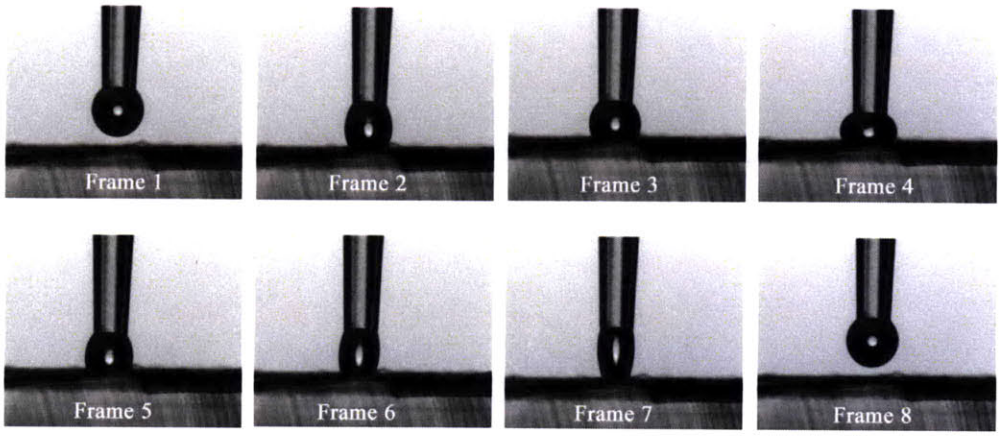

Figure 2-17. Nonwetting superhydrophobic surface results when PDMS is coated with Teflon AF.

2.3.8 Crystal Density

One of the difficulties of continuous crystallization is the high density of crystals and/or fast growth rate, resulting from the high driving force usually required for homogeneous nucleation. The higher density shortens the average distance between two crystals, increasing the interactions between them. The interaction between organic crystal systems are mainly of three types: a) non-bonded, non electrostatic such as van der Waals, London dispersion etc., b) electrostatic, and c) hydrogen bonding.[76] Decreasing the distance, increases the strength of some of these interactions significantly,

particularly of electrostatic. This plays an important role for positively and negatively charged glycine crystal surfaces. The various interactions give rise to such phenomena as agglomeration and coalescence. It is readily acknowledged that agglomeration and coalescence are much more common phenomena in organic systems than inorganic ones. Here, we use the term "agglomeration" or "aggregation" for the case when two or more entities come together through various interactions, but remain as separate entities. We use the term "coalescence" to represent the case when two or more entities combine to form one larger entity.[96] Aggregation and coalescence can cause the growth rate to be very high, yielding large crystals, which in turn can clog the channel by sedimentation followed by growth, straining or by deposition through various mechanisms.

Wyss et al. have shown that clogging at a single pore may be dictated by the ratio of pore to particle size, with the clogging time decreasing as ratio decreases.[79] This was in accordance with our observation of glycine crystals forming large aggregates and coalesced entities, leading to channel clogging. In order to address this issue, we used a hydrodynamic flow focusing device, with glycine solution flown through the core and the antisolvent flown as a sheath around it. By designing the dimension of the sheath and the core, as well as the flow rates, one can reduce the number density of crystals across the channel. We used a simple technique to create flow focusing device with a microcapillary (FHC Inc., ME) (Figure 2-18a). We designed a tee channel of 1.5mm×1.5mm dimension. We machined the negative image of the channel in PMMA (polymethylmethacrylate) and used it as the master for hot embossing PDMS molds (Figure 2-18a). The channels were sealed with a coated glass slide. A microcapillary with approximately 30 μm tip diameter was inserted through the head of the tee. The geometry of the capillary and the channel were used to center the tip of the capillary, and were glued in place with 5-min epoxy (Figure 2-18b). The two inlets on the sides of the tee were used for sheath flow and the capillary was used to flow glycine solution. A 360 μm outer diameter silica tubing (Polymicro Technolgies) and upchurch fittings (IDEX Health & Science) were used to interface the capillary with syringe pumps.

Sheath flow was successfully achieved with a sheath flow rate of 500 $\mu l \cdot min^{-1}$ to 1000 $ml \cdot min^{-1}$, and a core flow rate of 2 to 10 $\mu l \cdot min^{-1}$. Figure 2-18c illustrates the sheath flow obtained in our device. Approximately 20-40% saturated glycine in pure water was used

as the core solution, and approximately 90-100% aqueous ethanol was used as the sheath. The solution underwent spontaneous homogeneous nucleation. The nucleating crystals were mostly needles (Figure 2-18d), representing the beta form, with some smaller ones with a more regular habit, representing the alpha form (zoomed section of Figure 2-18d). The appearance of both forms, at as short a residence time as milliseconds, most likely indicates incomplete and slower mixing than required for nucleation, giving rise to high supersaturation regime for the nucleation of beta, as well as low supersaturation regime for the nucleation of alpha. Fast mixing was difficult to achieve across the 1.5×1.5 mm channel with only diffusion. The incomplete mixing also made it difficult to calculate the actual supersaturation present in the channel. Although we were able to run the experiment for a longer time, we found that the channels still became clogged over time, as illustrated in Figure 2-18d.

For sheath flow, the initial size range of the needle crystals were approximately in the same range as achieved previously with homogeneous nucleation in devices of 300×250 μm channels, while the channel dimensions were approximately 3.5 times larger. The amount of glycine crystallized, $\dot{m}_g$, was found to increase for the sheath flow experiments, as expected. $\dot{m}_g$ was calculated from the flow rates and glycine solubility.

$$\dot{m}_g = C_{s,i} \times S_i \times \dot{m}_{s,i} - C_{s,f} \times \dot{m}_{s,f} \qquad 2\text{-}9$$

where $C_{s,i}$ is solute solubility in the initial solvent composition, 100% water in our studies of glycine crystallization, S_i is the initial supersaturation, $\dot{m}_{s,i}$ is the solvent flow rate, $C_{s,f}$ is solute solubility in the final solvent-antisolvent composition, and $\dot{m}_{s,f}$ is the mass flow rate of the corresponding solvent-antisolvent. The glycine crystallized in the previous case of homogeneous nucleation was approximately 0.17 mg·min^{-1}, while the amount in the sheath flow reactor was approximately 0.35 mg·min^{-1} due to higher antisolvent-solution ratio and thus higher driving force. For similar size range, the density of crystals was therefore approximately twice in the sheath flow reactor than that in devices of Design 3. This might have contributed to the formulation of large aggregates, causing subsequent channel clogging.

In this study, we learned that the ratio of channel dimension to the total amount of solid crystallized plays an important role in channel clogging. The least amount of solid

that crystallizes from spontaneous homogeneous nucleation is somewhat fixed for a chosen set of solvent and antisolvent (it corresponds to the shortest metastable zone width). Thus, a solvent-antisolvent system that gives high yield of solid, such as water and ethanol for glycine, may clog the small-dimensioned microchannels. Consequently, in order to realize continuous crystallization in microchannels, it is imperative to choose a solvent-antisolvent system that gives high supersaturation ratio to cause nucleation, but a low crystal yield. We use exactly this idea to choose a suitable solvent-antisolvent system for a pharmaceutical compound and demonstrate continuous homogeneous crystallization in microchannels in chapter 5.

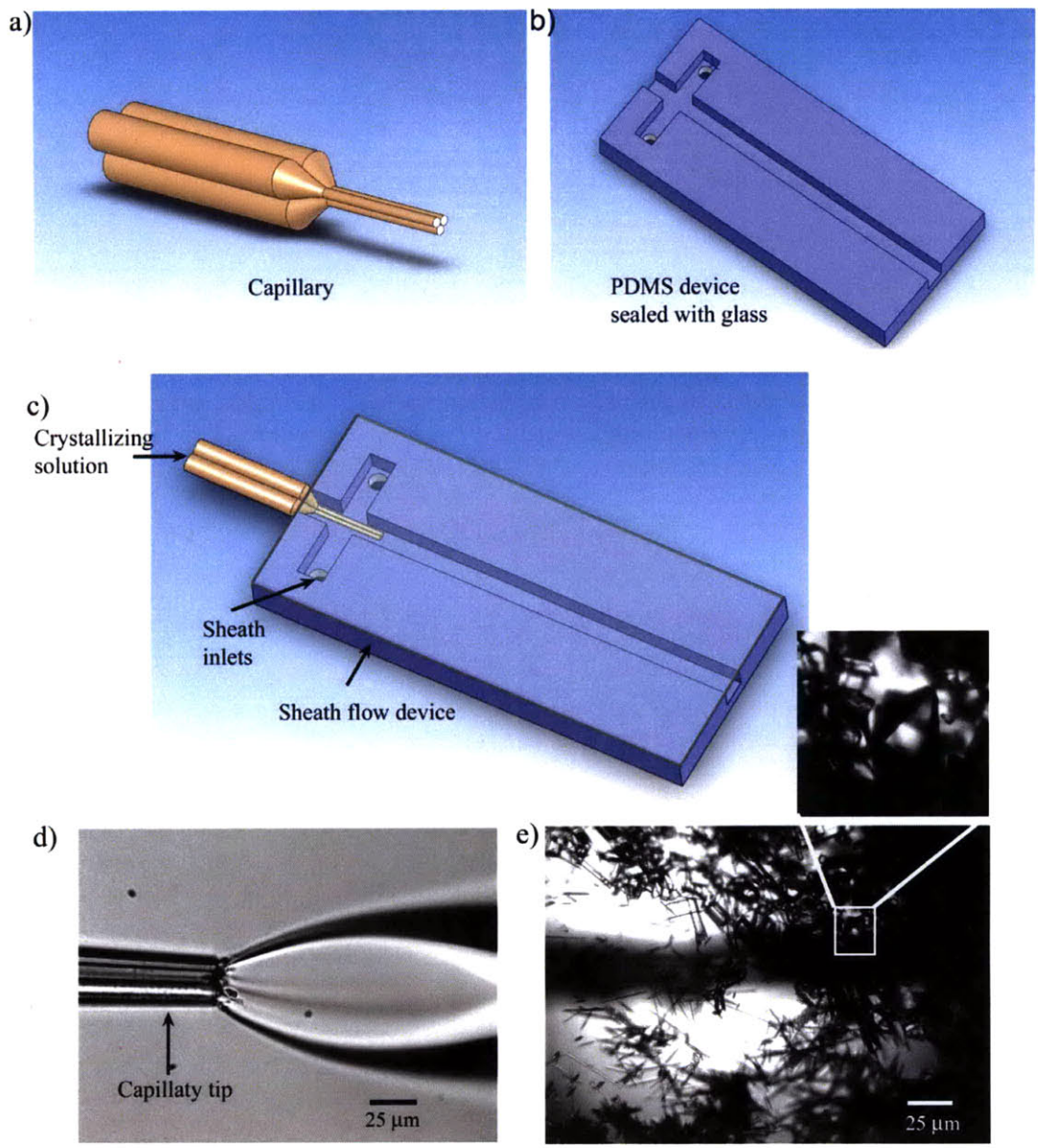

Figure 2-18. Sheath flow setup. a) Capillary used to create the core of the sheath flow. b) The single tee channel in fabricated in PDMS with hot embossing. c) The device assembled with the capillary. d) The sheath flow achieved in this reactor. e) Channel clogging resulting from a high yield of glycine crystals due to high driving force. The nucleated crystals were mostly needles, with a few regular shaped (in the zoomed up section).

2.4 Summary

This chapter discussed the challenges associated with continuous crystallization in microfluidic devices. Material selection and operating conditions were discussed in light

of crystallization of organic molecules. Device issues, relevant to particle synthesis, were also addressed. An understanding of channel clogging mechanism was developed for the case of organic solids. In addition, we obtained an understanding of the nucleation behavior of organic molecules, which is used in the following chapters to realize continuous crystallization.

Homogeneous nucleation is difficult to achieve in microfluidic devices for organic systems, particularly with a solvent-antisolvent system that gives a high yield. This results from the inherent nucleation behavior of organic systems. Comparing the nucleation behavior of the organic and inorganic systems gives insights into the potential difficulties (Figure 2-19) associated with continuous nucleation of the former system. For inorganic materials, the nucleation event desupersaturates the solution significantly, resulting in a small supersaturation, Δc, left for growth. Organic systems, on the other hand, do not desupersaturate the solution enough after the initial nucleation event. In fact, subsequent secondary nucleation often occurs due to high supersaturation still remaining in the solution. This high driving force may give high growth rates, that can bridge or cause coalescence between two or more crystals, or between crystals and channel surfaces. Many inorganic particles such as silica and titania, have repulsive interactions due to surface charge, and attractive interactions due to van der Waals. However, organic crystals usually have mostly attractive interactions such as van der Waals, electrostatic, and hydrogen bonding, which increases agglomeration and coalescence behavior. Moreover, similar attractive interactions may also be present between microchannel surface and crystals, increasing solid deposition on the channel walls. Furthermore, the abovementioned issues can be amplified with a difficult choice of solvent-antisolvent system. If a solvent with high solute solubility is chosen, then the high supersaturation usually required for homogeneous nucleation of organic solutes, results in a large amount of solid that is difficult to control in microchannels.

We use this understanding of nucleation and growth behavior of organic crystal systems to break the crystallization process into two parts. We decouple the nucleation and growth, and design separate devices for each process. In chapter 3, we develop a microfluidic device that can effectively suppress nucleation and perform continuous seeded crystallization. Because we focus only on the growth process, we can choose to

operate at a low enough supersaturation that minimizes coalescence. By choosing the seed density, we can also minimize agglomeration. Moreover, we control surface properties of the microchannels to minimize solid deposition. Furthermore, we choose the seed size to address sedimentation problems, enabling continuous seeded crystallization. In chapter 5, we develop a second microfluidic platform for continuous nucleation. We carefully choose the solute to minimize solid-channel surface interactions. Also, we use the solvent-antisolvent system so as to achieve high supersaturation, but comparatively lower yield. Finally, we use reactor design to control crystal density in the channels and to minimize crystal interactions with channel surfaces, successfully enabling continuous crystallization in microchannels.

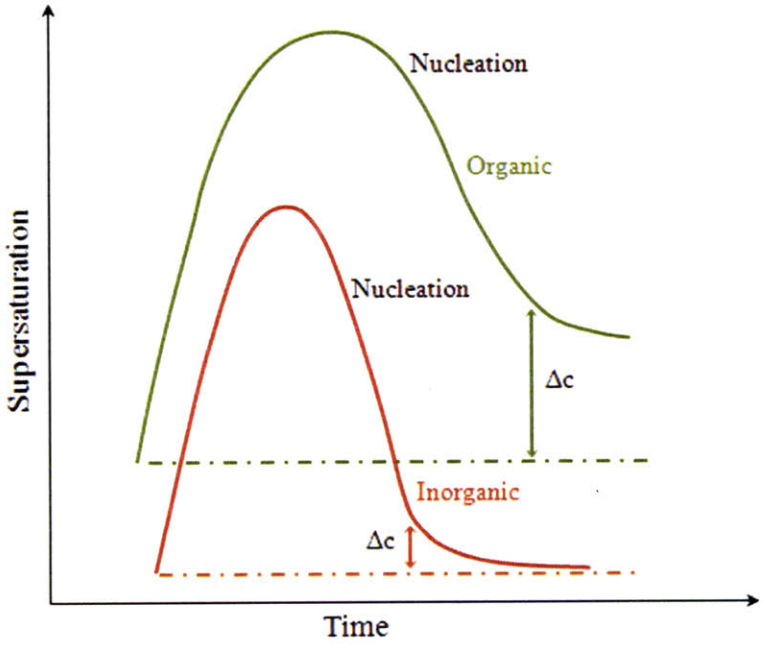

Figure 2-19. Nucleation behaviour of organic (green) and inorganic (red) systems. For inorganic systems, the nucleation event desupersaturates the solution, resulting in a small supersaturation, Δc, for growth. For organic systems, the nucleation does not desupersaturate the solution enough, leaving a large supersaturation, Δc, for growth and coalescence.

2.5 List of Variables

t_{ind}	induction time
t_n	nucleation time
J	rate of nucleation
t_g	time required for a nuclei to grow to a detectable size
G	growth rate
ΔT	temperature difference
t_M	characteristic mixing time
l	characteristic diffusion length
D	diffusion coefficient
S	supersaturation
C	solute concentration
C_s	solute solubility
Q	gas flow rate
p	gas permeability
A	surface area
h	thickness
ΔP	pressure difference
L	Ostwald coefficient
V_{gas}	gas volume
$V_{solvent}$	solvent volume
θ	contact angle
γ_s	surface energy of the solid sample
γ_l	surface energy of liquid droplet
γ_{ls}	interfacial tension between the solid and liquid phases
θ_a	advancing contact angle
θ_r	receding contact angle
$\dot{m}_g$	amount of glycine crystallized
$C_{s,i}$	solute solubility in the initial solvent composition

S_i	initial supersaturation
$\dot{m}_{s,i}$	solvent flow rate
$C_{s,f}$	solute solubility in the final solvent composition
$\dot{m}_{s,f}$	mass flow rate of glycine solute in the final solvent composition

2.6 References

[1] A. Abou-Hassan, O. Sandre, S. Neveu, & V. Cabuil, Synthesis of Goethite by Separation of the Nucleation and Growth Processes of Ferrihydrite Nanoparticles Using Microfluidics. *Angewandte Chemie-International Edition,* **2009**, *48*(13), 2342-2345.

[2] R. Karnik, F. Gu, P. Basto, C. Cannizzaro, L. Dean, W. Kyei-Manu, R. Langer, & O. C. Farokhzad, Microfluidic platform for controlled synthesis of polymeric nanoparticles. *Nano Letters,* **2008**, *8*(9), 2906-2912.

[3] S. A. Khan, A. Gunther, M. A. Schmidt, & K. F. Jensen, Microfluidic synthesis of colloidal silica. *Langmuir,* **2004**, *20*(20), 8604-8611.

[4] S. A. Khan, & K. F. Jensen, Microfluidic synthesis of titania shells on colloidal silica. *Advanced Materials,* **2007**, *19*(18), 2556-2560.

[5] S. Marre, & K. F. Jensen, Synthesis of micro and nanostructures in microfluidic systems. *Chemical Society Reviews,* **2010**, *39*(3), 1183-1202.

[6] S. Marre, J. Park, J. Rempel, J. Guan, M. G. Bawendi, & K. F. Jensen, Supercritical continuous-microflow synthesis of narrow size distribution quantum dots. *Advanced Materials,* **2008**, *20*(24), 4830-4834.

[7] J. Wagner, & J. M. Kohler, Continuous synthesis of gold nanoparticles in a microreactor. *Nano Letters,* **2005**, *5*(4), 685-691.

[8] B. K. H. Yen, A. Gunther, M. A. Schmidt, K. F. Jensen, & M. G. Bawendi, A microfabricated gas-liquid segmented flow reactor for high-temperature synthesis: The case of CdSe quantum dots. *Angewandte Chemie-International Edition,* **2005**, *44*(34), 5447-5451.

[9] D. Dendukuri, D. C. Pregibon, J. Collins, T. A. Hatton, & P. S. Doyle, Continuous-flow lithography for high-throughput microparticle synthesis. *Nature Materials,* **2006**, *5*(5), 365-369.

[10] C. L. Hansen, S. Classen, J. M. Berger, & S. R. Quake, A microfluidic device for kinetic optimization of protein crystallization and in situ structure determination. *Journal of the American Chemical Society,* **2006**, *128*(10), 3142-3143.

[11] C. L. Hansen, E. Skordalakes, J. M. Berger, & S. R. Quake, A robust and scalable microfluidic metering method that allows protein crystal growth by free interface diffusion. *Proceedings of the National Academy of Sciences of the United States of America,* **2002**, *99*(26), 16531-16536.

[12] J. Leng, & J. B. Salmon, Microfluidic crystallization. *Lab on a Chip,* **2009**, *9*(1), 24-34.

[13] B. Zheng, J. D. Tice, & R. F. Ismagilov, Formation of arrayed droplets of soft lithography and two-phase fluid flow, and application in protein crystallization. *Advanced Materials,* **2004**, *16*(15), 1365-1368.

[14] B. Zheng, J. D. Tice, L. S. Roach, & R. F. Ismagilov, A droplet-based, composite PDMS/glass capillary microfluidic system for evaluating protein crystallization conditions by microbatch and vapor-diffusion methods with on-chip X-ray diffraction. *Angewandte Chemie-International Edition,* **2004**, *43*(19), 2508-2511.

[15] C. J. Gerdts, V. Tereshko, M. K. Yadav, I. Dementieva, F. Collart, A. Joachimiak, R. C. Stevens, P. Kuhn, A. Kossiakoff, & R. F. Ismagilov, Time-controlled microfluidic seeding in nL-volume droplets to separate nucleation and growth

stages of protein crystallization. *Angewandte Chemie-International Edition,* **2006**, *45*(48), 8156-8160.

[16] E. Forsythe, F. Ewing, & M. Pusey, Studies on tetragonal lysozyme crystal-growth rates. *Acta Crystallographica Section D-Biological Crystallography,* **1994**, *50*, 614-619.

[17] J. Nyvlt, O. Sohnel, M. Matuchova, & M. Broul, *The Kinetics of Industrial Crystallization*, Elsevier, Amsterdam, **1985**.

[18] O. Sohnel, & J. W. Mullin, Interpretation of crystallization induction periods. *Journal of Colloid and Interface Science,* **1988**, *123*(1), 43-50.

[19] P. Barrett, B. Smith, J. Worlitschek, V. Bracken, B. O'Sullivan, & D. O'Grady, A review of the use of process analytical technology for the understanding and optimization of production batch crystallization processes. *Organic Process Research & Development,* **2005**, *9*(3), 348-355.

[20] A. M. Schwartz, & A. S. Myerson, Solutions and solution properties. in *Handbook of Industrial Crystallization* (Ed.: A. S. Myerson), **2002**, pp. 1-31.

[21] A. J. Mahajan, & D. J. Kirwan, Micromixing effects in a two-impinging-jets precipitator. *Aiche Journal,* **1996**, *42*(7), 1801-1814.

[22] B. K. Johnson, & R. K. Prud'homme, Chemical processing and micromixing in confined impinging jets. *Aiche Journal,* **2003**, *49*(9), 2264-2282.

[23] N. T. Nguyen, & Z. G. Wu, Micromixers - a review. *Journal of Micromechanics and Microengineering,* **2005**, *15*(2), R1-R16.

[24] T. M. Floyd, M. A. Schmidt, & K. F. Jensen, Silicon micromixers with infrared detection for studies of liquid-phase reactions. *Industrial & Engineering Chemistry Research,* **2005**, *44*(8), 2351-2358.

[25] A. J. deMello, Control and detection of chemical reactions in microfluidic systems. *Nature,* **2006**, *442*(7101), 394-402.

[26] H. V. Ehrfeld W, Lowe H, *Microreactors: New Technology for Modern Chemistry*, Wiley-VCH, Weinheim, **2000**.

[27] J. El-Ali, P. K. Sorger, & K. F. Jensen, Cells on chips. *Nature,* **2006**, *442*(7101), 403-411.

[28] J. B. Angell, S. C. Terry, & P. W. Barth, Silicon micromechanical devices. *Scientific American,* **1983**, *248*(4), 44-55.

[29] J. Arnold, U. Dasbach, W. Ehrfeld, K. Hesch, & H. Lowe, Combination of excimer-laser micromachining and replication processes suited for large-scale production. *Applied Surface Science,* **1995**, *86*(1-4), 251-258.

[30] J. C. McDonald, D. C. Duffy, J. R. Anderson, D. T. Chiu, H. K. Wu, O. J. A. Schueller, & G. M. Whitesides, Fabrication of microfluidic systems in poly(dimethylsiloxane). *Electrophoresis,* **2000**, *21*(1), 27-40.

[31] Y. N. Xia, & G. M. Whitesides, Soft lithography. *Annual Review of Materials Science,* **1998**, *28*, 153-184.

[32] W. Ehrfeld, H. Lehr, F. Michel, & A. Wolf, Micro electro discharge machining as a technology in micromachining. in *Micromachining and Microfabrication Process Technology Ii, Vol. 2879* (Eds.: S. W. Pang, S. C. Chang), Spie - Int Soc Optical Engineering, Bellingham, **1996**, pp. 332-337.

[33] O. Geschke, H. Klank, & P. Telleman, *Microsystem Engineering of Lab-on-a-Chip Devices*, Wiley-VCH, Weinheim, **2004**.

[34] P. Tabeling, *Introduction to Microfluidics*, Oxford University Press Inc., New York, **2005**.

[35] J. N. Lee, C. Park, & G. M. Whitesides, Solvent compatibility of poly(dimethylsiloxane)-based microfluidic devices. *Analytical Chemistry,* **2003**, *75*(23), 6544-6554.

[36] E. Kim, Y. N. Xia, & G. M. Whitesides, Polymer microstructures formed by molding in capillaries. *Nature,* **1995**, *376*(6541), 581-584.

[37] J. R. Anderson, D. T. Chiu, R. J. Jackman, O. Cherniavskaya, J. C. McDonald, H. K. Wu, S. H. Whitesides, & G. M. Whitesides, Fabrication of topologically complex three-dimensional microfluidic systems in PDMS by rapid prototyping. *Analytical Chemistry,* **2000**, *72*(14), 3158-3164.

[38] L. Yu, & K. Ng, Glycine crystallization during spray drying: The pH effect on salt and polymorphic forms. *Journal of Pharmaceutical Sciences,* **2002**, *91*(11), 2367-2375.

[39] A. J. Mahajan, & D. J. Kirwan, Nucleation and growth-kinetics of biochemicals measured at high supersaturations. *Journal of Crystal Growth,* **1994**, *144*(3-4), 281-290.

[40] H. Song, D. L. Chen, & R. F. Ismagilov, Reactions in droplets in microflulidic channels. *Angewandte Chemie-International Edition,* **2006**, *45*(44), 7336-7356.

[41] P. Laval, A. Crombez, & J. B. Salmon, Microfluidic Droplet Method for Nucleation Kinetics Measurements. *Langmuir,* **2009**, *25*(3), 1836-1841.

[42] A. Mersmann, *Crystallization Technology Handbook*, 2nd ed., Marcel Dekker, Inc., New York, **2001**.

[43] A. B. Subramaniam, M. Abkarian, & H. A. Stone, Controlled assembly of jammed colloidal shells on fluid droplets. *Nature Materials,* **2005**, *4*(7), 553-556.

[44] A. B. Subramaniam, D. Gregory, J. Petkov, & H. A. Stone, The effect of double-chain surfactants on armored bubbles: a surfactant-controlled route to colloidosomes. *Physical Chemistry Chemical Physics,* **2007**, *9*(48), 6476-6481.

[45] Biogeneral Inc. http://www.biogeneral.com/teflon.html. San Diego, CA. **2010**.

[46] M. H. Abraham, G. S. Whiting, W. J. Shuely, & R. M. Doherty, The solubility of gases and vapours in ethanol - the connection between gaseous solubility and water-solvent partition. *Canadian Journal of Chemistry-Revue Canadienne De Chimie,* **1998**, *76*(6), 703-709.

[47] J. Tokunaga, Solubilities of oxygen, nitrogen, and carbon-dioxide in aqueous alcohol solutions. *Journal of Chemical and Engineering Data,* **1975**, *20*(1), 41-46.

[48] J. L. Fritz, & M. J. Owen, Hydrophobic recovery of plasma-treated polydimethylsiloxane. *Journal of Adhesion,* **1995**, *54*(1-2), 33-45.

[49] J. Kim, M. K. Chaudhury, M. J. Owen, & T. Orbeck, The mechanisms of hydrophobic recovery of polydimethylsiloxane elastomers exposed to partial electrical discharges. *Journal of Colloid and Interface Science,* **2001**, *244*(1), 200-207.

[50] H. Hillborg, N. Tomczak, A. Olah, H. Schonherr, & G. J. Vancso, Nanoscale hydrophobic recovery: A chemical force microscopy study of UV/ozone-treated cross-linked poly(dimethylsiloxane). *Langmuir,* **2004**, *20*(3), 785-794.

[51] A. Olah, H. Hillborg, & G. J. Vancso, Hydrophobic recovery of UV/ozone treated poly(dimethylsiloxane): adhesion studies by contact mechanics and mechanism of surface modification. *Applied Surface Science,* **2005**, *239*(3-4), 410-423.

[52] Y. A. Liu, & G. D. Botsaris, Impurity effects in continuous-flow mixed suspension crysatllizers. *Aiche Journal,* **1973**, *19*(3), 510-516.

[53] D. Turnbull, & B. Vonnegut, Nucleation catalysis. *Industrial and Engineering Chemistry,* **1952**, *44*(6), 1292-1298.

[54] Y. J. Yi, & A. S. Myerson, Laboratory scale batch crystallization and the role of vessel size. *Chemical Engineering Research & Design,* **2006**, *84*(A8), 721-728.

[55] X. Y. Liu, Interfacial effect of molecules on nucleation kinetics. *Journal of Physical Chemistry B,* **2001**, *105*(47), 11550-11558.

[56] A. J. Mahajan, PhD Thesis. University of Virginia **1993**.

[57] A. Y. Lee, & A. S. Myerson, Particle engineering: Fundamentals of particle formation and crystal growth. *Mrs Bulletin,* **2006**, *31*(11), 881-886.

[58] G. Albrecht, The crystal structure of glycine. *Journal of the American Chemical Society,* **1939**, *61*(5), 1087-1103.

[59] E. Fischer, Synthese von Polypeptiden. *Berichte der Deutschen Chemischen Gesellschaft,* **1905**, *38*(3), 2914-2925.

[60] Y. Iitaka, New form of glycine. *Proceedings of the Japan Academy,* **1954**, *30*, 109-120.

[61] R. E. Marsh, A refinement of the crystal structure of glycine. *Acta Crystallographica,* **1958**, *11*(9), 654-663.

[62] J. Zaccaro, J. Matic, A. S. Myerson, & B. A. Garetz, Nonphotochemical, laser-induced nucleation of supersaturated aqueous glycine produces unexpected gamma-polymorph. *Crystal Growth & Design,* **2001**, *1*(1), 5-8.

[63] T. N. Drebushchak, E. V. Boldyreva, Y. V. Seryotkin, & E. S. Shutova, Crystal structure study of the metastable beta-modification of glycine and its transformation into the alpha-modification. *Journal of Structural Chemistry,* **2002**, *43*(5), 835-842.

[64] E. V. Boldyreva, V. A. Drebushchak, T. N. Drebushchak, I. E. Paukov, Y. A. Kovalevskaya, & E. S. Shutova, Polymorphism of glycine - Thermodynamic aspects. Part I. Relative stability of the polymorphs. *Journal of Thermal Analysis and Calorimetry,* **2003**, *73*(2), 409-418.

[65] G. L. Perlovich, L. K. Hansen, & A. Bauer-Brandl, The polymorphism of glycine - Thermochemical and structural aspects. *Journal of Thermal Analysis and Calorimetry,* **2001**, *66*(3), 699-715.

[66] Z. Berkovitchyellin, Toward an Abinitio Derivation of Crystal Morphology. *Journal of the American Chemical Society,* **1985**, *107*(26), 8239-8253.

[67] M. Lahav, & L. Leiserowitz, The effect of solvent on crystal growth and morphology. *Chemical Engineering Science,* **2001**, *56*(7), 2245-2253.

[68] Y. C. Zhang, J. P. Sizemore, & M. F. Doherty, Shape evolution of 3-dimensional faceted crystals. *Aiche Journal,* **2006**, *52*(5), 1906-1915.

[69] Y. Iitaka, The crystal structure of beta-glycine. *Acta Crystallographica,* **1960**, *13*, 35-45.

[70] I. Weissbuch, V. Y. Torbeev, L. Leiserowitz, & M. Lahav, Solvent effect on crystal polymorphism: Why addition of methanol or ethanol to aqueous solutions

induces the precipitation of the least stable beta form of glycine. *Angewandte Chemie-International Edition,* **2005**, *44*(21), 3226-3229.

[71] A. Bouchard, G. W. Hofland, & G. J. Witkamp, Solubility of glycine polymorphs and recrystallization of beta-glycine. *Journal of Chemical and Engineering Data,* **2007**, *52*(5), 1626-1629.

[72] J. Toth, A. Kardos-Fodor, & S. Halasz-Peterfi, The formation of fine particles by salting-out precipitation. *Chemical Engineering and Processing,* **2005**, *44*(2), 193-200.

[73] K. Park, J. M. B. Evans, & A. S. Myerson, Determination of solubility of polymorphs using differential scanning calorimetry. *Crystal Growth & Design,* **2003**, *3*(6), 991-995.

[74] C. J. Orella, & D. J. Kirwan, Correlation of Amino-Acid Solubilities in Aqueous Aliphatic Alcohol-Solutions. *Industrial & Engineering Chemistry Research,* **1991**, *30*(5), 1040-1045.

[75] H. G. Brittain, *Polymorphism in Pharmaceutical Solids*, Marcel Dekker, New York, **1999**.

[76] J. Bernstein, *Polymorphism in Molecular Crystals*, Clarendon Press, Oxford University Press, New York, **2002**.

[77] S. Hong, R. S. Faibish, & M. Elimelech, Kinetics of permeate flux decline in crossflow membrane filtration of colloidal suspensions. *Journal of Colloid and Interface Science,* **1997**, *196*(2), 267-277.

[78] R. Narayan, J. R. Coury, J. H. Masliyah, & M. R. Gray, Particle capture and plugging in packed-bed reactors. *Industrial & Engineering Chemistry Research,* **1997**, *36*(11), 4620-4627.

[79] H. M. Wyss, D. L. Blair, J. F. Morris, H. A. Stone, & D. A. Weitz, Mechanism for clogging of microchannels. *Physical Review E,* **2006**, *74*(6), 061402.

[80] V. Ramachandran, & H. S. Fogler, Plugging by hydrodynamic bridging during flow of stable colloidal particles within cylindrical pores. *Journal of Fluid Mechanics,* **1999**, *385*, 129-156.

[81] V. Ramachandran, R. Venkatesan, G. Tryggvason, & H. S. Fogler, Low Reynolds number interactions between colloidal particles near the entrance to a cylindrical pore. *Journal of Colloid and Interface Science,* **2000**, *229*(2), 311-322.

[82] S. L. Poe, M. A. Cummings, M. R. Haaf, & D. T. McQuade, Solving the clogging problem: Precipitate-forming reactions in flow. *Angew. Chem. Int. Edit.,* **2006**, *45*(10), 1544-1548.

[83] H. Song, D. L. Chen, & R. F. Ismagilov, Reactions in droplets in microflulidic channels. *Angew. Chem. Int. Edit.,* **2006**, *45*(44), 7336-7356.

[84] P. C. Hiemenz, & R. Rajagopalan, *Principles of colloid and surface chemistry*, Marcel Dekker, Inc., New York, **1997**.

[85] Y. S. Shin, K. Cho, S. H. Lim, S. Chung, S. J. Park, C. Chung, D. C. Han, & J. K. Chang, PDMS-based micro PCR chip with parylene coating. *Journal of Micromechanics and Microengineering,* **2003**, *13*(5), 768-774.

[86] A. R. Abate, D. Lee, T. Do, C. Holtze, & D. A. Weitz, Glass coating for PDMS microfluidic channels by sol-gel methods. *Lab on a Chip,* **2008**, *8*(4), 516-518.

[87] M. K. Chaudhury, & G. M. Whitesides, Correlation between surface free-energy and surface constitution. *Science,* **1992**, *255*(5049), 1230-1232.

[88] H. Makamba, J. H. Kim, K. Lim, N. Park, & J. H. Hahn, Surface modification of poly(dimethylsiloxane) microchannels. *Electrophoresis,* **2003**, *24*(21), 3607-3619.
[89] R. Manor, A. Datta, I. Ahmad, M. Holtz, S. Gangopadhyay, & T. Dallas, Microfabrication and characterization of liquid core waveguide glass channels coated with Teflon AF. *Ieee Sensors Journal,* **2003**, *3*(6), 687-692.
[90] M. K. Chaudhury, & G. M. Whitesides, Direct measurement of interfacial interactions between semispherical lenses and flat sheets of poly(dimethylsiloxane) and their chemical derivatives. *Langmuir,* **1991**, *7*(5), 1013-1025.
[91] G. S. Ferguson, M. K. Chaudhury, H. A. Biebuyck, & G. M. Whitesides, Monolayers on disordered substrates - self-assembly of alkyltrichlorosilanes on surface-modified polyethylene and poly(dimethylsiloxane). *Macromolecules,* **1993**, *26*(22), 5870-5875.
[92] B. Arkles, Tailoring surfaces with silanes. *Chemtech,* **1977**, *7*(12), 766-778.
[93] H. Y. Erbil, G. McHale, S. M. Rowan, & M. I. Newton, Determination of the receding contact angle of sessile drops on polymer surfaces by evaporation. *Langmuir,* **1999**, *15*(21), 7378-7385.
[94] D. Briggs, & G. Beamson, *High Resolution XPS of Organic Polymers: The Scienta ESCA300 Database*, John Wily & Sons, New York, **1992**.
[95] L. Feng, S. H. Li, Y. S. Li, H. J. Li, L. J. Zhang, J. Zhai, Y. L. Song, B. Q. Liu, L. Jiang, & D. B. Zhu, Super-hydrophobic surfaces: From natural to artificial. *Advanced Materials,* **2002**, *14*(24), 1857-1860.
[96] P. H. Karpinski, & J. S. Wey, Precipitation processes. in *Handbook of Industrial Crystallization* (Ed.: A. S. Myerson), Butterworth-Heinemann, **2002**, pp. 141-160.

3 Continuous Seeded Crystallization in Microfluidic Devices

3.1 Introduction

Crystallization is a complex process, with its final outcome being dictated by the interplay of solution thermodynamics and kinetics, as well as other physical and chemical processes such as mass and heat transfer, fluid dynamics, and molecular recognition phenomena. This makes the crystallization process sensitive to even minute changes in process parameters, which in turn makes it difficult to control and study the fundamentals of the process.[1] Microfluidic devices offer great control over the process parameters and well defined laminar flow profiles, and thus, have great potential for obtaining fundamental information on the nucleation and growth process. However, as discussed in Chapter 2, crystallization is not easy to achieve in microfluidic devices, readily clogging device channels.

One of the difficulties arises from the fact that the two key steps of the crystallization process, namely nucleation and growth, require a distinct set of optimum conditions for operation. For example, to carry out nucleation in microchannels, the device needs to be operated at high supersaturation, fast desupersaturation upon nucleation, and/or short residence time to prevent the crystals from growing too large to clog the channels. On the other hand, to carry out well controlled growth process, the device needs to be operated at smaller supersaturation, and thus for a longer residence time in order to observe a detectable growth. The different requirements for nucleation and growth pose a problem particularly for organic crystal systems because of their inherent broad nucleation behavior. To address this issue, we use seeded crystallization and reactor design to decouple the nucleation phenomenon from the growth process, as well as to control secondary nucleation, agglomeration and sedimentation of crystals. The enhanced metastable zone width in the microfluidic device aids in realizing seeded crystallization. In this chapter, we demonstrate continuous seeded crystallization of small organic

molecules in microfluidic devices for the first time. We demonstrate continuous nucleation in microfluidic devices in chapter 5. We describe the design, fabrication and operation of microfluidic devices for seeded crystallization in this chapter. We use the three polymorphic forms of glycine, namely alpha, beta and gamma, each with distinct properties, to demonstrate the versatility of this technique. We also integrate *in situ* measurement tools to characterize the crystals inline. To illustrate the use of our system, we successfully extract growth kinetics data for glycine polymorphs of various shapes, including high aspect ratio crystals such as that with acicular or plate-like habits. We also demonstrate the unique advantage these laminar flow based microfluidic devices offer over the current state-of-the art technology to more accurately measure the size, size distribution and growth kinetics for high aspect ratio crystals.

3.1.1 Seeded Crystallization

Seeding has been known as an effective technique to control the outcome of a crystallization process for a long time.[2] A large fraction of industrial crystallization processes is usually seeded,[3] mainly to initiate crystallization, control the crystal size distribution (CSD), control the polymorphic form, and most importantly to avoid spontaneous nucleation.[4] Cooling crystallization is often seeded to stabilize the process by avoiding primary, as well as secondary nucleation.[2] Secondary nucleation is undesirable most of the time because it gives bimodal size distribution.[5] Primary nucleation may be undesirable for resulting in poorer control over crystal products in terms of crystal size distribution and polymorphic form.

Cooling crystallization inherently operates at a comparatively lower supersaturation than antisolvent-driven crystallization since the solubility is far less sensitive to the temperature compared to solvent composition, as demonstrated in Chapter 2. Even then, slow cooling is required for successful seeded crystallization.[2] It is more difficult to achieve seeded crystallization in antisolvent based crystallization, and avoid secondary and primary nucleation, since the local concentration can be quite high at the point of addition or mixing.

Seeding techniques are mostly applied to batch crystallization. In continuous crystallizers, mostly continuous stirred tank reactors (CSTR), nucleation is known to

occur through secondary nucleation, where seeding is sometimes used to start-up and to dampen-out oscillations (CSTR).[4] However, continuous plug flow reactors offer better spatiotemporal resolution, and better spatial homogeneity of process parameters such as concentration and temperature. In particular, the sophisticated fabrication techniques enable the realization of complex microfluidic devices. In this chapter, we demonstrate seeded crystallization for an antisolvent crystallization process in a continuous microfluidic device.

3.1.2 Crystal Growth Kinetics Measurement

Crystals grow by the advancement of individual facets. Each facet may grow at a different rate under identical conditions, and the relative growth rates of the faces determine the crystal habit. The faster growing faces usually grow out and the most of the crystal surface is made up by the slowest growing faces.[6] Crystal growth rate measurement techniques are usually divided into two main groups - single crystal measurements, and measurements on populations of crystals. Single crystal growth techniques involve measuring the growth rates at the individual faces in a fixed crystal, and are usually used to study growth mechanisms. On the other hand, techniques with populations of crystals are used to determine the growth rate in a suspension, as well as the growth rate dispersion associated with organic crystals.[7] Growth rate dispersion refers to the phenomenon that crystals of the same material and size at identical conditions, may grow at different rates.[8] For population studies, growth rate can be obtained using population balance concepts developed by Randolph and Larson.[9]

Single crystal studies may be preferable to the population studies,[6] as they may provide growth rate information on multiple characteristic lengths, and more accurate information on each length, due to a better controlled environment. However, single crystal growth measurements may not be suitable for scale ups since the environment in an industrial crystallizer is different where crystals grow in a suspension.[7] In addition, organic crystals display growth rate dispersion, as discussed in Chapter 1, and thus the growth rate data for a single or a few single crystals is not necessarily an accurate representation of a population's growth rate.

There are mainly three ways of measuring and expressing the growth rate of crystals:

a) face growth rate, which is the velocity of each of the crystallographic face, measured perpendicular to the face;
b) total mass growth rate, which is usually expressed as the total mass flux to the crystal surface, and represents an average growth rate over the entire crystal; and
c) overall linear growth rate, which is defined as the rate of change of a characteristic dimension of the crystal.[6]

Among the three methods, only the face growth rate can be directly related to the fundamental theories of crystal growth. In some cases, linear growth rate may be related to the face growth rate through geometric relationships of a well defined crystal habit.

Microfluidic devices combine the advantages of single crystal studies and population studies in measuring the crystal growth kinetics. It not only provides laminar flow profiles and well-controlled environment as in single crystal studies, but also allows one to perform the experiments in suspension, to study flow effects as in continuous crystallizers, and to examine many crystals in the same environment, which is necessary to obtain meaningful data for processes with statistical phenomenon such as crystal growth. In this thesis, we use continuous microfluidic devices to measure the linear growth rate of characteristic dimensions and then use them to extract face growth rates using habit geometry.

3.1.3 *In Situ* Monitoring

In situ characterization techniques, also known as Process Analytical Technologies (PATs), allow for fast acquisition of more reliable information on crystallization.[10-13] *In situ* detection tools eliminate the artifacts that may arise from the post-processing necessary for some of the offline characterization techniques such as SEM, TEM and X-ray. This issue is especially important for organic crystals with multiple polymorphic forms, as the form produced in the reactor may go through polymorphic transition during the post-processing steps and give inaccurate information about product properties such as polymorphic form and shape. The crystals may also agglomerate or aggregate due to their surface chemistry, as they sit in the solution for too long or as the solvent dries

during the post-processing steps, giving inaccurate information on the size and size distribution of the actual products.[1, 14-16]

The particle size distribution and polymorphism are the most important properties of the final crystal products. The particle size distribution determines several important properties of the pharmaceutical compounds, including crystal appearance, dissolution rate, crystal storage, crystal transportation, and bioavailability.[17, 18] CSD can be determined with a variety of off-line or *in situ* tools, by measuring optical, chemical or electrical properties of the crystals.[19] *In situ* size measuring techniques for batch reactors include laser light scattering,[20-22] coulter counters,[23, 24] image analysis,[25, 26] and ultrasonic attenuation.[27-29] The various techniques, along with their approximate operating ranges are summarized in Table 3-1.

Table 3-1. *In situ* tools for particle characterization

Techniques	*Size Range [μm]*	*Size Parameter*
Sieving	5 – 125000	Particle diameter
Video microscopy & image analysis	0.5 – 150	Projected area diameter of a circle
Laser Diffraction	0.1 – 1000	Number / volume size distribution
Backward light scattering (FBRM)	1 – 1000	Chord length distribution
Ultrasonic spectroscopy	0.01 – 1000	Number / volume size distribution
Electro-zone sensing (coulter counter)	0.4 - 1200	Number / volume size distribution

Lasentech has developed Focused Beam Reflectance Method (FBRM) and Particle Vision and Measurement (PVM), both of which allows on-line and *in situ* measurements. FBRM determines the chord length distribution, and has been used for a number of

crystal systems.[30, 31] PVM, on the other hand, is an image analysis system that determines the CSD and shapes from the image of the crystals.[32] FBRM and PVM both are immersion probes, which make them difficult to integrate with sealed microchannels.

The polymorphic forms of organic molecules are mostly characterized by thermal methods such as differential scanning calorimetry (DSC); X-ray crystallography; and spectroscopy tools including infrared (IR), Raman and solid state nuclear magnetic resonance (SSNMR).[33, 34] X-ray diffraction is definitive in identification and characterization of polymorphs in most cases;[34] however, it is usually used as an off-line technique. Most of the materials used for microfluidic devices have high absorption coefficient for X-rays, causing excessive beam attenuation or scattering.[35, 36] IR has been one of the most promising techniques for polymorph detection.[10] However, a limitation of IR as an *in situ* detection tool is the significant absorption of light by fiber optics,[1] as well as by most device materials. Near-IR (NIR) and Raman are not limited by this problem, and can work through glass or transparent plastic media. A major drawback of NIR, though, is the complexity of the information-rich spectra that is quite diffused and non-specific, requiring the use of "black-box" multivariate calibration with extensive and cautious experimental work. On the other hand, Raman spectra are usually less complicated and present well-resolved peaks.[1]

We take advantage of the transparent device materials and use transmission microscopy to obtain high resolution images. Then, we use image analysis techniques for the *in situ* characterization of crystal size. For *in situ* detection of the polymorphic form, we use Raman Spectroscopy in this work.

3.1.4 Raman Spectroscopy

Raman spectroscopy has been used with microreactors for reaction monitoring,[37] characterizing flow profiles,[38] monitoring chemical processes,[39] and detecting structural changes.[40] It is also becoming a useful *in situ* tool for applications related to crystallization.[1] Raman has been used to characterize the solid state forms, including polymorphs, pseudo-polymorphs, and amorphous,[41-43] as well as to study polymorphic transformation,[44] hydrate transformation,[15, 45] and crystallization.[46, 47] In addition to solid form detection, Raman spectroscopy has the potential to detect the formation of

solution structures, caused by supersaturation, as well as nucleation, and provide information on the intermolecular interactions, such as hydrogen bonding network. However, due to the weak signal and lack of sufficient sensitivity at the present state, Raman spectroscopy has not met the initial expectations regarding crystallization monitoring.[17] Raman spectroscopy is a nonintrusive technique that can work with a minute amount of sample, without any post-processing. Moreover, it provides fast measurements and instantaneous analysis. This capability makes it an attractive analytical technique for real-time process monitoring.[1, 48]

Raman scattering is the inelastic scattering of photons by molecular vibrations, or by optical lattice vibrations in crystals known as phonons. The scattering process involves the annihilation of the incident photon, emission or annihilation of one or more excitation quanta, and finally, the emission of a scattered photon. The scattered photon is related to the incident photon by a frequency, ω, which is also called the Raman shift.[49] Inelastic scattering in solids originates from the polarization, P, induced by the oscillating electric field of the incoming light, E.

$$P = \alpha E \tag{3-1}$$

where α is the polarizability of the molecule. Although quantum mechanical treatment is required for the complete theory of inelastic scattering, classical treatment also gives insights into the phenomenon. Classical treatment of Raman scattering is based on the effects of molecular vibrations on α, which is expressed as

$$\alpha = \alpha_0 + \left(\frac{\delta\alpha}{\delta Qi}\right) Q_i + \ldots \tag{3-2}$$

where α_0 is the inherent polarizability of the molecule, and Q_i is the normal mode of molecular vibration for the characteristic harmonic frequency v_i. Q_i is expressed in terms of time, t, as:

$$Q_i = Q_i^o \cos 2\pi v_i t \tag{3-3}$$

For an incident photon with a frequency, v_0, the electric field can be expressed in terms of time, t, as:

$$E = E_0 \cos 2\pi v_0 t \tag{3-4}$$

Ignoring the higher order terms of the polarizability, the polarization caused by the incident photon, P, results in the following expression.

$$P = \alpha_0 E_0 \cos 2\pi \nu_0 t + E_0 Q_i^o \left(\frac{\delta\alpha}{\delta Q_i} \right) \frac{\cos 2\pi(\nu_0 + \nu_i)t + \cos 2\pi(\nu_0 - \nu_i)t}{2} \qquad 3\text{-}5$$

Therefore, the light is scattered at three frequencies: ν_0, $\nu_0+\nu_i$, and $\nu_0-\nu_i$. The first term represents scattering at the same frequency as the incident light and is known as the elastic Rayleigh scattering. The second term represents inelastic Raman scattering, with $\nu_0+\nu_i$, and $\nu_0-\nu_i$ corresponding to anti-Stokes and Stokes Raman scattering, respectively. The three types of scattering are illustrated in Figure 3-1. Equation 3-5 also dictates the primary selection rule for Raman scattering, which is $\delta\alpha/\delta Q \neq 0$; in other words, a nonzero change in the polarizability with respect to molecular vibration. $\delta\alpha/\delta Q$ is usually much smaller than α_0, resulting in a much weaker Raman scattering than Rayleigh scattering.[48]

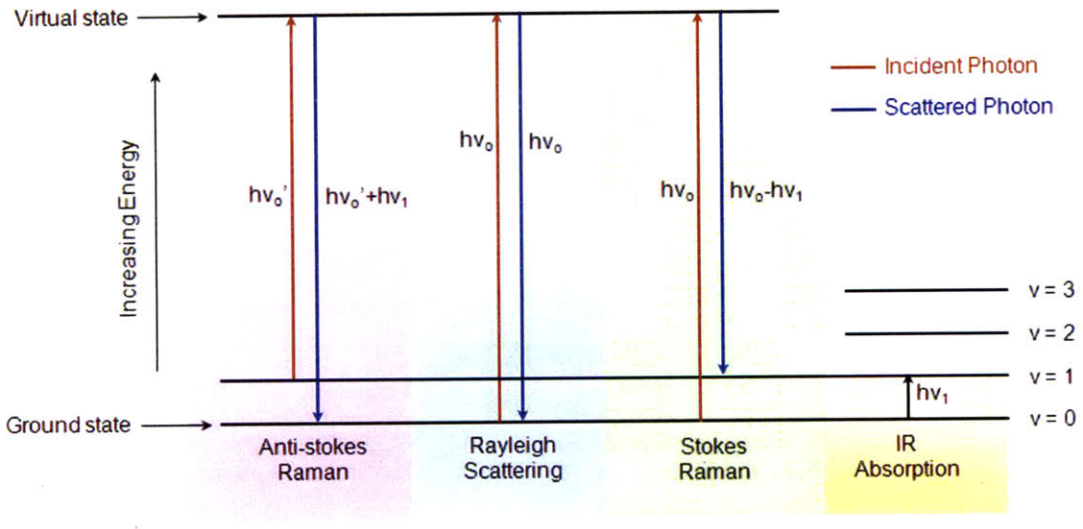

Figure 3-1. Spectroscopic transitions underlying vibrational spectroscopy. v_o represents the laser frequency, and v represents the vibrational quantum number. The virtual state is a short-lived distortion of the electron distribution by the electric field of the incident light. Raman scattering occurs when the scattered photon is shifted from the incident photon by one or more energy quanta corresponding to the vibration modes.

3.1.5 Model System: the Three Polymorphs of Glycine

Amino acids are widely used as model systems because of their well-established physicochemical properties and their ability to crystallize in multiple polymorphic forms.[50] Glycine, the simplest amino acid, is a common pharmaceutical excipient.[51] In aqueous solution, it is known to exist in zwitterionic form, with an isoelectric point of 5.97. In the solid form, glycine forms hydrogen bonded crystals of three known structures at atmospheric pressure, namely alpha, beta and gamma.[52-55] The three polymorphs differ in the packing arrangement of glycine zwitterions through hydrogen bonding. Figure 3-2 presents the unit cell, the smallest region that fully describes the pattern of the three dimensional crystal lattice, of the three polymorphic forms.

The alpha form is the metastable form,[56, 57] and usually crystallizes as centrosymmetric bipyramids in a monoclinic space group ($P2_1$).[58-60] In the crystal lattice of alpha glycine, dimers are laterally hydrogen-bonded to form bilayer sheets, which are held together along the b-axis by Van der Waals interactions. The beta form is the unstable form, and usually crystallizes as noncentrosymmetric, high aspect ratio habits such as needles in a monoclinic space group ($P2_1/n$).[61, 62] In the crystal lattice of the beta form, individual parallel layers are linked by hydrogen bonds in a three dimensional network. The most stable form is gamma,[56, 57] and it usually crystallizes as noncentrosymmetric pyramids in a polar space group ($P3_1$ / $P3_2$).[63-65] In the gamma form, the glycine zwitterions are linked to each other in a three dimensional polar helical network. The relative stabilities of the three polymorphs are related to the crystal lattice energy through the strength of the hydrogen bonds.[57] A fourth polymorph of glycine has been reported recently that forms at high pressures.[66]

Each of the three glycine polymorphs, alpha, beta and gamma, has its own set of challenges in terms of stability, rheological properties, and surface properties that make it difficult to achieve continuous crystallization in a microfluidic platform. We use the three polymorphs of glycine to demonstrate continuous seeded crystallization in microfluidic devices, as well as the use of this technique to extract growth kinetics information. The applicability of this method to the widely varied habits of different glycine polymorphs illustrates the versatility of this technique.

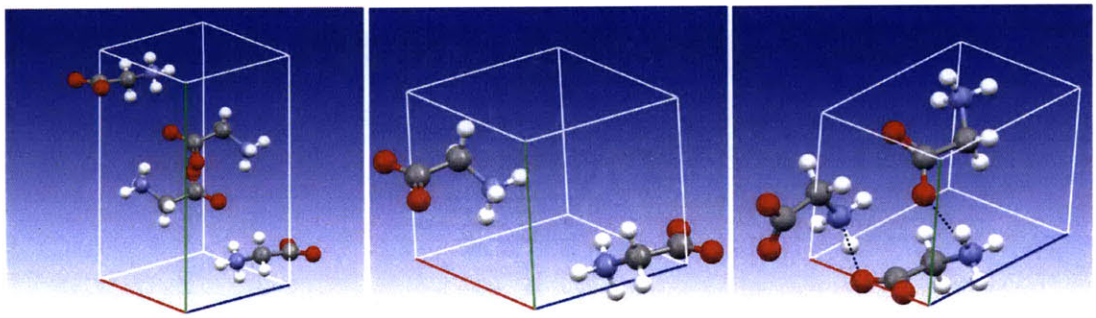

Figure 3-2. The unit cell of the three polymorphic forms of glycine used in this work: alpha, beta, and gamma.

3.2 Experimental

3.2.1 Seed Synthesis: Alpha, Beta and Gamma

Glycine (≥ 99% pure) and anhydrous ethanol were purchased from Sigma Aldrich. Spectroscopy grade water was purchased from VWR. X-ray diffraction showed that the commercial glycine purchased was usually a mixture of alpha and gamma crystals, with varied percentages of each in different batches. It is important to use pure polymorphic forms as seeds because a mixture of multiple forms can give erroneous measurements in two ways. First, since the properties and characteristics, including the growth kinetics, of different polymorphic forms are different, having a 50:50 mixture, for example, will result in a growth rate of an intermediate value that is representative of neither form. Secondly, a mixture of multiple forms, with one being more stable than other(s), induces polymorphic transition, and the data for such an unstable system becomes difficult to interpret. Consequently, seeds of each of the 3 polymorphs were carefully prepared in order to achieve purity.

α-glycine seeds were prepared from aqueous solution. Commercial glycine was dissolved in water (0.3g gly/g water) by heating the solution up to 50°C. The solution was filtered with a hot 0.2 μm filter and brought to room temperature while stirring. As soon

as nucleation was detected, equal volume of saturated glycine solution (with respect to the alpha form) was added to dilute out the seeds and prevent agglomeration.

γ-glycine was prepared by suspending excess glycine in a solvent composed of water and acetic acid in a 2:1 ratio for a week. The crystals were filtered through a 0.2 μm filter with vacuum suction, followed by a wash with a small amount of filtered deionized water. The crystals were dried in a vacuum oven at 50 °C for a few hours and the polymorphic form was confirmed with X-ray diffraction. γ-glycine made this way was used as seeds to make further gamma glycine by suspending the seeds with excess glycine in deionized water for at least 7 days. Gamma crystals were then grinded, filtered with 5-7 μm sieves (Gilson company, Inc.), and added to pure water to give the desired seed density. Seeds were handled in a laminar flow hood to avoid contamination. Alpha and gamma seeds were matured for at least 24 hours and checked with X-ray diffraction before use.

It is important to "age" the crystals in slurry for a sufficient time whenever possible, and allow the natural process of "crystal perfection". Togkalidou et al. have demonstrated that different growth rates are obtained for dry and slurry seeds due to the different nature of the crystal surfaces.[67] The surface of the dried seed is usually rough and fractured during the drying and milling process, resulting in a large number of growth sites, while the slurry crystals are in equilibrium with solution, allowing the molecules to redistribute and perfect local defects in an attempt to minimize the energy.

The beta seeds were carefully prepared by a method proposed by Drebushchak et al.[68, 69] A solvent composed of water and acetic acid in a 2:1 ratio was saturated with glycine and aged for at least 3 days. The solution was then filtered with a 0.2 μm filter. Acetone and the filtered solution were simultaneously added to a new vial at a 2:1 ratio, which precipitated beta glycine. The precipitated solution was immediately vacuum filtered with a 0.2 μm filter. The precipitate was thoroughly washed with plenty of acetone (vacuum filtered with a 0.2 μm filter) in order to remove any solvent. The crystals were subsequently dried at 50°C in a vacuum oven for a few hours and stored in the glove box until use. X-ray diffraction was used to confirm the polymorphic form before using it for experiments. Right before the experiment, β-glycine was grinded, sieved with a 10 μm filter (Gilson company, Inc.), and added to ethanol in the glove box. The solution was then taken out of the glove box, and appropriate amount of water was added to it to reach

the desired solvent composition. The suspension was stirred and loaded into airtight syringes immediately.

3.2.2 Seed Characterization

The final seed size in case of all the polymorphs was analyzed with optical microscopy using glass bottom culture dishes (Mat Tek Corp., MA) before performing each experiment. The seed density was roughly estimated by drawing a measured amount of seed solution with a pipette, dispensing into the covered glass bottom culture dishes and counting the number.

X-ray power diffraction was used to characterize the polymorphic form of the seeds. A PANalytical X-pert Pro Multipurpose Diffractometer with copper Kα radiation (λ = 1.5418 Å), high-speed high-resolution X'Celerator detector, and divergence optics are used for polymorphic form detection of the seeds. Dispersion samples were prepared by uniformly transferring a thin layer of sample on a zero background plate, a silicon plate with (510) face. Samples of the beta form were prepared in an air-sensitive sample holder inside the glove box. A dispersion was made by adding processed beta glycine seeds to acetone. A zero background plate was covered with a thin layer of the crystals by adding drops of beta glycine dispersion. Next, acetone was evaporated and the zero background plate was tightly capped with a crypton film before taking it out of the glove box for measurement. All the diffraction data was processed with Jade.

3.2.3 Raman Setup

Raman Spectroscopy is mostly performed in two configurations, 90° angle and 180° angle. The two configurations refer to the cases when the incoming beam and collection beam are at 90°, or coincident, respectively. It is critical to choose the right geometry and collection optics since Raman is a very weak signal. The alignment of the optical components and sample positioning also affect the signal strength strongly, with 90° geometry being more sensitive.[48]

In order to minimize misalignment effects, we use 180° geometry, and put together a Raman spectroscopy setup for polymorph detection. The setup is illustrated in Figure 3-3. Choosing the laser wavelength is also critical in obtaining the most optimal signal. The

intensity of the Raman signal is inversely proportional to the fourth power of the wavelength. However, shorter wavelengths magnify fluorescence signal that simply floods the weak Raman signal.[48] We used a 632.8 nm helium neon laser with 35 mW power (Melles Griot). A laser-line filter (Maxline^{TM} laser-line filter, Semrock) was used to remove any spurious lines in the incident beam and to achieve a monochromatic light by reducing unwanted beam width. A dichroic mirror (Chroma) was used to reflect the laser-line on the sample and transmit the scattered photons coming back from the sample. The incident beam was focused onto the sample with a microscope objective, which also collimated the collected photons before passing them onto the dichroic mirror. Any remaining laser-line photons, resulting from Rayleigh scattering and/or any reflection of the incident beam, were subsequently removed from the transmitted beam with a Raman notch filter (RazorEdge^{TM} Raman Filter, Semrock). A 300 μm diameter fiber optics was used to transfer the collected photons to a spectrometer. We used a spectrograph with 600 groves/mm grating, centered at 500nm, coupled with a thermoelectric peltier-cooled, back-illuminated Charged-Coupled Device (CCD) (InSpectrum, Princeton Instruments). The spectrometer was connected to a laptop and controlled with a software called SpectraSense (Princeton Instruments). We used a mercury lamp to calibrate the wavelength. The data was obtained with SpectraSense as photon counts as a function of the photon wavelength. The photon wavelength, λ, was then converted to the Raman Shift, ω_{Raman} as follows.

$$\omega_{Raman} = \left(\frac{1}{\lambda_{laser}} - \frac{1}{\lambda} \right) \qquad 3\text{-}6$$

The setup was successfully used to characterize liquid and some solid samples. Figure 3-4 shows typical Raman spectrum achieved with the setup for acetone with 2 seconds exposure, and compares with standard literature spectrum.[70] One of the problems of this setup, though, was strong fluorescence signal for many solid materials, as well as PDMS, due to the short wavelength used to obtain stronger signal.

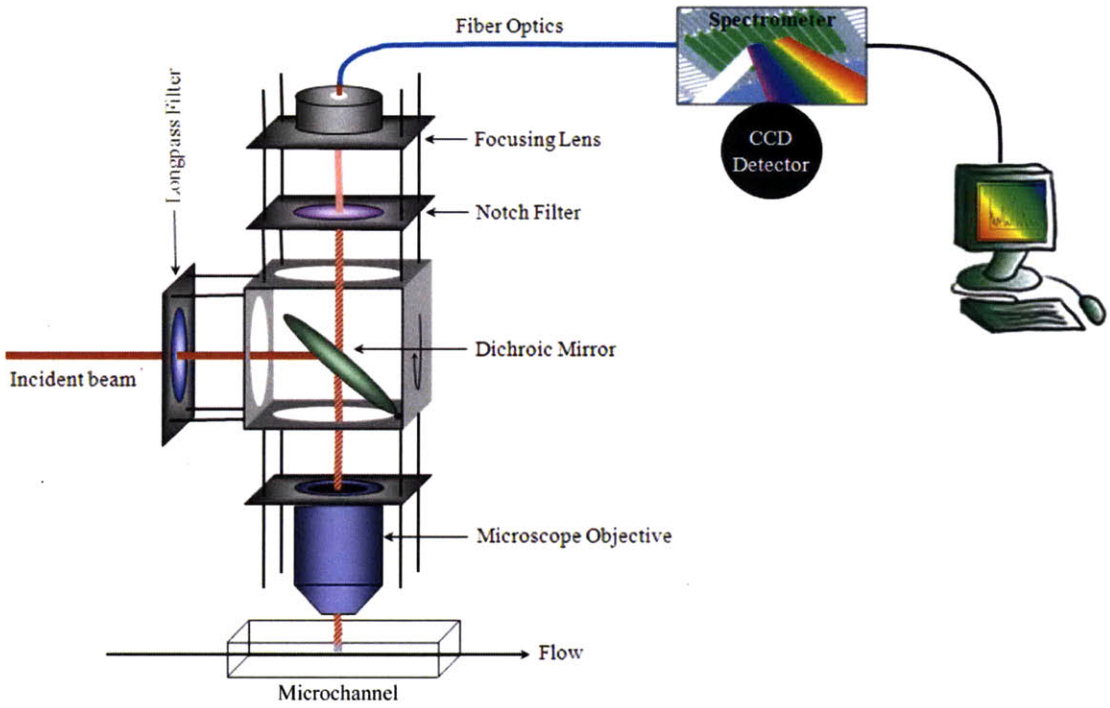

Figure 3-3. Configuration of the Raman setup.

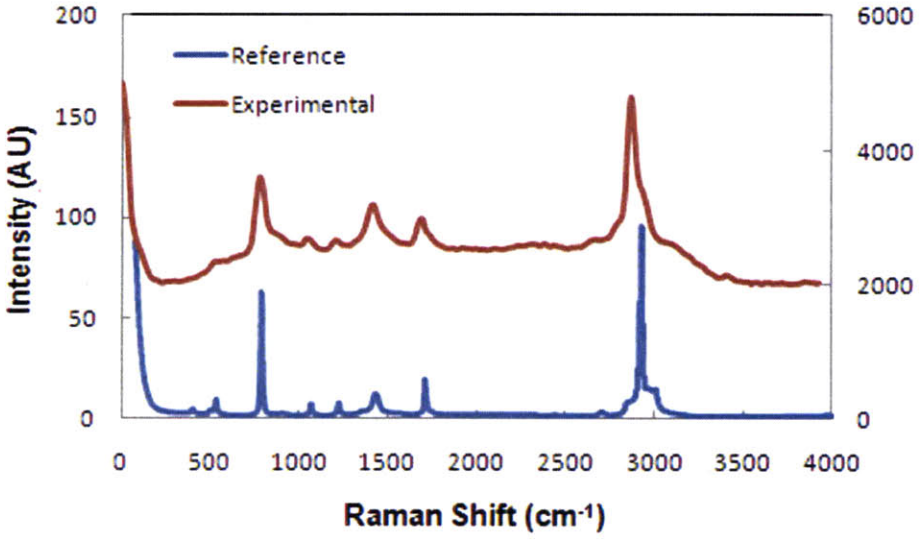

Figure 3-4. Comparison of Raman Spectra of acetone acquired from the built setup (with 1 second exposure time) with literature.[70]

For *in situ* measurements, better spatial resolution was desired to avoid fluorescence of PDMS. As a result, we used a commercial Raman confocal microscope, coupled with video microscopy, for the *in situ* measurements of crystals inside the microchannels. A 784.8 nm excitation from a solid-state Invictus laser (Kaiser Optical Systems, Inc.) was used in a 180° backscattered geometry via a 15 μm optical fiber. Scattered photons were collected by a Raman microprobe and transferred to a transmission grating (HoloPlex, Kaiser Optical Systems, Inc.) with a liquid-nitrogen cooled CCD through a 15 μm optical fiber. Such small diameter optical fiber was used for both excitation and collection in order to obtain better spatial resolution. The wavelength and the intensity were calibrated using a mercury lamp and a white lamp, respectively. The accuracy of the measured Raman Shifts was verified with cyclohexane and was found to have a tolerance of 0.02 cm^{-1}. *In situ* measurements were carried out on the crystals, grown inside microreactors, by carefully focusing the laser at the center of microchannels so as to avoid signal from PDMS. For *in situ* measurements, long residence time reactors were used and large crystals were grown for better signal. Video microscopy was used to focus at the bottom of the channel and then a controller was used to move the focus up 125 μm in the z direction. For each polymorphic form, 20 spectra were taken with 20 seconds exposure each. The glass and blank spectra were subtracted from each spectrum. Then, the subtracted spectra were used to average the final spectrum for comparison.

3.2.4 Device Design

We use three inlets, the first one for introducing seeds into the reactor, the second one for introducing crystallizing solution, and the third one for introducing antisolvent. We mix the solution and antisolvent to create a supersaturation in the metastable zone and introduce the supersaturated solution into the main channel where seeds grow. Figure 3-5a illustrates this concept of seeded crystallization. Device specifics were designed based on tentative growth calculations of the glycine polymorphs. The fluid dynamics, as well as the concentration of the three species, namely solute, solvent and antisolvent, was modeled simultaneously, as will be discussed under the results section. The modeling results, along with solubility data, were used to calculate the supersaturation. The composition, concentration, and the flow rate of each stream were chosen such that the

supersaturation never exceeded the metastable limit. In addition, the seed density was chosen so as to obtain a constant precursor concentration in the channel. In other words, the solute consumption in the growth process was controlled through the seed density such that the consumption was insignificant compared to the total precursor available for growth.

An undersaturated solution of a solvent and the precursor was mixed with an antisolvent in order to generate a supersaturated solution on chip. On chip supersaturation generation in these closed systems allows one to avoid undesired and uncontrolled nucleation at the air-solution interface present in batch systems, and provides a tool to study seeded crystallization. The supersaturated solution was, then, carefully added to the seed solution in the main channel in a way such that the concentration was always below the metastable limit, but above the solubility limit. This way of increasing the supersaturation in the main channel prevents nucleation that may have otherwise occurred when antisolvent is added directly to the seed solution, due to high local supersaturation at their interface. The flow rates of the three inlets provide a good control over the supersaturation achieved in the reactor and an easy way to vary the supersaturation by varying their ratios.

Multiple side channels for adding supersaturated solution to the main channel are useful in either keeping the supersaturation constant in the main channel during significant consumption of precursors, as shown by Khan et al.,[71] or in changing the supersaturation in the main channel between each of the two consecutive side channels. The former allows the crystals with a slow growth rate, and significant precursor consumption, to grow to a detectable size in a long residence time reactor. The latter enables multiple experiments to be performed simultaneously at two different supersaturation values. Figure 3-5b demonstrates the concept of multiple addition inlets.

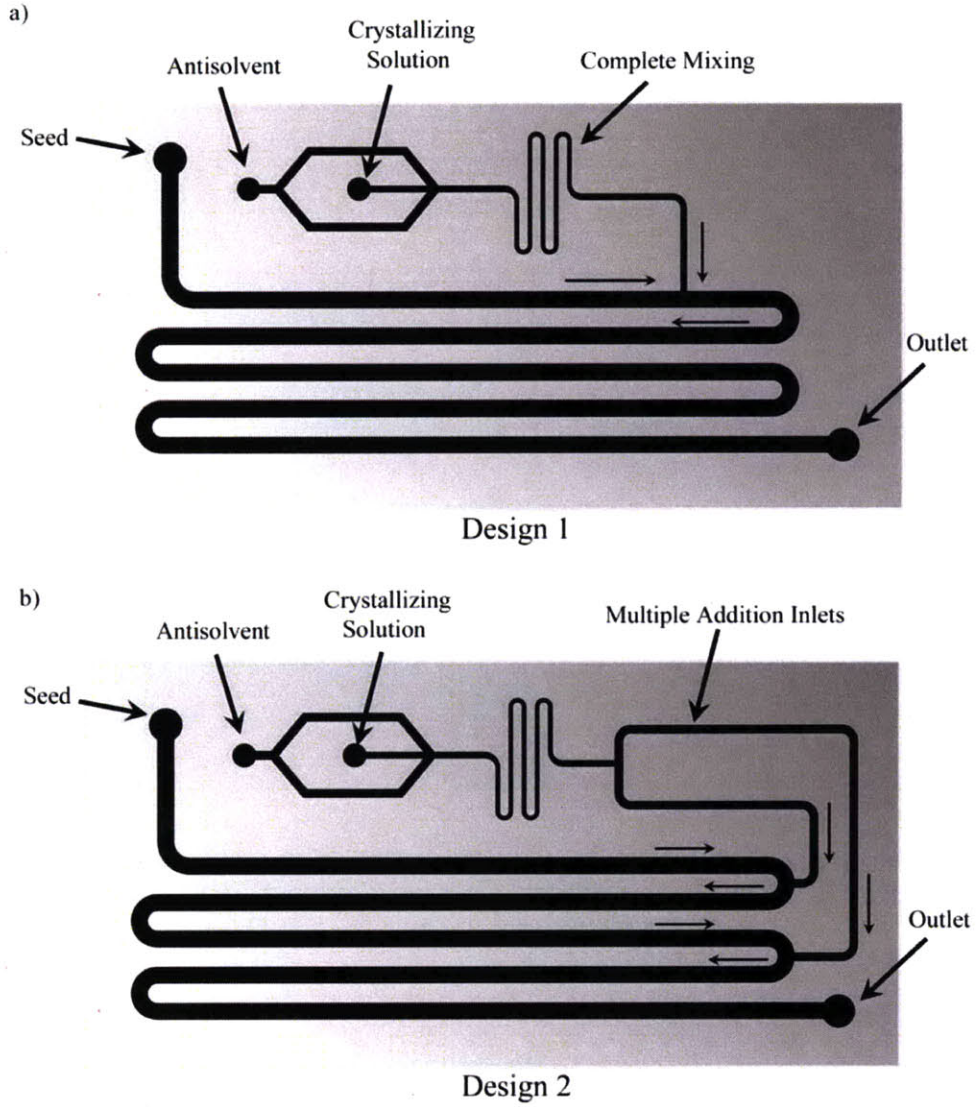

Figure 3-5. Reactors used for seeded crystallization. a) Crystallizing solution is mixed with antisolvent to generate supersaturation, which is then introduced to the main channel where seeds grow. b) Multiple addition streams can create multiple supersaturation in the main channel, enabling multiple experiments to be performed simultaneously.

We designed microfluidic devices with two or four side channels in this work. Complete mixing was achieved between the solution and antisolvent, similar to the previous case, and then the supersaturated solution was distributed between the various side inlets. The desired distribution ratios can be achieved precisely by properly designing the channel dimensions. Here, we illustrate the design concept for a device

with two side channels for simplicity. However, a similar procedure can be used to design devices with more side channels.

Figure 3-6a shows the fluidic network for a device with two side channels. We used Hagen-Poiseulle equation to model the laminar flow present between any two points in the device. According to Hagen-Poiseulle equation, the liquid flow rate, Q, between two points, is directly proportional to the pressure drop, ΔP, between them, with the hydraulic resistance, R, as the proportionality constant. This is completely analogous to Ohm's Law for linear electrical circuits, where the current I is proportional to the voltage drop ΔV, and the linear proportionality constant is the electrical resistance R.[72]

$$\Delta P = R \times Q \Leftrightarrow \Delta V = R \times I \qquad 3\text{-}7$$

Moreover, the conservation of flow, or mass balance, present at each intersection (of channels), is also directly analogous to Kirchhoff's law for current at nodes that requires the sum of all currents entering a node to equal zero.[72] For example, applying Kirchhoff's law to one of the nodes in Figure 3-6a results in the following equation.

$$Q_a - Q_6 - Q_7 = 0 \qquad 3\text{-}8$$

Therefore, the microfluidic network can be solved in a way similar to linear circuits, for the cases when the hydraulic resistance is also linear. For laminar flow present in the microchannels, the hydraulic resistance is indeed linear:

$$R = \frac{8\mu L}{\pi\left(\frac{D_E}{2}\right)^4} \qquad 3\text{-}9$$

where μ is the liquid viscosity, L is the length between the two points under consideration, and D_E is the 'equivalent diameter.' For a rectangular microchannel, as in our case, D_E is expressed as:

$$D_E = \left(\frac{128wh^3}{\pi K}\right)^{1/4} \qquad 3\text{-}10$$

where w is the width of the microchannel, h is the height of the microchannel, and K is a constant that depends on the channel aspect ratio, w/h. K values can be found in *Perry's Chemical Engineering Handbook* for different aspect ratios.[73] For a given set of dimensions of height (h), width (w), and length (L), for each of the channel segments, and

incoming flow rates of antisolvent (Q_a), solution (Q_s) and seed (Q_{seed}) streams, there are 13 unknowns, as shown in Figure 3-6a. These unknowns are pressures, P_1 to P_7, and flow rates, Q_1 to Q_7. The Hagen-Poiseulle equation can be applied to the 8 hydraulic resistances, and Kirchhoff's law can be applied to the 5 nodes, giving a total of 13 linear equations that can be solved simultaneously to obtain the unknown pressures and flow rates.

We designed the reactor using an iterative procedure, similar to that used by Khan et al., with two additional steps in the iteration loop. Khan et al. used the flow rates of side channels as the target and varied the channel dimensions to achieve equal flow rates in each side inlet.[71] Here, we used supersaturation as the target to guide us with channel dimensions. As shown in Figure 3-6b, the flow rates were first set for each of the inlets, and the fluidic network was solved for the unknown pressures and flow rates in each channel segment. Then, the flow rates in each of the channel segments were used to determine their respective solvent composition, which was then used, along with the solubility, to calculate the respective supersaturation. The process was iterated until we achieved the desired supersaturation in all the channel segments.

Backflow of liquid was carefully eliminated by controlling the pressure drops because any backflow from the main reaction channel into the side channels gave rise to high local supersaturation, causing uncontrolled nucleation and subsequent channel clogging. The depth of all the channels in the device was approximately 250 μm. The width of the main channel was 300 μm, but the length was varied for the different polymorphs in order to achieve the desired residence times, as mentioned in the next section. The supersaturation was used to roughly estimate the growth rates for each of the form, and the length was designed to achieve the target size of crystals for each polymorphic form. The width of the mixing channel was 40 μm, and the length was four times the calculated required length, L, to ensure mixing through diffusion.

$$L = \frac{w^2 v}{D} \qquad 3\text{-}11$$

where w is the characteristic length of mixing, v is the velocity calculated from flow rates and channel cross-section, and D is the diffusion coefficient. The length and width of the

side channels were iteratively varied to achieve the desired supersaturation in the main channel.

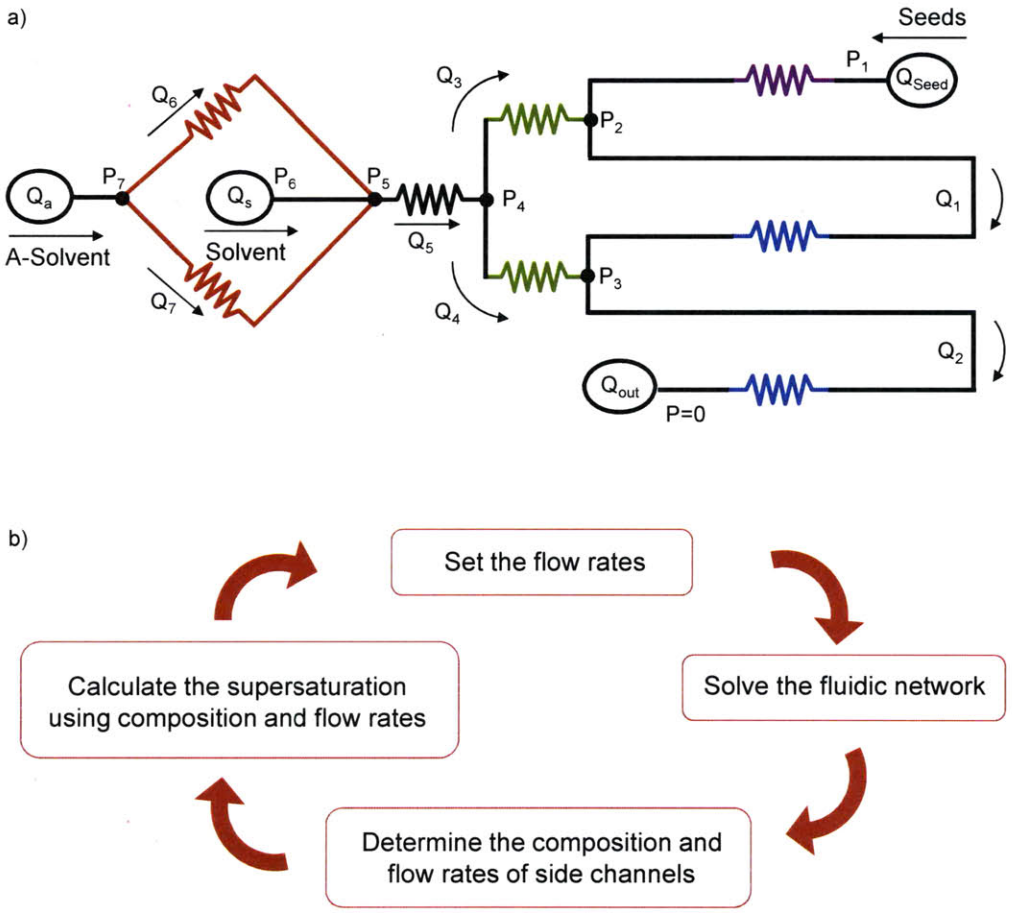

Figure 3-6. a) Fluidics network for devices with two side channels for supersaturation addition. b) The iterative process used to design the channel dimensions.

3.2.5 Fabrication and Packaging

Microfluidic devices are fabricated in PDMS by using standard soft lithographic techniques.[74] PDMS was chosen as the device material because realizing complicated reactor designs in PDMS is fast, easy and inexpensive. Also, the transparency of the material allows one to use microscopy tools to obtain high resolution images of the crystals, as well as to integrate spectroscopy tools, such as Raman, for *in situ* polymorph detection. SU-8 (Microchem Corporation, MA), a negative resist, was used to make

master devices that were used for molding. Two layers of approximately 125 μm thick SU-8 films were spun on 100 mm diameter silicon wafers (Silicon Quest International). Standard photolithography techniques were used to pattern negative images of the microfluidic device on SU-8. Finally, the wafers were developed using SU-8 Developer (Microchem Corporation). PDMS (Dow Corning Sylgard Brand 184 Silicone Elastomer, Essex-Brownell Inc.) was molded on the SU-8 masters in the following way. PDMS was prepared by mixing Sylgard 184 and its activator (Dow Corning) in a 10 to 1 weight ratio. The mixture was degassed, casted onto the master wafer, and cured at 80°C for 2 hours. After reticulation, the devices were peeled off the mold, cut, and inlets and outlets were punched with a 5/64" leather punch. Each device was cleaned, surface was activated with a Harrick PDC-32G oxygen plasma chamber for 35 seconds, and finally, was covalently bonded to a surface modified glass slide. Pre-cleaned glass slides (75 x 50 mm, 1 mm thick, Corning Glass Works) were spin-coated with PDMS (~100 μm) and were cured at 80 °C for 30 minutes. PEEK tubing (IDEX Health & Science) was inserted in the inlets and was glued in place with 5-min epoxy (Devcon). The epoxy was cured at 70 °C for 12 hours or at room temperature overnight.

3.2.6 Device Operation

The antisolvent and undersaturated glycine solution were loaded in separate syringes (GasTight, Hamilton), and were delivered to the microchannels with Syringe pumps. Solubility of glycine polymorphs at different solvent-antisolvent composition was taken from the literature,[75-78] and was used to design the experiments. The flow rates used for each of the inlets ranged from 2-10 $\mu l \cdot min^{-1}$, giving a residence time ranging from 30 seconds to 12 minutes, depending on the polymorphic form. Approximately 70-100% ethanol in water was used as the antisolvent, and aqueous solution of glycine with a concentration of 2-12 g glycine/100 mL water was used as the undersaturated solution. Dilute seeds of the three polymorphic forms were prepared with the desired size range. The details of seed preparation technique are discussed in seed preparation section. The seed solution was purely aqueous for the stable forms, namely alpha and gamma. The beta form is unstable and readily converts to the alpha form, with the conversion time depending on the moisture/solvent composition among other factors.[75, 79] Consequently,

an aqueous mixture of 70 wt% ethanol was used as the seed solution for the beta form. The residence time was designed to be short, ranging from 30 seconds to 2 minutes. The fast growth rate of beta allowed significant growth even at such short residence times. For alpha and gamma, on the other hand, longer residence time was used to observe detectable growth. The supersaturation achieved in the main channel was between 1-1.6 with respect to the alpha form. The experiments were performed at room temperature.

3.2.7 Pressure Driven Flow for Seed Inlet

One of the difficulties with seeded crystallization is that seeds of high density polymorphic forms, such as α-glycine, may settle at the bottom of the seed container over a long period of time, resulting in an inconsistent density of seeds fed to the reactor. We used pressure-driven flow to deliver α-glycine seeds into the device, which allowed us to continuously stir the seed solution over the duration of experiments, and thus, to flow a consistent density of seeds over time. A control loop was used to control the seed flow rate in Labview. Helium gas tank was used as the pressure source and was connected to the seed solution. Fast response of the setup was achieved by using two lines, between gas tank and solution, in parallel, one with higher resistance, used when the measured flow rate is close to the desired flow rate, and the other with lower resistance, used when the measured flow rate is much smaller than the desired flow rate. On-off valves (Lee Company) were used to direct the gas flow through the desired resistance. Two pressure sensors (Honeywell) were used with a resistance in between them. According to the Hagen-Poiseuille equation, the pressure drop is directly proportional to the flow rates. Hence, the pressure drop between the sensors was measured and correlated to flow rates. A data acquisition device (National Instruments) was used to control the valves and to receive signal from the pressure sensors. The flow rate was calibrated with respect to the pressure drop by flowing a known amount of solution with a syringe pump. After calibration, a Labview routine was run to either reach or maintain the desirable flow rate. Figure 3-7a shows a schematic of the setup used to achieve pressure-driven flow, and Figure 3-7b shows a typical calibration curve obtained for the flow rate of glycine seed solution.

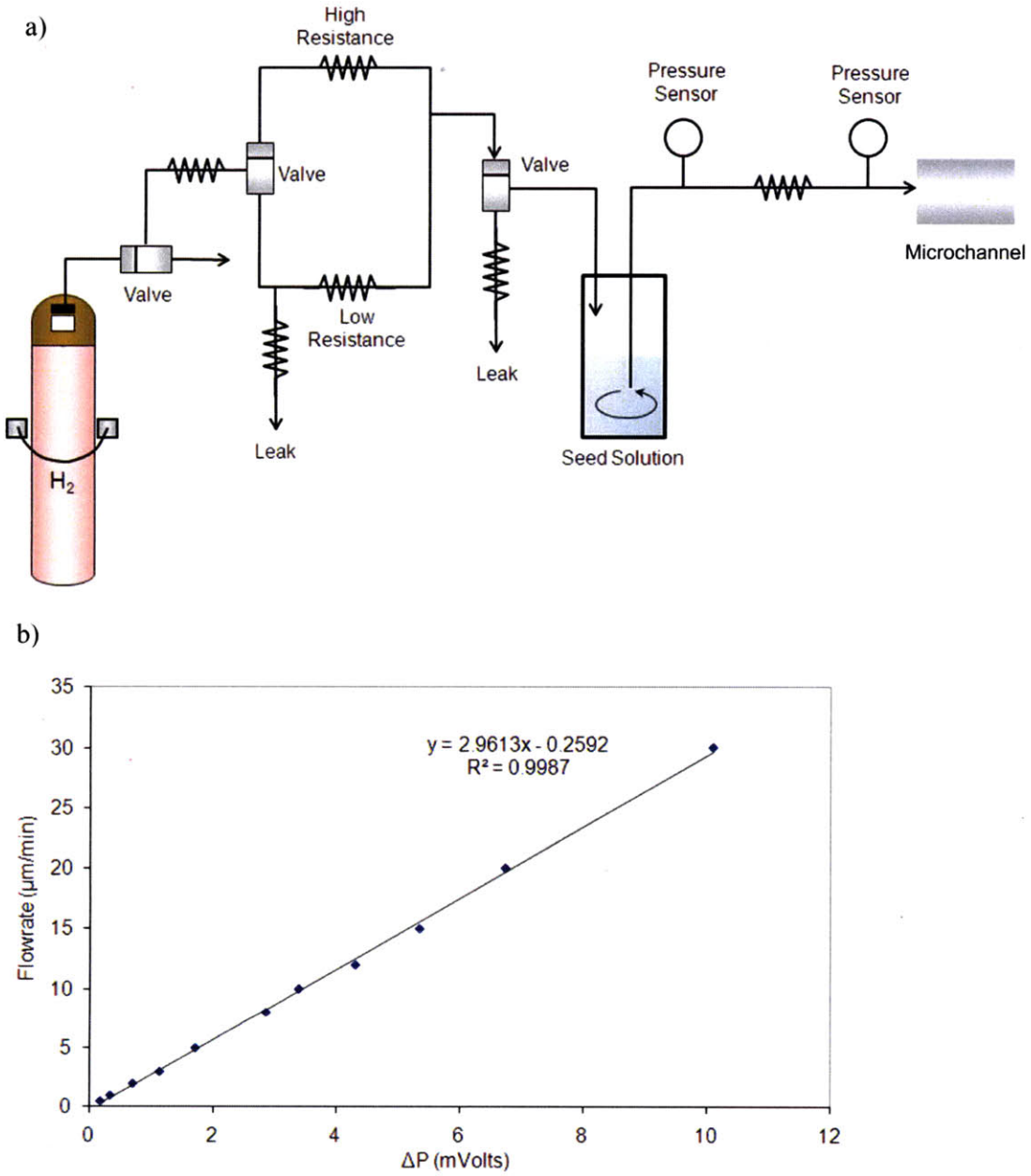

Figure 3-7. a) A schematic of the setup used to achieve pressure-driven for the seed solution. A Labview routine is used to control the flow rate. b) Typical calibration curve obtained for the flow rate with respect to the pressure drop.

3.2.8 Image Acquisition, Processing and Data Analysis

A Nikon TE2000-E inverted microscope is used with Nikon CF DL 5x, 10X, and 20X objectives, and a Plan Neofluar 100X/1.30 oil immersion objective. A high resolution CCD camera with a full frame (PCO Sensicam QE doubleshot, 1280 x 1025 pixels, 9 fps) was used for image acquisition. Images of many crystals were taken at different residence times of the reactor; the sampling volume was attempted to be kept the same in order to eliminate errors from large dispersion in seed size. For alpha and gamma, data were collected downstream of the reactor such that seeds were able to grow for a few minutes (~ half of the residence time) before data collection was started. However, for the beta form, data collection was started immediately because of its high growth rate. Recorded images were saved as 8-bit files. The frame rate of the camera was adjusted to values between 2 and 8 frames per second (fps) by the image acquisition software (IPLab, BioVision Technologies). The frames were analyzed in Adobe Photoshop.

3.2.9 Growth Rate Calculation

Continuous crystallization was achieved with seeded crystallization by carefully controlling the seed density, the residence time of the reactor, and the supersaturation achieved in each of the channel segments in the device in order to suppress secondary nucleation, significant agglomeration, and sedimentation of crystals. The interaction of the hydrophilic glycine crystals with the channel walls was also minimized through hydrophobic modification. As a result, we are able to avoid channel plugging and run crystallization continuously. To illustrate the use of our system, we use these devices to extract growth kinetics data for crystals of various shapes, including high aspect ratio crystals, such as those with acicular or plate-like habits. The transposition of the reaction time onto the spatial coordinates of microfluidic devices provides an elegant method to measure the growth kinetics of crystals. Figure 3-8 presents a schematic of the final setup of seeded crystallization, and also illustrates the idea of measuring growth kinetics. Images of crystals can be captured at different resident times, t_0, t_1 and t_2, for example, as in Figure 3-8, which can then be analyzed to extract growth over the known residence time between t_0, t_1 and t_2. The growth rates then can be correlated to supersaturation present in the channel segments corresponding to the time periods of t_1 - t_0, and t_2 - t_1.

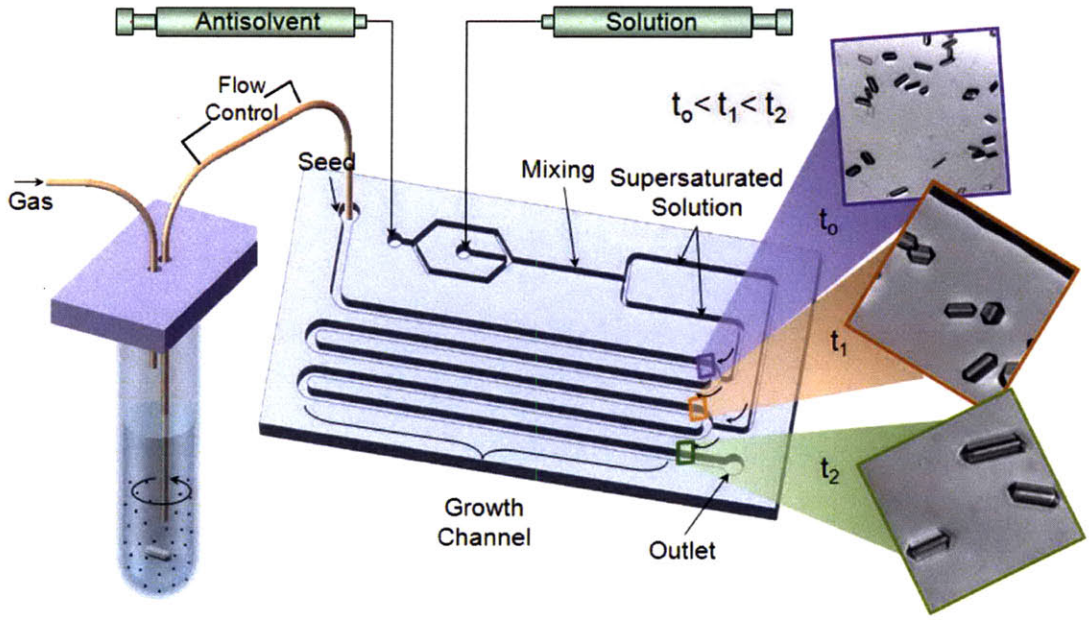

Figure 3-8. Schematic of the continuous seeded crystallization setup (not drawn to scale). The growth kinetics of the crystals can be extracted by capturing images at times, t_0, t_1 and t_2, and analyzing them.

The size of the crystals was analyzed from the images using Adobe Photoshop. The residence time of the crystals was calculated by averaging the residence time of many crystals for each of the polymorphs. For α-glycine, two characteristic dimensions, L_c and L_b, were measured. The growth rate of the different faces was then calculated using the geometric relationship between the faces and the measured dimensions, as shown in Figure 3-9.

$$G_{\{011\}} = \frac{1}{2}\sin 67.5^0\left(\frac{dL_c}{dt}\right) \qquad 3\text{-}12$$

$$G_{\{010\}} = \frac{1}{2}\sin 68.5^0\left(\frac{dL_b}{dt}\right) \qquad 3\text{-}13$$

For the beta form, the characteristic length of the longer dimension, L_b, was measured. This is also the fastest growing dimension and typically is of most interest. Because beta is non-centrosymmetric, the growth rate is not equal at the two ends of the fastest-

growing dimension. Since the growth rate in the $+b$ direction is much faster than that in the $-b$ direction,[62] $G_{(010)}$ was approximated as:

$$G_{(010)} = \left(\frac{dL_b}{dt}\right) \qquad 3\text{-}14$$

For γ-glycine, two characteristic dimensions, L_c and L_b, were measured, and the growth rate was approximated in similar ways as alpha and beta glycine. Since the gamma form is known to grow in the $-c$ direction, the flat end, at a much faster rate than in the $+c$ direction,[80] $G_{(00\bar{1})}$ is approximated with equation 3-15. The growth rate of {100} and {010} were assumed to be equal and was calculated with equation 3-16.

$$G_{(00\bar{1})} = \left(\frac{dL_c}{dt}\right) \qquad 3\text{-}15$$

$$G_{\{100,010\}} = \frac{1}{2}\left(\frac{dL_b}{dt}\right) \qquad 3\text{-}16$$

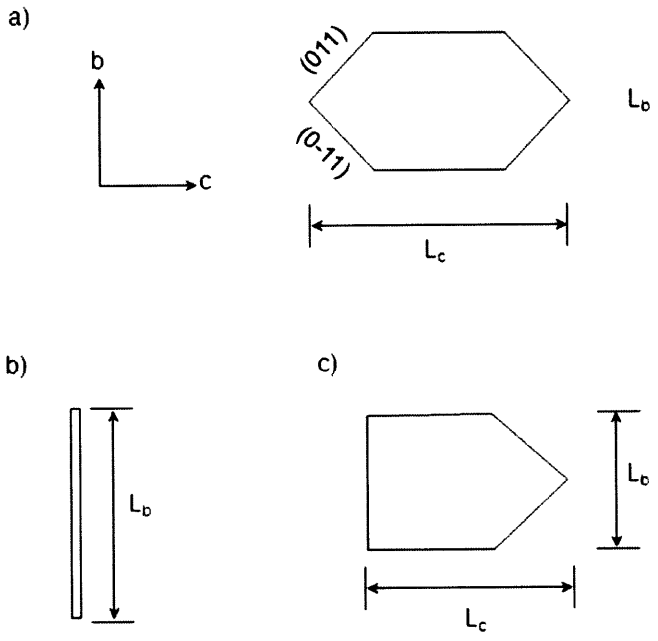

Figure 3-9. The orientation and dimensions used to calculate the growth rate of various faces in case of a) α-glycine, b) β-glycine, and c) γ-glycine.

3.3 Results and Discussion

We achieved continuous seeded crystallization and *in situ* detection of small organic molecules in microfluidic devices by decoupling the nucleation phenomenon from the growth process. We used seeds to control secondary nucleation, agglomeration, and sedimentation of crystals. The great particulate control achieved in the sealed microchannels also helped to suppress nucleation. We minimized significant interaction of crystals with channel walls by modifying channel surfaces. Consequently, we were able to avoid channel plugging and run seeded crystallization continuously. To illustrate the use of our system, we use these devices to extract growth kinetics data for crystals of the three glycine polymorphs, namely alpha, beta and gamma, each with different shapes. We carefully prepare the seeds for each polymorph with desirable density and size range. Then, we introduce the seeds to the microchannels, where supersaturation is generated, allowing the crystals to grow. Moreover, we demonstrate a unique advantage these microfluidic-based microcrystallizers offer over the current state-of-the art technology in more accurately measuring the size, size distribution and growth kinetics for high aspect ratio crystals, such as beta glycine. In the next section, we discuss the preparation of seeds, then the modeling of fluid dynamics, coupled with mass transfer, which is used to calculate the supersaturation. Afterwards, we discuss the growth kinetics of the three forms, followed by *in situ* polymorph detection. Finally, we discuss limitations of such growth kinetics extraction and conclude with a discussion of an especial advantage achieved in these laminar flow devices for high aspect ratio crystals, as well as particles.

3.3.1 Seed Synthesis

Seeds were carefully prepared to achieve the desired purity, size as well as density. It was important to use pure polymorphs in order to eliminate artifacts from issues, such as polymorphic transition. Controlling the size was important for eliminating sedimentation, and controlling the seed density was important for minimizing agglomeration. Seeds were characterized before performing the crystallization experiments. The size and density of seeds were characterized with optical microscopy, and the purity and polymorphic form were characterized with X-ray diffraction, as discussed in the experimental section. The microcopy data and the X-ray diffraction data for alpha glycine seeds are presented in

Figure 3-10 and Figure 3-11, respectively. 100% purity was easily achieved for the alpha form, since glycine most readily crystallizes in this form.[81] The challenge for the alpha seeds was to control aggregation and coalescence, which tends to yield large seeds. This issue was addressed by carefully diluting the seeds with filtered glycine solution, saturated with respect to the alpha form.

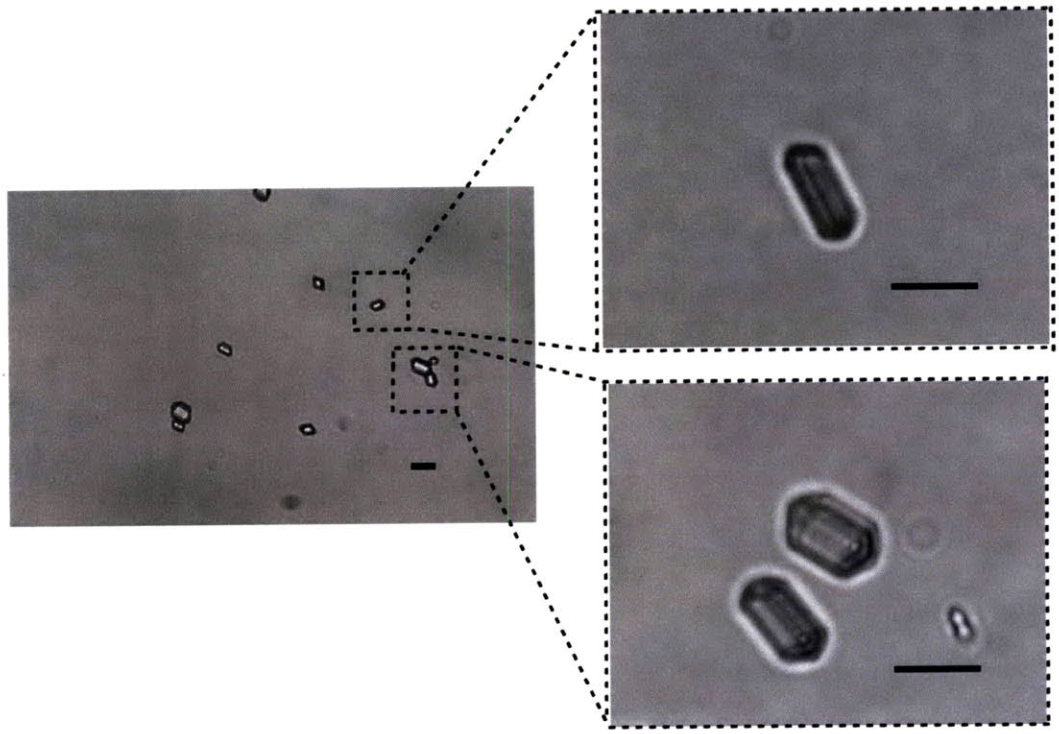

Figure 3-10. Seeds of alpha-glycine. The scale bar in the zoomed images is 5 μm, and in the zoomed-out image is 10 μm.

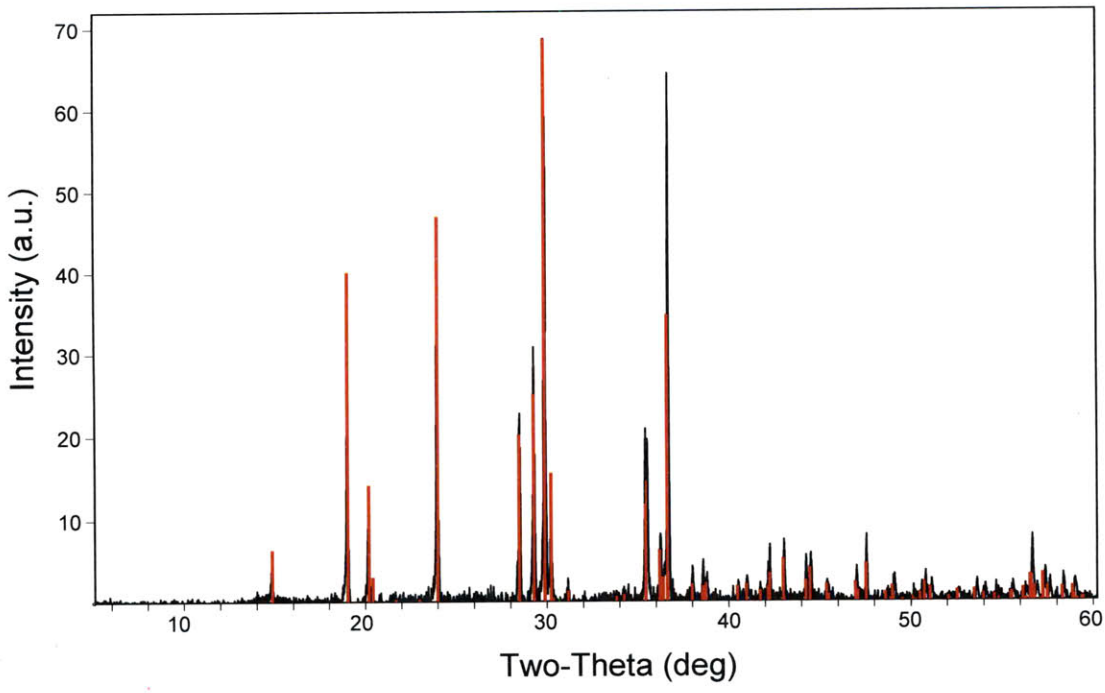

Figure 3-11. X-ray diffraction pattern of α-glycine seeds. The plot in black represents the sample data and the red lines represent simulated peaks from reference data for α-glycine.[55]

The purity was the most difficult to control in case of the beta form. Beta is the most unstable form, and readily converts to the more stable forms, alpha and gamma, in an environment with high moisture content. The instability of the beta seeds made it difficult to process and characterize them, particularly using optical microcopy. It was noticed that inconsistent results, in terms of purity, were easily obtained if the steps mentioned in the experimental section were not carefully followed. Understanding the dynamics of the solution speciation of glycine is required to produce the pure beta form. In solution, glycine can exist as a cation, Gly^+, an anion, Gly^-, or a zwitterion, $^+Gly^-$. The mole fraction of each of these species as a function of pH is shown in Figure 3-12. In the preparation of beta glycine, acetic acid was used to lower the pH to approximately 3.2, which decreased the concentration of $^+Gly^-$, and increased the concentration of Gly^+.

It is argued by many authors that the alpha form most likely grows through the addition of cyclic dimers.[82] The decrease in $^+Gly^-$ concentration may disrupt dimer formation, affecting the nucleation and growth of α-glycine. In addition, Towler et al.

have proposed that Gly^+ may have self-poisoning effect on the faces of α-glycine, inhibiting its nucleation.[83] Therefore, lowering the pH essentially controls the kinetics of alpha form. The gamma form, on the other hand, is believed to nucleate through the formation of polar chains.[81] At high or low pH, the concentration of ionic species increases, possibly leading to an increase in polar chain formation. However, the kinetics of gamma nucleation is quite slow. Hence, instantaneous crystallization of most of the glycine molecules with enough antisolvent (such as acetone) at low pH, and quick wash out of the solvent, yield the formation of sufficiently pure β-glycine. Peaks of any other form were not detected in the X-ray diffraction data of the prepared beta seeds, as presented in Figure 3-14. The size of the beta glycine seeds ranged from 10-20 μm. Figure 3-13a shows pre-processed beta glycine seeds, and Figure 3-13b shows processed, namely grinded and sieved, seeds of beta glycine.

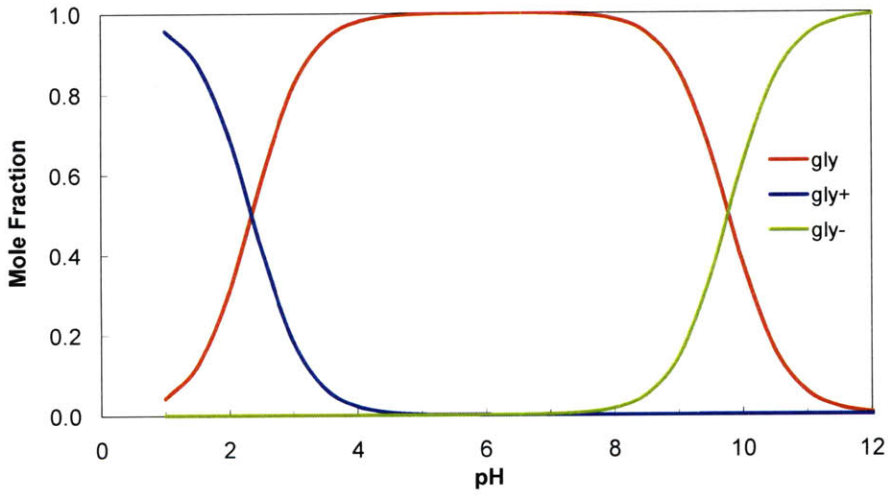

Figure 3-12. Solution speciation of glycine as a function of pH. pK_{a1} = 2.34 and pK_{a2} = 9.6. The red, blue and green curves represent the mole fraction of zwitterionic, cationic and the anionic glycine, respectively.

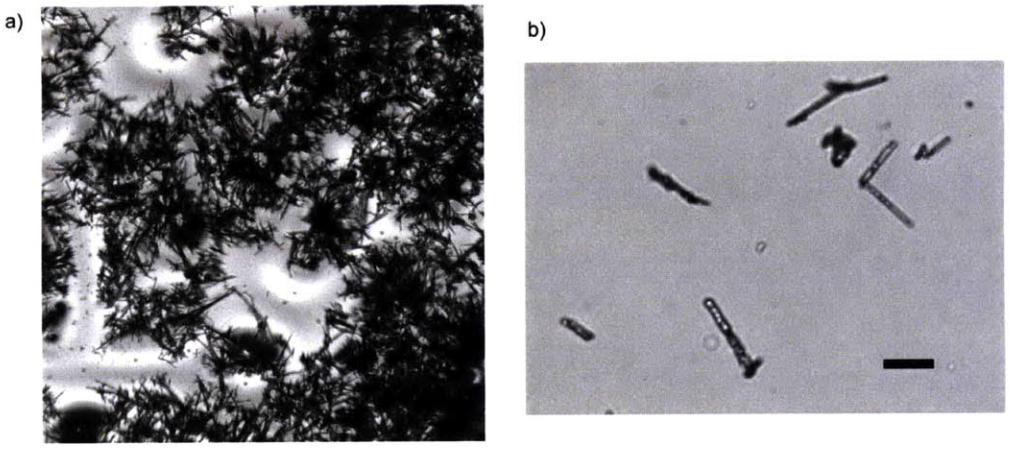

Figure 3-13. Seeds of beta-glycine. The scale bar is 10 μm.

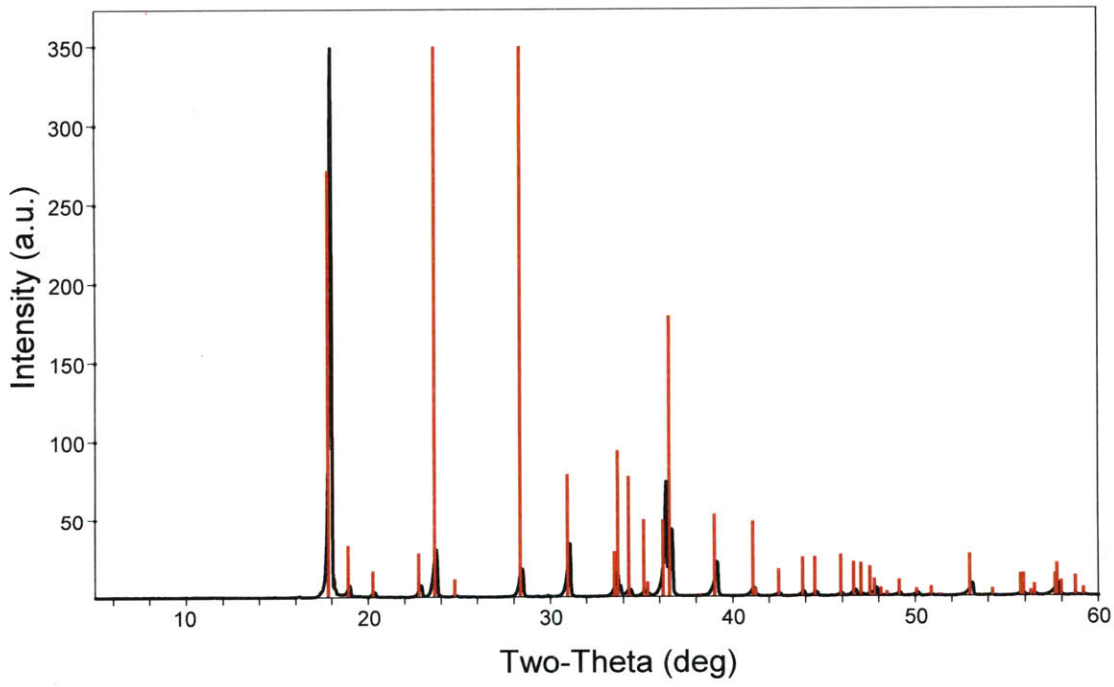

Figure 3-14. X-ray diffraction pattern of β-glycine seeds; black line represents the sample data and red line represents reference peaks of β-glycine.[61]

Dry beta glycine was found to be stable over a long period of time, particularly when stored in a glove box or a hygroscopic jar. However, beta glycine converted to the more stable polymorphic forms in solution. Beta is known to transform through solution

mediated transformation.[79] The time needed for polymorphic transition strongly depends on (i) the presence of other forms that can act as seeds; (ii) the amount of other two forms present, with larger amount yielding faster transition; (iii) the moisture content, with increasing water content giving faster transition;[79, 84] (iv) temperature, with a higher transition rate at higher temperature;[84] and (v) supersaturation, with a higher supersaturation causing faster transition because nucleation of other forms becomes faster. The stability of beta glycine was required to design the experiments. We followed a protocol, similar to Dang et al.,[84] and Ferrari et al.,[79] to measure the stability, and used the change in crystal shapes to obtain an approximation for the transformation kinetics for different composition of the solvent and antisolvent, water and ethanol, respectively. The first appearance of the alpha form was taken as the transition point. The measured stability of beta glycine is presented in Figure 3-15 as a function of the ethanol weight percent, and compared to that obtained by Ferrari et al. It is worth noting that the conversion time in our case was significantly higher. This most probably indicates that beta glycine was crystallized with a higher purity in this study than using the method described by Ferrari et al. We used the minimum value of the conversion time to design the residence time of our device in order to suppress polymorphic transformation.

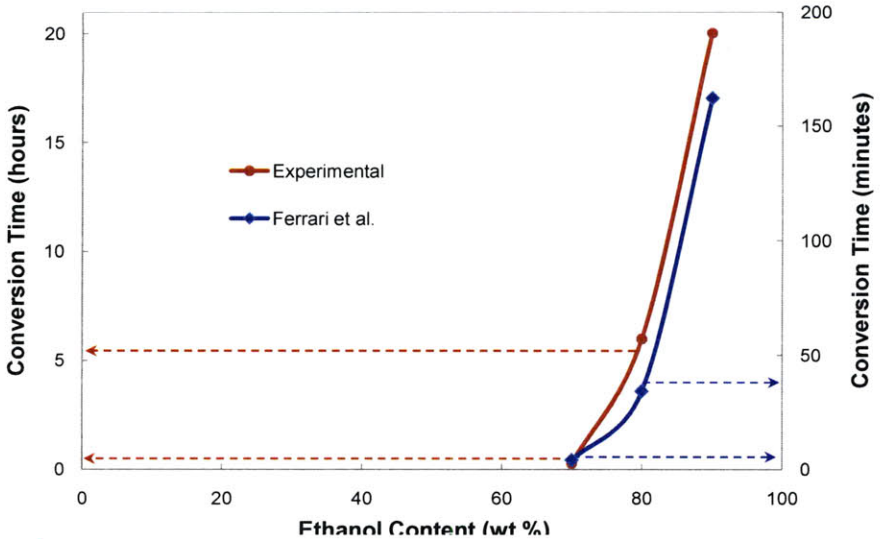

Figure 3-15. The stability of beta glycine, produced in this study, as a function of ethanol content. The red curve represents the conversion time achieved in our study, and the blue curve represents the conversion time achieved by Ferrari et al.[79]

Being the most stable of the three polymorphic forms, producing pure gamma seeds was straightforward. The size of the gamma seeds was approximately 5-7 μm. The images of gamma glycine seeds are presented in Figure 3-16, and the X-ray diffraction pattern is presented in Figure 3-17. Gamma seeds were found to have minimal agglomeration. However, behavior similar to crystal twinning was observed in a small fraction of the gamma seeds.

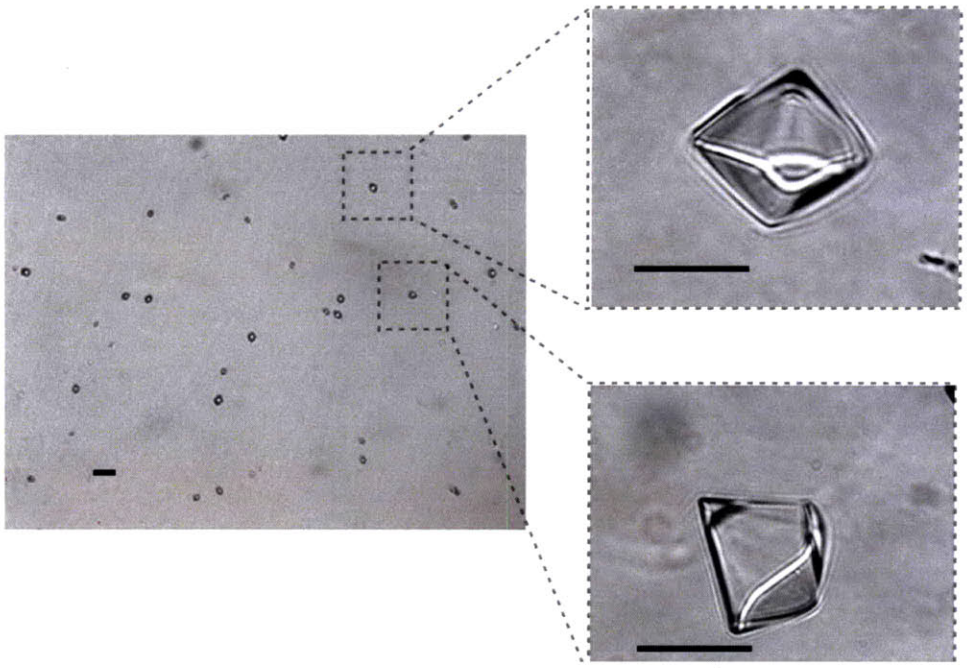

Figure 3-16. Seeds of gamma-glycine. The scale bar in the zoomed images is 5 μm, and in the zoomed-out image is 10 μm.

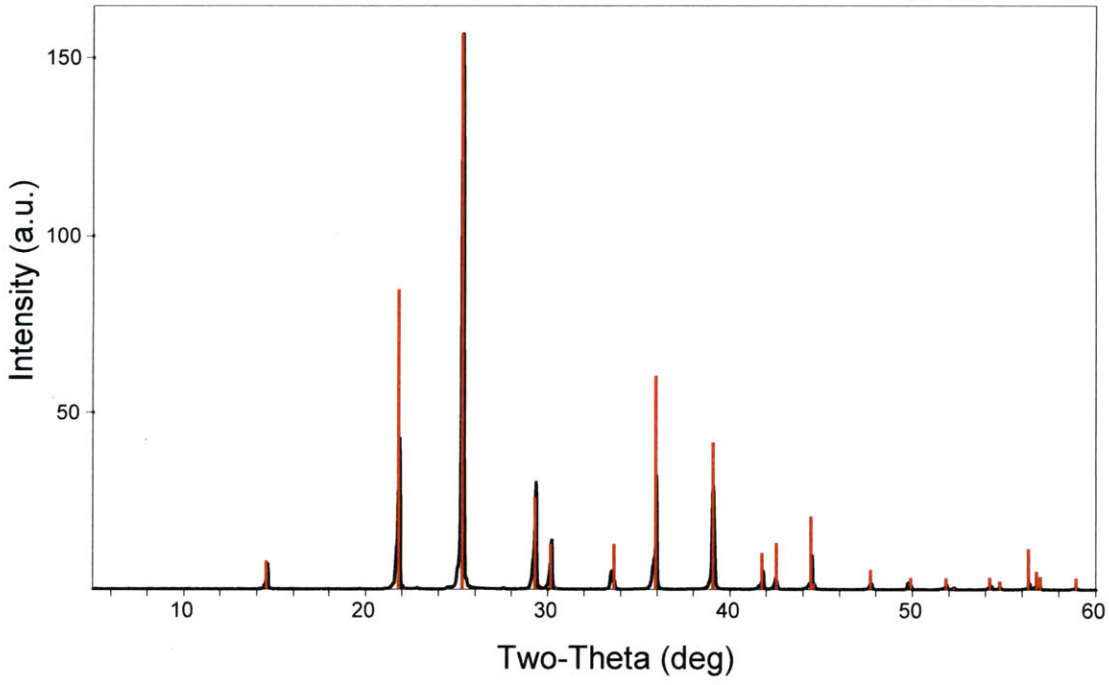

Figure 3-17. X-ray diffraction pattern of γ-glycine seeds; black line represents the sample data and red line represents reference peaks of γ-glycine.[64]

3.3.2 Simulation of the Fluid Dynamics and Mass Transfer

The growth rate of the crystals is dictated by the supersaturation, which in turn, is determined by the concentration of each of the three species, namely crystallizing solute, solvent, and antisolvent, in the microchannel. The mass transfer of the three species is coupled with fluid dynamics. Hence, building a model, which simultaneously solves for the velocity profiles and the concentration of the three species, was necessary. The transport of the three species, as well as their intermixing in the laminar flow device, was modeled in 2-D using COMSOL, a multiphysics modeling and simulation software that uses finite element analysis. A section of the device, where the interesting physical processes occurred, was chosen. It consisted of a 4 mm long main channel, a 1000 μm segment of the side channel, and the intersection of the two, as shown in Figure 3-18. Saturated solution of aqueous glycine was set to enter the main channel, and supersaturated solution was set to enter the side channel. The flow rates of all the streams were 6 μl/min, and the composition of the different streams was 100% aqueous for the seed and glycine solution, and 90% aqueous ethanol for the antisolvent. The simulation results were used to calculate the supersaturation, $S = C/C_S$, across the channel at different residence times. The calculated supersaturation is presented in Figure 3-19 as a function of the channel width, Y (as in Figure 3-18), at different R values. R is the percentage of total residence time used for growth.

$$R = \frac{\tau}{\tau_{total}} \times 100\% \qquad 3\text{-}17$$

In equation 3.17, τ is the residence time at a particular length of the microchannel, and τ_{total} is the total residence time used for a specific growth condition.

Simulation results show that the local supersaturation always remains below the metastable limit, $S \sim 1.9$, even at the point where supersaturated stream meets the seed solution, and thus, preventing nucleation. In addition, substantially uniform supersaturation (more than 95%) is achieved within 4% of the residence time, even for the smallest residence time operated for alpha glycine. Since growth in proportional to S, for S >1.1, the dispersion in supersaturation corresponds to ~ 5% dispersion in growth rates, which is much smaller than the dispersion inherent in the growth process of organic crystals, such as glycine (~ 30%).[85]

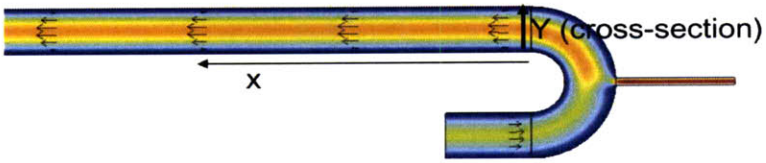

Figure 3-18. The segment of the microfluidic device used for finite element modelling. The fluid dynamics and the mass transfer of solute, solvent, as well as antisolvent, were simultaneously modelled. The arrows represent the velocity vectors.

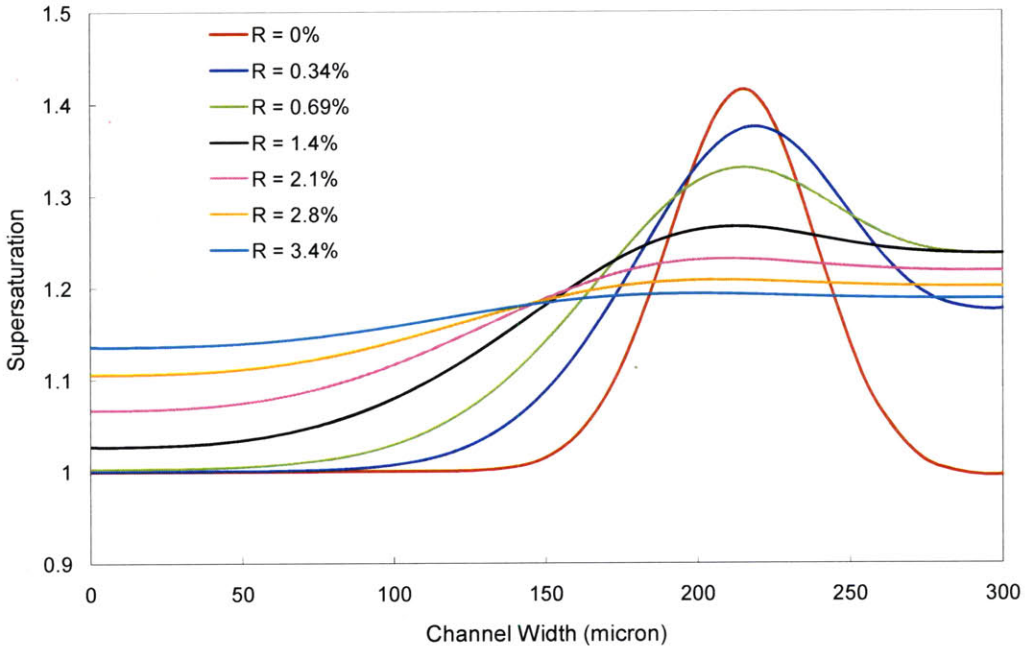

Figure 3-19. Typical supersaturation achieved in seeded crystallization devices across the channel, at various residence times from the mixing point. R represents the percentage of the total residence time used for a specific growth condition.

3.3.3 Growth Kinetics Extraction

Seeds of each of the three polymorphic forms of glycine were grown inside the microchannels. Figure 3-20 shows the seeds of each of the polymorphic forms introduced to the microfluidic device (first column), and the crystals grown inside the reactor (second column). Under flow conditions, crystals oriented themselves to minimize shear, and the largest faces lied on the visual planes. Most of the times, α-glycine crystals were oriented so as to display faces perpendicular to the $\pm a$ direction. The centrosymmetric

nature of the alpha form made it possible to calculate the growth rates of {010} and {011} faces by measuring lengths along the *b* and *c* direction, respectively (Figure 3-9). The growth rates obtained for these faces at different supersaturation are presented in Table 3-2. Alpha is known to grow by screw dislocation mechanism (BCF theory).[85] The surface entropy of alpha glycine faces were calculated to be approximately 3.9 and 5.5 for {011} and {010} faces, respectively, indicating a smooth interface between the crystal and the solution, characteristic of screw dislocation mechanism. Hence, the measured rates were compared with the literature values presented for the growth of alpha using BCF theory.[85] The data for both sets of faces, {011} and{010}, matched well with the literature values. Unlike the reference work, we generated supersaturation with ethanol, which was between 15-20 wt% of the final solvent composition for the alpha form. However, we did not notice any detectable change in growth rates, either as a result of ethanol addition or when varying ethanol content in the final solvent composition to a small extent. This is probably because the growth rate dispersion in these systems is higher than the change in growth rate due to small change in solvent composition. Growing large crystals of alpha was avoided because of sedimentation problems, which ultimately would have clogged the channels, and also because larger crystals tended to have significantly higher growth rates with a larger standard deviation. Li et al. had observed similar phenomenon in his work.[85] This phenomenon is most likely due to larger surface area, and thus, more defects in larger crystals, compared to that in smaller crystals.

Table 3-2. Growth rates of the {011} and {010} faces of α-glycine

$ln(C/C_{s,\alpha})$*	$G_{\{011\},exp}$ *(μm/min)*	$G_{\{011\},ref}$† *(μm/min)*	$G_{\{010\},exp}$ *(μm/min)*	$G_{\{010\},ref}$† *(μm/min)*
0.56	3.34 ± 0.43	3.74 ± 1.29	0.74 ± 0.16	0.47 ± 0.53
0.33	2.22 ± 0.91	2.17 ± 0.75	0.40 ± 0.25	0.28 ± 0.32
0.28	2.02 ± 0.39	1.83 ± 0.63	0.23 ± 0.09	0.23 ± 0.26
0.17	1.21 ± 0.22	1.03 ± 0.36	0.31 ± 0.14	0.14 ± 0.16
0.08	0.73 ± 0.22	0.42 ± 0.15	-	0.07 ± 0.07

*C = concentration of glycine [g glycine/100g solvent]; $C_{s,\alpha}$ = solubility of α-glycine [g glycine/100 g solvent]. †The reference values were calculated from the kinetic parameters presented in the reference work.[85] The errors in the growth rates were calculated by propagating the errors of the kinetic parameters, presented in the literature.

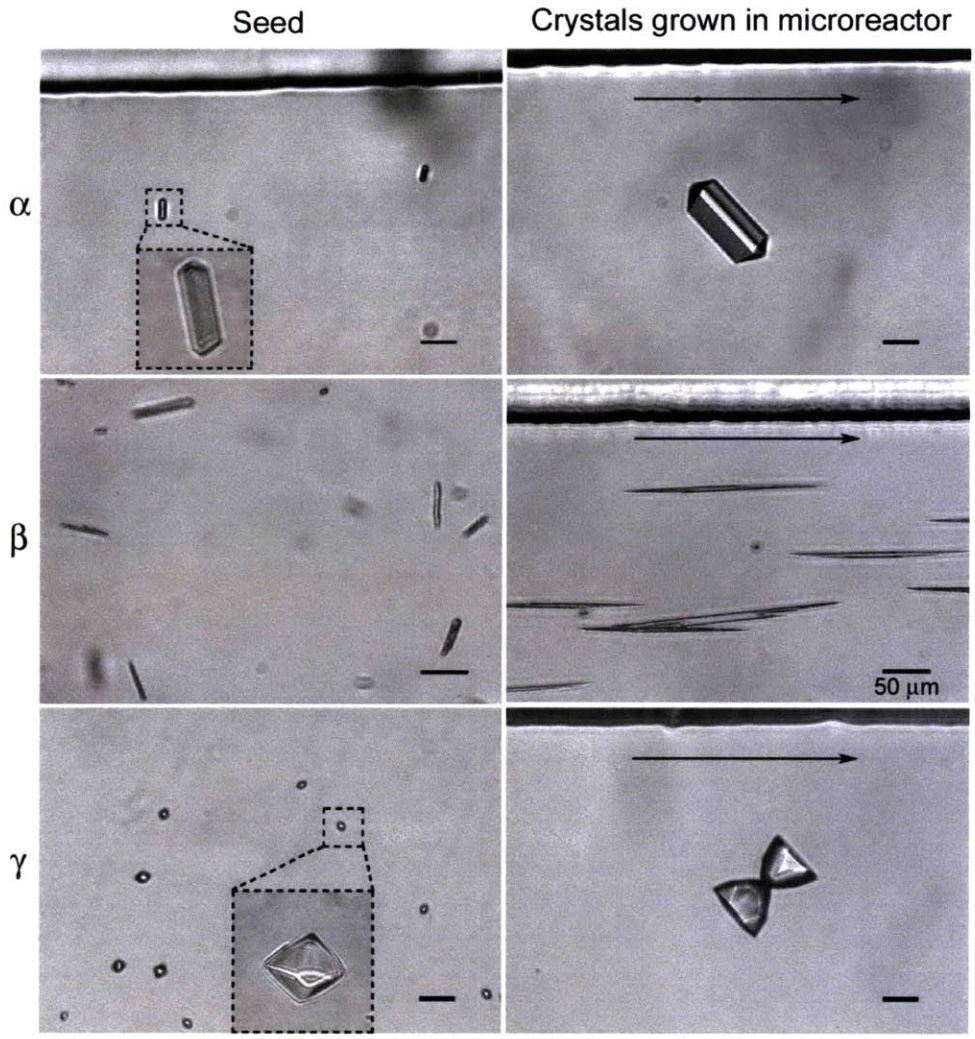

Figure 3-20. Continuous seeded crystallization in microfluidic devices. Seeds of α-, β-, and γ-glycine used for the process (first column) and the crystals of the corresponding form grown inside the microchannels (second column). The arrow shows the flow direction. Scale bar: 50 μm in grown β-glycine, and 10 μm in rest of the images.

β-glycine usually grows to assume high aspect ratio shapes, mostly needles. The growth rate of the beta form was calculated along the longest dimension, the *b* direction, which has the largest growth rate, and is of the most significance. The growth rate of beta is presented with respect to the supersaturation of the alpha form (Table 3-2), as the solubility of the beta form is difficult to measure accurately for stability reasons.[75] Weissbuch et al. have shown that the growth rate at the (010) face, the +*b* end, of

noncentrosymmetric beta needles is much higher than that at the opposite end.[62] Therefore, the growth in length was attributed to the growth of (010) face (Table 3-3). Due to the fast growth in the $+b$ direction, the residence time for the beta form was designed to be short, ranging from 30 seconds to 90 seconds. As a result, significant growth in the smaller dimensions was not observed. The growth expressions of different mechanism could not be applied to the kinetics data for beta glycine, as the supersaturation with respect to beta glycine solubility needed to be accurately known at the conditions of operation. However, as mentioned earlier, the low solubility at high ethanol content solution and the high instability of the beta form makes it a challenge to measure the solubility accurately.

It must be emphasized that the kinetics for an unstable form, such as beta glycine, is quite challenging in batch because the nucleation of alpha, a more stable form, readily induces solvent mediated transformation. Microfluidic devices enabled the extraction of such kinetics data through the controlled addition of supersaturated solution, which prevented the nucleation of alpha. Measurement of such kinetics data is also facilitated by the laminar flow, which orients the longest dimension of beta needles to coincide with the flow direction.

Table 3-3. Growth rates of β-glycine

$ln(C/C_{s,a})$	$G_{(010)}$ ($\mu m/min$)
0.30	194 ± 55
0.39	235 ± 43
0.47	250 ± 52

Most of the times, γ-glycine crystals were oriented so as to display faces perpendicular to either a or b axis, enabling measurement along the c axis (Figure 3-9). Since, gamma is known to have a much higher growth rate at the flat end in the $-c$ direction, compared to the pyramidal end in the $+c$ direction,[80] growth along the c axis was attributed to (00-1).

The growth mechanism of gamma is known to be complex, and to vary depending on the experimental conditions.[86] It was observed that uncontrolled and high supersaturation, for lnS > 0.5, gave rise to very fast growth rates for gamma, possibly due to a change in mechanism. Such fast growth rate almost always caused the crystals to potentially sediment and / or bridge with microchannel surfaces, clogging the reactor. The increasing control over supersaturation in our devices allowed for operation at lower supersaturation, thus preventing the 'very fast growth' regime, and allowed us to successfully extract growth kinetics data for gamma. The growth rate of {100, 010} and (00-1) faces are presented in Figure 3-21a and Figure 3-21b, respectively. To elucidate on the growth mechanism of gamma, we use a semi-empirical growth equation:

$$G = K_g(\ln S)^a \qquad 3\text{-}18$$

where G is the growth rate, K_g is the growth constant, and S is the supersaturation, S = C/C_s. Equation 3-18 is linearized by taking the natural log to give equation 3-19.

$$\ln G = \ln K_g + a \ln S \qquad 3\text{-}19$$

The natural log of the growth rates of the various faces is plotted against the natural log of the supersaturation. As discussed in chapter 1, the exponent a is 1 or 2 for the BCF model, depending on the supersaturation. For rough growth, a is also 1. When a is greater than 2.5, growth is known to occur through surface nucleation mechanism. The fit of the growth rate data of {100,010} and (00-1) faces to the above linearized model is presented in Figures 3-22a and 3-22b, respectively. Linear regression analysis yields the following growth rate equations for the different faces:

$$\ln G_{\{100,010\}} = 1.20 + 3.47 \times \ln S \qquad 3\text{-}20$$

$$\ln G_{(00-1)} = 0.62 + 5.07 \times \ln S \qquad 3\text{-}21$$

Therefore, a is found to be 3.47 and 5.07 for {100,010} and (00-1) faces, respectively, indicating growth by surface nucleation mechanism, at the conditions we operated in. The rate constant, K_g, in equation 3-19, was calculated to be 3.33 and 1.85 for {100,010} and (00-1) faces, respectively.

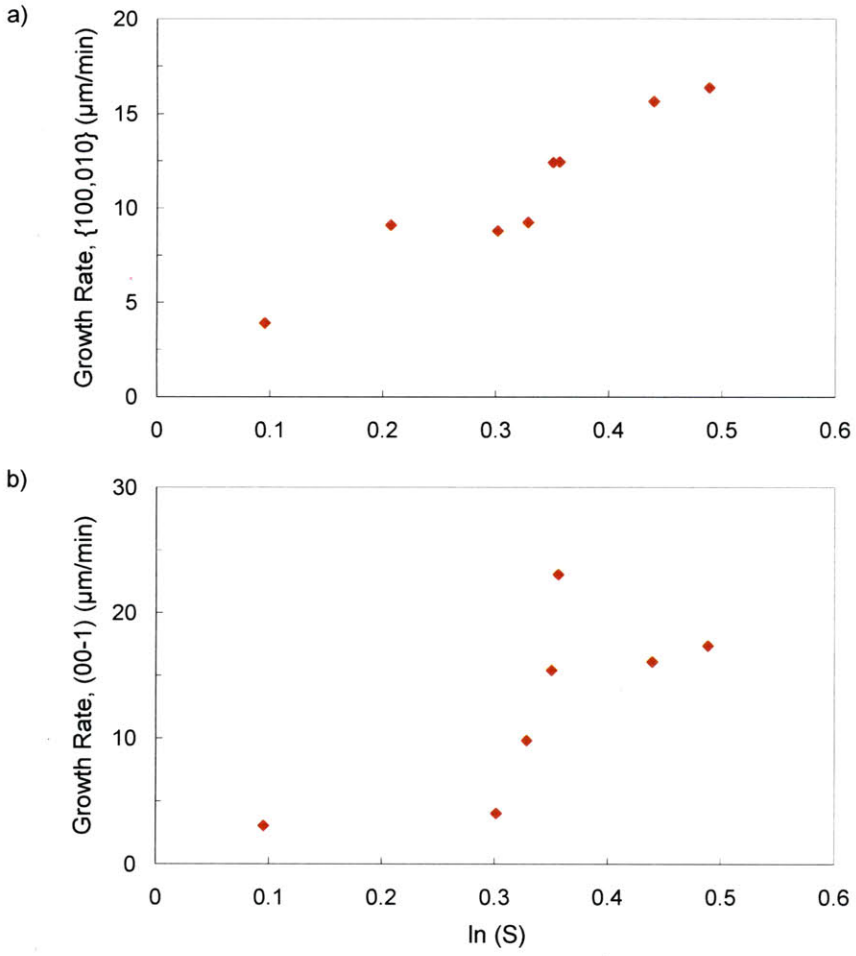

Figure 3-21. Growth kinetics of gamma glycine. The growth rates are plotted against the log of supersaturation with respect to gamma for a) $\{100,010\}$, and b) (00-1) faces.

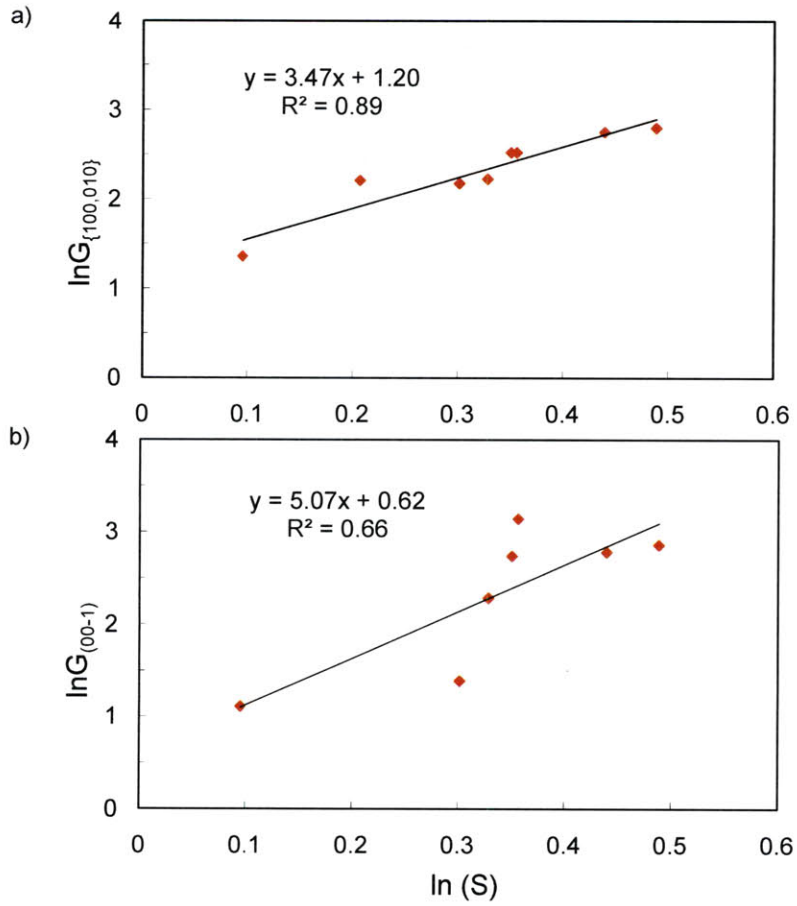

Figure 3-22. Determination of growth mechanism of gamma glycine. The growth rate data is fitted to a linearized semi-empirical model for a) {100,010}, and b) (00-1) faces.

If a birth and spread surface nucleation model, the most widely used surface nucleation model,[87] is applied to the growth data, the surface tension of the nuclei with the solution can be determined from the following equation.

$$G = k_{BS}(\ln S)^{5/6} \exp\left(-\frac{\pi \gamma_E{}^2}{3(k_B T)^2 \ln S}\right) \qquad 3\text{-}22$$

where k_{BS} is the rate constant of growth, γ_E is the edge surface tension, k_B is the Boltzmann constant, and T is the temperature. γ_E is related to the surface tension, σ, as:

$$\gamma_E = \sigma * d^2 \qquad 3\text{-}23$$

In equation 3-23, d is the mean diameter, and is approximated from the molecular volume, v_m, of gamma glycine as $d = v_m^{1/3}$. The molecular volume of gamma glycine is taken from the literature to be 235.24 Å.[88] Linearizing equation 3-22 and performing a linear regression analysis on the growth data yields a good fit for both for {100,010} and (00-1) faces, as shown in Figure 3-23. The surface tension is calculated to be 7.1 and 8.8 mJ/m2 for {100,010} and (00-1) faces, respectively, and the rate constant, k_{BS}, is found to be 50.7 and 90.4 μm/min for the respective faces. The surface tension of glycine was reported to be ~41 mJ/m^2 by Black and Davey,[50] larger than what we find in our study. This is most likely because in the case of growth by surface mechanism, nucleation occurs on the crystal surface, and thus is heterogeneous, while the reference data represents homogeneous nucleation, which would result in a higher surface tension between the crystallite and solution. In the same work, Black and Davey discussed the surface tension of L-glutamic acid, also a small amino acid. They found that the surface tension calculated from the nucleation data of L-glutamic acid was ~6 mJ/m^2, while the expected value was ~53 mJ/m^2. They argued that the nucleation occurred through a heterogeneous mechanism, and thus the surface tension was a magnitude smaller than expected.[50] In this study, we find the surface tension, σ, of gamma glycine to be in a very similar range, when determining σ from growth rate data using birth and spread model that depicts growth through heterogeneous nucleation. In addition, He et al. deduced the surface tension of glycine to be 8.37 mJ/m^2 from the nucleation data measured in hanging drop experiments.[89] Nucleation at the low supersaturation used by He et al. in hanging drops, most likely occurs at the air-liquid interface, and thus through a heterogeneous mechanism. Therefore, the surface tension of 8.37 mJ/m^2 most likely represents heterogeneous nucleation and matches with our calculated value remarkably well.

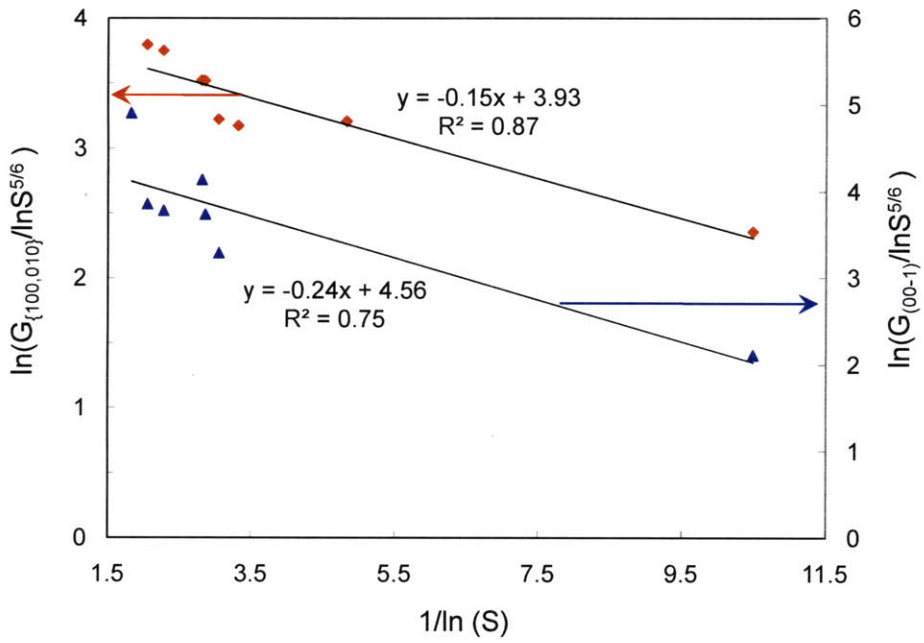

Figure 3-23. The growth rate expression for birth and spread model applied to the growth rate data for {100,010} and (00-1) faces.

3.3.4 Mass Transfer Limited vs. Surface Integration Limited

In order for crystal growth to occur, the solute molecules have to diffuse from the bulk to the crystal surface. In laminar flow regime, since mixing occurs only through diffusion, crystals can grow in a diffusion-limited process at low flow rates. Diffusion-limited growth can be an interesting process for producing uniform particles through size focusing;[90] however, it does not elucidate the fundamentals of the crystal growth process. In order to ensure operation in the surface integration-controlled regime, we performed two sets of exercises, as described below, as well as looked into the theoretical model for diffusion-controlled growth.

First, defect density in crystals seeds was increased, and its effects on crystal growth rate were observed. Alpha and gamma crystals were milled, sieved and used as seeds without any ageing, which did not allow them to go through the natural crystal perfection, and increased the defect density. The higher defect density introduced in this way was expected to have no effect on the crystal growth rate in the diffusion-limited growth regime. On the other hand, the crystal growth rate is expected to increase with an increase

in defect density, when the growth is controlled by surface integration. We found that in the case of seeds with increased defect density, the growth rate increased up to ~ 10-15 times compared to the growth rate of mature seeds at the same conditions and supersaturation.

Moreover, the theoretical model for diffusion-controlled growth did not match with our observation in this study. For the diffusion-controlled regime, the growth rate, G, can be expressed as:

$$G = \frac{\beta}{\alpha} k_d \frac{\Delta c}{\rho_c} \qquad 3\text{-}24$$

where α and β are shape factors of the crystal, ρ_c is the density of the crystalline phase, Δc is the concentration gradient between the bulk and crystal surface (usually taken as the solubility), and k_d is the mass transfer coefficient.[91] k_d is expressed as a function of the diffusion coefficient, D, and the mass boundary layer thickness, δ.

$$k_d = \frac{D}{\delta} = \frac{Sh \times D}{d_p} \qquad 3\text{-}25$$

In equation 3-25, d_p is the particle diameter, and Sh is Sherwood number. The Sherwood number is related to Reynolds number, Re, and Schmidt number, Sc, through the Frossling correlation.[92]

$$Sh = 2 + 0.6\,\mathrm{Re}^{1/2}\, Sc^{1/3} \qquad 3\text{-}26$$

Reynolds number, in this case, is expressed as a function of the kinematic viscosity, v, the particle diameter, d_p, and the fluid velocity, U:

$$\mathrm{Re} = \frac{d_p U}{v} \qquad 3\text{-}27$$

and Schmidt number is expressed as $Sh = v/D$. The typical Schmidt number for our system was ~1000. However, the small crystals we used (tens of microns), and the small velocity in the microfluidic devices, result in a Reynolds number of ~0.02, which makes the second term of equation 3-26 less than 1. Therefore, k_d can be roughly approximated as:

$$k_d = \frac{2 \times D}{d_p} \qquad 3\text{-}28$$

The implication of equation 3-28 is that the growth rate should be inversely proportional to the particle diameter. In our case, however, we do not observe the growth rate to decrease as a function of increasing crystal size for the size range we operate in. We do observe a decrease in growth rate for very large crystals, larger than ~120 μm. This is consistent with the theoretical model of diffusion limited growth. The boundary layer thickness increases almost proportionally with the particle diameter at the operating conditions, and thus, a ten times increase in the particle size increases the mass boundary layer thickness significantly, almost by a factor of 10, pushing the system into diffusion-controlled regime.

Furthermore, the mass transfer coefficient, k_d, in the diffusion limited growth model, can be increased with an increase in the fluid velocity.[91] In order to observe the effects of velocity on individual crystals, we used a microfluidic device with a charged surface (e.g. uncoated glass), and introduced dilute seeds that became attached to the charged surface. We then varied the flow rate of supersaturated solution over 10 to 30 $\mu l \cdot min^{-1}$. However, the crystal growth rate was found not to be a function of the crystal size, for crystals that were less than ~120-150 μm in size. Therefore, crystal growth was not limited by diffusion in our studies, but by surface integration, mostly because of the small size of crystals we used in our systems.

3.3.5 *In situ* Raman Spectroscopy

Since the growth rate of different polymorphic forms vary significantly, as discussed above, it is important to characterize the polymorphic form *in situ*, in order to ensure that the correlation of growth rate data to the supersaturation is correct. Otherwise, the data analysis fails to provide correct insights into the fundamentals of the growth process. The different polymorphic forms of glycine have distinct shapes in pure aqueous-ethanol solutions, which can be used with image analysis techniques for determining the polymorphic form. However, even a small amount of impurities can modify the habits of the glycine polymorphs.[93-96] Therefore, shape is not always conclusive in characterizing the polymorphic form. Hence, we use *in situ* Raman Spectroscopy to complement our video microscopy data.

Alpha, beta and gamma glycine have distinct Raman bands (e.g. peak positions) that results from the differences in molecular vibrations in the crystal lattice.[97] Calibrated spectra of the pure polymorphic forms were first prepared with crystals that were previously confirmed with X-ray diffraction data. We use these calibrated spectra to compare the spectra measured *in situ*. For the *in situ* experiments, a larger density of seeds were used, and the crystals were grown larger, up to 50-70 μm, with long residence time reactors to achieve detectable signal.

Obtaining *in situ* spectra in the microfluidic devices was challenging due to a number of factors. Even though the transparency of glass and PDMS is useful for spectroscopic techniques, both PDMS and glass may have fluorescence signal that overwhelms the sample peaks. The intensity of the fluorescence signal depends on the laser wavelength, significantly increasing at lower wavelength. Although PDMS was found to fluoresce at 785 nm, the wavelength used for *in situ* measurements, we were able to eliminate fluorescence by three means: careful focusing of the collection at a point significantly away from PDMS, using confocal microscope to limit the sample volume, and using a small collection fiber that acted at a spatial filter. However, with this configuration, we still observed significant signal from glass, as shown in the original spectrum obtained for the alpha and gamma crystals (Figure 3-24).

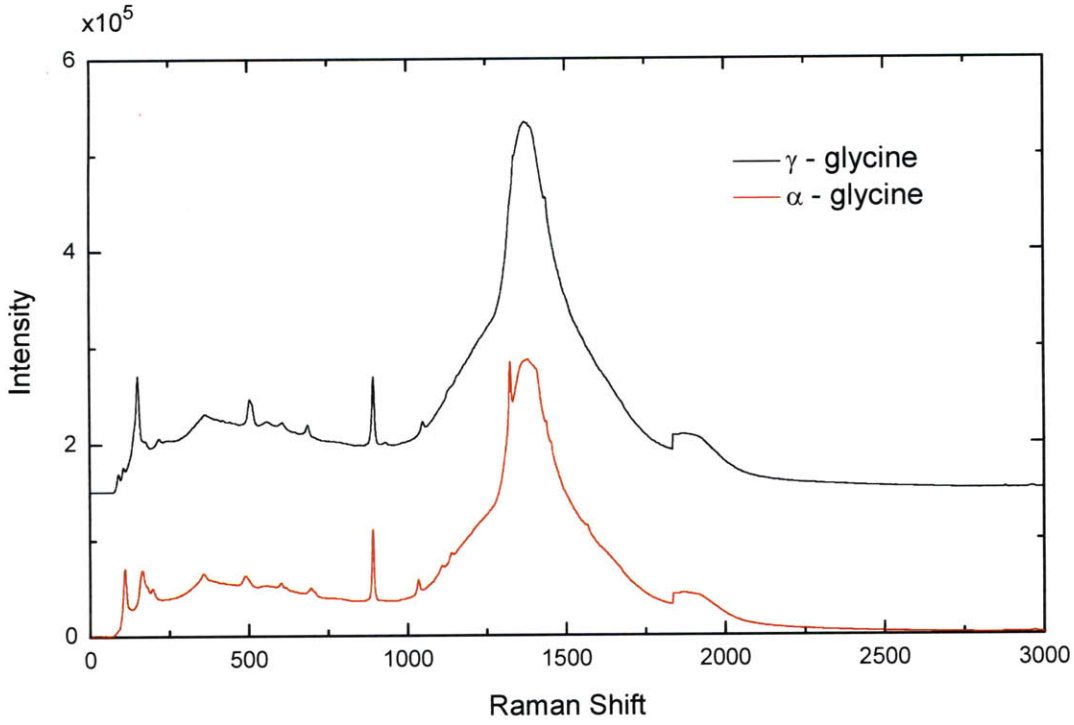

Figure 3-24. *In situ* Raman spectra acquired for α-, and γ-glycine before any data processing. The *in situ* signals appeared to be overwhelmed by the Raman spectra of glass.

It was found that the overwhelming background signal obtained in the *in situ* measurements was due to the Raman spectra of glass, and not fluorescence. Raman signal is linear and reproducible, while fluorescence signal is difficult to model. Hence, we acquired blank spectrum for subsequent *in situ* measurements, by using similar microfluidic devices at identical conditions. The blank spectrum was subtracted from each of the initial *in situ* spectra, and was used to compare the alpha and gamma forms. The subtracted spectra are presented in Figure 3-25 in the range of 0-1600 cm^{-1}. The spectra obtained for the two forms have high enough resolution to distinguish between the two polymorphic forms.

The Raman spectrum of both α- and γ-form was found to be consistent with the standard crystals, as well as with literature.[97] As seen in Figure 3-25, many differences in Raman bands exist between two polymorphic forms. However, in this study, CH_2 rocking, CH_2 twisting, CH_2 wagging, and CH_2 bending modes are compared in the region of 900-1500 cm^{-1} because these differences have been well established in the

literature.[97-100] CH_2 rocking and twisting modes are present at 915 cm^{-1} and 1323 cm^{-1} in gamma, respectively, but are absent in alpha. CH_2 wagging mode appears at 1326 cm^{-1} in alpha, but at 1337 cm^{-1} in gamma. There are two CH_2 bending modes at 1440 cm^{-1} and 1456 cm^{-1} in alpha, but only one at 1439 cm^{-1} in gamma.

Therefore, the Raman bands for the alpha and gamma forms obtained from the *in situ* measurements were substantially different and were sufficient to verify the polymorphic form grown in the microfluidic devices. The beta form, however, was difficult to measure inside the microchannels *in situ*, as the thin needles, with approximately 1-3 μm width, constituted a small fraction of the sampling volume.

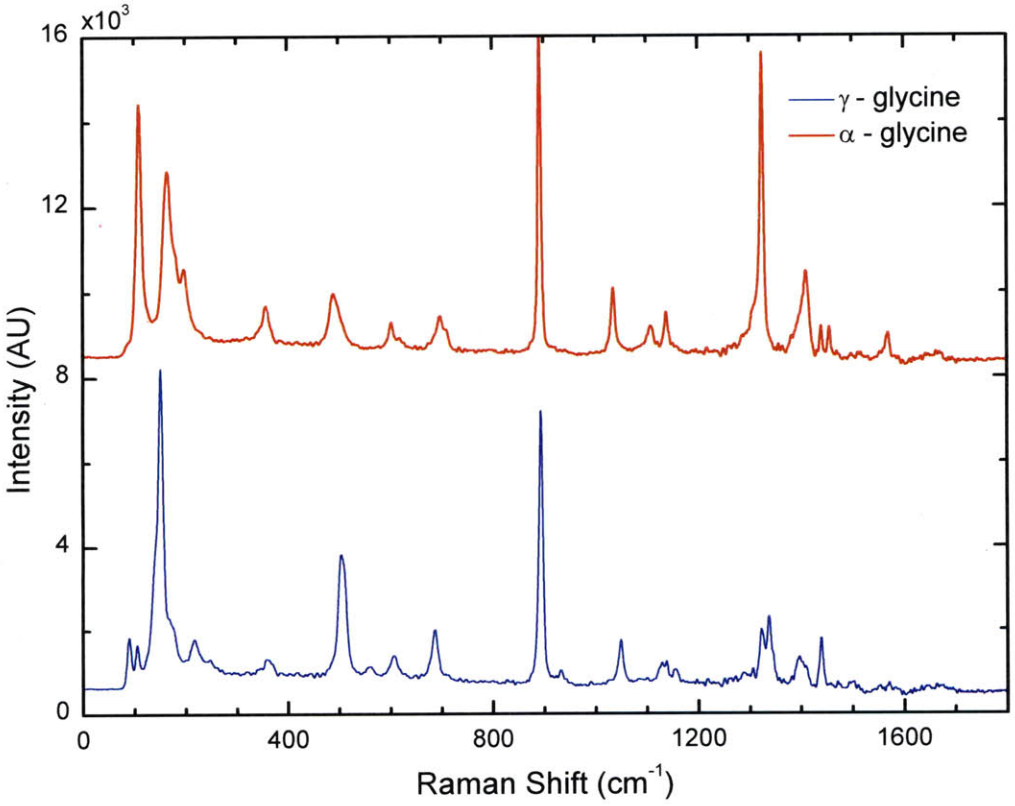

Figure 3-25. *In situ* Raman spectra acquired for α-, and γ-glycine (after subtracting background spectra).

3.3.6 Self Alignment of Acicular Crystals

Microfluidic devices offer elegant solutions for measuring growth kinetics of various shapes, including high aspect ratio crystals. In addition to uniform process parameter and well-controlled environment, these laminar flow devices exhibit an additional advantage for the high aspect ratio crystals. We observe that the high aspect ratio crystals, such as needles, rods and plates align themselves parallel to the streamlines in order to minimize the shear created by continuous laminar flow. This phenomenon is observed for all high aspect ratio crystal systems we investigated, including modified alpha glycine crystals with rod shape (Figure 3-26a), and plate shape (Figure 3-26b), β-glycine (Figure 3-26c), and lovastatin (Figure 3-26d). Hence, the self-alignment of high aspect ratio particles was not a system specific phenomenon, but a more general one, as the phenomenon is the result of a physical effect. Such self-alignment facilitates much more accurate measurement of crystal size, size distribution, and thus, growth kinetics than can be achieved with the existing techniques.

The most popular state-of-the art technique for measuring the crystal size distribution and the crystallization kinetics is to use a Lasentech probe that measures the chord length distribution of crystals by measuring the light reflected from the solid phase.[32] Figure 3-27 illustrates the working principle of the Lasentech probe. While the chord length distribution is somewhat reflective of the actual size distribution for crystals of regular shapes, it does not resemble the actual size distribution for acicular crystals (needles) or other high aspect ratio crystals very well. For example, if the crystal in the highlighted portion of the beaker in Figure 3-27 is measured with a Lasentech probe, the crystal size distribution achieved can be represented as in Figure 3-28a. However, the actual size of the crystals, presented in Figure 3-28b, is much larger. Hence, the length of the needles, which is the major growth dimension, is grossly underestimated by the Lasentech probe. Microfluidic devices, on the other hand, exerts shear on the free flowing crystals, making them align with the direction of flow. As a result, actual size, presented in Figure 3-28b, is achieved with microfluidic devices.

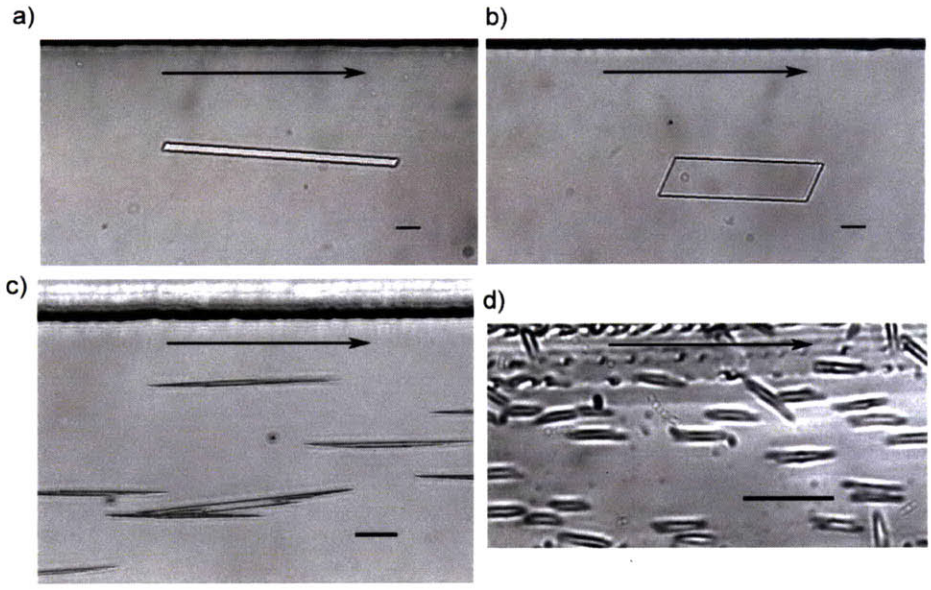

Figure 3-26. Self-alignment of different high aspect ratio crystal systems under laminar flow: a) rods of modified α-glycine, a) plates of modified α-glycine, c) needles beta glycine, and d) needles of lovastatin. Scale bar: 50 μm in β-glycine, and 10 μm in rest of the images.

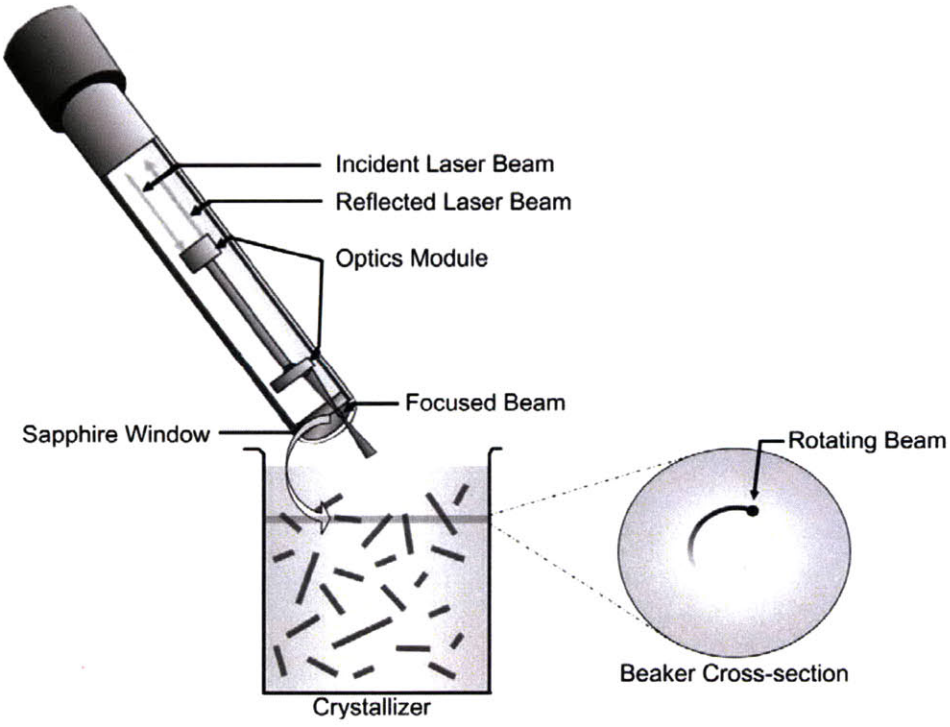

Figure 3-27. Working principle of Lasentech probe.

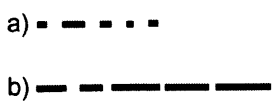

Figure 3-28. a) Size distribution achieved when the crystals in the highlighted section of the beaker in Figure 3-27 is measured with a Lasentech probe; b) The actual size distribution of the crystals.

3.4 Conclusions

We have designed a continuous microfluidic system for seeded crystallization of small organic molecules such as active pharmaceuticals. We have used seeds to decouple the nucleation process from the growth phenomenon, which allows us to operate at a low supersaturation regime, ideal for crystal growth. We have also integrated an *in situ* Raman Spectroscopy tool for determining polymorphic form of the crystals. With *in situ* microscopy and image analysis, we have developed a complete tool that can be used as a platform for fast screening of process parameter effects and optimization, as well as to gain insight into the fundamentals of crystal growth process.

We have demonstrated the use of our integrated device for continuous seeded crystallization of the three polymorphs of glycine: α-, β- and γ-form of glycine. We have used the *in situ* characterization tools to successfully determine the crystal growth rates of all the three forms. Growth rates compared well with the known growth mechanism for the alpha form. In addition, the growth mechanism has been successfully determined for the gamma glycine crystals, and fundamental information about the crystal system has been determined. The insights into the fundamental growth mechanisms may provide guidance for operating crystallizers at the optimum conditions and obtaining crystal products of controlled size and shape.

Using microfluidic devices to measure growth kinetics combines the advantages of single crystal studies and ensemble studies. It not only provides laminar flow profiles and well-controlled environment as in single crystal studies, but also allows one to study flow effects for continuous crystallizers, as well as to examine many crystals in the same environment, which is necessary to obtain meaningful data for processes with statistical phenomenon, such as crystal growth. Moreover, it provides a platform to easily vary

process parameters, such as supersaturation and solvent composition, by simply varying flow rates, and scan their effects.

The applicability of seeded crystallization microfluidic devices to the three glycine polymorphs, each with a distinct habit and a different set of challenges, shows the versatility of our method. In addition, we have demonstrated that microfluidic devices provide an elegant tool to accurately measure the growth rates of high aspect ratio crystals by exerting shear on them and causing them to self-align.

3.5 List of Variables

ω	frequency of light
P	polarization
E	electromagnetic field of incoming light
α	polarizability of a molecule
α_0	inherent polarizability of a molecule
Q_i	normal mode of molecular vibration
v_i	characteristic harmonic frequency
v_0	incident photon frequency
λ	photon wavelength
ω_{Raman}	Raman Shift
Q	liquid flow rate
ΔP	pressure drop
R	hydraulic resistance
μ	liquid viscosity
L	mixing length scale
D_E	equivalent diameter
w	width of the microchannel
h	height of the microchannels
K	a constant that depends on the channel aspect ratio, w/h
Q_a	antisolvent flow rate
Q_s	solution flow rate
Q_{seed}	flow rate of seed stream
L_c	characteristic dimension
L_b	characteristic dimension
Y	channel width
S	supersaturation
τ	residence time
τ_{total}	total residence time

G	growth rate
K_g	rate constant of growth
k_{BS}	rate constant of growth for birth and spread model
γ_E	edge surface tension
k_B	Boltzmann constant
T	temperature
σ	surface tension
d	mean diameter
v_m	molecular volume
α and β	shape factors of the crystal
ρ_c	density of the crystalline phase
Δc	concentration gradient
k_d	mass transfer coefficient
D	diffusion coefficient
δ	mass boundary layer thickness
d_p	particle diameter
Sh	Sherwood number
Re	Reynolds number
Sc	Schmidt number
v	kinematic viscosity
U	fluid velocity

3.6 References

[1] G. Fevotte, In situ raman spectroscopy for in-line control of pharmaceutical crystallization and solids elaboration processes: A review. *Chemical Engineering Research & Design,* **2007**, *85*(A7), 906-920.

[2] N. Kubota, N. Doki, M. Yokota, & A. Sato, Seeding policy in batch cooling crystallization. *Powder Technology,* **2001**, *121*(1), 31-38.

[3] T. Togkalidou, H. H. Tung, Y. Sun, A. T. Andrews, & R. D. Braatz, Parameter estimation and optimization of a loosely bound aggregating pharmaceutical crystallization using in situ infrared and laser backscattering measurements. *Industrial & Engineering Chemistry Research,* **2004**, *43*(19), 6168-6181.

[4] W. Beckmann, Seeding the desired polymorph: Background, possibilities, limitations, and case studies. *Organic Process Research & Development,* **2000**, *4*(5), 372-383.

[5] N. Doki, N. Kubota, M. Yokota, S. Kimura, & S. Sasaki, Production of sodium chloride crystals of uni-modal size distribution by batch dilution crystallization. *Journal of Chemical Engineering of Japan,* **2002**, *35*(11), 1099-1104.

[6] J. Garside, A. Mersmann, & J. Nyvlt, *Measurement of Crystal Growth and Nucleation Rates*, 2nd ed., Institution of Chemical Engineers (IChemE), Rugby, UK, **2002**.

[7] A. S. Myerson, & R. Ginde, Crystals, crystal growth, and nucleation. in *Handbook of Industrial Crystallization* (Ed.: A. S. Myerson), Butterworth-Heinemann, **2002**, pp. 33-65.

[8] J. Garside, & R. J. Davey, Secondary contact nucleation - kinetics, growth and scale-up. *Chemical Engineering Communications,* **1980**, *4*(4-5), 393-424.

[9] A. D. Randolph, & M. A. Larson, *Theory of Particulate Processes*, Academic Press, Inc., **1988**.

[10] G. Fevotte, New perspectives for the on-line monitoring of pharmaceutical crystallization processes using in situ infrared spectroscopy. *International Journal of Pharmaceutics,* **2002**, *241*(2), 263-278.

[11] H. Groen, & K. J. Roberts, Nucleation, growth, and pseudo-polymorphic behavior of citric acid as monitored in situ by attenuated total reflection Fourier transform infrared spectroscopy. *Journal of Physical Chemistry B,* **2001**, *105*(43), 10723-10730.

[12] F. Lewiner, J. P. Klein, F. Puel, & G. Fevotte, On-line ATR FTIR measurement of supersaturation during solution crystallization processes. Calibration and applications on three solute/solvent systems. *Chemical Engineering Science,* **2001**, *56*(6), 2069-2084.

[13] L. X. Yu, R. A. Lionberger, A. S. Raw, R. D'Costa, H. Q. Wu, & A. S. Hussain, Applicatlons of process analytical technology to crystallization processes. *Advanced Drug Delivery Reviews,* **2004**, *56*(3), 349-369.

[14] M. E. Auer, U. J. Griesser, & J. Sawatzki, Qualitative and quantitative study of polymorphic forms in drug formulations by near infrared FT-Raman spectroscopy. *Journal of Molecular Structure,* **2003**, *661*, 307-317.

[15] Z. P. Chen, G. Fevotte, A. Caillet, D. Littlejohn, & J. Morris, Advanced calibration strategy for in situ quantitative monitoring of phase transition processes in suspensions using FT-Raman spectroscopy. *Analytical Chemistry,* **2008**, *80*(17), 6658-6665.

[16] P. H. Karpinski, & J. S. Wey, Precipitation processes. in *Handbook of Industrial Crystallization* (Ed.: A. S. Myerson), Butterworth-Heinemann, **2002**, pp. 141-160.

[17] H. G. Brittain, *Polymorphism in Pharmaceutical Solids*, Marcel Dekker, New York, **1999**.

[18] D. B. Patience, P. C. Dell'Orco, & J. B. Rawlings, Optimal operation of a seeded pharmaceutical crystallization with growth-dependent dispersion. *Organic Process Research & Development,* **2004**, *8*(4), 609-615.

[19] D. B. Patience, University of Wisconsin-Madison (Madison), **2002**.

[20] J. B. Rawlings, S. M. Miller, & W. R. Witkowski, Model identification and control of solution crystallization processes - a review. *Industrial & Engineering Chemistry Research,* **1993**, *32*(7), 1275-1296.

[21] W. R. Witkowski, S. M. Miller, & J. B. Rawlings, Light-scattering measurements to estimate kinetic-parameters of crystallization. in *Crystallization as a Separations Process, Vol. 438* (Eds.: A. S. Myerson, K. Toyokura), International Chemical Congress Pacific Basin Society, Honolulu, HI, **1990**, pp. 102-114.

[22] A. M. Neumann, H. J. M. Kramer, M. Zhemua, & B. Scarlett, On-line Measurement Techniques for Industrial Crystallization. in *Proceedings of the 14th International Symposium on Industrial Crystallization*, Institution of Chemical Engineers, Rugby, U.K., **1999**, p. 1993.

[23] M. Kitamura, & H. Endo, Growth-proess of ammonium-sulfate crystals produced by secondary nucleation in stirred-tank crystallizer. *Journal of Chemical Engineering of Japan,* **1991**, *24*(5), 593-599.

[24] R. L. Ryall, R. G. Ryall, I. R. Doyle, & V. R. Marshall, The dependence of the measurement of crystal-growth on the the state of crystal aggregation - implications for urolithiasis research. *Journal of Crystal Growth,* **1993**, *133*(1-2), 87-94.

[25] M. Kempkes, T. Vetter, & M. Mazzotti, Measurement of 3D particle size distributions by stereoscopic imaging. *Chemical Engineering Science,* **2010**, *65*(4), 1362-1373.

[26] X. Z. Wang, K. J. Roberts, & C. Ma, Crystal growth measurement using 2D and 3D imaging and the perspectives for shape control. *Chemical Engineering Science,* **2008**, *63*(5), 1173-1184.

[27] A. K. Hipp, B. Walker, M. Mazzotti, & M. Morbidelli, In-situ monitoring of batch crystallization by ultrasound spectroscopy. *Industrial & Engineering Chemistry Research,* **2000**, *39*(3), 783-789.

[28] J. S. Tebbutt, T. Marshall, & R. E. Challis, Monitoring of copper(II) sulfate pentahydrate crystallization using ultrasound. *Langmuir,* **1999**, *15*(9), 3356-3364.

[29] P. Mougin, K. Roberts, & D. Wilkinson, Monitoring the Crystallization of Urea Using Acoustic Attenuation Spectroscopy. in *Proceedings of the 14th International Symposium on Industrial Crystallization*, Institution of Chemical Engineers, Rugby, U.K., **1999**, p. 1996.

[30] W. Yu, & K. Erickson, Chord length characterization using focused beam reflectance measurement probe - methodologies and pitfalls. *Powder Technology,* **2008**, *185*(1), 24-30.

[31] J. Worlitschek, T. Hocker, & M. Mazzotti, Restoration of PSD from chord length distribution data using the method of projections onto convex sets. *Particle & Particle Systems Characterization,* **2005**, *22*(2), 81-98.

[32] Lasentec & Mettler Toledo Ltd. www.mt.com\lasentec.

[33] R. Hilfiker, *Polymorphism in the Pharmaceutical Industry*, Wiley-VCH, Weinheim, **2006**.

[34] J. Bernstein, *Polymorphism in Molecular Crystals*, Clarendon Press, Oxford University Press, New York, **2002**.

[35] R. Barrett, M. Faucon, J. Lopez, G. Cristobal, F. Destremaut, A. Dodge, P. Guillot, P. Laval, C. Masselon, & J. B. Salmon, X-ray microfocussing combined with microfluidics for on-chip X-ray scattering measurements. *Lab on a Chip,* **2006**, *6*(4), 494-499.

[36] E. D. Greaves, & A. Manz, Toward on-chip X-ray analysis. *Lab on a Chip,* **2005**, *5*(4), 382-391.

[37] P. D. I. Fletcher, S. J. Haswell, & X. L. Zhang, Monitoring of chemical reactions within microreactors using an inverted Raman microscopic spectrometer. *Electrophoresis,* **2003**, *24*(18), 3239-3245.

[38] D. Schafer, M. Muller, M. Bonn, D. W. M. Marr, J. van Maarseveen, & J. Squier, Coherent anti-Stokes Raman scattering microscopy for quantitative characterization of mixing and flow in microfluidics. *Optics Letters,* **2009**, *34*(2), 211-213.

[39] T. Araki, K. Ueno, H. Misawa, & N. Kitamura, Raman microspectroscopy/imaging study on phase-vanishing processes of fluorous biphase systems in microchannel-microheater chips. *Analytical Sciences,* **2006**, *22*(10), 1283-1289.

[40] D. H. Pan, Z. Ganim, J. E. Kim, M. A. Verhoeven, J. Lugtenburg, & R. A. Mathies, Time-resolved resonance Raman analysis of chromophore structural changes in the formation and decay of rhodopsin's BSI intermediate. *Journal of the American Chemical Society,* **2002**, *124*(17), 4857-4864.

[41] M. de Matas, H. G. M. Edwards, E. E. Lawson, L. Shields, & P. York, FT-Raman spectroscopic investigation of a pseudopolymorphic transition in caffeine hydrate. *Journal of Molecular Structure,* **1998**, *440*(1-3), 97-104.

[42] A. C. Jorgensen, I. Miroshnyk, M. Karjalainen, K. Jouppila, S. Siiria, O. Antikainen, & J. Rantanen, Multivariate data analysis as a fast tool in evaluation of solid state phenomena. *Journal of Pharmaceutical Sciences,* **2006**, *95*(4), 906-916.

[43] S. G. Kazarian, & G. G. Martirosyan, Spectroscopy of polymer/drug formulations processed with supercritical fluids: in situ ATR-IR and Raman study of impregnation of ibuprofen into PVP. *International Journal of Pharmaceutics,* **2002**, *232*(1-2), 81-90.

[44] L. E. O'Brien, P. Timmins, A. C. Williams, & P. York, Use of in situ FT-Raman spectroscopy to study the kinetics of the transformation of carbamazepine polymorphs. *Journal of Pharmaceutical and Biomedical Analysis,* **2004**, *36*(2), 335-340.

[45] H. Wikstrom, P. J. Marsac, & L. S. Taylor, In-line monitoring of hydrate formation during wet granulation using Raman spectroscopy. *Journal of Pharmaceutical Sciences,* **2005**, *94*(1), 209-219.

[46] Y. R. Hu, J. K. Liang, A. S. Myerson, & L. S. Taylor, Crystallization monitoring by Raman spectroscopy: Simultaneous measurement of desupersaturation profile and polymorphic form in flufenamic acid systems. *Industrial & Engineering Chemistry Research,* **2005**, *44*(5), 1233-1240.

[47] N. Rodriguez-Hornedo, S. J. Nehru, K. F. Seefeldt, Y. Pagan-Torres, & C. J. Falkiewicz, Reaction crystallization of pharmaceutical molecular complexes. *Molecular Pharmaceutics,* **2006**, *3*(3), 362-367.

[48] R. L. McCreery, *Raman Spectroscopy for Chemical Analysis, Vol. 157*, John Wiley & Sons, Inc., New York, **2000**.

[49] I. Gregora, Raman scattering. in *International Tables for Crystallography: Physical properties of crystals, Vol. D* (Ed.: A. Authier), Kluwer Academic Publishers, Norwell, **2003**.

[50] S. N. Black, & R. J. Davey, Crystallization of amino-acids. *Journal of Crystal Growth,* **1988**, *90*(1-3), 136-144.

[51] L. Yu, & K. Ng, Glycine crystallization during spray drying: The pH effect on salt and polymorphic forms. *Journal of Pharmaceutical Sciences,* **2002**, *91*(11), 2367-2375.

[52] G. Albrecht, The crystal structure of glycine. *Journal of the American Chemical Society,* **1939**, *61*(5), 1087-1103.

[53] E. Fischer, Synthese von Polypeptiden. *Berichte der Deutschen Chemischen Gesellschaft,* **1905**, *38*(3), 2914-2925.

[54] Y. Iitaka, New form of glycine. *Proceedings of the Japan Academy,* **1954**, *30*, 109-120.

[55] R. E. Marsh, A refinement of the crystal structure of glycine. *Acta Crystallographica,* **1958**, *11*(9), 654-663.

[56] E. V. Boldyreva, V. A. Drebushchak, T. N. Drebushchak, I. E. Paukov, Y. A. Kovalevskaya, & E. S. Shutova, Polymorphism of glycine - Thermodynamic aspects. Part I. Relative stability of the polymorphs. *Journal of Thermal Analysis and Calorimetry,* **2003**, *73*(2), 409-418.

[57] G. L. Perlovich, L. K. Hansen, & A. Bauer-Brandl, The polymorphism of glycine - Thermochemical and structural aspects. *Journal of Thermal Analysis and Calorimetry,* **2001**, *66*(3), 699-715.

[58] Z. Berkovitchyellin, Toward an Abinitio Derivation of Crystal Morphology. *Journal of the American Chemical Society,* **1985**, *107*(26), 8239-8253.

[59] M. Lahav, & L. Leiserowitz, The effect of solvent on crystal growth and morphology. *Chemical Engineering Science,* **2001**, *56*(7), 2245-2253.

[60] Y. C. Zhang, J. P. Sizemore, & M. F. Doherty, Shape evolution of 3-dimensional faceted crystals. *Aiche Journal,* **2006**, *52*(5), 1906-1915.

[61] Y. Iitaka, The crystal structure of beta-glycine. *Acta Crystallographica,* **1960**, *13*, 35-45.

[62] I. Weissbuch, V. Y. Torbeev, L. Leiserowitz, & M. Lahav, Solvent effect on crystal polymorphism: Why addition of methanol or ethanol to aqueous solutions induces the precipitation of the least stable beta form of glycine. *Angewandte Chemie-International Edition,* **2005**, *44*(21), 3226-3229.

[63] Y. Iitaka, The crystal structure of gamma-glycine. *Acta Crystallographica,* **1958**, *11*, 225-226.

[64] Y. Iitaka, The crystal structure of gamma-glycine. *Acta Crystallographica,* **1961**, *14*, 1-10.

[65] L. J. W. Shimon, F. C. Wireko, J. Wolf, I. Weissbuch, L. Addadi, Z. Berkovitchyellin, M. Lahav, & L. Leiserowitz, Assignment of Absolute Structure of Polar Crystals Using Tailor-Made Additives - Solvent-Surface Interactions on the Polar Crystals of Alpha-Resorcinol, (R,S) Alanine and Gamma-Glycine. *Molecular Crystals and Liquid Crystals,* **1986**, *137*(1-4), 67-86.

[66] A. Dawson, D. R. Allan, S. A. Belmonte, S. J. Clark, W. I. F. David, P. A. McGregor, S. Parsons, C. R. Pulham, & L. Sawyer, Effect of high pressure on the crystal structures of polymorphs of glycine. *Crystal Growth & Design,* **2005**, *5*(4), 1415-1427.

[67] T. Togkalidou, R. D. Braatz, B. K. Johnson, O. Davidson, & A. Andrews, Experimental design and inferential modeling in pharmaceutical crystallization. *Aiche Journal,* **2001**, *47*(1), 160-168.

[68] T. N. Drebushchak, E. V. Boldyreva, Y. V. Seryotkin, & E. S. Shutova, Crystal structure study of the metastable beta-modification of glycine and its transformation into the alpha-modification. *Journal of Structural Chemistry,* **2002**, *43*(5), 835-842.

[69] V. A. Drebushchak, E. V. Boldyreva, T. N. Drebushchak, & E. S. Shutova, Synthesis and calorimetric investigation of unstable beta-glycine. *Journal of Crystal Growth,* **2002**, *241*(1-2), 266-268.

[70] K. Tanabe, & J. Hiraishi, Spectral Database for Organic Compounds. *Vol. 2010*, National Institute of Advanced Industrial Science and Technology, Japan, Japan.

[71] S. A. Khan, & K. F. Jensen, Microfluidic synthesis of titania shells on colloidal silica. *Advanced Materials,* **2007**, *19*(18), 2556-2560.

[72] S. D. Senturia, *Microsystem Design*, Kluwer Academic Publishers, Norwell, **2001**.

[73] J. N. Tilton, Fluid and particle dynamics. in *Perry's Chemical Engineers' Handbook*, 8th ed. (Ed.: R. H. G. Perry, D. W.), McGraw-Hill, New York, **2007**, pp. 1-56.

[74] Y. N. Xia, & G. M. Whitesides, Soft lithography. *Annual Review of Materials Science,* **1998**, *28*, 153-184.

[75] A. Bouchard, G. W. Hofland, & G. J. Witkamp, Solubility of glycine polymorphs and recrystallization of beta-glycine. *Journal of Chemical and Engineering Data,* **2007**, *52*(5), 1626-1629.

[76] J. Toth, A. Kardos-Fodor, & S. Halasz-Peterfi, The formation of fine particles by salting-out precipitation. *Chemical Engineering and Processing,* **2005**, *44*(2), 193-200.

[77] K. Park, J. M. B. Evans, & A. S. Myerson, Determination of solubility of polymorphs using differential scanning calorimetry. *Crystal Growth & Design,* **2003**, *3*(6), 991-995.

[78] C. J. Orella, & D. J. Kirwan, Correlation of Amino-Acid Solubilities in Aqueous Aliphatic Alcohol-Solutions. *Industrial & Engineering Chemistry Research,* **1991**, *30*(5), 1040-1045.

[79] E. S. Ferrari, R. J. Davey, W. I. Cross, A. L. Gillon, & C. S. Towler, Crystallization in polymorphic systems: The solution-mediated transformation beta to alpha glycine. *Crystal Growth & Design,* **2003**, *3*(1), 53-60.

[80] L. J. W. Shimon, M. Vaida, L. Addadi, M. Lahav, & L. Leiserowitz, Molecular Recognition at the Solid-Solution Interface - a Relay Mechanism for the Effect of Solvent on Crystal-Growth and Dissolution. *Journal of the American Chemical Society,* **1990**, *112*(17), 6215-6220.

[81] B. A. Garetz, J. Matic, & A. S. Myerson, Polarization switching of crystal structure in the nonphotochemical light-induced nucleation of supersaturated aqueous glycine solutions. *Physical Review Letters,* **2002**, *89*(17), 175501-175504.

[82] D. Gidalevitz, R. Feidenhansl, S. Matlis, D. M. Smilgies, M. J. Christensen, & L. Leiserowitz, Monitoring in situ growth and dissolution of molecular crystals: Towards determination of the growth units. *Angewandte Chemie-International Edition in English,* **1997**, *36*(9), 955-959.

[83] C. S. Towler, R. J. Davey, R. W. Lancaster, & C. J. Price, Impact of molecular speciation on crystal nucleation in polymorphic systems: The conundrum of gamma glycine and molecular 'self poisoning'. *Journal of the American Chemical Society,* **2004**, *126*(41), 13347-13353.

[84] L. P. Dang, H. Y. Yang, S. Black, & H. Y. Wei, The Effect of Temperature and Solvent Composition on Transformation of beta- to alpha-Glycine As Monitored in Situ by FBRM and PVM. *Organic Process Research & Development,* **2009**, *13*(6), 1301-1306.

[85] L. Li, & N. Rodriquez-Hornedo, Growth kinetics and mechanim of glycine crystals. *Journal of Crystal Growth,* **1992**, *121*, 33-38.

[86] B. N. Moolya, A. Jayarama, M. R. Sureshkumar, & S. M. Dharmaprakash, Hydrogen bonded nonlinear optical gamma-glycine: Crystal growth and characterization. *Journal of Crystal Growth,* **2005**, *280*(3-4), 581-586.

[87] A. Mersmann, A. Eble, & C. Heyer, Crystal Growth. in *Crystallizaiton Technology Handbook*, 2nd ed. (Ed.: A. Mersmann), Marcel Dekker, Inc., New York, **2001**, pp. 81-143.

[88] P. Selvarajan, J. G. A. Raj, & S. Perumal, Characterization of pure and urea-doped gamma-glycine single crystals grown by solution method. *Journal of Crystal Growth,* **2009**, *311*(15), 3835-3840.

[89] G. W. He, V. Bhamidi, R. B. H. Tan, P. J. A. Kenis, & C. F. Zukoski, Determination of critical supersaturation from microdroplet evaporation experiments. *Crystal Growth & Design,* **2006**, *6*(5), 1175-1180.

[90] H. Reiss, The growth of uniform colloidal dispersions. *Journal of Chemical Physics,* **1951**, *19*(4), 482-487.

[91] J. W. Mullin, *Crystallization*, Butterworth-Heinemann, Oxford, **2001**.

[92] S. H. Fogler, *Elements of Chemical Reaction Engineering*, 3rd ed., Prentice-Hall, Inc., Englewood Cliffs, N.J., **1999**.

[93] I. Weissbuch, L. Addadi, Z. Berkovitchyellin, E. Gati, S. Weinstein, M. Lahav, & L. Leiserowitz, Centrosymmetric Crystals for the Direct Assignment of the Absolute-Configuration of Chiral Molecules - Application to the Alpha-Amino-Acids by Their Effect on Glycine Crystals. *Journal of the American Chemical Society,* **1983**, *105*(22), 6615-6621.

[94] I. Weissbuch, L. Addadi, M. Lahav, & L. Leiserowitz, Molecular Recognition at Crystal Interfaces. *Science,* **1991**, *253*(5020), 637-645.

[95] I. Weissbuch, L. Leiserowiu, & M. Lahav, Direct assignment of the absolute configuration of molecules from crystal morphology. *Chirality,* **2008**, *20*(5), 736-748.

[96] I. Weissbuch, R. Popovitzbiro, M. Lahav, & L. Leiserowitz, Understanding and control of nucleation, growth, habit, dissolution and structure of 2-dimensional and 3-dimensional crystals using tailor-made auxiliaries. *Acta Crystallographica Section B-Structural Science,* **1995**, *51*(2), 115-148.

[97] A. Y. Lee, I. S. Lee, & A. S. Myerson, Factors affecting the polymorphic outcome of glycine crystals constrained on patterned substrates. *Chemical Engineering & Technology,* **2006**, *29*(2), 281-285.

[98] M. N. Bhat, & S. M. Dharmaprakash, Effect of solvents on the growth morphology and physical characteristics of nonlinear optical gamma-glycine crystals. *Journal of Crystal Growth,* **2002**, *242*(1-2), 245-252.

[99] K. Machida, A. Kagayama, Y. Saito, Y. Kuroda, & T. Uno, Vibrational-spectra and intermolecular potential of alpha-form crystal of glycine. *Spectrochimica Acta Part a-Molecular and Biomolecular Spectroscopy,* **1977**, *33*(5), 569-574.

[100] H. Stenback, Raman-spectra of solid natural alpha-glycine and solid N-15-substituted alpha-glycine. *Journal of Raman Spectroscopy,* **1976**, *5*(1), 49-55.

4 Microfluidic Devices for Crystal Habit Modification

One of the advantages of continuous microfluidic devices is the high spatiotemporal resolution that can be achieved. The transposition of the reaction time onto spatial coordinates have enabled the detection of microsecond[1] to millisecond[2] reaction events, and even nanosecond structural changes.[3] This advantage can be exploited in applications related to crystallization, particularly for looking into the habit evolution of organic crystals in the presence of impurities or additives.

Crystallization is a complex process, and is influenced by many parameters, including solvent, supersaturation, temperature, and impurities. Impurities can selectively interact with and become incorporated into particular crystal facets. This idea is readily exploited in doping of organic materials for electronic use.[4] Inducing particular crystal morphology using dopants or impurities is also a widespread technological tool. For example, a small amount of ion, such as Pb^{2+}or SO_4^{2-} have been used for a long time in the industrial production of large NaCl single crystals for spectroscopy applications.[5] Moreover, the sugar technologists have recognized the important role oligosaccharides play in determining the habit of sucrose crystals.[6]

Habit modification is also an important concept in the pharmaceutical and fine chemical industry. The habit of a crystal may strongly influence the product properties relevant to downstream processes, such as filtration, centrifugation, formulation, and compaction.[7] The natural crystal habit may be an undesired one, in which case, impurities can be used to induce a habit with more desirable properties. The byproducts of a process or other impurities may modify a natural habit with desirable properties to an undesirable habit.[8-10] Hence, understanding the mechanism of habit modification by impurities can greatly facilitate crystal habit engineering either by deliberately adding impurities or by detecting and addressing them.

In addition to crystal habit modification, designer additives have also been used to stabilize metastable polymorphs,[11] to control the polymorphic form,[12, 13] to control

solvent mediated phase transformation,[14] to amplify a particular chiral form of conglomerates,[15] and to control dissolution rates.[16] However, it is acknowledged that not enough efforts have been focused in understanding the mechanism of crystal habit modification by impurities.[5]

Hence, the goal of this chapter is to exploit the advantages of microfluidic devices for impurity screening, and for obtaining fundamental information on crystal habit modification process. In this chapter, we use a continuous microfluidic device and seeded crystallization to study the effects of impurities on crystal habits. We use alpha glycine as the model system and other alpha amino acids as impurities. We take advantage of the high spatiotemporal resolution of microfluidic devices to look into the evolution of different crystal facets, which ultimately yields the final modified habit, over time, and obtain information on the kinetics of habit modification in the presence of different impurities. Finally, we develop an understanding of the mechanism of crystal habit modification of alpha glycine. Such information may not only provide insights into impurity-crystal interactions, but also serve as a powerful tool for the design of impurities that can be deliberately added to the solution to improve the crystallization process.

4.1 Introduction

4.1.1 Effects of Impurities on Crystal Growth

Crystallization is a supramolecular process, in which an ensemble of random molecules in solution come together to form an ordered three dimensional structure. Naturally, crystal growth is a process that occurs specifically with the solute molecules, and hence, usually rejects the impurities and solvents from the growing facets. As a result, relatively high purity solid materials can be produced through crystallization with very little amount of impurities.[17] However, some impurities can interact with or adsorb onto the growing crystal surfaces through a process called "molecular trickery," influencing the attributes of final crystal products. Impurities can significantly influence both the nucleation and growth of crystals.[12, 18, 19] In this chapter, we focus on the effects of impurities on only the crystal growth process.

The shape or habit of a crystal is determined by the relative growth rates of the individual facets. As different functional group can be present at the different faces, impurities can selectively interact with specific functional groups, or adsorb on to particular faces, retarding their growth, and thereby, can modify the crystal habit. A two-dimensional schematic is presented in Figure 4-1 that illustrates the evolution of crystal habit due to impurities adsorbing selectively on "A" faces. Consequently, the "B" faces grow out, changing the crystal habit.[5] Impurities, of as small a concentration as parts per million, may have significant effects on crystal growth by sitting at and thus, poisoning the kink sites, the location where the solute molecules become incorporated with the lattice in order for crystal growth to occur. Once incorporated into the growing crystal face, the impurities hinder the attachment of incoming solute molecules to the crystal surface.

The impurities that have a structure similar to that of the crystallizing solute are known as tailor-made additives. These additives consist of two moieties, a binder that have a similar structure as the primary solute, and a perturber that is different from the primary solute. A stereochemical relationship between the crystal structure and the molecular structure of additives has been established by investigating a number of host-guest molecular crystal systems.[15, 20] When structurally similar guest molecules are added to the crystallizing solution, they can be recognized at specific faces of the growing crystal because of moieties that are identical to the host molecule. The additives then bind to those faces, and subsequently impede their growth in a stereospecific manner, without or slightly affecting the growth of other faces.

The impurities that are usually utilized for habit modification, have been called with many different terms in the literature, including "impurity", "additive", "auxiliary molecule," "imposter", and "tailor made additive". In this study, we use these terms interchangeably.

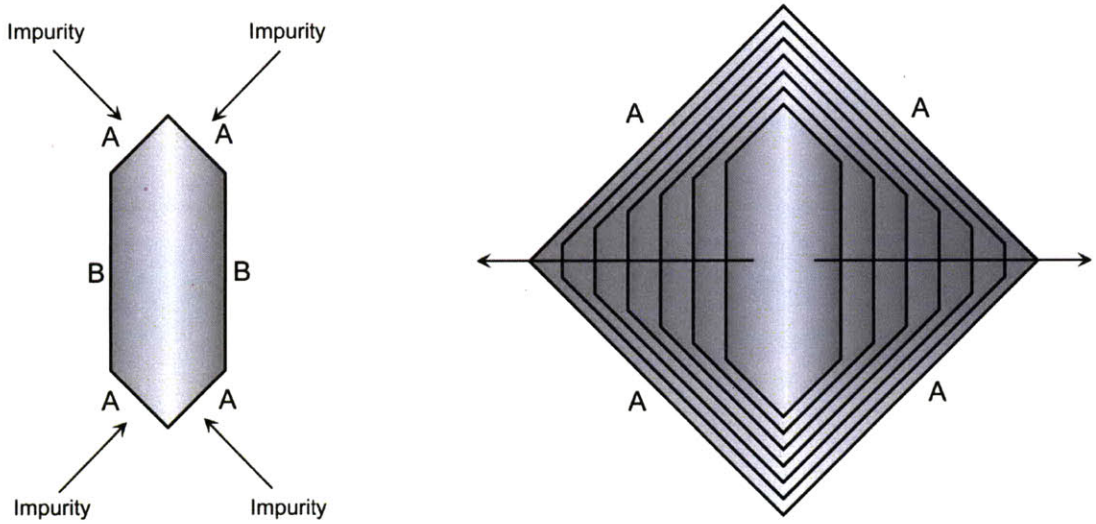

Figure 4-1. Effects of impurities on crystal habit. Impurities selectively adsorb on "A" faces, slowing their growth. The unhindered "B" faces grow out as a result, and change the crystal habit.

4.1.2 Habit Modification Led by Molecular Recognition

Previous studies have used a structural approach to look into the habit modification of organic crystals with tailor-made additives. Black et al. have demonstrated that while (*S*)-asparagine monohydrate crystallizes into a prismatic morphology, dominated by {012} faces and with *a* as the preferred growth direction, in pure aqueous solution, addition of a small amount of (*S*)-glutamic acid changes the habit to one dominated by {101} and with *b* as the preferred growth direction. The habit modification is rationalized with a stereoselective docking mechanism, in which a glutamic acid molecule adsorbs on a site in (101) face, causing disruption in the hydrogen bonding along the *a* axis.[21]

Davey et al. have shown the habit modification of adipic acid. It usually crystallizes into a plate-like habit, with dominant (100) face bound by (001), (102), and (011), in pure aqueous solution. However, the presence of n-alkanoic monocarboxylic acids, such as caproic acid, the growth rates of (011) and (001) faces are inhibited. Davey et al. have proposed that a monocarboxylic acid, with a structure similar to adipic acid, can utilize its carboxylate functionality and linear conformation to occupy a growth site on (001) face.

This subsequently can block the growth site with a methyl group exposed in place of the expected carboxylic acid, hindering expected interaction with the incoming adipic acid molecules, and thus, hindering the growth of (001).[22] Davey et al. have also illustrated habit modification of urea crystals from needles to much smaller blocks in the presence of biuret, a dimer of urea that forms during urea production. The influence of impurity is explained by the replacement of two urea molecules in the crystal lattice by a biuret molecule, which disrupts the hydrogen bonding along the *c*-axis, the direction of fastest growth in pure solution.[23]

Berkovitchyellin and coworkers have presented an interesting case of benzamide habit modification by selectively retarding the growth along *b*, *a* and *c* directions with the additions of benzoic acid, *o*- and *p*-toluamide, respectively. They have argued that benzoic acid molecules can bind to the benzamide lattice due to a synplanar conformation (O=C–OH), and hinder hydrogen bonding along the *b*-axis. This essentially impedes the growth along *b*-axis, and forms needles with the longer dimension along *a*-axis. *O*-toluamide, on the other hand, can adsorb to the lattice, without disrupting the hydrogen bonding chain along the *b*-direction, but instead the emergence of *o*-methyl group from the (10-4) impedes the growth along the *a*-direction. The adsorption of p-toluamide changes the crystal habit yet again. The p-methyl group perturbs the weak Van der Waals interactions between the phenyl layers along the *c*-direction, and produces thinner plates.[24, 25]

Habit modification has also been demonstrated for paracetamol crystals by using structurally related additives. Hendriksen et al. have shown that *p*-acetoxyanilide (an ester with a larger group), in the p-position instead of the –OH in paracetamol, and no proton donor to contribute to the hydrogen bonding network, can easily result in growth inhibition. Acetanilide can also result in growth inhibition due to the lack of proton donor.[26] Also, Koolman and Rousseau have shown that the habit of (*S*)-isoleucine can be modified from needlelike to hexagonal blade crystals using (*S*)-leucine as the additive, due to the similarity in structures.[27]

In all of the above examples, molecular recognition of additives at the growing crystal surfaces has been used to explain growth impedance at specific crystal facets that ultimately leads to habit modification.

4.1.3 Model System: Alpha Glycine

Amino acids serve as interesting set of model systems because of their common functionality at one end, $NH_3^+CHCOO^-$, which may act as the binder, coupled with side chains with a variety of functionalities at the other end, which may act as the perturber. In this study, we use α-glycine as the model system because of the simplicity of the molecule and the symmetric habit.

Glycine packs in its crystalline alpha form in a centrosymmetric space group $P2_1/n$.[28] Zwitterionic glycine molecules form centrosymmetric dimers through N–H···O hydrogen bonds, and chains of these dimers are formed along the c-axis with an additional N–H···O hydrogen bond. The dimer chains form bilayer sheets through hydrogen bonding with a second dimer chain. The bilayer sheets are held together along the b-axis by Van der Waals interactions. The packing arrangement of α-glycine perpendicular to the *a*-axis is presented in Figure 4-2. The structure results in a centrosymmetric bipyramidal habit in aqueous solution, delineated by {010} facets along the *b*-axis and {011} facets along the *c*-axis.

The crystal structure of α-glycine has a number of symmetry relations between the molecules in the *bc* plane. There are four different types of crystallographic sites, as numbered from 1 to 4 in Figure 4-2. The glycine molecules in a dimer, as at sites 1 and 2 or at 3 and 4, are related by a center of inversion symmetry. The molecules at alternate layers, on the other hand, as at site 1 and 3 or at 2 and 4, are related by 2-fold screw symmetry. In addition, one of the two C-H bonds, the C2-H4 bond in the individual glycine molecule shown in Figure 4-2, is parallel to the *b*-axis, while the other C-H bond, C2-H5, is placed almost in the *ac* plane. Molecules at site 1 and 3 are oriented such that their methyl group (C2-H4), labeled as $C\text{-}H_{Me}$ in Figure 4-2, points in the $+b$ direction, and hence, emerges from the (010) face. On the other hand, molecules at site 2 and 4 are oriented such that their methyl group, C2-H4, labeled as $C\text{-}H_{Si}$ points in the $-b$ direction, emerges from the (0-10) face.[29] Though glycine is a nonchiral molecule, substituting the methyl group under discussion (C2-H4) with a different side group, yields a chiral molecule. This characteristic makes α-glycine a prochiral molecule, and the two methyl groups (C2-H4) on (010) and (0-10) faces can be considered as pro-(*R*) and pro-(*S*)

configurations. Therefore, the *b*-axis of α-glycine is enantiopolar, and {010} the facets are enantiotopic.[30]

α-glycine has provided a classic example for studying the impact of structurally related impurities on the crystal growth process.[12, 20, 29, 31, 32] α-glycine usually crystallizes in a centrosymmetric bipyramidal habit, as shown in Figure 4-3, with a slight elongation along the *c*-axis, representing the direction of faster growth. The extent of elongation, however, depends on the supersaturation trajectory during the growth process. In contrast, Weissbuch et al. have shown that the presence of other α-amino acids strongly influence the habit of α-glycine crystal. They have demonstrated that the addition of chirally resolved amino acids, such as *R*- and *S*-amino acids, results in chiral pyramids, while the addition of racemic (*R,S*)-amino acids results in plate-like habits.[31]

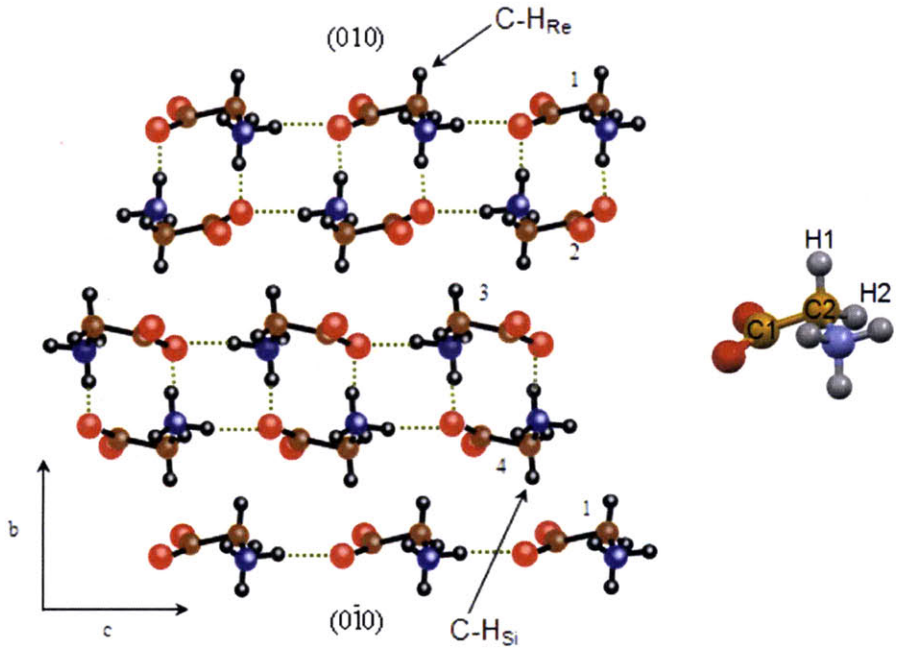

Figure 4-2. Packing arrangement of alpha glycine perpendicular to the *a*-axis. The molecules at site 1 and 3 are oriented so as to point their methyl group, C-H_{Re} toward the + *b*-direction, and molecules at sites 2 and 4 are oriented so as to point their methyl group, C-H_{Si}, toward the -*b* direction.

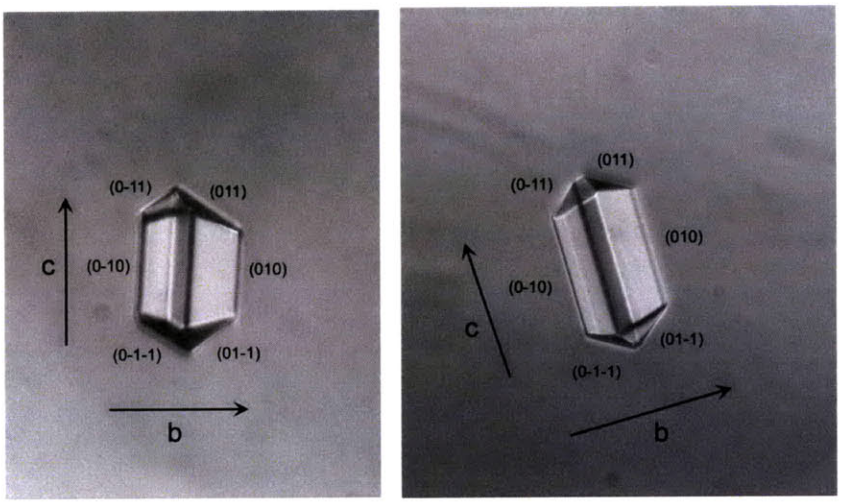

Figure 4-3. Alpha glycine crystals grown from pure aqueous solution. The centrosymmetric, bipyramidal habit is usually elongated along the *c*-axis, representing higher growth rate.

4.1.4 Batch Approaches of Habit Modification

Crystallization is traditionally performed in batch reactors. Most of the crystal habit modification studies have also been demonstrated in batch reactors using cooling crystallization. Typical habit modification involves the following steps. The primary solute and the desired amount of impurities are dissolved in a solvent by heating. The hot solution is then cooled to a lower temperature in order to induce crystallization. In this way, both nucleation and growth occur in the presence of impurities. Thus, additives can hinder growth of the stereoselective faces at a very early stage of the nuclei/crystallite. Consequently, the modification of habit is nearly complete by the time the crystals reach a detectable size. Figure 4-4 illustrates how habit modification is usually performed in batch reactors. This method treats habit modification process almost as a black box, and does not allow one to obtain information on the kinetics of habit modification. In addition, many impurities may influence the nucleation, as well as the growth process. For example, Towler et al. have proposed a mechanism for charged ions or molecules to interact with alpha glycine faces, affecting both its nucleation, as well as growth.[33] The mechanism is consistent with experimental observation.[30, 34] The black-box type of

treatment of the crystallization process in the presence of additives may fail to decouple the effects of impurities on the two steps of crystallization: nucleation and growth.

In contrast to the batch reactors, continuous microfluidic devices offer high spatiotemporal resolution, which can be exploited to study the kinetics of habit modification. Information on the kinetics of habit modification can provide insights into the mechanism of the process, as well as on the effectiveness of different impurities in modifying a particular crystal habit. Thus, this tool may also be useful in screening impurities. In addition, continuous seeded crystallization can be used in these devices to decouple the effects of impurities on the growth process from nucleation.

In this study, we apply the continuous microfluidic platform we developed in Chapter 3 for seeded crystallization to habit modification studies, and demonstrate some of the advantages discussed in the previous section.

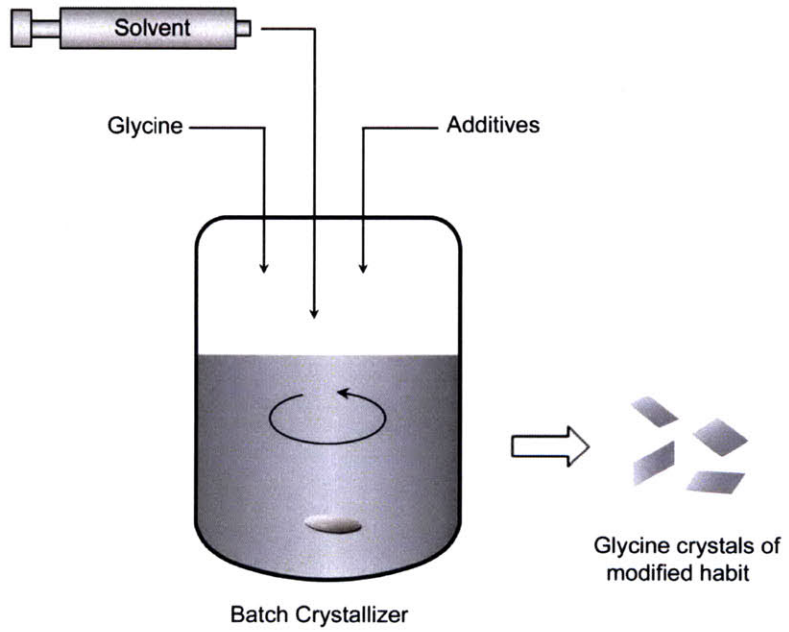

Figure 4-4. Schematic of crystal habit modification in batch reactors. The primary solute, additive and solvent are added to the reactor, heated to dissolve the solids, and then cooled down to a lower temperature to induce crystallization. The habit modification process is usually complete by the time crystals are collected.

4.2 Microfluidic reactors

4.2.1 Device Design

The solubility of α-glycine in the presence of additives, as well as the solubility of additives themselves, was taken into consideration when designing the microfluidic device for habit modification studies. It has been shown that the solubility of glycine is not affected much by the presence of small amount of amino acid additives.[34, 35] We also performed quick experiments to estimate the solubility of glycine at the operating conditions in the presence of 0.5-2% additives, and did not find a detectable difference. Hence, we used the pure glycine solubility from the literature[36-39] to calculate the supersaturation and to design the experiments.

We use a microfluidic for continuous seeded crystallization, developed in the last chapter. We use three inlets, the first one for introducing seeds into the reactor, the second one for introducing crystallizing solution, along with impurities, and the third one for introducing antisolvent. We mix the solution and antisolvent to create a supersaturated glycine solution that contains the desired concentration of additives. The supersaturation is controlled through the flow rates, and the composition of each stream is such that it always remains in the metastable zone. We then introduce the supersaturated solution into the main channel where seeds grow in the presence of impurities. Figure 4-5 illustrates the device design.

One of the difficulties of using antisolvent to generate supersaturation in the presence of additives is the similar structure of "tailor-made" additives that often results in similar solubility behavior as the primary solute in solvent-antisolvent system. This means that the additives may crystallize themselves with the addition of antisolvent, if the device is not operated below the metastable limit of the additives at all times. The solubility of (*S*)-glutamic acid in water-ethanol mixtures was taken from the literature.[40] The solubility of (*R,S*)-methionine in pure water and ethanol was also taken from the literature,[41] and extrapolated for ensuring that the device is operated below the solubility limits of the additives at all times.

Additions of additives in small aliquots enabled by the multiple side inlets of the presented crystallizer can maintain a steady additive concentration over time without

having to add a large amount at once which may crystallize or precipitate out the additive itself. Here we design microfluidic devices with two side channels for addition. The depth of all the channels in the device was approximately 250 μm. The width growth channel was 300 μm, and the length was varied from 0.5 m to 0.75 m. The width and length of the mixing channel were 40 μm and 70 mm, respectively. The length of the mixing channel was designed to ensure complete mixing between the solution and the antisolvent before being split into multiple addition channels. The desired flow distribution ratio between the addition channels is achieved precisely by controlling the pressure drop in each of the side channels. Using Hagen-Poiseulle equation to calculate the pressure drops, and mass balance at each intersection, a set of linear equations is achieved for the flow rates at each channel and pressure at each junction. The linear set of equations is then simultaneously solved using MATLAB. The details of generating the relevant set of linear equations, and solving them are presented in Chapter 3. The flow rates are subsequently used to calculate the supersaturation of both the solute, as well as the impurity. The final channel dimensions are calculated in an iterative process to ensure supersaturation with respect to glycine and undersaturation with respect to the additive.

One of the difficulties with seeded crystallization is that seeds of high density polymorphic forms, such as α-glycine, may settle over a long period of time, resulting in an inconsistent density of seeds fed to the reactor. We used pressure-driven flow to deliver α-glycine seeds into the device, which allowed us to continuously stir the seed solution over the duration of experiments, and thus, to flow a consistent density of seeds. We use a routine in Labview in order to control the seed flow rate. The details of the pressure-driven flow setup are discussed in Chapter 3.

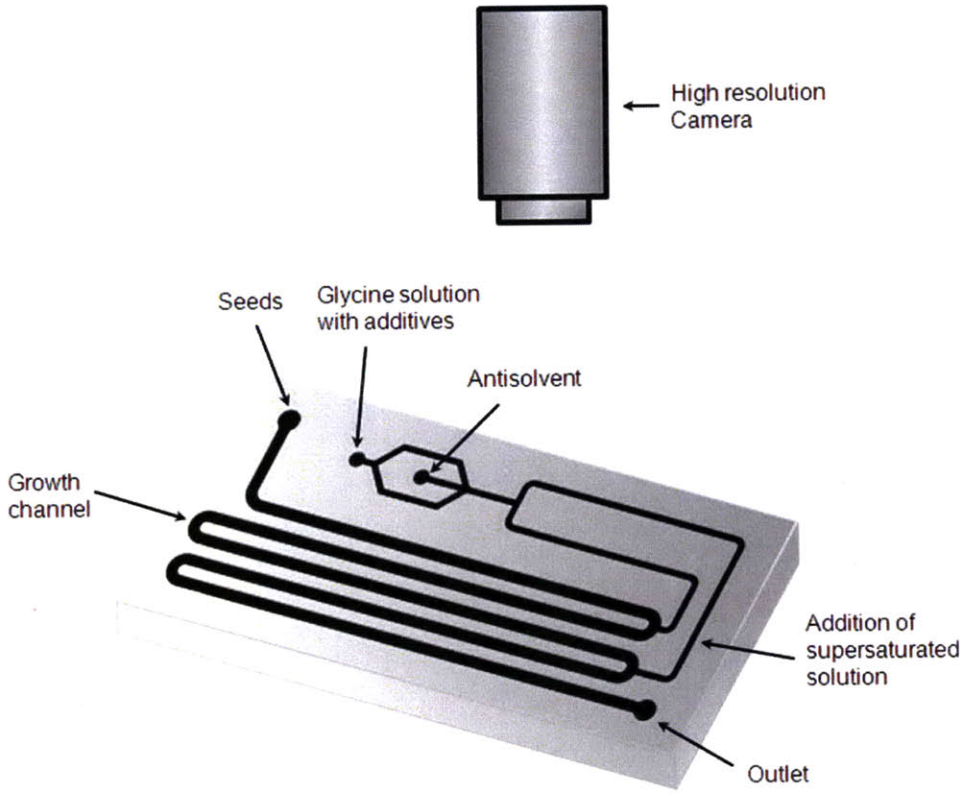

Figure 4-5. Experimental setup used. The reactor has three inlets: one for providing seeds, one for undersaturated glycine solution with impurities, and one for the antisolvent. Supersaturation is generated by the addition of antisolvent to the solution, which then is added to the seeds in the growth channel. The depth of all the channels is ~250 μm. The width of the growth channel and the mixing channel is 300 μm and 40 μm, respectively.

4.2.2 Microfabrication and Packaging

Microfluidic devices are fabricated in PDMS by using standard soft lithographic techniques.[42] PDMS was chosen as the device material because realizing complicated reactor designs in PDMS is fast, easy and inexpensive. Also, the transparency of PDMS provides an opportunity to use microscopy tools to obtain high resolution images of the crystals. SU-8 (Microchem Corporation, MA), a negative resist, was used to make master devices that were used for molding. Two layers of approximately 125 μm thick SU-8 films were spun on 100 mm diameter silicon wafers (Silicon Quest International). Standard photolithography techniques were used to pattern negative images of the microfluidic device on SU-8. Finally, the wafers were developed using SU-8 Developer

(Microchem Corporation). PDMS (Dow Corning Sylgard Brand 184 Silicone Elastomer, Essex-Brownell Inc.) was molded on the SU-8 masters in the following way. PDMS was prepared by mixing Sylgard 184 and its activator (Dow Corning) in a 10 to 1 weight ratio. The mixture was degassed, casted onto the master wafer and was cured at 80°C for 2 hours. After reticulation, the devices were peeled off the mold, cut, and inlets and outlets were punched with a 5/64" leather punch. Each device was cleaned, surface was activated with a Harrick PDC-32G oxygen plasma chamber for 35 seconds, and finally, was covalently bonded to a surface modified glass slide. Pre-cleaned glass slides (75 x 50 mm, 1 mm thick, Corning Glass Works), were spin-coated with PDMS (~100 μm) and were cured at 80 °C for 30 minutes. PEEK tubing (IDEX Health & Science) was inserted in the inlets and was glued in place with 5-min epoxy (Devcon). The epoxy was cured at 70 °C for 12 hours or at room temperature overnight.

4.3 Experimental

In this study, we use α-amino acid derivatives of glycine as the additives. (*S*)-glutamic acid and (*R,S*)-methionine are chosen as tailor-made additives because of their higher solubility, compared to some of the other amino acids, in water-ethanol mixtures. (*R,S*)-methionine (purity>99.95%, Sigma Aldrich), (*S*)-glutamic acid (Sigma Aldrich), Glycine (purity>99%, Sigma Aldrich), ethanol (anhydrous, Sigma Aldrich), and spectroscopy grade water (VWR) were used as obtained without any further purification.

4.3.1 Seed Preparation

Seeds of α-glycine were carefully prepared with desirable characteristics. X-ray diffraction showed that the commercial glycine purchased was usually a mixture of alpha and gamma crystals, with varied percentages of each in different batches. It is important to use pure polymorphic forms as seeds because a mixture of multiple forms can induce polymorphic transition, resulting in an unstable solution. Seeds were prepared by dissolving commercial glycine in water (0.3g gly/g water) at 50°C. The solution was filtered with a hot 0.2 μm filter, and was brought to room temperature while stirring. As soon as nucleation was detected, equal volume of saturated glycine solution (with respect to the alpha form) was added to dilute out the seeds and to prevent agglomeration. One

fourth volume of a slightly supersaturated solution was added to the seed solution in order to mature and produce well-developed faces. The polymorphism of the obtained seeds was confirmed with X-ray diffraction, and the seed size obtained was characterized using optical microscopy to be 10-15 μm.

4.3.2 Habit Modification in Batch Reactors

Habit modification in batch reactors was carried out using cooling crystallization. Typically, glycine was dissolved in water (0.3g gly/g water) at 60°C. Then, either (*S*)-glutamic acid, or (*R,S*) methionine, in the amount of 0.5 or 1.0 weight% of glycine, respectively, was added to the glycine solution. The solution was kept at 60°C for at least three hours. A preheated 0.2 μm filter was used to filter the solution and transfer it to a pre-cleaned glass vial (20 mL, borosilicate, VWR Scientific). The solution was then cooled down to room temperature with natural convection. A magnetic stir bar (PTFE, VWR Scientific) was used to continuously agitate the solution. The polymorphic form was confirmed to be alpha glycine with X-ray diffraction. Optical microscopy was used to characterize the crystal habit. A few drop of solution was transferred to a glass bottom culture dish (Mat Tek Corp., MA) with a pipette, and was covered immediately with a lid to prevent solvent evaporation. The culture dish was put on the microscope stage directly for analysis.

4.3.3 Habit Modification in Microfluidic Devices

In this part of the study, we introduced dilute and well developed seeds of bipyramidal α-glycine with visible faces into the microcrystallizer. Supersaturated solution, adulterated with tailor-made additives, was flown from the side channels, as shown in Figure 4-5, to the main channel, where crystal growth took place. (*S*)-glutamic acid and (*R,S*)-methionine were used as additives, and were added to the supersaturated solution so as to yield ~0.5-2 weight% additive with respective to glycine molecules in solution. The seed solution was delivered to the reactor with pressure-driven flow at a flow rate of 2-10 $\mu l \cdot min^{-1}$. The supersaturation was generated by adding an antisolvent with an adulterated undersaturated glycine solution at flow rates between 2-10 $\mu l \cdot min^{-1}$. Approximately 70-90% ethanol in water was used as the antisolvent. Adulterated glycine solution was made

with 0.0822 g glycine/g of water and 0.03 – 0.08g additive/g of water. This concentration of additive typically achieved 0.5-1.5 weight% of additive with respect to the amount of glycine available in solution in the main channel (this excludes the glycine in the solid form). The antisolvent and glycine solution, adulterated with additives, were loaded in separate syringes (GasTight, Hamilton), and were delivered to the microchannels with Harvard syringe pumps. The residence time of the reactor varied from 2 to 8 minutes. The side channels were designed to yield different distribution of flow rates among them. The flow rate ratios among the side inlets varied from 1 to 3 for different reactors, in order to achieve different supersaturation and additive concentration in the main channel.

As a demonstration, the calculations are made for a typical set of flow rates of 5, 5 and 6 $\mu l \cdot min^{-1}$ for seed solution, antisolvent with 90% aqueous ethanol, and 40% saturated aqueous glycine, respectively. Additives are added to the undersaturated solution at an amount of 0.036 and 0.073 g/g glycine for (*S*)-glutamic acid and (*R,S*)-methionine, respectively. For a device with 1:2 volume distribution among the first and second side channels, the additive amount, the additive weight percent in the main channel with respect to available glycine molecules in the solution, and the resulting superstation ratio are calculated and presented in Table 4-1 and Table 4-2 for (*S*)-glutamic acid and (*R,S*)-methionine, respectively.

Table 4-1. Distribution of (*S*)-glutamic acid in the side channels

Main channel location	***(S)-glutamic acid (g/g glycine in liquid)×100%***	***Supersaturation, (C/C_s)***
Initially	0	0
After 1st side channel	0.5%	1.3
After 2nd side channel	0.8%	1.5

Table 4-2. Distribution of (*R,S*)-methionine in the side channels

Main channel location	*(R,S)-methionine (g/g glycine in liquid) ×100%*	*Supersaturation, (C/C_s)*
Initially	0	0
After 1st side channel	1%	1.3
After 2nd side channel	1.6%	1.5

4.3.4 Image Acquisition, Processing and Data Analysis

A Nikon TE2000-E inverted microscope is used with Nikon CF DL 5x, 10X, and 20X objectives, and a Plan Neofluar 100X/1.30 oil immersion objective. A high resolution CCD camera with a full frame (PCO Sensicam QE doubleshot, 1280 x 1025 pixels, 9 fps) was used for image acquisition. Images of crystals were captured at marked lengths of the reactor, corresponding to different residence times. Habit modification of a single crystal was captured with a routine that acquires images at a specified time delay. The routine was run while following a single crystal by moving a motorized stage to compensate for the crystal velocity. For growth rate measurement, a similar procedure was used to capture images for single crystals. Data from at least five single crystals were averaged. The recorded images were saved as 8-bit files. The frame rate of the camera was adjusted to values between 2 and 8 frames per second (fps) by the image acquisition software (IPLab, BioVision Technologies). The frames were analyzed in Adobe Photoshop and Matlab.

4.4 Results and discussion

4.4.1 Habit Modification in Batch Reactors

Cooling crystallization of glycine in batch reactors, in the presence of both (*S*)-glutamic acid, and (*R,S*)-methionine, yielded alpha glycine crystals with a modified habit. In pure aqueous solution, alpha glycine usually crystallizes in a bipyramidal habit. In contrast, the presence of (*R,S*)-methionine, at a concentration of 0.01 g/g glycine, produced crystals with a plate-like habit, as shown in Figure 4-6a. In addition, in the presence of (*L*)-glutamic acid, and at a concentration of 0.005 g/g glycine, crystals formed in mostly pyramidal or half-pyramidal (a pyramid with the top half cut off) habit, as illustrated in Figure 4-6b. These observations are consistent with the work of Weissbuch and coworkers.[31, 32]

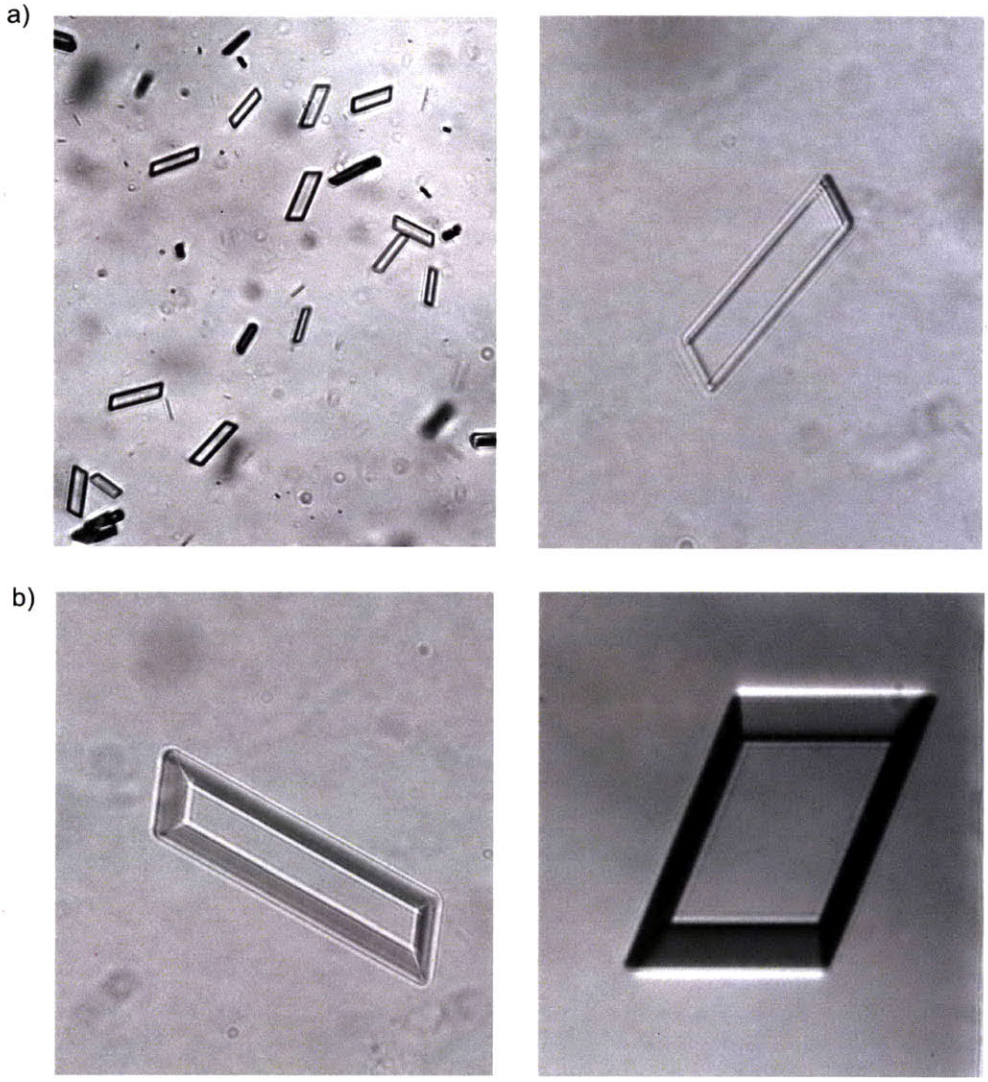

Figure 4-6. Habit modification of alpha glycine crystals in batch reactors. Glycine was crystallized in a cooling crystallization in the presence of a) (*R,S*)-methionine at a concentration of 0.01g/g glycine, and b) (*S*)-glutamic acid at a concentration of 0.005g/g glycine.

Weissbuch et al. have proposed a stereoselective mechanism in order to rationalize the habit modification observed for α-glycine in the presence of other amino acids. The amino acids act as 'tailor-made' additives, and stereospecifically adsorb on to either (010) or (0-10) face of the growing α-glycine crystal, depending on their configuration. The cross-section of α-glycine crystal lattice in *bc*-plane, presented in Figure 4-2, shows that glycine molecules have C2-H4 methyl groups exposed at both (010) and (0-10) faces.

However, substituting the exposed methyl group of nonchiral glycine with a side chain at the (010) face leads to molecules of (*R*)-configuration, and similar substitution at the (0-10) face leads to (*S*)-configuration. Consequently, only (*R*)-amino acid additives can replace a glycine molecule at the (010) face, and only (*S*)-amino acid additives can replace a glycine molecule at the (0-10) face. This constraint results from the steric requirement that the additive molecule be recognized at the crystal surface as a substrate molecule (i.e., glycine), with the amino acid side chain, which is the perturber part of the additive, emerging out of the crystal face.[29] Therefore, chirally resolved amino acids, such as (*R*)- or (*S*)-amino acids, result in a pyramidal habit, as shown in Figure 4-7, with (010) and (0-10) faces as the basal plane, respectively. On the other hand, when racemic amino acids are used as additives, both (010) and (0-10) faces are hindered, resulting in plate-like habits (Figure 4-7).[31]

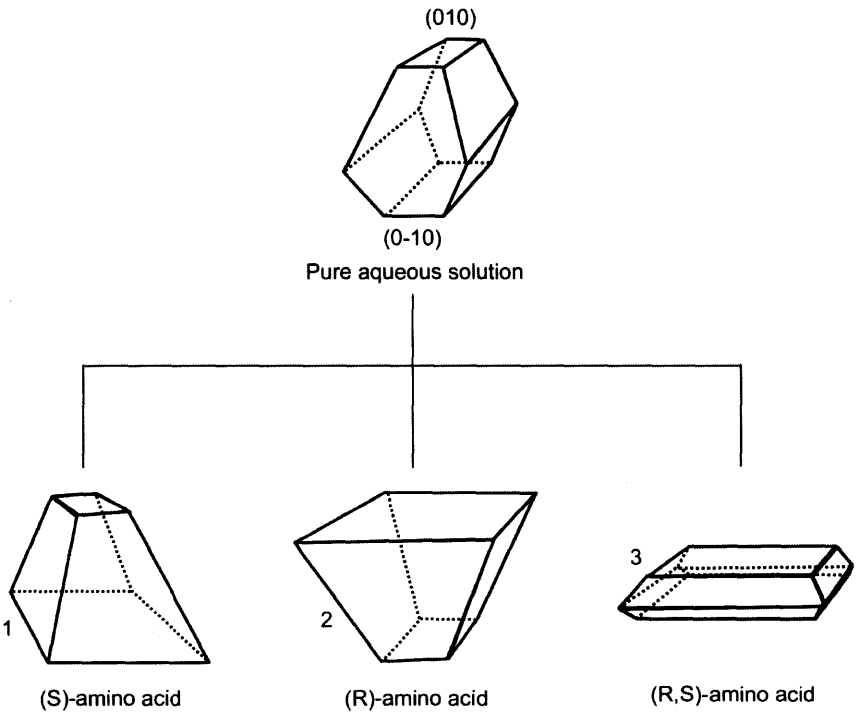

Figure 4-7. Habit modification of α-glycine. Habit of α-glycine when crystallized from pure glycine solution (1), and in the presence of (*S*)-amino acid (2), (*R*)-amino acid, and (*R,S*)-amino acid additives.

4.4.2 Habit Modification in Continuous Microfluidic Devices

In contrast to the batch reactors, we were able to use seeded crystallization in continuous microfluidic devices, add additives in a controlled manner, and observe how the presence of additives affected the growth of each of the crystal facets of alpha glycine. In this method, we can obtain information not only on the final modified habit, but also on the dynamics of the individual facets over time that ultimately results in the final modified habit. We used crystals with well-developed faces as the seeds; aqueous ethanol as the antisolvent to generate the supersaturation, the driving for growth; and two amino acids with different chirality: (*S*)-glutamic acid and (*R,S*)-methionine, as the additives. The effects of these two additives on alpha glycine habit are discussed in the next two sub-sections.

4.4.3 (*S*)-Glutamic Acid

We found that the presence of (*S*)-glutamic acid modifies the centrosymmetric, bipyramidal shape of the alpha seeds into a pyramidal habit, similar to the habit produced in batch cooling crystallization. In addition, we were able to capture the dynamics of habit evolution over time from bipyramidal to pyramidal. The top row of Figure 4-8 presents a series of images that were captured every minute following the growth of an individual crystal in the presence of (*S*)-glutamic acid. The image at t = 0 min corresponds to the seed introduced to the reactor. Supersaturated solution, along with impurity, is added to the main channel right after t = 0 min. We observe that one of the {010} faces, (0-10) according to the structural argument presented in the last section, is inhibited, while (010) keeps growing. Faces adjacent to (0-10), namely (-1-11), (1-1-1), (1-10) and (-1-10) grew out over time. Interestingly, we find that the growth rate along the c axis and of (010) was 2 to 4 times higher than that in the absence of impurities.

In addition, it is interesting to note that the faces adjacent to the inhibited face grow at a faster rate than the corresponding faces adjacent to the uninhibited {010} face. This concept is illustrated by a schematic in Figure 4-9 by considering a two-dimensional cross-section of the crystal in the *ab* plane. In the case of (*S*)-glutamic acid (Figure 4-9-1), for example, (-1-10) face, next to the inhibited (0-10) face, grows at a faster rate than the corresponding (-110) face, which is next to the uninhibited (010) face. Similarly, (1-10)

grows at a faster rate than (110). The change in growth rate of the symmetric faces ultimately results in a pyramidal shape. Figure 4-9 also illustrates corresponding effects of (*R*)-amino acids (2) and (*R,S*) amino acids (3) on bipyramidal habit of alpha glycine.

4.4.4 Racemic Methionine

The presence of (*R,S*)-methionine results in a transformation of the bipyramidal habit of alpha glycine seeds into plates, similar to the habit produced in batch cooling crystallization. The bottom row of Figure 4-8 presents a series of images that were captured following the habit modification of an individual crystal in the presence of (*R,S*)-methionine. Similar to the (*S*)-glutamic acid case, the image at t=0 seconds corresponds to the seed inside the microchannel right before the additive is introduced. As racemic methionine is added to the growth channel, along with supersaturation, the habit goes through modification within a few seconds. As racemic methionine inhibits growth at both the {010} faces, the crystals are seen to reorient themselves displaying their larger faces, {010} (Figure 4-7b). As observed in the presence of (*S*)-glutamic acid, the relative growth rates of the remaining faces appear to change with a few faces completely growing out in the ± *c* direction. Therefore, (*R,S*) methionine also causes the symmetry of the original alpha glycine habit to break down by changing the relative growth rates of symmetry-related faces, which ultimately results in the final plate-like habit.

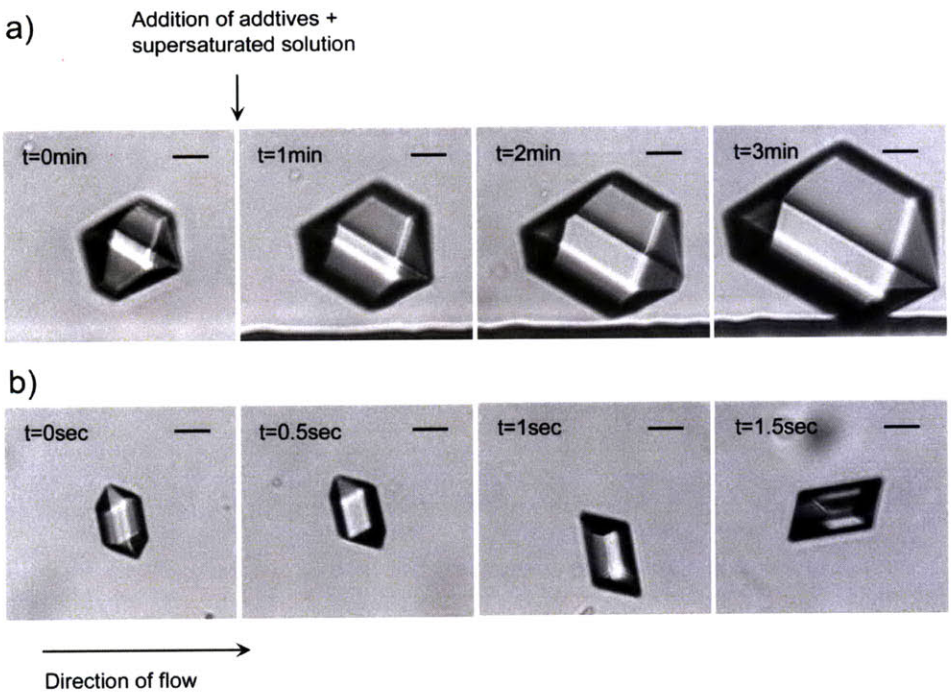

Figure 4-8. Habit evolution of α-glycine over time when bipyramidal seeds are grown in the presence of: a) 1% (*S*)-glutamic acid, and b) 2% (*R,S*)-methionine.

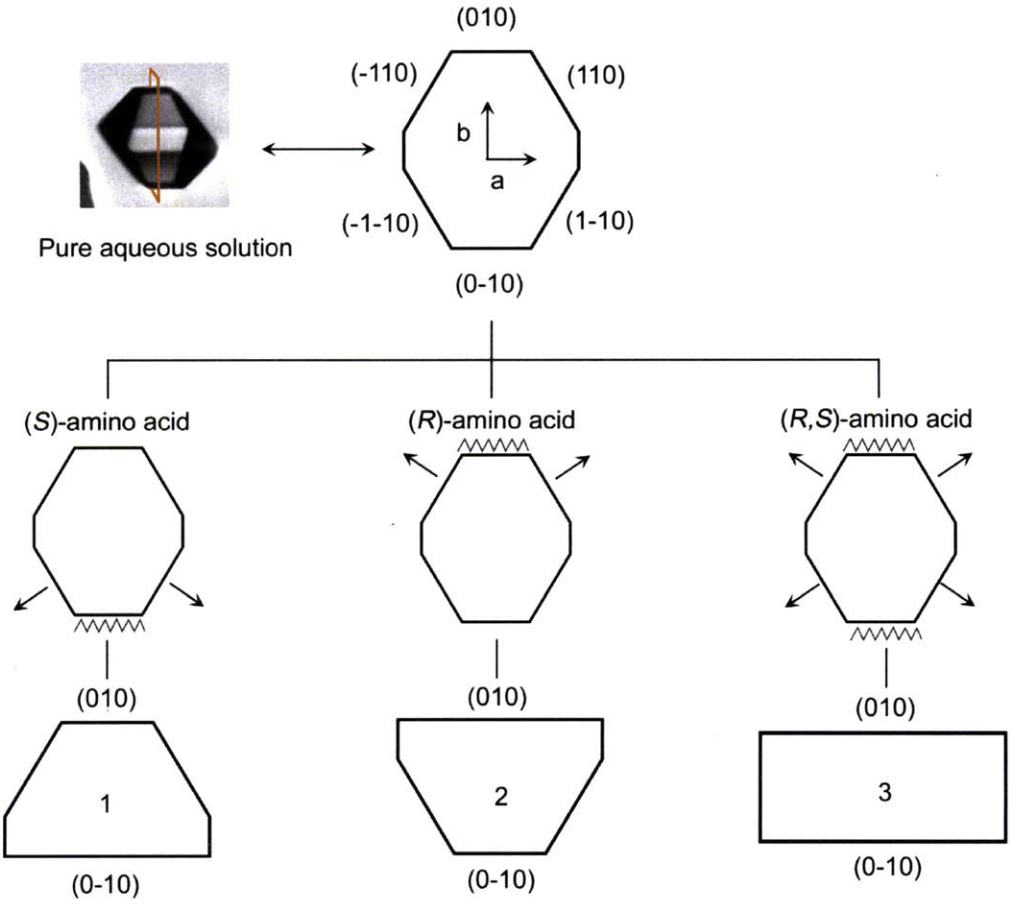

Figure 4-9. Modifying the habit of alpha glycine. 2-D cross-sections of modified habits when bipyramidal seeds of alpha glycine are grown in the presence of (*S*)-amino acid (1), (*R*)-amino acid (2) and (*R,S*)-amino acid (3) additives. The (*S*)-, (*R*)-, and (*R,S*)-amino acids retard the growth of (0-10), (010), and {010} faces. The squiggly line represents growth inhibition by additives.

Even though impurities are found to inhibit particular faces, they are found to increase the growth rate of the remaining crystal facets in case of both impurities, as discussed above. This observation is consistent with the studies of Li et al. They also reported an enhancement of the growth rate of uninhibited faces of α-glycine in the presence of (*S*)-leucine, up to three times depending on the impurity concentration.[35] They suggested that the growth rate increase resulted from a change in the interfacial tension and an increase in dimer formation in the presence of impurities.[35] However, we believe that the increase in growth rate results from an increase in effective concentration of glycine

molecules near the growing faces. The interaction of glycine molecules in the solid lattice with the free glycine molecules in solution may cause their adsorption onto the crystal surface. However, the adsorbed molecules may not become incorporated to the crystal lattice due to the impurities. This then may promote the surface migration of the adsorbed glycine molecules to the remaining faces, particularly to the faces adjacent to the inhibited one. Such phenomenon essentially increases the effective concentration of glycine molecules, and thus, the supersaturation at the faces adjacent to the inhibited one. This explanation is consistent with our observation that although impurities increase the growth rate of all uninhibited faces, such enhancement is highest for the faces adjacent to the inhibited face, which also contributes to break the symmetry of the original alpha glycine habit.

Moreover, we report that the rate, at which the habit modification occurs (in other words, the time it takes for the initial habit to reach the final modified habit), varies significantly between the two additives used. The time scale for reaching the final habit in the presence of (*S*)-glutamic acid is found to be in the order of minutes, while the time scale in the presence of (*R,S*)-methionine is found to be in the order of seconds. One of the factors to cause such a difference in habit evolution rate may be the due to the side chain of additives. As shown in Figure 4-10, the side chain of glutamic acid ends with –COOH, a hydrophilic functional group, while the side chain of methionine ends with –SCH_3, a much more hydrophobic functional group. The incoming glycine molecules may interact with the side chain of glutamic acid through hydrogen bonding, though eventually might not become incorporated to the lattice because the offset caused by the larger side chain may not allow all the required hydrogen bonds to form, leading to an increase in energy. This essentially may cause a delay in rejection of the incoming glycine molecules from the inhibited face. On the other hand, the hydrophobic side chain of methionine repulses the incoming glycine molecules from the inhibited face immediately, which may then increase the effective concentration of glycine and result in a faster growth rate of adjacent faces. In short, the molecular recognition, from an incoming glycine molecule's perspective, of the additive is slower in case of glutamic acid due the structural similarity, but is much faster in case of methionine. A second factor that may contribute to faster habit evolution in the case of (*R,S*)-methionine is the

fact that in this case, both {010} faces are inhibited, resulting in surface migration of twice as many adsorbed glycine molecules to the uninhibited faces, increasing the supersaturation more than in the case of (*S*)-glutamic acid.

This type of kinetics information of habit modification process may be useful as a measure of the efficacy of a chosen additive. It can be used to screen impurities, and develop an understanding for engineering the best additive for a given application.

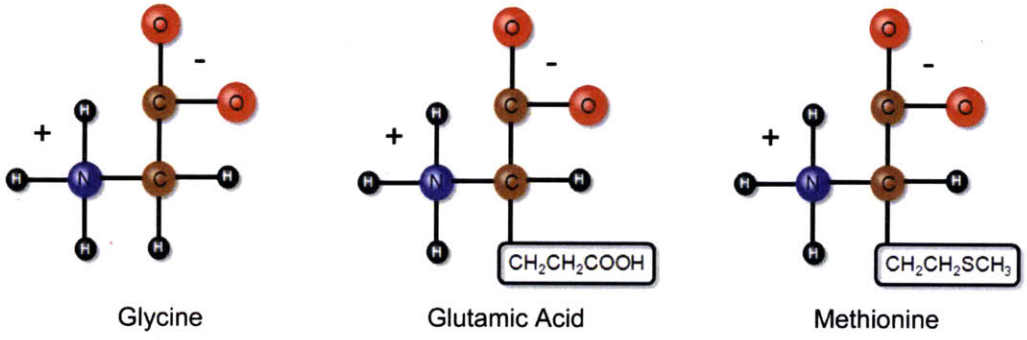

Figure 4-10. The molecular structure of the primary solute, glycine, and the tailor made additives, glutamic acid and methionine. The structures are similar except one of the side chains that act as a perturber.

4.5 Conclusions

In this chapter, we have demonstrated the use of a continuous microfluidic device for investigating the dynamics of crystal habit modification in the presence of impurities for the first time. We have shown that the developed platform can be used to extract kinetics information of the habit modification process, which can provide new insights into the fundamental mechanism of the process. It can also be used to screen impurities, and to determine their efficacy in modifying a certain crystal habit, which may subsequently facilitate the engineering of most desirable additives.

We use alpha glycine, with centrosymmetric bipyramidal habit, as the model system. Seeds with well-developed faces are introduced into the microchannel. Then an additive, along with supersaturation, is added to the growth channel, where seeds are allowed to

grow in the presence of additives. We use (*S*)-glutamic acid and (*R,S*)-methionine as the additive, which modify the habit to pyramids and plates, respectively. Using the dynamics of habit evolution, enabled by the high spatiotemporal resolution of microfluidic devices, we are able to extract new information on the effects of an inhibited face on the remaining faces. With the new piece of information, we offer new insights into the habit modification mechanism.

It has been known for some time that additives break down the symmetry of alpha glycine habit. However, we have shown that this break down of symmetry occurs not only from the inhibition of a particular face, but also from the growth rate change in adjacent faces. This may result from the fact that the glycine molecules that are adsorbed to or nearby the inhibited crystal face due to various interactions with the molecules in the lattice cannot become incorporated into the lattice due to the presence of additives. These molecules may increase the effective concentration, and thus, supersaturation at the remaining faces, causing an increase in the growth rate. We have also shown that the growth rate enhancement is the highest for faces adjacent to the inhibited face, which supports the proposed argument.

In addition, we have shown that (*R,S*)-methionine causes faster transformation of alpha glycine habit, and thus, may be more effective than (*S*)-glutamic acid. This may indicate that molecular recognition plays a key role in the kinetics of crystal habit evolution. A perturber that is significantly different from the functional groups of the host molecule may cause a faster habit modification, and thus, may be more effective as an additive than a perturber that is similar to the functional groups of the host molecule, given that the perturber does not significantly interfere with the binding of the additive to the crystal surface.

4.6 References

[1] D. E. Hertzog, X. Michalet, M. Jager, X. X. Kong, J. G. Santiago, S. Weiss, & O. Bakajin, Femtomole mixer for microsecond kinetic studies of protein folding. *Analytical Chemistry,* **2004**, *76*(24), 7169-7178.

[2] E. M. Chan, M. A. Marcus, S. Fakra, M. ElNaggar, R. A. Mathies, & A. P. Alivisatos, Millisecond kinetics of nanocrystal cation exchange using microfluidic X-ray absorption spectroscopy. *Journal of Physical Chemistry A,* **2007**, *111*(49), 12210-12215.

[3] D. H. Pan, Z. Ganim, J. E. Kim, M. A. Verhoeven, J. Lugtenburg, & R. A. Mathies, Time-resolved resonance Raman analysis of chromophore structural changes in the formation and decay of rhodopsin's BSI intermediate. *Journal of the American Chemical Society,* **2002**, *124*(17), 4857-4864.

[4] D. J. Kirwan, & C. J. Orella, Crystallization in the pharmaceutical and bioprocessing industries. in *Handbook of Industrial Crystallization* (Ed.: A. S. Myerson), Butterworth-Heinemann, **2002**, pp. 249-266.

[5] L. Addadi, Z. Berkovitchyellin, I. Weissbuch, J. Vanmil, L. J. W. Shimon, M. Lahav, & L. Leiserowitz, Growth and dissolution of organic-crystals with tailor-made inhibitors - implications in stereochemistry and material science. *Angewandte Chemie-International Edition in English,* **1985**, *24*(6), 466-485.

[6] B. M. Smythe, Sucrose crystal growth. 3. Relative growth rates of faces and their and their effect on sucrose crystal shape. *Australian Journal of Chemistry,* **1967**, *20*(6), 1115-1131.

[7] B. Y. Shekunov, & P. York, Crystallization processes in pharmaceutical technology and drug delivery design. *Journal of Crystal Growth,* **2000**, *211*(1-4), 122-136.

[8] W. M. L. Wood, A bad (crystal) habit - and how it was overcome. *Powder Technology,* **2001**, *121*(1), 53-59.

[9] F. Puel, P. Marchal, & J. Klein, Habit transient analysis in industrial crystallization using two dimensional crystal sizing technique. *Chemical Engineering Research & Design,* **1997**, *75*(A2), 193-205.

[10] A. Ballabh, D. R. Trivedi, P. Dastidar, P. K. Ghosh, A. Pramanik, & V. G. Kumar, A practical approach to produce near-spherical common salt crystals with better flow characteristics. *Crystal Growth & Design,* **2006**, *6*(7), 1591-1594.

[11] R. J. Davey, N. Blagden, G. D. Potts, & R. Docherty, Polymorphism in molecular crystals: Stabilization of a metastable form by conformational mimicry. *Journal of the American Chemical Society,* **1997**, *119*(7), 1767-1772.

[12] I. Weissbuch, L. Leisorowitz, & M. Lahav, Tailor-made and charge-transfer auxiliaries for the control of the crystal polymorphism of glycine. *Advanced Materials,* **1994**, *6*(12), 952-956.

[13] V. Y. Torbeev, E. Shavit, I. Weissbuch, L. Leiserowitz, & M. Lahav, Control of crystal polymorphism by tuning the structure of auxiliary molecules as nucleation inhibitors. The beta-polymorph of glycine grown in aqueous solutions. *Crystal Growth & Design,* **2005**, *5*(6), 2190-2196.

[14] T. Mukuta, A. Y. Lee, T. Kawakami, & A. S. Myerson, Influence of impurities on the solution-mediated phase transformation of an active pharmaceutical ingredient. *Crystal Growth & Design,* **2005**, *5*(4), 1429-1436.

[15] L. Addadi, Z. Berkovitchyellin, N. Domb, E. Gati, M. Lahav, & L. Leiserowitz, Resolution of conglomerates by stereoselective habit modificaitons *Nature,* **1982**, *296*(5852), 21-26.

[16] I. Weissbuch, L. Leiserowitz, & M. Lahav, "Tailor-Made" Additives and Impurities. in *Crystallizaiton Technology Handbook*, 2nd ed. (Ed.: A. Mersmann), Marcel Dekker, Inc., New York, **2001**, pp. 563-616.

[17] R. J. Davey, & J. Garside, *From Molecules to Crystallizers*, Oxford University Press, U.K., **2000**.

[18] K. Sangwal, & E. Mielniczek-Brzoska, Effect of impurities on metastable zone width for the growth of ammonium oxalate monohydrate crystals from aqueous solutions. *Journal of Crystal Growth,* **2004**, *267*(3-4), 662-675.

[19] J. W. Mullin, *Crystallization*, Butterworth-Heinemann, Oxford, **2001**.

[20] I. Weissbuch, M. Lahav, & L. Leiserowitz, Toward stereochentical control, monitoring, and understanding of crystal nucleation. *Crystal Growth & Design,* **2003**, *3*(2), 125-150.

[21] S. N. Black, R. J. Davey, & M. Halcrow, The kinetics of crystal-growth in the presence of tailor-made additives. *Journal of Crystal Growth,* **1986**, *79*(1-3), 765-774.

[22] R. J. Davey, S. N. Black, D. Logan, S. J. Maginn, J. E. Fairbrother, & D. J. W. Grant, Structural and kinetic features of crystal-growth inhibition - adipic acid growing in the presence of n-alkanoic acids. *Journal of the Chemical Society-Faraday Transactions,* **1992**, *88*(23), 3461-3466.

[23] R. Davey, W. Fila, & J. Garside, The influence of biuret on the growth-kinetics of urea crystals from aqueous solutions. *Journal of Crystal Growth,* **1986**, *79*(1-3), 607-613.

[24] Z. Berkovitchyellin, J. Vanmil, L. Addadi, M. Idelson, M. Lahav, & L. Leiserowitz, Crystal morphology engineering by tailor-made inhibitors - a new probe to fine intermolecular interactions. *Journal of the American Chemical Society,* **1985**, *107*(11), 3111-3122.

[25] I. Weissbuch, R. Popovitzbiro, M. Lahav, & L. Leiserowitz, Understanding and control of nucleation, growth, habit, dissolution and structure of 2-dimensional and 3-dimensional crystals using tailor-made auxiliaries. *Acta Crystallographica Section B-Structural Science,* **1995**, *51*(2), 115-148.

[26] B. A. Hendriksen, D. J. W. Grant, P. Meenan, & D. A. Green, Crystallisation of paracetamol (acetaminophen) in the presence of structurally related substances. *Journal of Crystal Growth,* **1998**, *183*(4), 629-640.

[27] H. C. Koolman, & R. W. Rousseau, Effects of isomorphic compounds on the purity and morphology of L-isoleucine crystals. *Aiche Journal,* **1996**, *42*(1), 147-153.

[28] P. G. Jonsson, & A. Kvick, Precision neutron-diffraction structure determination of protein and nucleic-acid components.3. Crystal and molecular structure of amino-acid alpha-glycine. *Acta Crystallographica Section B-Structural Crystallography and Crystal Chemistry,* **1972**, *B 28*(6), 1827-1833.

[29] I. Weissbuch, R. Popovitz-Biro, L. L., & M. Lahav, Lock-and-key processes at crystalline interfaces: relevance to the spontaneous generation of chirality. in *The lock and key principle* (Ed.: J. Behr), John Wiley & Sons, Inc., New York, **1994**, pp. 173-246.

[30] S. K. Poornachary, P. S. Chow, R. B. H. Tan, & R. J. Davey, Molecular speciation controlling stereoselectivity of additives: Impact on the habit modification in alpha-glycine crystals. *Crystal Growth & Design,* **2007**, *7*(2), 254-261.

[31] I. Weissbuch, L. Addadi, Z. Berkovitchyellin, E. Gati, S. Weinstein, M. Lahav, & L. Leiserowitz, Centrosymmetric Crystals for the Direct Assignment of the Absolute-Configuration of Chiral Molecules - Application to the Alpha-Amino-Acids by Their Effect on Glycine Crystals. *Journal of the American Chemical Society,* **1983**, *105*(22), 6615-6621.

[32] I. Weissbuch, L. Addadi, M. Lahav, & L. Leiserowitz, Molecular Recognition at Crystal Interfaces. *Science,* **1991**, *253*(5020), 637-645.

[33] C. S. Towler, R. J. Davey, R. W. Lancaster, & C. J. Price, Impact of molecular speciation on crystal nucleation in polymorphic systems: The conundrum of gamma glycine and molecular 'self poisoning'. *Journal of the American Chemical Society,* **2004**, *126*(41), 13347-13353.

[34] S. K. Poornachary, P. S. Chow, & R. B. H. Tan, Influence of solution speciation of impurities on polymorphic nucleation in glycine. *Crystal Growth & Design,* **2008**, *8*(1), 179-185.

[35] L. Li, D. Lechugaballesteros, B. A. Szkudlarek, & N. Rodriguezhornedo, The effect of Additives on Glycine Crystal-Growth Kinetics. *Journal of Colloid and Interface Science,* **1994**, *168*(1), 8-14.

[36] A. Bouchard, G. W. Hofland, & G. J. Witkamp, Solubility of glycine polymorphs and recrystallization of beta-glycine. *Journal of Chemical and Engineering Data,* **2007**, *52*(5), 1626-1629.

[37] J. Toth, A. Kardos-Fodor, & S. Halasz-Peterfi, The formation of fine particles by salting-out precipitation. *Chemical Engineering and Processing,* **2005**, *44*(2), 193-200.

[38] K. Park, J. M. B. Evans, & A. S. Myerson, Determination of solubility of polymorphs using differential scanning calorimetry. *Crystal Growth & Design,* **2003**, *3*(6), 991-995.

[39] C. J. Orella, & D. J. Kirwan, Correlation of Amino-Acid Solubilities in Aqueous Aliphatic Alcohol-Solutions. *Industrial & Engineering Chemistry Research,* **1991**, *30*(5), 1040-1045.

[40] V. A. Pertzoff, The solubility of glutamic acid in water and certain organic solvents. *Journal of Biological Chemistry,* **1933**, *100*(1), 97-104.

[41] H.-D. Belitz, W. Grosch, & P. Schieberle, *Food Chemistry*, 3rd ed., Springer-Verlag Berlin Heidelberg, **2004**.

[42] Y. N. Xia, & G. M. Whitesides, Soft lithography. *Annual Review of Materials Science,* **1998**, *28*, 153-184.

5 Microfluidic Devices for Continuous Supercritical Crystallization

5.1 Introduction

In this chapter, we conceptualize, design and demonstrate a continuous microfluidic device for supercritical crystallization, enabling formation of micron and sub-micron sized crystalline drug particles with increased bioavailability. We use the knowledge obtained earlier in this thesis, particularly in Chapter 2 and Chapter 3, to address the challenges associated with continuous homogeneous crystallization in microchannels. In supercritical antisolvent crystallization, we have a process that can achieve high supersaturation, as well as fast mixing, required for homogeneous nucleation. High supersaturation, however, is generally accompanied by a high yield of solid formation that usually clogs the microchannels. In this chapter, we develop a 3-dimensional sheath flow device that can operate at high pressure regime. By controlling the dimensions of the sheath and core, one can reduce the crystal density in the channel. Sheath flow also ensures the formation of crystals in the bulk, away from channel surfaces, and thus, minimizes interactions of crystals with channel surfaces. Using this platform, we demonstrate that continuous nucleation of small organic molecules in microfluidic devices can be realized for poorly and moderately soluble organic systems. We use silicon\pyrex devices for their capability of withstanding high pressure, and we use acetaminophen in various organic solvents as the model system. We demonstrate the production of micron-sized crystals in a continuous manner with supercritical antisolvent process. The crystallinity of the products is established with X-ray diffraction and Raman spectroscopy. Also, we illustrate the use of our developed platform for screening crystallization conditions by showing the effects of pressures and various solvents on the crystal size, habit and polymorphic form.

In addition to producing micron-sized crystalline particles, the device we develop in this chapter may also be used as a tool to safely explore new reaction domains,

particularly high pressure, high temperature, near-critical and supercritical conditions in microchannels – with controlled environment and optical access – for new polymorph discovery. It is of great interest to the pharmaceutical industry to discover new polymorphic forms of active ingredients. The different solid forms of an active ingredient may have very different physical and chemical properties that may affect the bioavailability, shelf life, toxicity or ease of manufacture.[1, 2] A newly discovered form may have more desirable properties than the existing ones. Moreover, the pharmaceutical companies are interested in discovering new polymorphs in order to extend patent protection time as they reach patent expiration for the existing polymorphs.[3]

Supercritical crystallization of organic molecules has mostly been done in macroscopic systems in batch or semi-batch mode, but not in continuous microfluidic devices.[4] In this work, we provide the first example of a microfluidic device for continuous supercritical crystallization.

5.1.1 Supercritical Antisolvent Process

Many industries in the field of specialty chemicals, cosmetics, nutraceuticals and, most importantly, pharmaceuticals, are interested in fine crystals with a narrow crystal size distribution (CSD). Submicron and micron sized crystals of active pharmaceuticals can increase the dissolution rate due to higher surface to volume ratio and enhanced solubility; and hence, can increase the bioavailability of poorly water-soluble drugs.[5, 6] In addition, fine pharmaceutical actives with a narrow CSD are necessary in order to maximize the efficacy, and thus minimize the side effects, of inhalation aerosols, injectable suspensions, controlled release dosage forms, and other specialized modes of drug delivery such as transdermal.[4, 7, 8] Small crystals of narrow size distribution may also be useful for highly potent pharmaceuticals such as cancer drugs.

Supercritical fluids have been acknowledged as one of the promising technologies for producing small particles or crystals with controlled properties.[9] Particles can be produced with a number of different supercritical methods, including 'Rapid Expansion of Supercritical Solutions' (RESS),[10, 11] 'Gas/Supercritical fluid Anti-Solvent' (GAS/SAS),[12] 'Particles from Gas-Saturated Solutions or Suspensions' (PGSS),[13] and some variations of the above processes.[4] In this thesis, we focus on GAS/SAS method,

in which a supercritical fluid is used as the antisolvent that significantly reduces the solubility of the solute, initially dissolved in a liquid solvent.[4] Supercritical fluid techniques may reduce the particle size and residual solvent content in one step, preventing agglomeration of nuclei, which often occurs in organic crystallization. In addition, this method may allow for control over the polymorphic purity and crystal habits.[9]

A supercritical fluid (SCF) is defined as a substance that exists as a single fluid phase above its critical temperature (T_c), and critical pressure (P_c). The physical properties of supercritical fluids vary between the properties of gases and liquids, depending on the temperature and pressure. Typically, SCF has larger density than gases to solubilize other solvents or chemicals, yet has lower viscosity and higher diffusivity than liquid, providing enhanced mixing. This is useful for nucleation processes, as faster mixing is required for homogeneous nucleation. The properties of SCFs are compared with that of gases and liquids in Table 5-1. [14]

Table 5-1. Comparison of supercritical fluids with gases and liquids[14]

	Density (kg/m^3)	*Viscosity ($\mu Pa.s$)*	*Diffusivity(m^2/s)*
Gases	1	10	10^{-6}-10^{-5}
Supercritical Fluids	100-1000	50-100	10^{-8}-10^{-7}
Liquids	1000	500-1000	10^{-9}

Carbon dioxide is the most commonly used supercritical fluid due to easily achievable critical temperature and pressure.[9] It is chemically inert, non-toxic and non-flammable. Moreover, it is an easy substance to dispose off and thus is environmentally friendly. Furthermore, the properties of the supercritical carbon dioxide vary significantly around the critical pressure as demonstrated in Figure 5-1,[15, 16] and therefore, can be used to

tune product properties by varying the pressure. Hence, we use supercritical carbon dioxide as the antisolvent in this study.

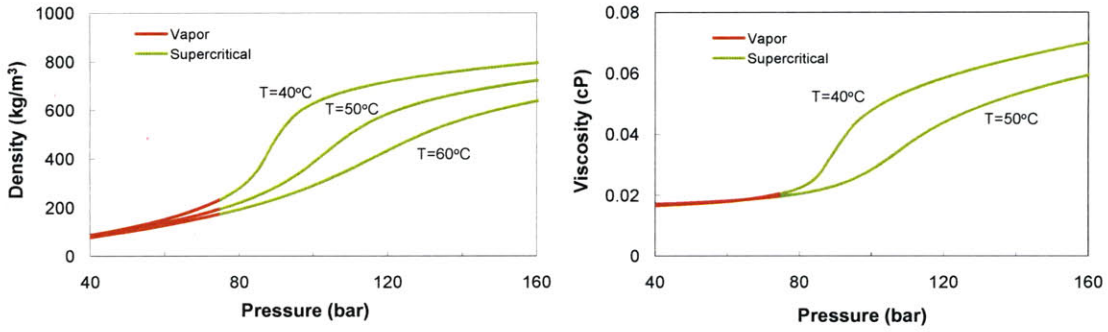

Figure 5-1. The properties of supercritical carbon dioxide.[15, 16] The density, viscosity and other properties vary significantly around the critical pressure and thus can be tuned by control the pressure.

5.1.2 Model System - Acetaminophen

Acetaminophen (*N*-acetyl para-amino phenol, APAP) is an important analgesic and antipyretic agent. It is also used as an intermediate in the manufacture of azodyes, other pharmaceuticals, and photographic chemicals.[17] The unit cell of the most stable polymorphic form of acetaminophen is presented in Figure 5-2a. The predicted morphologies using Bravais-Friedel-Donnay-Harker (BFDH) model yields a regular habit, as shown in Figure 5-2b. Acetaminophen is chosen as the model system in this part of the study for several reasons. First, it is well-representative of poorly water-soluble drugs that are needed in small size to increase the bioavailability. Secondly, the surface properties of acetaminophen crystals make it a suitable solid to be used in silicon/glass microreactor. Figure 5-2c-d present the dominant faces, {001} and {110}, of acetaminophen that mostly consist of hydrophobic functional groups. This indicates that the interactions between crystals and hydrophilic reactor surfaces would be minimal. Thirdly, the physicochemical properties of are suitable for supercritical crystallization process, with supercritical CO_2 used as the antisolvent. Acetaminophen is almost insoluble in carbon dioxide,[18] but is soluble in a number of organic solvents that are miscible with supercritical CO_2.

Acetaminophen is known to have three crystalline polymorphs.[19-21] The most stable form is Type I that crystallizes in a monoclinic lattice (space group $P2_1/a$), and is found in most commercial products. Type II is a metastable polymorph that crystallizes in an orthorhombic group.[22] Type III is highly unstable, and has been mostly formed in thin films.[23] The most common polymorphic form, Type I, is known to display various habits, including prisms, rods, and plates, depending on a number of factors including temperature,[24, 25] supersaturation,[26] rate of supersaturation generation,[27] and presence of impurities.[28, 29]

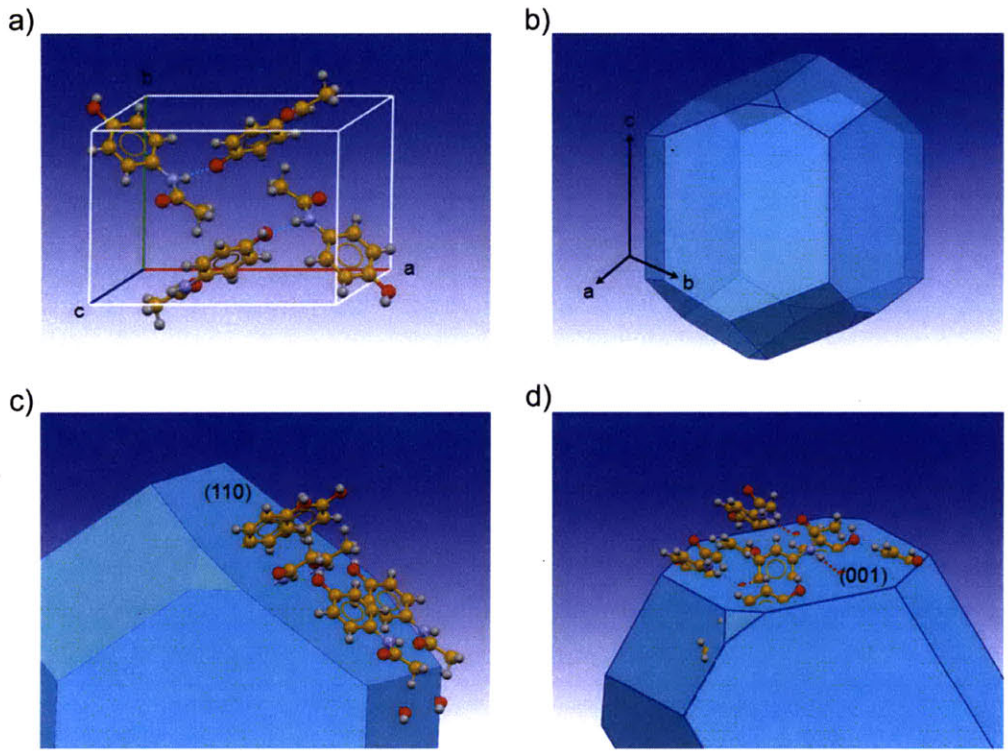

Figure 5-2. Model system: Acetaminophen. a) Unit cell of Type I form; b) The predicted morphology using the BFDH model. c-d) The dominant faces, {001} and {110}, of Type I form, and the functional groups on them.

5.1.3 Solubility Prediction

Although supercritical systems are an exciting prospect for producing micronized crystals, or particles, the general lack of fundamental solubility data and difficulty of

measuring the solubility accurately in such systems is one of the major limitations for its use in fluid extraction or precipitation processes.[30] Therefore, a model for predicting the solute solubility over the range of operating temperature and pressure is useful. The thermodynamic behavior of supercritical carbon dioxide has been studied by many authors; however, models for predicting solid solubility in supercritical solvents at high pressures have not been well developed.[31] In this study, we employ a procedure proposed by Kumhom et al. to calculate the predicted solubility of acetaminophen in supercritical carbon dioxide and solvent mixtures.[30] The ternary system of solute-SCF-solvent is modeled as a pseudobinary system with SCF-solvent pair being modeled as a single pseudocomponent. Kay's mixing rules are used to estimate the pseudocomponent properties.[32]

The solubility of organic solids in supercritical fluid is usually small. Therefore, the solute fugacity coefficient can be approximated by the fugacity coefficient at infinite dilution.[33] Then, the solute solubility, y_2^*, in a solvent can be calculated from the iso-fugacity criterion:[34]

$$y_2^* = \frac{P_2^s \varphi_2^{solid}}{P \varphi_2} \exp\left(\frac{(P - P_2^s) V_2^s}{RT} \right), \tag{5.1}$$

where $P_2^s(T,P)$ is the sublimation pressure of the pure solid, $\varphi_2(T,P)$ is the fugacity coefficient of the solute at the saturation pressure, $V_2^s(T,P)$ is the solid molar volume, and $\varphi_2(T,P)$ is the fugacity coefficient of the solute in the supercritical phase. The above equation assumes that the solid phase is pure, the value of φ_2^{solid} is unity due to the very low solid solute vapor pressure, and neither the solvent nor the cosolvent dissolves in the solid. We estimate P_2^s from the Watson correlation for solids.[35]

$$\ln P_2^s \approx \frac{\Delta H_{vb}}{\Delta Z_b R T_b} \left[1 - \frac{(3 - 2T_{pb})^m}{T_{pb}} - 2m(3 - 2T_{pb})^{m-1} \ln T_{pb} \right] \tag{5.2}$$

where T_b is the boiling point of the solute, ΔH_{vb} is the enthalpy of vaporization at T_b, ΔZ_b is a compressibility factor, and can be estimated to be 0.97,[36] m is a constant that depends on the boiling point and critical temperature, and T_{pb} is a function of the critical temperature, T_c.

$$T_{pb} = T_b / T_c \tag{5.3}$$

ΔH_{vb} is calculated using a modified version of Watson correlation.[37]

$$\frac{\Delta H_{vb}}{T_b} = K_F(8.75 + R\ln T_b) \tag{5.4}$$

In equation 5.4, K_F is Fishtine constant and depends on the dipole moments of polar and non-polar molecules. K_F for acetaminophen is taken to be 1.15. R is the gas constant and is 1.987cal/mol.K in equation 5.4. m is 0.36 if T_{pb} is greater than 0.6, 0.8 if T_{pb} is between 0.5 and 0.6, and 1.19 if T_{pb} is smaller than 0.5.

The critical properties and acentric factor of all the components, including the solute, are crucial for an accurate representation of experimental behavior. A critical point of a substance is defined by the critical temperature (T_c), critical pressure (P_c) and critical volume (V_c). We estimate these properties for all components, including acetaminophen, and various solvents, with a group contribution method that employs only the molecular structure. We follow the method proposed by Constantinou and Gani.[38]

$$T_c = t_{c0}\ln\left[\sum_i N_i t_{c1i} + W\sum_j M_j t_{c2j}\right] \tag{5.5}$$

$$P_c = (p_{c1} + \left[p_{c2} + \sum_i N_i p_{c1i} + W\sum_j M_j p_{c2j}\right]^{1/2}).10^{-5} \tag{5.6}$$

$$V_c = (v_{c0} + \sum_i N_i v_{c1i} + W\sum_j M_j v_{c2j}).10^{-3} \tag{5.7}$$

In equations 5.5-5.7, t_{c0}, p_{c1}, p_{c2} and v_{c0} are constants. The first term of each equation is the contribution from different groups in the molecular structure, and the second term represents the second order contributions from the molecular skeleton. Pitzer's acentric factor, ω, is estimated using the Lee-Kesler correlation.[39]

$$\omega = \frac{3}{7}\frac{\theta}{1-\theta}\log_{10} P_c - 1.0 \tag{5.8}$$

$$\theta = T_b / T_c \tag{5.9}$$

Using the critical properties and the acentric factor of all the components, the fugacity coefficients can be determined. Here, we use generalized Lee-Kesler equation of state. The fugacity coefficient of a pure compound, φ, is given by:

$$\ln\varphi = \ln\varphi^{(0)} + \frac{\omega}{\omega^{(r)}}(\ln\varphi^{(r)} - \ln\varphi^{(0)}) \tag{5.9}$$

$$\ln\varphi = z - 1 - \ln z + \frac{B}{v_r} + \frac{C}{2v_r^{\,2}} + \frac{D}{5v_r^{\,5}} + E \tag{5.10}$$

where z for a compound of interest is calculated using the compressibility factor of a simple fluid $z(0)$ and of a reference fluid $z(r)$. v_r is the reduced volume. B, C, D and E are functions of reduced temperature and some constants of the simple fluid and the reference fluid. z is expressed as:

$$z = z^{(0)} + \frac{\omega}{\omega^{(r)}}(z^{(r)} - z^{(0)}) \tag{5.11}$$

The fugacity coefficient for some component i in a mixture, $\hat{\emptyset}_i$, can be found by first obtaining fugacity coefficient of the mixture, φ_M($\varphi_M$can be calculated in the same way as φ with mixture properties), and then by differentiating it.

$$\ln\hat{\varphi}_i = \ln\varphi_M - \sum_{j\neq i} Z_j \left(\frac{\partial \ln\varphi_M}{\partial Z_j}\right)_{Z_k} \qquad (k \neq i,j) \tag{5.12}$$

Performing the differentiation analytically, $\hat{\emptyset}_i$ can be expressed by the following equation. [34]

$$\ln\hat{\varphi}_i = \ln\varphi_M - \frac{1}{T}\frac{\Delta h_M}{R.T_{cM}} \sum_{j\neq i} Z_j \left(\frac{dT_{cM}}{dZ_j}\right)_{Z_k} + \frac{z_M - 1}{p_{c_M}} \sum_{j\neq i} Z_j \left(\frac{dp_{cM}}{dZ_j}\right)_{Z_k}$$

$$- \left(\frac{\partial \ln\varphi_M}{\partial \omega_M}\right)_{T_r p_r} \sum_{j\neq i} Z_j \left(\frac{d\omega_{cM}}{dZ_j}\right)_{Z_k} \qquad (k \neq i,j) \tag{5.13}$$

With, $$\left(\frac{\partial \ln\varphi_M}{\partial \omega_M}\right)_{T_r p_r} = \frac{1}{\omega^{(r)}}\left[(\ln\varphi_M)^{(r)} - (\ln\varphi_M)^{(0)}\right] \tag{5.14}$$

The mixture critical properties are calculated with the mixing rules proposed by Plocker, Knapp and Prausnitz.[40] The derivatives of the pseudo critical are thus defined by equations 5.15-5.19.

$$\left(\frac{dT_{cM}}{dZ_j}\right)_{Z_k} = \left[2\sum_l Z_l\left(v_{clj}{}^{\eta}T_{clj} - v_{cli}{}^{\eta}T_{cli}\right) - \eta v_{cM}{}^{\eta-1}\left(\frac{dv_{cM}}{dZ_j}\right)_{Z_k} T_{cM}\right] \Big/ v_{cM}{}^{\eta} \tag{5.15}$$

$$\left(\frac{dv_{cM}}{dZ_j}\right)_{Z_k} = 2\sum_l Z_l\left(v_{clj} - v_{cli}\right) \tag{5.16}$$

$$\left(\frac{dp_{cM}}{dZ_j}\right)_{Z_k} = p_{cM}\left[\left(\frac{dz_{cM}}{dZ_j}\right)_{Z_k} \Big/ z_{cM} + \left(\frac{dT_{cM}}{dZ_j}\right)_{Z_k} \Big/ T_{cM} - \left(\frac{dv_{cM}}{dZ_j}\right)_{Z_k} \Big/ v_{cM}\right] \tag{5.17}$$

$$\left(\frac{dz_{cM}}{dZ_j}\right)_{Z_k} = -0.0085\left(\frac{d\omega_{cM}}{dZ_j}\right)_{Z_k}.R \tag{5.18}$$

$$\left(\frac{d\omega_M}{dZ_j}\right)_{Z_k} = \omega_j - \omega_i \tag{5.19}$$

5.2 Microreactor design and fabrication

5.2.1 Reactor Design

The microfluidic device was designed to address the challenges associated with continuous nucleation (Chapter 2). Silicon/pyrex devices were used for achieving high pressure required to reach the supercritical regime. Another advantage of silicon devices for supercritical applications is the high thermal conductivity of silicon, which allows for better temperature control. A silica tubing was inserted into the microchannel to achieve 3-dimensional hydrodynamic flow focusing. The geometry of the channel and the silica tubing was used to center the tubing inside the microchannel. This type of sheath flow serves several purposes for supercritical antisolvent crystallization. It enhances mixing as diffusion occurs from all around the core. Since the supercritical crystallization process typically uses high supersaturation ratio, nucleation is usually rapid. Thus, the enhanced mixing can provide significant advantage for such fast nucleating processes. Moreover, the confinement of the core by the sheath ensures that the crystals would form in the

solution and not on the reactor wall. This may prevent interactions between crystals and channel surfaces, one of main factors of channel clogging, as discussed in Chapter 2. Furthermore, sheath flow can alleviate the difficulty of handling a high density of crystals that usually result from high supersaturation and spontaneous nucleation. By designing the dimensions of the core and the sheath, it is possible to dilute the density of crystals and hence, minimize channel clogging. Thus, the use of supercritical fluid as the antisolvent, along with sheath flow to introduce crystallizing solution, helps to achieve high supersaturation, yet lower number density of crystals, for organic systems with limited solubility in the chosen solvent.

Figure 5-3 presents the microfluidic device used for supercritical crystallization. The front and back mask used for fabrication are presented in Appendix B. As discussed in Chapter 2, fast nucleating systems should be operated at short residence times, since the crystals can grow, agglomerate and clog the microchannels over a longer residence time. Hence, we used a short channel for the supercritical crystallization studies with a few seconds residence time. The channel width, depth, and length were 500 μm, 200 μm, and 5.3 cm, respectively. The inner diameter of the silica tubing was 20 μm, which yielded a characteristic mixing time of 5 to 10 milliseconds, when using 2×10^{-8} m^2/s as the diffusion coefficient of supercritical CO_2. The outer diameter of the silica tubing was 187 μm, which helped to achieve vertical centering of the tubing inside the microchannel. Horizontal centering was achieved by positioning the silica tubing under an optical microscope.

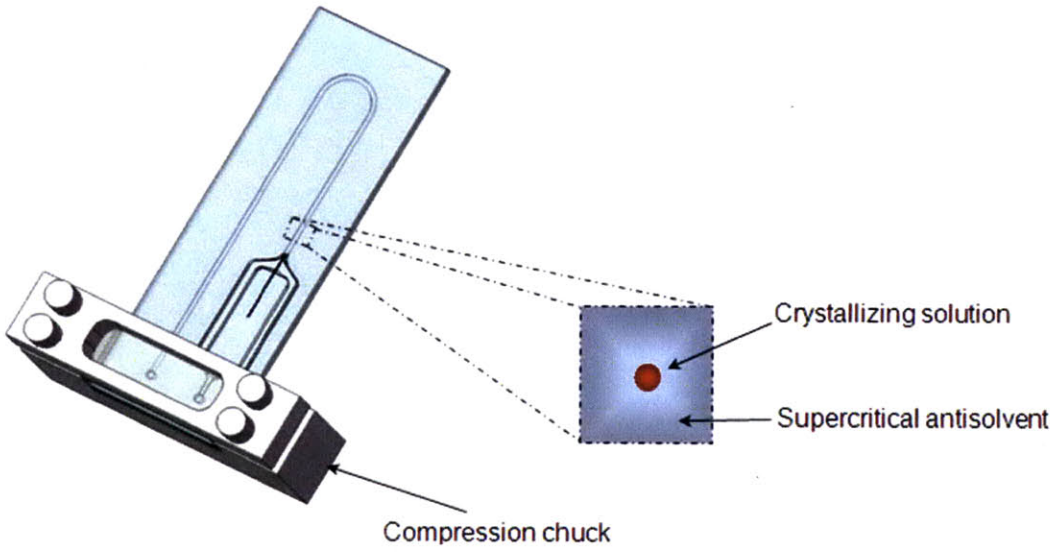

Figure 5-3. Microfluidic device used for continuous supercritical crystallization. The device achieves a sheath flow (right), with crystallizing solution as the core and supercritical antisolvent as the sheath. The rectangular channel is 500 μm wide and 300 μm deep. The core is 20 μm in diameter.

5.2.2 Microfabrication and Packaging

Silicon was used as the device material because of its ability to sustain high pressure.[41] Another advantage of silicon is its compatibility with many organic solvents[42, 43] that are also miscible with supercritical CO_2. The microfluidic device was fabricated using standard silicon fabrication techniques. Channels were etched into silicon wafers (diameter = 15 cm, thickness = 0.8mm, Siliconquest International, Inc.) with deep reactive ion etching (DRIE). Through holes were etched to make inlets and outlets by patterning the backside of the wafer. A 0.5 μm oxide layer was grown on silicon with wet oxidation, and the channels were subsequently sealed with an anodically bonded pyrex wafer (thickness = 0.76 mm). The fabrication details are given in Appendix C.* A silica tubing (Polymicro Technologies) was inserted into one of the microchannels and glued in place with 5-min epoxy (Devcon). The epoxy was cured for at least 4-6

* Microfabrication of silicon wafers was performed by Dr. Soubir Basak, who at the time was a post-doctoral associate in Prof. Jensen's research group.

hours before using. The silica tubing was directly connected to stainless steel tubing (1/16" OD) with upchurch fittings (IDEX Health & Science).

We used packaging techniques that enabled the device to operate at high pressure and high temperature conditions. High-pressure fluidic connections were realized by compressing the device between two stainless steel parts using hard viton O-rings. The compression chuck was build in-house. A thick glass slab (~2cm thick) was used between the device and the top compression part to help the device withstand high pressure. Figure 5-4 illustrates the packaging technique. Stainless steel tubings (1/16" OD) were connected to the compression part with conventional Swagelok fittings (Swagelok).

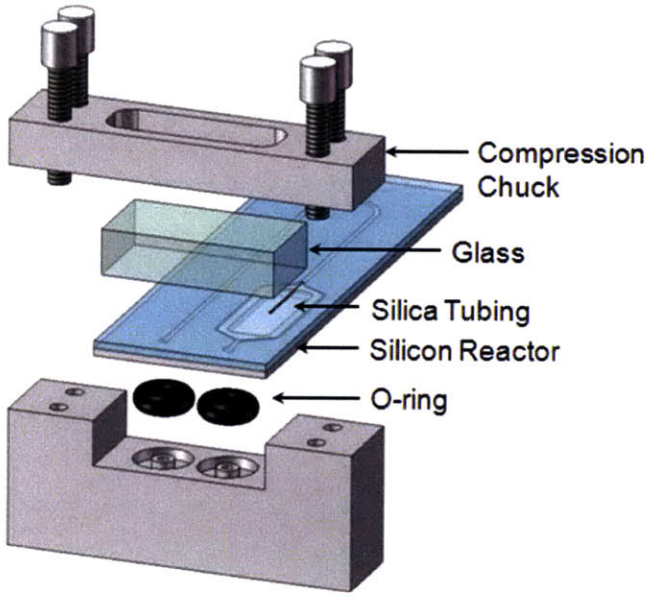

Figure 5-4. Compression packaging for high pressure operation.

5.3 Experimental

5.3.1 Materials and Methods

In order to look at the solvent effects on acetaminophen crystal habit, we used 5 different solvents. Acetaminophen (purity>99%), ethanol (anhydrous), acetone

(anhydrous), ethyl acetate, isopropanol, and n-butanol were purchased from Sigma Aldrich and were used as obtained without further purification. CO_2 and N_2 gas cylinders were obtained from Airgas Inc. Saturated solutions of acetaminophen were prepared by adding sufficient amount of solid to each solvent, equilibrating for at least 24 hours while stirring, and then filtering with a 0.2 μm filter. Undersaturated solutions were prepared by adding appropriate amount of pure solvent to the saturated solution.

5.3.2 Crystallization in Microfluidic Devices

Acetaminophen solution and CO_2 were loaded into two separate high pressure syringe pumps (Teledyne Isco, Inc.). A chiller was used to cool CO_2 to 0^oC for at least 3-4 hours in order to ensure that CO_2 had completely liquefied. Compressing CO_2 to reach high pressure, up to 200 bar, was also found helpful for quickly reaching a stable liquid phase. The entire setup was first pressurized with nitrogen gas through a backpressure regulator built in-house. After reaching the desired operating pressure, acetaminophen solution and CO_2 were pressured to a few bars above the operating pressure. Finally, the valves between the high pressure syringe pumps and the reactor were opened to flow the crystallizing solution and supercritical CO_2 into the microchannel. The syringe pumps were operated in the constant flow rate mode. A high speed digital camera (Cohu, Inc.) was used to capture *in situ* images.

An aluminum chuck built in-house was used to heat the device. A catridge heater (Omega Engineering, Inc.) was used to heat the aluminum chuck. A *j*-type thermocouple was placed in contact with the microfluidic device and was used to measure the device temperature. A temperature controller (Omega Engineering, Inc.) was used to control the temperature of the setup. Figure 5-5 shows a schematic of the final setup for supercritical crystallization. The lines illustrate the connections between the individual components of the setup such as the packaged device, syringe pumps and the collection unit.

The setup was operated at a pressure range of 80-100 bar. When the pressure was increased, the reactor was found to fail around 100-105 bar for the particular channel dimensions, wafer thickness, and channel dimensions used. However, the break-up point may vary depending on the specifics of packaging, reactor geometry and dimensions. The failure appeared to occur mostly at the silicon-pyrex interface, possibly due to bonding

issues. The optimum temperature for operation was found to be between 50 and 60°C. At higher temperature, the solubility was found to increase, and thus the supersaturation decreased significantly. The flow rate of the supercritical carbon dioxide ranged from 500 to 1000 $\mu l \cdot min^{-1}$, and the flow rate of acetaminophen solution ranged from 5 to 10 $\mu l \cdot min^{-1}$. These flow rates yielded a residence time of approximately 2 to 6 seconds for the reactor and the outlet tubing. The Reynolds number was calculated to be approximately 400 to 800, using the density and viscosity of supercritical carbon dioxide at the operating conditions. Therefore, well-controlled laminar flow was achieved in this device even at supercritical conditions.

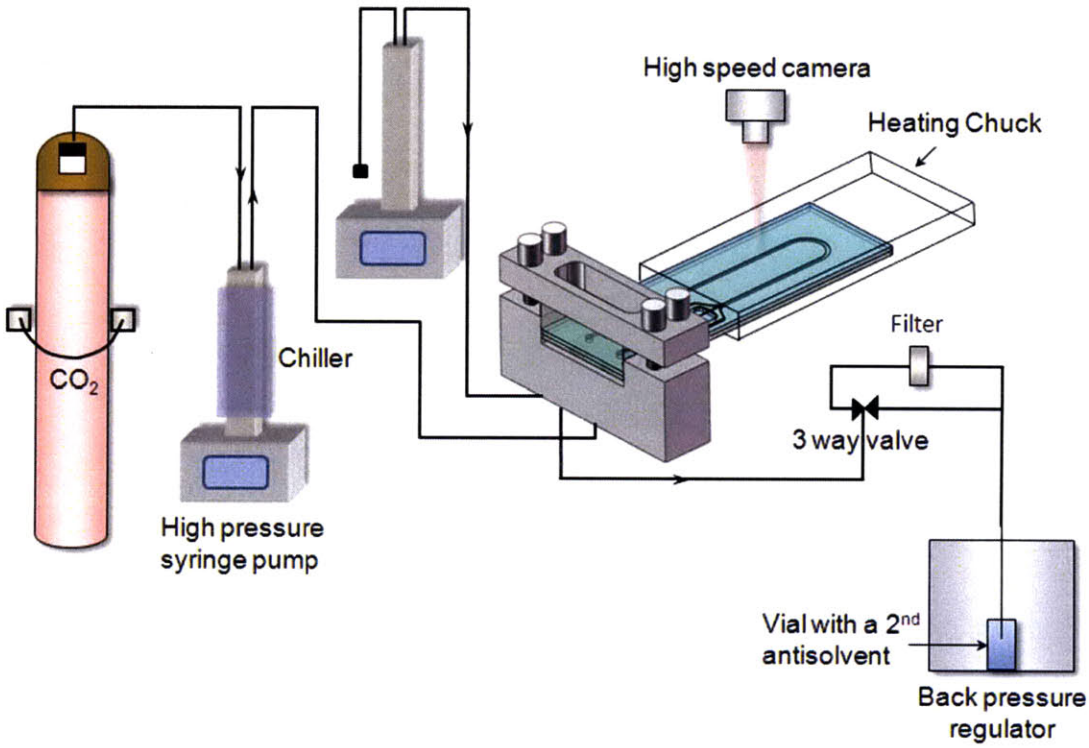

Figure 5-5. Supercritical crystallization setup. The lines show the connections between the various components of the setup, including the packaged device, syringe pumps and the collection unit.

5.3.3 Sample Collection and Characterization

We used two methods for collecting the solid products formed in the supercritical crystallization process. An inline high pressure filter (IDEX Heath & Sciences) was placed in a parallel line between the reactor outlet and the backpressure regulator (Figure 5-5). A 3-way valve (Swagelok) was used to control the flow direction. Once the setup reached steady state, the 3-way valve was switched to initiate product collection. After collecting sample for approximately 20 minutes, the valve between the syringe pump containing crystallizing solution and the reactor was closed. Subsequently, supercritical CO_2 was flown for 15-20 minutes to remove any remaining solvent from the filter. After that, the 3-way valve was switched to the initial line. Finally, the setup was depressurized, and sample was collected. The advantage of this collection method is that the solvent is removed as part of the product collection process, eliminating solvent-based agglomeration or polymorphic transformation. Another advantage of this technique is that the sample is concentrated on the filter, which can directly be used for sample characterization without any post-processing that may change the actual product properties. However, one disadvantage of this collection method is that it is semi-continuous. One has to stop the experiment in order to collect the sample.

The second collection method we used was to collect the samples in a second antisolvent placed inside the backpressure regulator. In this study, we used water as the second antisolvent. The advantage of this method is that it is a continuous process. However, the disadvantage is that it requires collection for a long period of time in order to first saturate the antisolvent and then to obtain a concentrated enough sample for characterization. The entire collection system was immersed in a water bath. The temperature of the water bath was controlled using a temperature controller (Omega Engineering, Inc.). Figure 5-6 shows a schematic of the collection setup, including the filter and a second antisolvent.

The crystal size, size distribution and crystal habit were determined from image analysis of electron micrographs taken with environmental scanning microscope (FEI/Philips XL 30 FEG ESEM). The samples, filters with the collected crystals on top, were coated with a 10 nm gold layer and were directly placed inside the ESEM chamber for measurements. The ESEM was operated at a low vacuum mode with a voltage of 10-

15kV. The average size and standard deviation of particles were calculated by measuring approximately 100-200 crystals for each sample, except when limited by the number of crystals available on the filter. Images were analyzed using Adobe Photoshop. The number of crystals counted for each sample, along with a summary of size and aspect ratio is presented in the Appendix D. The crystallinity and the polymorphic form of the products were characterized with X-ray diffraction and Raman Spectroscopy.

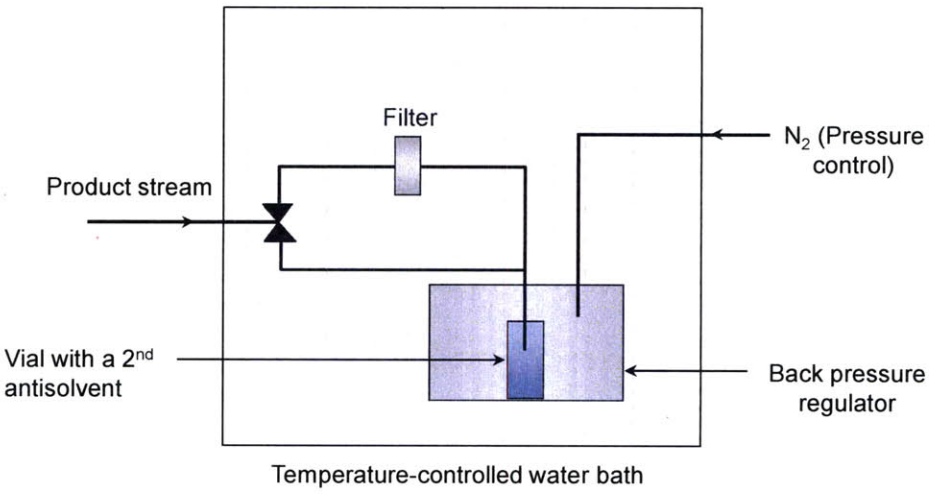

Figure 5-6. Collection unit of the supercritical crystallization process. Solid products are collected in two ways: in a filter, or in a second antisolvent, placed inside the back-pressure regulator.

5.3.4 X-ray Diffraction

The X-ray powder diffraction (XRPD) of the sample was measured by a Bruker D8 X-ray diffractometer (Bruker AXS, UK) using characteristic Cu-Kα radiation. A 0.3 mm diameter collimator was used, and data for each sample were collected over a 2 theta range with a chi (tilt) of 5°. The filters used for sample collection were directly mounted on the sample holder and used for measurements without any post-processing. A motorized stage was used to bring the sample into the exact focus of the beam. Figure 5-7a shows the focusing of the collection plane on the sample, and Figure 5-7b shows the beam size with respect to the sample size. The samples were rotated during collection in order to increase signal to noise ratio. The size of the product crystals was assessed for any peak broadening effect due to nanocrystalline grain. Silver behenate crystallites,

which were approximately 100nm in size, were used as a standard to deconvolute the instrument contribution and sample contribution to peak broadening.

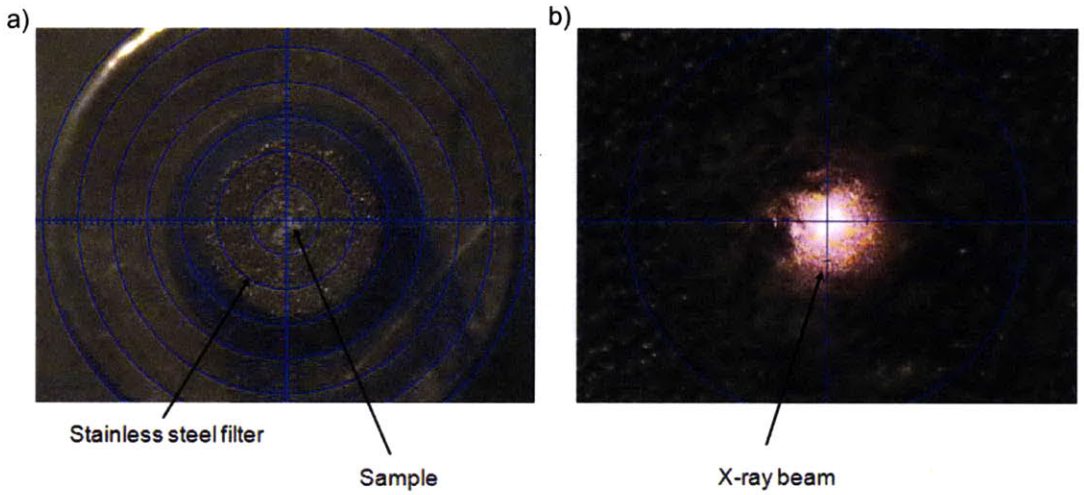

Figure 5-7. Using the filter directly for X-ray diffraction. a) Sample on filter-top was brought to the collection focus. b) X-ray beam on sample.

5.3.5 Raman Spectroscopy

Raman Spectroscopy was also used to characterize the crystallinity and polymorphic form of the product crystals. A 784.8 nm excitation from a solid-state Invictus laser (Kaiser Optical Systems, Inc.) was used in a 180° backscattered geometry via a 15 μm optical fiber. A video camera was used to focus the beam onto the sample with a 10x objective (Nikon). The scattered photons were collected by a Raman microprobe and transferred to a transmission grating (HoloPlex, Kaiser Optical Systems, Inc.) with a liquid-nitrogen cooled CCD through a 15 μm optical fiber. Such small diameter optical fiber was used for both excitation and collection in order to obtain better spatial resolution. The wavelength and the intensity were calibrated using a mercury lamp and a white lamp, respectively. The accuracy of the measured Raman Shifts was checked with cyclohexane and found to have a tolerance of 0.02 cm^{-1}. The filters with samples were directly placed under the incoming beam. The spectrum was acquired for each sample for 60 seconds.

5.4 Results and discussion

In this section, we first discuss the model developed to predict the solute solubility in supercritical fluids. We apply the model to a standard organic compound and compare the predicted solubility with other studies. Next, we discuss the experimental results of continuous supercritical crystallization in sheath flow microfluidic devices. The results of product characterization with ESEM, X-ray diffraction and Raman Spectroscopy are presented and discussed. Finally, we present the use of the developed microfluidic platform for screening crystallization conditions and discuss the effects of varied pressure and different organic solvents on acetaminophen crystal size, size distribution, habit and polymorphic form.

5.4.1 Solubility Prediction

The solubility of organic solutes was predicted using only the molecular structure of the compounds of interest. The ternary system of solute-supercritical antisolvent-solvent was modeled as a pseudobinary system with supercritical CO_2-solvent pair being modeled as a single pseudocomponent. The model used Lee-Kesler-Plocker equation of state to estimate the solubility. The critical properties were estimated by the group contribution method for the different compounds of interest, and are summarized in Table 5-2. The properties are compared to the experimental values for some of the compounds, and are found to be within 5% of the measured values, except for the critical pressure of ethanol, which is ~10% smaller than the measured critical pressure. These properties were subsequently used to calculate the predicted solute solubility.

Table 5-2. Critical property estimation of different compounds used in this study

	$T_c(K)$		$P_c(MPa)$		$V_c(m^3/kmol)$		$T_b(K)$	
	Pred	Exp	Pred	Exp	Pred	Exp	Pred	Exp
Acetaminophen	743.1		3.23		0.413		561.6	
Ethanol	489.3	513.9	5.54	6.15	0.165	0.167	330.0	352
Acetone	490.1	508.1	4.88	4.70	0.21	0.21	330	330
Ethyl Acetate	526.2	530.6	4.16	4.01	0.28	0.28	349.9	350
Isopropanol	508.7	503.4	4.75	4.76	0.22	0.22	347.7	356
n-butanol	558.9		4.19		0.28		393.9	

A Matlab code was written to solve for the predicted solubility (presented in Appendix E). To validate the solubility prediction, the model was applied to the solubility of beta carotene, an organic molecule for which the solubility data is readily available. The predicted solubility of beta carotene in pure supercritical CO_2 is presented in Figure 5-8 over a range of reduced pressure of supercritical CO_2 in terms of solute mole fraction. The predicted data compare well with the predicted values found in the literature at similar conditions.[44]

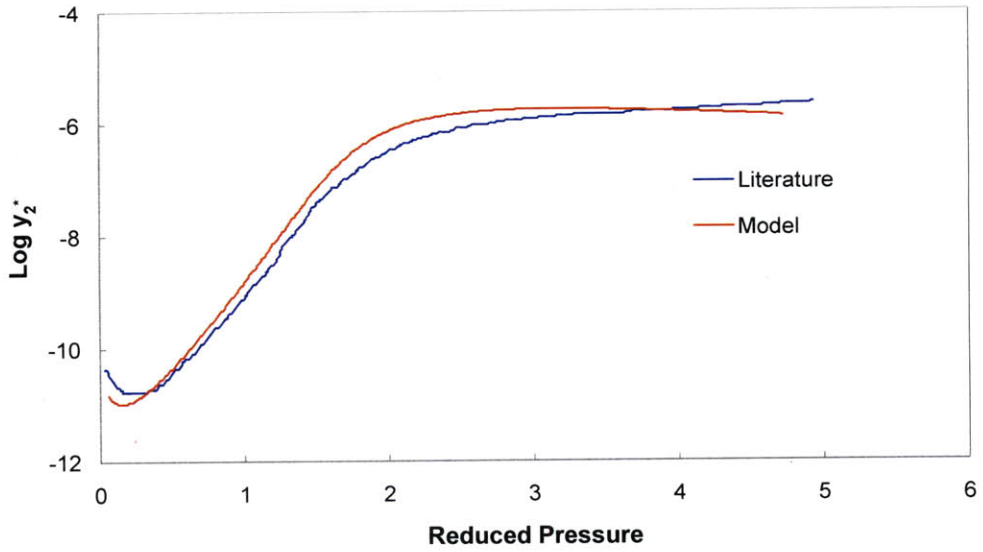

Figure 5-8. A comparison of the solubility predicted by the developed model with literature data for beta-carotene at 67°C in pure supercritical CO_2.[44]

The solubility of acetaminophen was predicted in pure supercritical CO_2, as well as in mixtures of CO_2 and different organic solvents, at 50 and 60 °C over a range of pressures. The solubility in pure supercritical CO_2 at 50°C is presented in logarithm of mole fraction as a function of pressure over a range of 1 to 35 Mega Pascal (MPa) (Figure 5-9). The values range between 3.7×10^{-7} and 1.2×10^{-6} over the operating range of 8 to 10 MPa of pressure. The experimental solubility of acetaminophen is reported to be $\sim(2\text{-}7)\times10^{-6}$ in the literature at similar conditions.[33] However, it has been reported that the low solubility of acetaminophen in supercritical CO_2 makes it challenge to measure the values accurately, and that large errors may be present in measured values. A lower solubility of $\sim4\times10^{-7}$ has also been reported at similar conditions (10 MPa).[45] The predicted solubility values are thus in the same order of magnitude as the experimental values and compare well with the reported literature data. The solubility data of acetaminophen in binary solvent systems, namely supercritical CO_2 and an organic solvent, are used to estimate relative supersaturation and are discussed with respect to product characteristics in a later section.

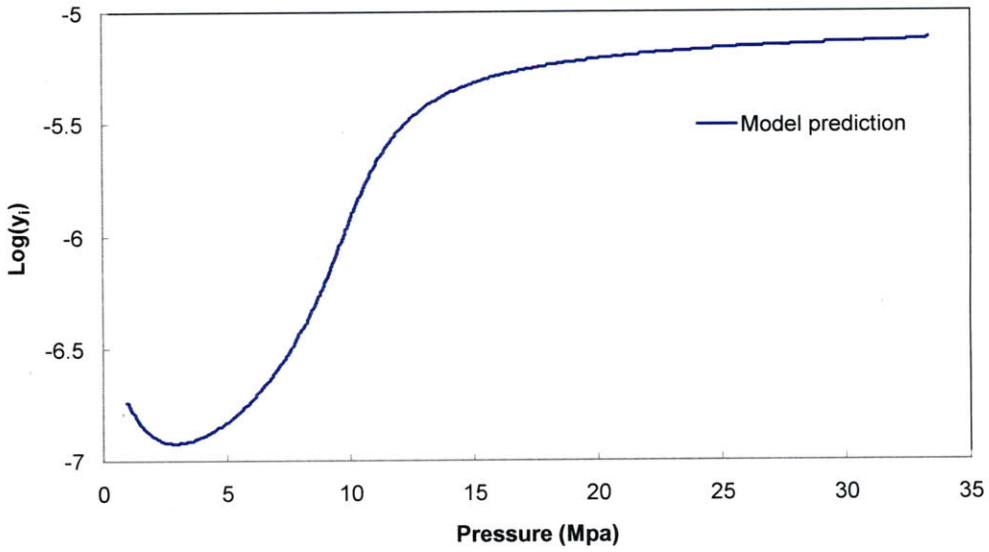

Figure 5-9. Acetaminophen solubility in pure supercritical CO_2 predicted by the developed model (T=50°C).

5.4.2 Crystallization in 3-D Flow Focusing Device

The transparency of silicon/pyrex devices enabled visualization and detection of the point when carbon dioxide and organic solvent mixtures reached their critical point. The controlled introduction, as well as enhanced mixing of the solvent and antisolvent, makes this device an ideal tool to quickly and easily study the phase diagram of different solvent composition. The five organic solvents used in this study, ethanol, acetone, ethyl acetate, isopropanol and n-butanol were found to be miscible with supercritical carbon dioxide. The temperature controller was used to increase the temperature in steps and miscibility was recorded. At 85 bar, the transition temperature was found to be approximately 45-50°C at the operating flow rate ratios for the different solvents. Hence, the device was operated at 50°C.

The solvents were chosen so as to yield a moderate to low solubility of acetaminophen. Solvents with high acetaminophen solubility,[46] such as dimethyl sulfoxide, dimethylformamide, and methanol were avoided to lower crystal density produced in microchannels. The solute concentration was determined with a trial and error method. An initial solute concentration was calculated from the expected solid yield, and was used to perform supercritical antisolvent crystallization in the device. If the initial

concentration was found to clog the channels, the concentration was reduced until the crystallization was achieved continuously. The highest concentration for each solvent that operated the device continuously without plugging was used for the remaining experiments. This concentration is presented in Table 5-3 for all the solvents used. With a supercritical carbon dioxide flow rate of 500 $\mu l \cdot min^{-1}$ and a solution flow rate of 5 $\mu l \cdot min^{-1}$, at the optimum concentration, nucleation appeared to occur almost instantaneously. Figure 5-10 presents a digital image demonstrating nucleation in microchannel with ethanol as the solvent. The temperature and pressure were 50°C and 85 bar, respectively.

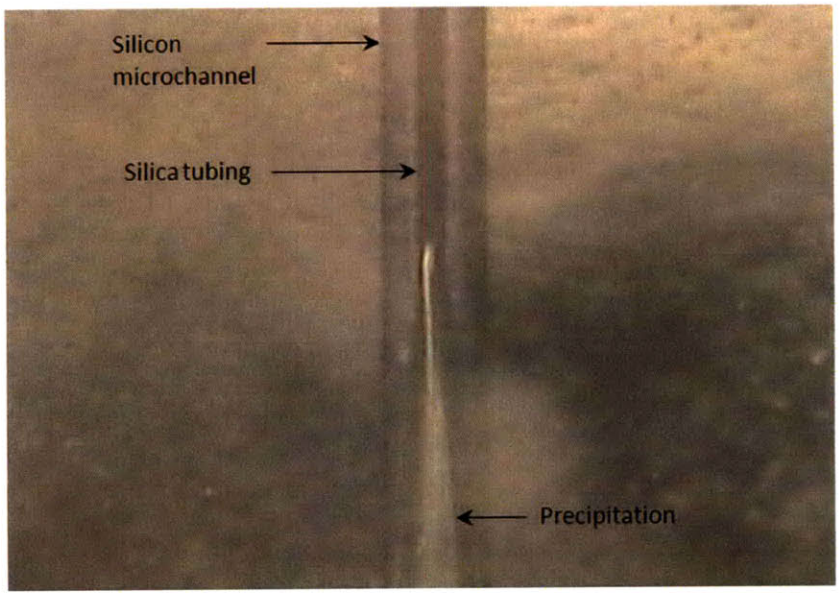

Figure 5-10. Spontaneous nucleation at the core of microchannel, enabled by 3-D hydrodynamic flow focusing. 20% saturated ethanol was used as the solvent. The depth and width of the silicon microchannel were 200 μm and 300 μm, respectively, and the inner diameter of the silica tubing was 20 μm. The flow rates were 5 $\mu l \cdot min^{-1}$ and 500 $\mu l \cdot min^{-1}$ for the solution and antisolvent, respectively. T=50°C, P=85bar.

Table 5-3. Solubility and concentration of acetaminophen used in different solvents.[46]

	Solubility (mg/ml)	*% Saturated*
Ethanol	225	20
Acetone	110	20
Ethyl Acetate	20	40
Isopropanol	145	40
n-butanol	90	30

5.4.3 X-ray Diffraction

X-ray diffraction was performed on all the samples, each of which were found to be crystalline with well defined peaks. The raw spectrum of all the samples was found to contain large background. This resulted from the fluorescence of stainless steel filters that were used to collect sample and then directly used with the sample for product characterization. However, the background was easily subtracted in X-ray data processing software called Jade. The raw data is presented in Appendix F and the processed spectra are presented in Figure 5-11 for samples produced from ethanol (a), acetone (b), ethyl acetate (c), isopropanol (d), and n-butanol (e). Comparing the data with the reference powder diffraction patterns of the different polymorphic forms of acetaminophen, it was found that Type I polymorph was produced from all the solvents over the pressure range of 8 to 10 MPa at 50°C. The black curve in Figure 5-11 represents the sample data and the red lines represent the literature data for Type I polymorph.[20] All the samples share most of the major peaks present in the reference data, except for samples produced from n-butanol. Samples from n-butanol as the solvent have a major

peak at a 2θ of ~18° that is characteristic of the Type I polymorph (Figure 5-11e). The two major peaks of Type I reference pattern at 23.5 and 24.5° also appear in the sample pattern (Figure 5-11e), albeit with a weaker signal. The weaker signal of the two major peaks, as well as the absence of some of the other peaks, may result from preferred orientation. The SEM results also corroborate the formation of thin structures, as will be discussed in the following section.

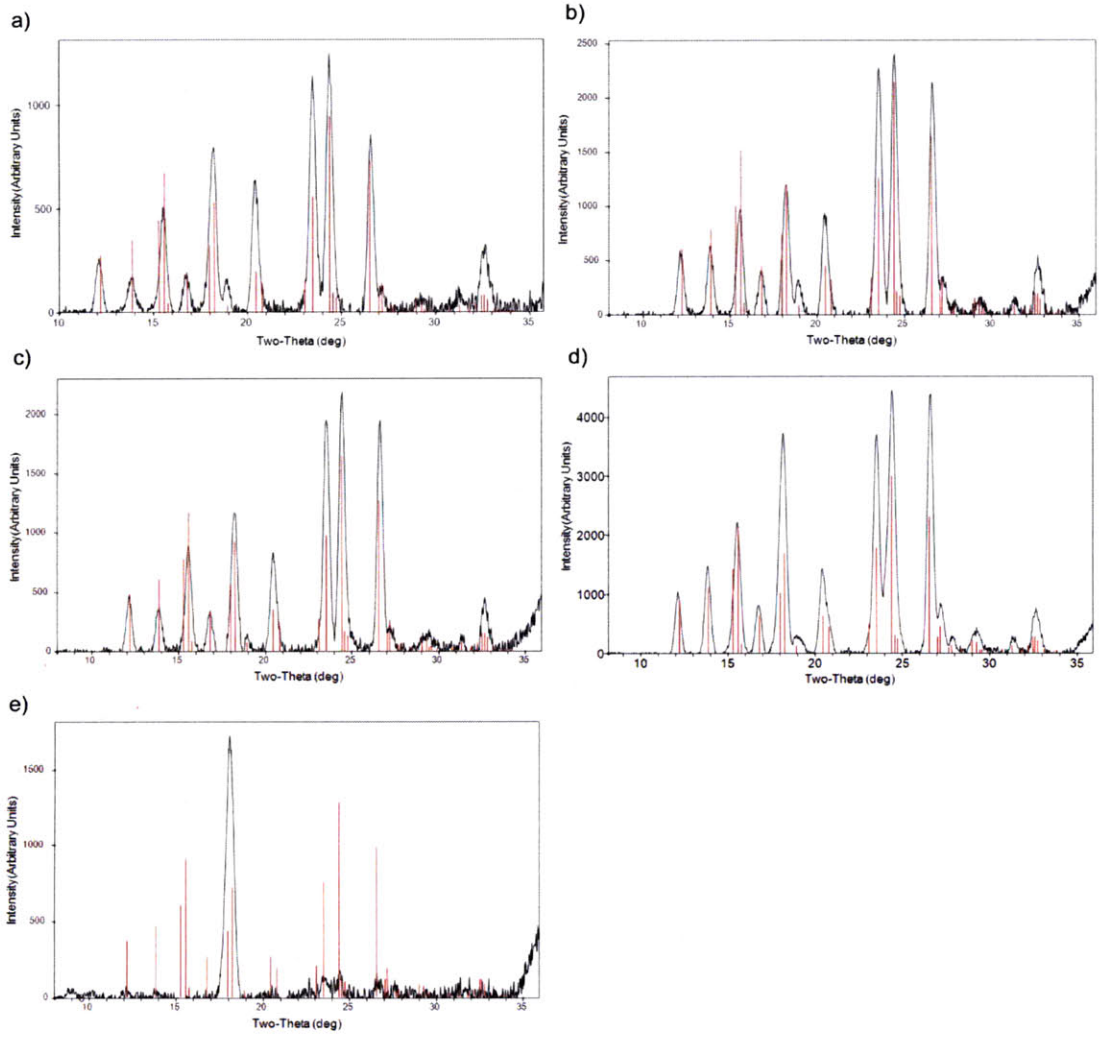

Figure 5-10. Powder diffraction pattern of the samples made from the supercritical antisolvent process using a) ethanol, b) acetone, c) ethyl acetate, d) isopropanol and e) n-butanol as the solvent, at T=50°C, P=85bar. The black curve represents the sample data after background subtraction and the red lines represent reference peaks for Type I acetaminophen crystals.[20]

The sample patchiness, or the inhomogeneity of the crystalline grains on the filter, was investigated by acquiring spectrum for a stationary sample and comparing it with the spectrum acquired from rotating the same sample. The results are presented for the sample produced from ethanol at 85 bar and 50°C and flow rates of 5 and 500 $\mu l \cdot min^{-1}$ for the solution and CO_2, respectively. Figures 5-12a and b show the diffraction pattern obtained for the stationary sample and the rotating sample, respectively. The stationary sample indicates the presence of hundreds of individual grains, but not large enough number to make the diffraction rings continuous. The number of crystals, however, is sufficient to give continuous rings when the sample is slowly rotated at approximately 1 rpm.

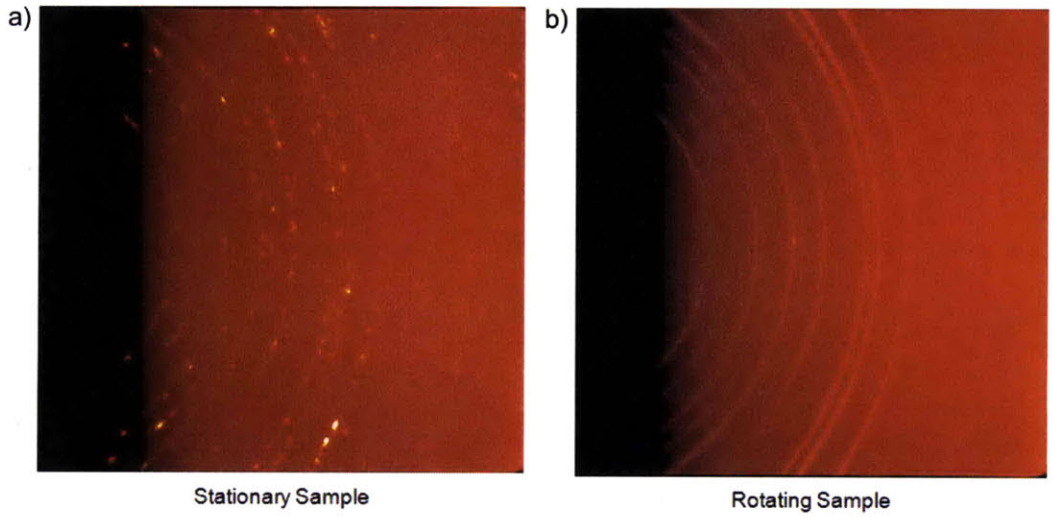

Figure 5-12. Sample patchiness displayed by the stationary sample (a). Rotating samples appeared to yield continuous rings.

The crystal products made from the supercritical antisolvent process were also used to investigate the grain size from peak broadening effects. The Scherrer equation can be used to measure the crystallite size from the peak broadening effects due to small size:

$$B(2\theta) = \frac{K\lambda}{L\cos\theta} \tag{5-20}$$

where B is the peak width, K is the Scherrer constant, λ is the wavelength of X-ray radiation, θ is the ½ the diffraction angle, and L is the crystallite size. Although peak

width is proportional to the crystallite size, the peak profile is a function of many factors, including instrumentation, crystallite size, microstrain and solid inhomogeneity. Therefore, instrumental broadening effects and specimen broadening effects have to be deconvoluted for determining the crystallite grain size.[47] We used nanocrystals of silver behenate (size: 100nm) as the standard that causes very slight peak broadening due to size. Coincidentally, silver behenate was found to share a peak with acetaminophen sample at ~ 23.5°, and the peaks could be simply compared visually. The red curve in Figure 5-13 presents the powder diffraction pattern of the sample and the blue curve presents the pattern of silver behenate. A comparison of the two patterns illustrates that the common peak at ~23.5° is in fact slightly broader for silver behenate, implying that there is no peak broadening effect in the sample pattern due to the crystallite size, and that any peak broadening present in the sample pattern is most likely due to instrumentation only. This also means that the crystal products produced from the supercritical antisolvent process in this study are not aggregates of small nanocrystals, but whole grains of larger size.

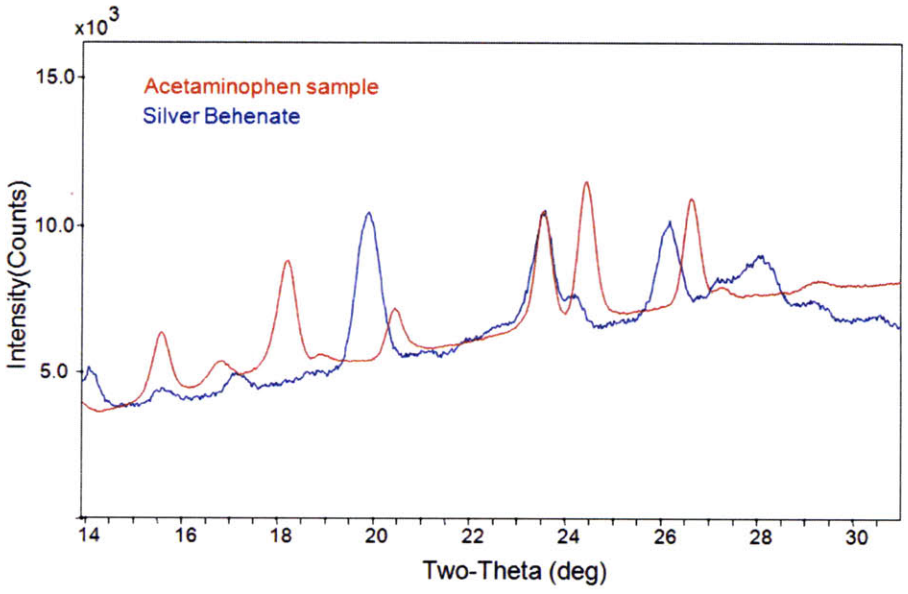

Figure 5-13. Comparison of the X-ray diffraction pattern of a typical sample with silver behenate to determine peak broadening effects.

5.4.4 Raman Spectroscopy

Raman spectroscopy was also used to investigate the crystallinity and the polymorphic form of the crystal products. Collection filters with the crystal products on top of them were directly used to acquire the Raman Spectrum for each of the samples. The stainless steel filter was found to strongly fluoresce at the laser wavelength used, 785nm (Figure 5-14). Although some of the acetaminophen peaks were still visible in samples with sufficient amount of product material, as in the presented spectrum, fluorescence often hid those peaks for samples with less material and with weaker signal. Hence, we used an iterative curve fitting technique to subtract fluorescence signal from all the raw spectra.[48] The procedure used is presented in Figure 5-15 and the Matlab code is appended to this thesis (Appendix G). The processed spectrum is presented in Figure 5-16 for samples produced from ethanol (a), acetone (b), ethyl acetate (c), and isopropanol (d). For n-butanol sample, we were not able to acquire a discernable signal due to insufficient material. The presence of sharp peaks, as well as the characteristic Raman Shift of crystalline acetaminophen at ~1650 cm^{-1} confirms the crystallinity of all the samples. Kauffman et al. have shown that the peaks of amorphous acetaminophen are much broader, and the Raman Shift at ~1650 cm^{-1} is only present in crystalline acetaminophen.[49] The spectrum of each sample (blue curve) is compared with that of the commercial Type I polymorph (red curve) in Figure 5-15. The Raman Shifts for all the samples shared the characteristic peaks of Type 1 polymorph, particularly at 837 and 1234 cm^{-1}.[49] Thus, the Raman data supports the conclusions from X-ray diffraction patterns that the products made from the supercritical crystallization process are crystalline and are of Type I polymorph.

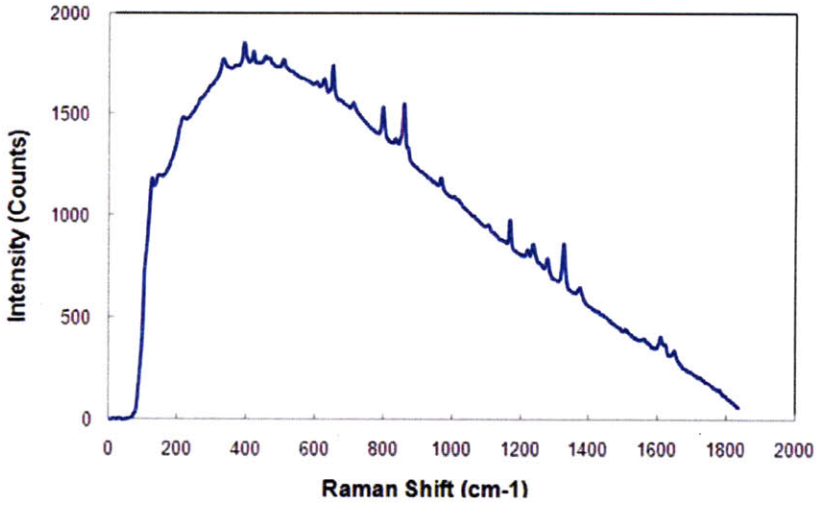

Figure 5-14. Fluorescence signal of stainless steel filter hides the sample spectra.

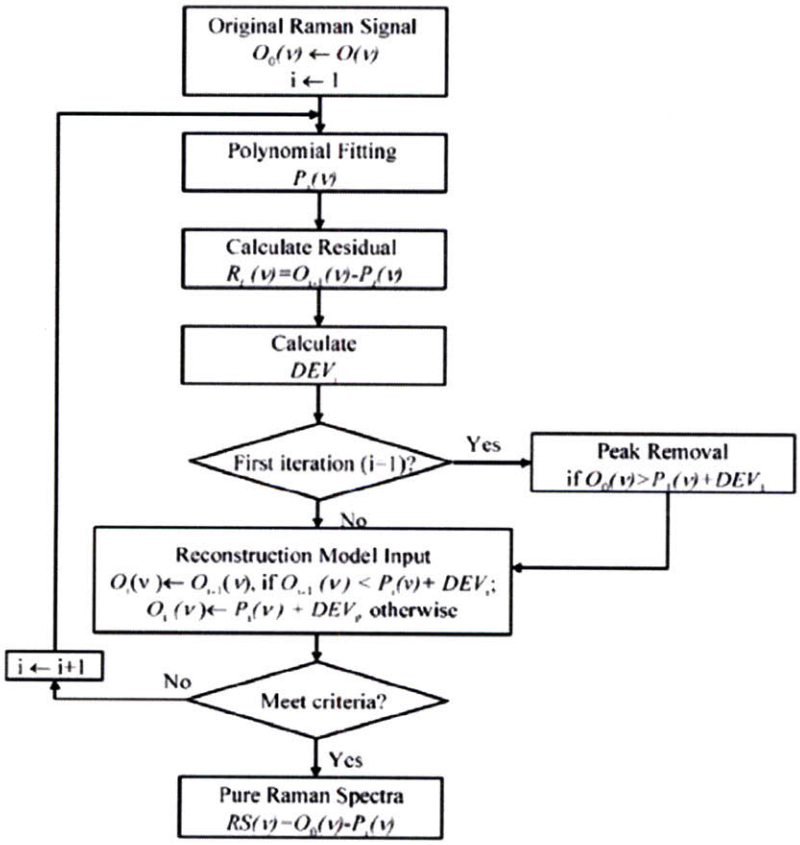

Figure 5-15. Procedure used to subtract fluorescence signal.[48]

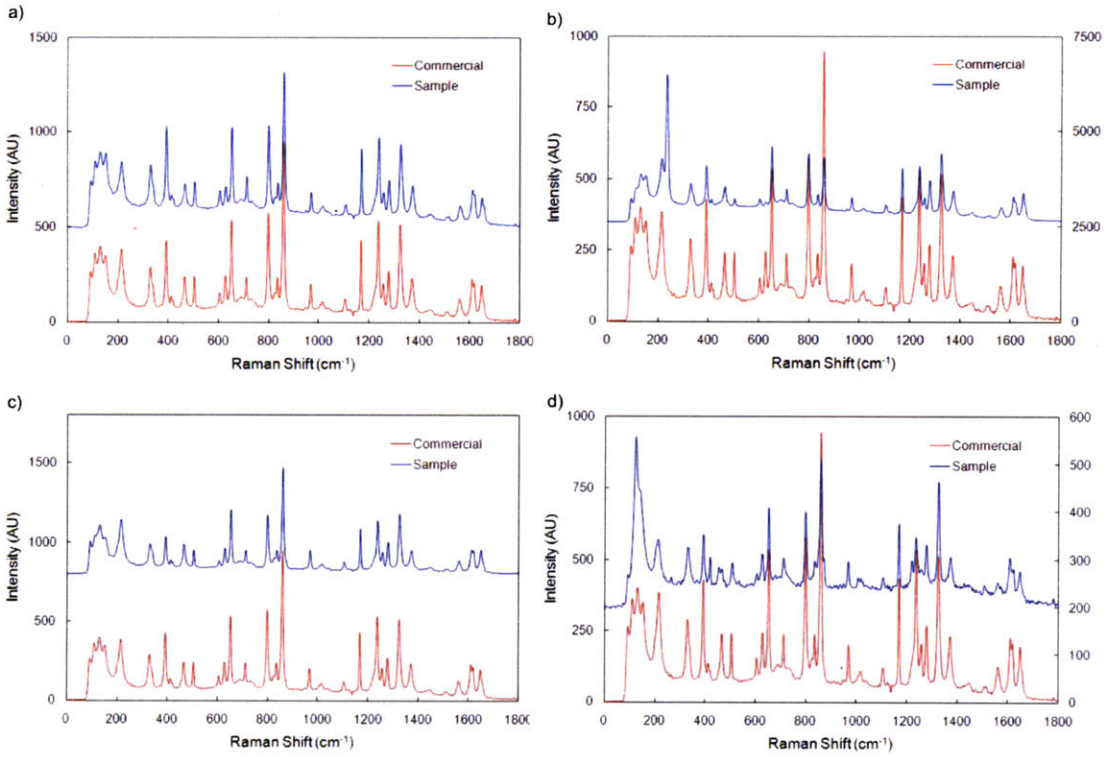

Figure 5-16. Raman Spectrum of acetaminophen samples produced from a) ethanol, b) acetone, c) ethyl acetate, and d) isopropanol.

5.4.5 Crystal Size and Habits

The size, aspect ratio and habit of the crystalline product were characterized with SEM images for samples produced from different organic solvents, namely ethanol, acetone, ethyl acetate, isopropanol and n-butanol, at pressures ranging from 80 to 95 bar and a temperature of 50 °C. In this discussion, we use the term "crystal size" to refer to the largest dimension, and the term "aspect ratio" to refer to the ratio of the two largest dimensions of the crystal. Product characteristics were also investigated for samples produced from subcritical fluid at 40°C and 70 bar using acetone as the solvent, and were compared with the samples produced from supercritical fluid using the same solvent and solute concentration. Four distinct habits of acetaminophen were found for the different samples: prism, cubic, plate and rod. Typical images of these habits are presented in Figures 5-17 a-d. Prisms were usually of the size ranging from submicron (~400nm) to a few micron (~5 μm). They displayed multiple facets, as shown in Figure 5-17a. We use

the term "cube" for habits that displayed comparative growth in all three dimensions (Figure 5-17b). Cubic crystals typically ranged from a few micron (~5 μm) to ~20 μm in size. The habits with comparative growth in two large dimensions are referred to as plates (Figure 5-17c). Crystals with an aspect ratio smaller than four are considered as plates. The size of the plate-like crystals ranged from a few micron to tens of micron. The thickness was typically between ~200 nm to 2 μm. The term "rod" is used for needle-like habits, with an aspect ratio greater than 4 (Figure 5-17d). The typical width and length of the rods were found to be a few micron and tens of microns, respectively. The thickness was found to be similar to that of plates. In this section, we first present the product characteristics of samples produced from supercritical and subcritical carbon dioxide–acetone in terms of crystal size, aspect ratio and habit. Next, we present the product characteristics of samples produced from the different organic solvents and supercritical carbon dioxide. Finally, we discuss the characteristics of samples produced at different pressures.

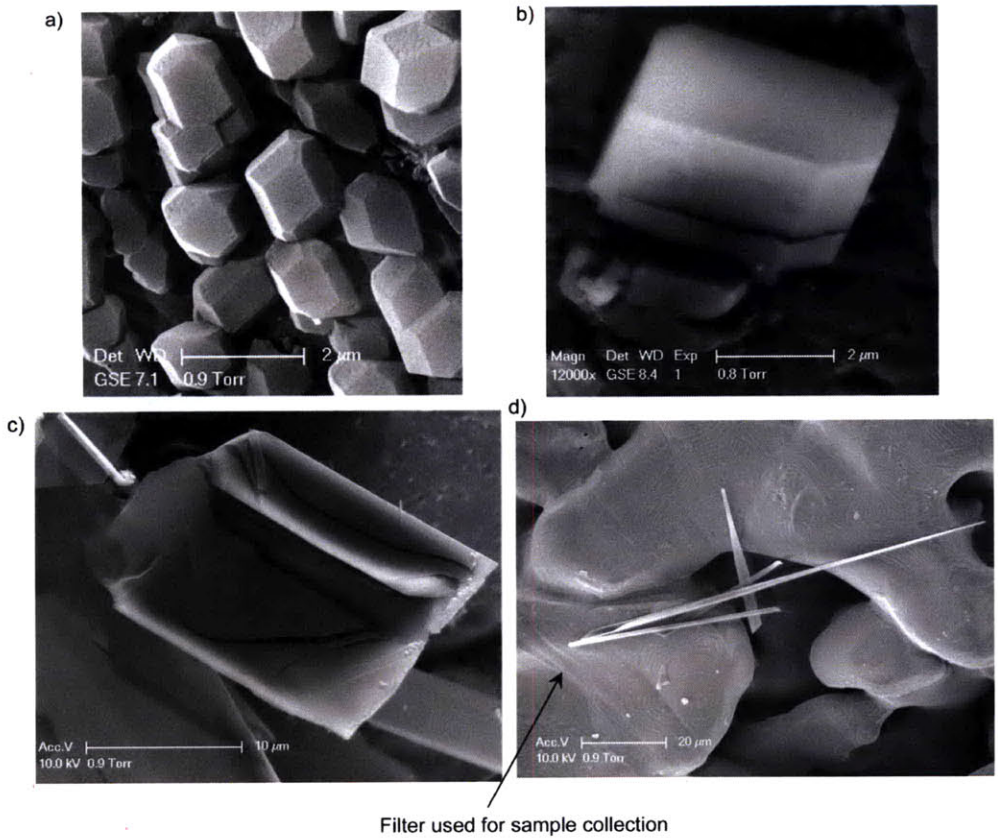

Figure 5-17. The four distinct habits observed for acetaminophen crystals: a) prism, b) cube, c) plate, and d) rod.

Twenty percent saturated acetone was used as the solution for investigating the effects of supercritical fluid on crystal properties. The supercritical crystallization was performed at 50°C and 88 bar with flow rates of 5 $\mu l \cdot min^{-1}$ and 500 $\mu l \cdot min^{-1}$ for the solution and carbon dioxide, respectively. Subcritical crystallization was performed at 40°C and 70 bar with the same flow rates and solute concentration. The crystals produced from acetone solution were found to have mixtures of the four habits in both supercritical and subcritical solution (Figure 5-18a). More than 80% of the crystals produced in the supercritical fluid consisted of regular habits such as prisms and cubes, and less than 20% of the crystals consisted of plates and rods. On the other hand, the percentage of prismatic crystals decreased to 30 when produced in the subcritical fluid, and the percentage of comparatively larger crystals, such as plates and rods, increased to 70. The average size

of the crystals also increased from 4.7±1.5 μm to 15.3±5.7 μm when subcritical fluid was used in place of supercritical fluid. Figure 5-18b shows that the average size of all the different habits increased more or less in case of the subcritical fluid. However, the overall average size increased significantly due to the increased percentage of plate and rod-like crystals. This can be also observed for the aspect ratio, presented in Figure 5-18c. The aspect ratio for each of the different habits is comparable for the crystals produced from supercritical and subcritical fluid. However, the average aspect ratio increased from 2.3±0.6 μm to 4.8±2.1 μm for crystals produced from subcritical fluid due to the increased percentage of plates and rods.

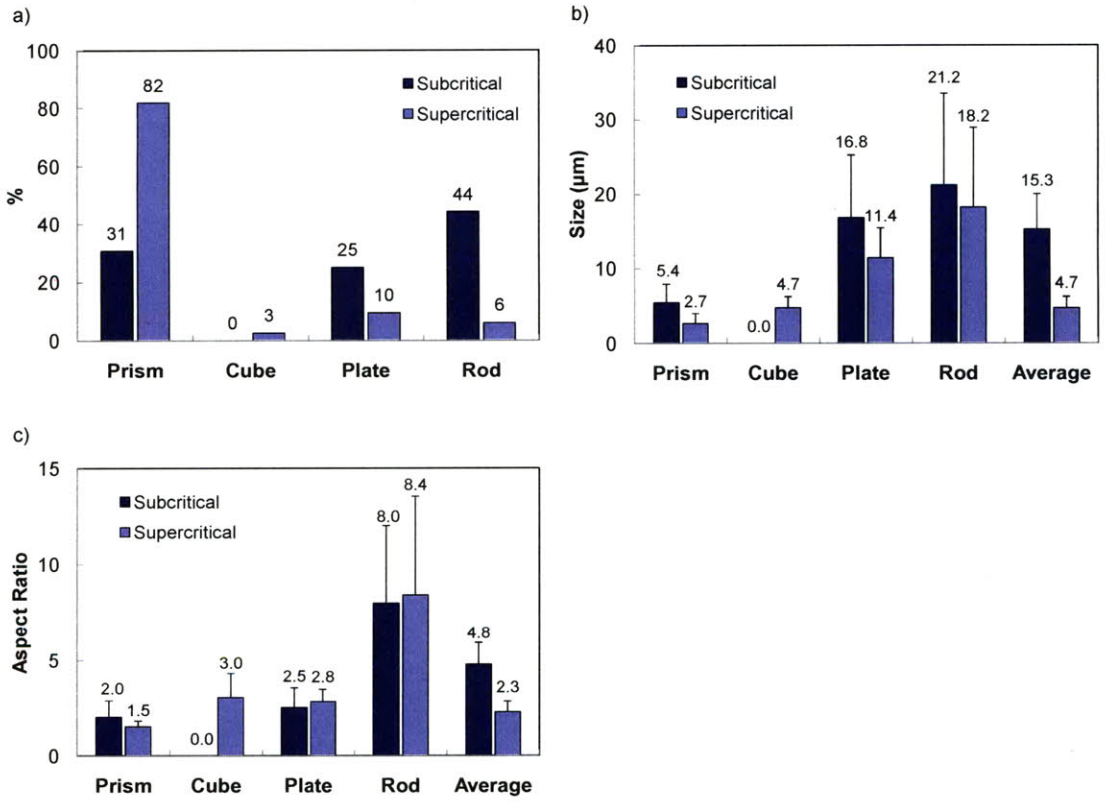

Figure 5-18. Product characteristics of crystals produced from supercritical and subcritical fluids. a) The distribution of the various habits. b) The average size of the different habits and the overall average size. c) The aspect ratio of the different habits and the overall average. Acetone was used as the solvent.

The crystal size, aspect ratio and habit were found to vary for different solvents as well. Twenty percent saturated ethanol was found to produce prismatic crystals of uniform size and low aspect ratio at a temperature of 50°C and a pressure between 81 and 95 bar. The size of crystals ranged from 1 to 3 μm, and the aspect ratio ranged from 1 to 3. Figure 5-19a demonstrates the uniformity of crystal size, as well as the prismatic habit. The zoomed image in Figure 5-19b illustrates the typical size of the crystals. For ethyl acetate, forty percent saturated solution was used for supercritical crystallization at the same pressure range and temperature. Uniform, prismatic crystals of small size and low aspect ratio were produced. The size of the crystals typically ranged from 1 – 3 μm, and the aspect ratio was between 1 and 2.

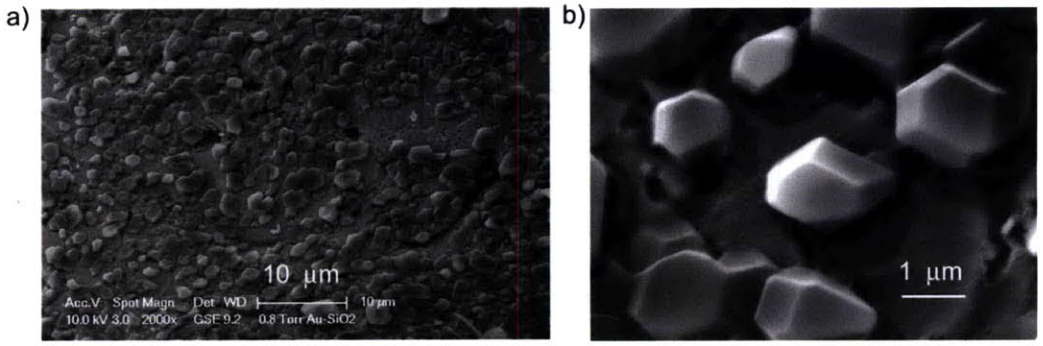

Figure 5-19. Acetaminophen crystallization from ethanol at 85 bar and 50°C (a-b).

On the other hand, isopropanol and n-butanol were found to produce mostly high aspect ratio crystals such as thin plates and rods. Forty and thirty percent saturated isopropanol and n-butanol, respectively, were used as the solvents for supercritical crystallization at 50°C and 95 bar. The size of the crystals produced from isopropanol ranged from 5 to 50 μm for both plates and rods. The aspect ratio was typically between 2 and 4 for plates, and between 4 and 30 for rods. The crystals produced from n-butanol were found to have similar size, as well as aspect ratio, for both plates and rods. Typical images of the crystals produced from the different solvents are presented in Figure 5-20.

The distribution of the four habits produced from the different solvents at 81 and 95 bar is summarized in Figures 5-21a and 5-21b, respectively. As discussed earlier, the

habit of crystals produced from ethanol and ethyl acetate was mostly prismatic. The crystals produced from acetone had a distribution of all four habits. At 81 bar, 87% were prismatic, 3% were cubic, 3% were plates, and 7% were rods. At 95 bar, the number of cubic crystals was found to increase to 15% and the number of prismatic crystals was found to decrease to 76%. Plates and rods were 4 and 5%, respectively. On the other hand, the crystals produced from isopropanol were 16% plates and 84% rods at 81 bar. The distribution remained the same when the pressure was increased to 95 bar. Similarly, the crystals produced from n-butanol were 11% plates and 89% rods at 81 bar, and 13% plates and 87% rods at 95 bar.

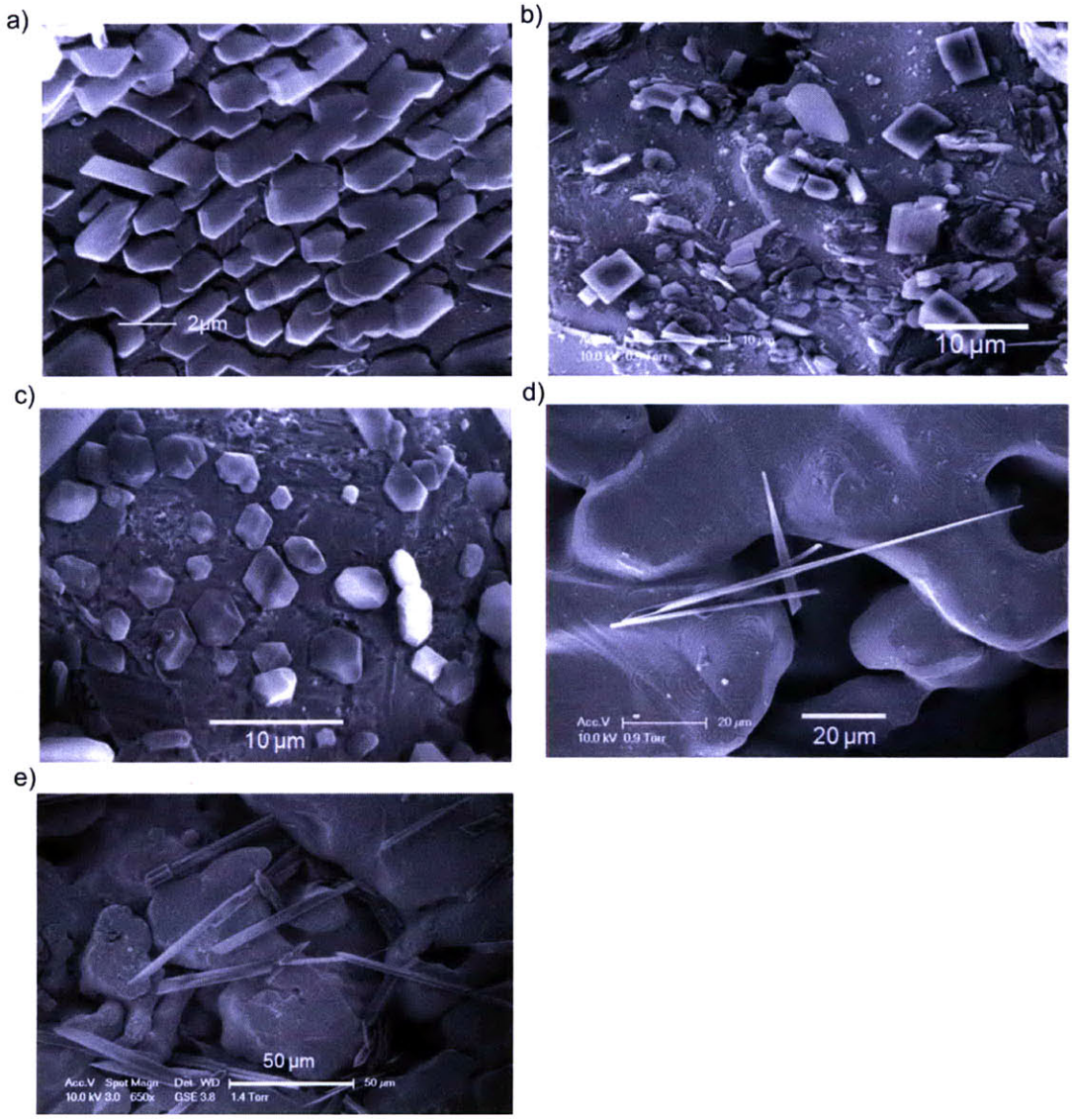

Figure 5-20. Acetaminophen crystals produced from supercritical antisolvent process, with a) ethanol, b) acetone, c) ethyl acetate, d) isopropanol and e) n-butanol as the solvent. T=50°C, P=85bar. Stainless steel filters used for sample collection can be seen underneath the crystals.

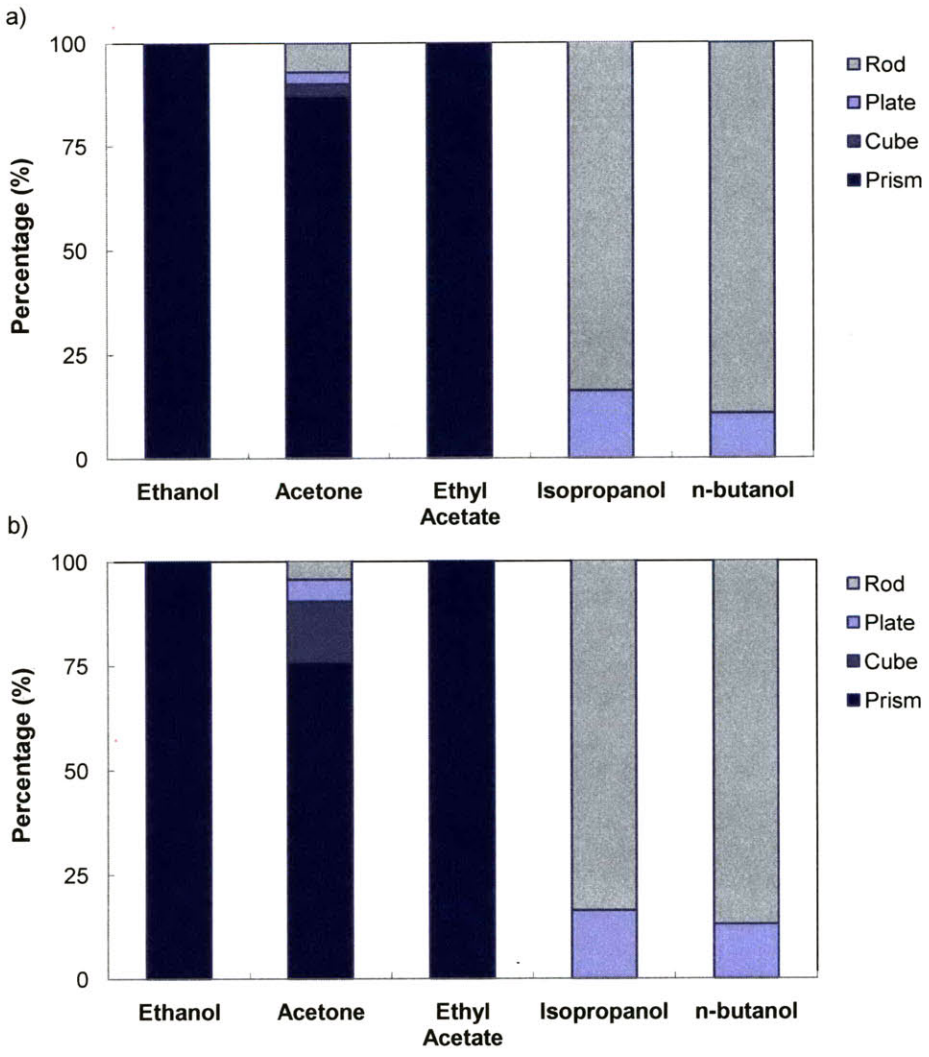

Figure 5-21. Distribution of habits for different organic solvents at 81 bar (a) and 95 bar (b). T=50°C.

The average size and the aspect ratio of the crystals produced from different solvents at 81 bar and 50°C are summarized in Figures 5-22a and 5-22b, respectively. Ethanol and ethyl acetate were found to yield crystals of the smallest size and the lowest aspect ratio. The average size was 2.25±0.86 μm and the average aspect ratio was 1.83±0.79 for crystals produced from ethanol, whereas the average size was 2.10±1.12 μm and the average aspect ratio was 1.52±0.49 for crystals produced from ethyl acetate. Acetone produced crystals of slightly larger size, namely 3.96±1.33 μm, and of slightly larger aspect ratio, namely 2.35±0.71. As discussed earlier, the presence of mostly plate-like

and rod-like crystals resulted in a comparatively larger average size and aspect ratio for crystals produced from isopropanol (IPA) and n-butanol. The average size and aspect ratio for the products from isopropanol were 24.73±8.26 μm, and 8.37±3.42, respectively. Similarly, the average size and aspect ratio for the products from n-butanol were 15.57±6.71 μm, and 15.36±7.90, respectively. In general, a trend was observed between the crystal size and the aspect ratio. Larger aspect ratio was usually found to accompany larger crystal size. We discuss these discuss the observed differences in light of supersaturation present in the system at the time of nucleation in the following section.

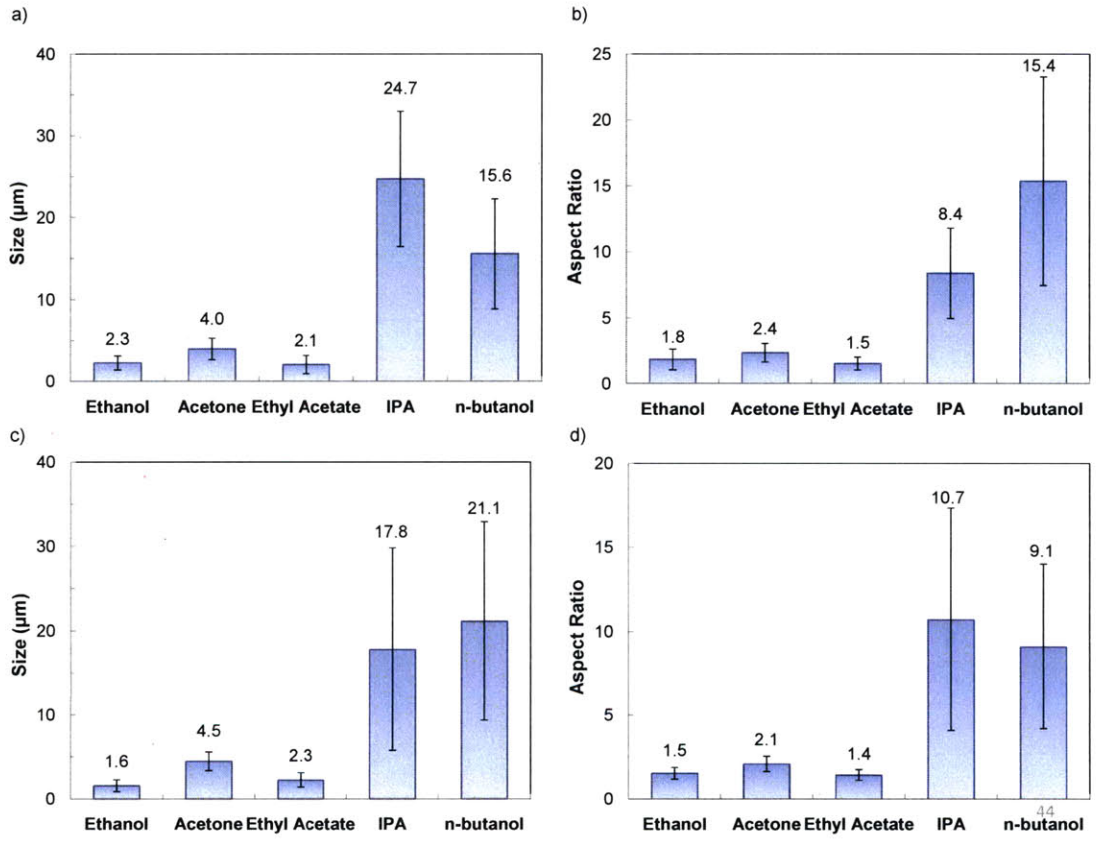

Figure 5-22. The average size and aspect ratio of crystals produced from the different solvents at P=81 bar (a-b) and P=95 bar; T=50°C.

The ability of continuous microfluidic devices to easily and quickly scan reaction parameters was also employed to investigate the effects of pressure on the crystal size, habit and aspect ratio. Ethanol, ethyl acetate and acetone were used as the solvents for

this study, and supercritical antisolvent crystallization was performed at different pressures between 81 and 95 bar. Higher pressure (e.g. up to 150 bar) would have been interesting to look at since the properties of supercritical CO_2 is most sensitive in 100 – 150 bar regime at 50°C. However, we were limited to 95 bar due to the limitations of the reactor. The average size and aspect ratio of the crystals produced at the different pressures are presented in Figures 5-23a and 5-23b for each of the three solvents.

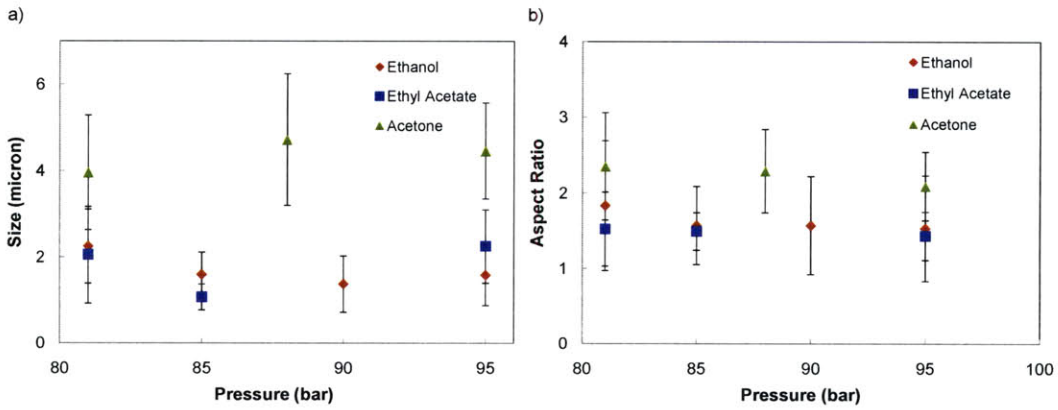

Figure 5-23. Pressure effects on the average size (a) and aspect ratio (b) of crystals produced from ethanol, acetone and ethyl acetate. T:50°C in all cases.

As Figure 5-23 demonstrates, pressure was found not to have a significant effect on the crystal size or habit in the range of 81 to 95 bar at 50°C. The average size, as well as the average aspect ratio, at the different pressures remained within the error limits of each other for all the solvents. As Figure 5-1 shows, the properties of supercritical carbon dioxide does not vary significantly over 81 to 95 bar at 50°C. Hence, the lack of significant pressure effects is expected. The summary of all the raw data is presented in the Appendix D.

5.4.6 Supersaturation Analysis

The display of the various habits of acetaminophen in different solvents may result from two factors: solvent-solute interaction or supersaturation. If solvent-solute interaction were present in our studies, the plate-like and thin rod-like habit, resulting from isopropanol and n-butanol, would be the probable candidates. The high aspect ratio

would indicate hindered growth in at least one direction, most likely due to interactions with solvents or impurities.[50] However, hydrogen bonding ability decreases significantly with the length of carbon chain, and so appears unlikely to play a major role in case of n-butanol. Therefore, the more likely factor to cause a difference in habits may be the supersaturation of the system at the time of nucleation. This supersaturation is not the expected supersaturation upon complete mixing of the solvent with antisolvent, because nucleation most likely occurs due to high supersaturation before complete mixing can take place. Here, we use the solubility prediction model to estimate relative supersaturation for an assumed nucleation time. We calculate the supersaturation, *S*, as:

$$S = \frac{y}{y_s^*} \tag{5-21}$$

where y is the actual mole fraction of the solute, and y_s^* is the solute mole fraction at the solubility limit. In the hydrodynamic flow focusing device, the concentration of supercritical CO_2, solute and the solvent is not uniform across the 300 μm wide channel by the time when nucleation occurs, although mixing across the 20 μm wide core is achieved in milliseconds. In order to estimate the mole fraction of the solute, the amount of CO_2 that has diffused into the core is required. We estimate this amount for all the solvents by considering a common residence time. The diffusion coefficient of acetone and ethanol are obtained from the literature.[51, 52] For the other solvents, the diffusion coefficient is estimated from the dependency on viscosity:

$$D = \frac{k_B T}{c\pi\mu} \tag{5-22}$$

where k_B is the Boltzmann coefficient, T is the temperature, c is a constant and μ is the viscosity. Using the amount of carbon dioxide, the solute-free mole fraction of each solvent is calculated, which then is applied to the cosolvent-model discussed earlier in this chapter to calculate y_s^*. The actual solute mole fraction is calculated from the solvent feed rate, $\dot{v}_s$, the initial solute mole fraction in the solvent, y_i, and the respective moles of the solvent and antisolvent, n_s and n_a, respectively:

$$y = \frac{\dot{v}_s y_i}{\dot{v}_s y_i + n_s + n_a} \tag{5-23}$$

Since nucleation is observed almost instantaneously for this study, a common residence time of 20 milliseconds is used for all the calculations. In real case, nucleation most probably occurs even earlier than 20 milliseconds. Nevertheless, it should give a comparable estimate for supersaturation for the different solvents. The results of the supersaturation analysis are summarized in Table 5-4. The supersaturation in the case of ethanol and ethyl acetate appears to be the largest, followed by acetone. The supersaturation is the lowest in the case of isopropanol and n-butanol. Thus, the supersaturation is indeed correlated to the crystal habit observed in our experiments. Mostly, prisms are observed in ethanol, acetone and ethyl acetate experiments, and plates and rods are observed in isopropanol and n-butanol. This is consistent with previous studies on acetaminophen habits. Prasad et al. have demonstrated that an increase in the supersaturation transforms acetaminophen habit from columnar to prismatic.[28] Finnie et al. have demonstrated by single crystal growth measurements that at lower supersaturation, growth rates of [010] and [001] are comparable, while the growth rate of [110] is much smaller, resulting in higher aspect ratio crystals. On the other hand, at higher supersaturation, the growth rate of [110] catches up with that of [010] and [001], yielding more regular shaped prisms.[26, 53] This hypothesis is supported by the fact that the number of crystals observed is much less in the case of isopropanol and n-butanol, compared to that in case of ethanol, ethyl acetate and acetone (Figure 5-20). Also, the larger standard deviation present in case of isopropanol and n-butanol suggests that nucleation occurred over a longer period of time compared to that for the other three solvents. This indicates that the supersaturation was most likely generated over a longer period of time in the case of isopropanol and n-butanol, implying slower mixing of the antisolvent and solvent, which is shown in the calculations as well.

In addition, the difference observed in the average size, aspect ratio and habit of crystals produced from supercritical and subcritical fluid can also be explained by the above hypothesis. In subcritical conditions, acetone is not completely miscible with liquid CO_2.[54] Moreover, liquid CO_2 has higher density and viscosity, and lower diffusivity than its supercritical phase. This translates into a slower supersaturation generation in the microchannel. Thus, the increased size and aspect ratio observed for subcritical systems may result from a comparatively lower supersaturation, as in the case

of isopropanol and n-butanol. The smaller number of crystals observed for subcritical samples indicates a smaller nucleation rate at these conditions, suggesting a lower supersaturation.

Table 5-4. Supersaturation of acetaminophen in different solvents and supercritical CO_2

	Solvent Mole Fraction at the Channel Center after 20 ms	*Predicted Solubility (at Corresponding Solvent Composition)*	*Supersaturation*
Ethanol	0.09	4.97×10^{-6}	530
Acetone	0.03	6.22×10^{-7}	410
Ethyl acetate	0.04	5.36×10^{-7}	470
Isopropanol	0.14	9.98×10^{-6}	229
n-butanol	0.20	2.07×10^{-5}	281

5.5 Summary

In this chapter we demonstrated the realization of continuous supercritical crystallization of small organic molecules in microfluidic devices for the first time. We have addressed the issues of nucleation so as to achieve continuous spontaneous nucleation in these devices. We used acetaminophen as the model system and supercritical carbon dioxide as the antisolvent. The low solubility of organic molecules in supercritical carbon dioxide enables it to act as an antisolvent and achieve high supersaturation. The reduced density and viscosity of supercritical fluid also provide enhanced mixing, which can be critical for spontaneous nucleation. We developed a sheath flow device for supercritical crystallization that further enhanced mixing, helped

to lower crystal density in the microchannel, and to minimize interactions of crystals with channel surfaces. Using the developed platform, we demonstrated continuous crystallization of acetaminophen crystals.

In addition, the high supersaturation achieved from the supercritical antisolvent process enabled the formation of submicron to micron-sized acetaminophen crystals. The crystallinity of the products was independently verified with X-ray diffraction and Raman Spectroscopy. Individual crystals of submicron size have been reportedly formed on nanostructures,[6] and in nanoporous materials.[55] However, this work presents one of the first examples of producing such small organic crystals in bulk, particularly in continuous manner. This technique may be very useful in the pharmaceutical industry for increasing bioavailability of poorly soluble drugs,[56] as well as for achieving small crystals of highly potent active pharmaceuticals or inhalable aerosols with a narrow size distribution.

Finally, we demonstrated that the continuous microfluidic platform developed in this work may be used to easily screen process parameters or solvents for crystallization. We investigated the effects of pressure over a range of 81 to 95 bar, as well as the effects of solvents. Pressure was found to have no significant effect on the product characteristics, namely crystal size, aspect ratio, habit and the polymorphic form, over the operating range. Solvents, on the other hand, significantly affected the product characteristics. Ethanol, acetone and ethyl acetate were found to yield mostly prismatic crystals of smaller size and aspect ratio. However, isopropanol and n-butanol produced mostly larger crystals with a larger aspect ratio and plate-like or rod-like habit. We used supersaturation to explain the observed effects. A solubility prediction model was used to estimate supersaturation in the supercritical fluid. The calculated supersaturation was shown to be directly related to the product characteristics, with lower supersaturation giving rise to crystals of larger size and aspect ratio.

The developed platform can not only be used to screen the effects of process parameters and optimize crystallization conditions, but also as a useful tool to safely and quickly navigate through the supercritical domain in search of new polymorphic forms. This can be particularly useful for the pharmaceutical industry where searching for new polymorphic form is a routine task.

5.6 List of Variables

y_2^*	solubility of solute "2" in supercritical fluid
$P_2^s(T,P)$	sublimation pressure of pure solid "2"
$\varphi_2(T,P)$	fugacity coefficient of the pure solute
$V_2^s(T,P)$	solid molar volume
T_b	boiling point of the solute
ΔH_{vb}	enthalpy of vaporization at T_b
ΔZ_b	change in compressibility factor
m	constant that depends on the boiling point and critical temperature
T_{pb}	function of the critical temperature, T_c and operating temperature T
K_F	Fishtine constant
R	gas constant
T_c	critical temperature
P_c	critical pressure
V_c	critical volume
t_{c0}	temperature constant
p_{c1}, p_{c2}	pressure constants
v_{c0}	volume constant
ω	Pitzer's acentric factor
φ	fugacity coefficient of a pure compound
φ_M	fugacity coefficient of the mixture
$\hat{\varphi}_2$	fugacity coefficient for component *2* in a mixture
B	peak width
K	Scherrer constant
λ	wavelength of X-ray radiation
θ	½ the diffraction angle
L	crystallite size
S	supersaturation
y	solute mole fraction

y_s^*	solute mole fraction at the solubility limit
k_B	Boltzmann coefficient
T	temperature
c	constant
μ	viscosity
$\dot{v}_s$	solvent feed rate
y_i	initial solute mole fraction in the solvent
n_s	moles of solvent
n_a	moles of antisolvent

5.7 References

[1] J. Bernstein, *Polymorphism in molecular crystals*, Clarendon Press, Oxford University Press, New York, **2002**.

[2] H. G. Brittain, *Polymorphism in pharmaceutical solids*, Marcel Dekker, New York, **1999**.

[3] A. Goho, Tricky business: the crystal form of a drug can be the secret to its success. *Science News,* **2004**, *166*(8).

[4] J. Jung, & M. Perrut, Particle design using supercritical fluids: Literature and patent survey. *Journal of Supercritical Fluids,* **2001**, *20*, 179-219.

[5] R. Muller, Jacobs, C, and Kayser, O, Nanosuspensions as particulate drug formulations in therapy rationale for development and what we can expect for the future. *Advanced drug delivery reviews,* **2001**, *47*, 3-19.

[6] K. Kim, I. S. Lee, A. Centrone, T. A. Hatton, & A. S. Myerson, Formation of Nanosized Organic Molecular Crystals on Engineered Surfaces. *Journal of the American Chemical Society,* **2009**, *131*(51), 18212-18213.

[7] F. Dehghani, & N. R. Foster, Dense gas anti-solvent processes for pharmaceutical formulation. *Current Opinion in Solid State & Materials Science,* **2003**, *7*(4-5), 363-369.

[8] A. Shariati, & C. J. Peters, Recent developments in particle design using supercritical fluids. *Current Opinion in Solid State & Materials Science,* **2003**, *7*(4-5), 371-383.

[9] V. Majerik, G. Charbit, E. Badens, G. Horvath, L. Szokonya, N. Bosc, & E. Teillaud, Bioavailability enhancement of an active substance by supercritical antisolvent precipitation. *Journal of Supercritical Fluids,* **2007**, *40*(1), 101-110.

[10] M. Perrut, J. Jung, & E. Leboeuf, Enhancement of dissolution rate of poorly soluble active ingredients by supercritical fluid processes Part II: Preparation of composite particles. *International Journal of Pharmaceutics,* **2005**, *288*(1), 11-16.

[11] M. Turk, P. Hils, B. Helfgen, K. Schaber, H. J. Martin, & M. A. Wahl, Micronization of pharmaceutical substances by the Rapid Expansion of Supercritical Solutions (RESS): a promising method to improve bioavailability of poorly soluble pharmaceutical agents. *Journal of Supercritical Fluids,* **2002**, *22*(1), 75-84.

[12] C. J. Roberts, & P. G. Debenedetti, Engineering pharmaceutical stability with amorphous solids. *Aiche Journal,* **2002**, *48*(6), 1140-1144.

[13] A. M. Juppo, C. Boissier, & C. Khoo, Evaluation of solid dispersion particles prepared with SEDS. *International Journal of Pharmaceutics,* **2003**, *250*(2), 385-401.

[14] M. A. McHugh, & V. J. Krukonis, *Supercritical Fluid Extraction: Principles & Practice*, Butterworth-Heinemann, Boston, **1994**.

[15] R. Span, & W. Wagner, A new equation of state for caron dioxide covering the fluid region from the triple-point temperature to 1100 K at pressures up to 800 MPa. in *NIST Chemistry Webbook*, National Institute of Standards and Technology, Gaithersburg, MD, **1996**, (http://webbook.nist.gov).

[16] A. Fenghour, W. A. Wakeham, & V. Vesovic, The viscosity of carbon dioxide. in *NIST Chemistry Webbook*, National Institute of Standards and Technology, Gaithersburg, MD, **1998**, (http://webbook.nist.gov).

[17] S. X. M. Boerrigter, H. M. Cuppen, R. I. Ristic, J. N. Sherwood, P. Bennema, & H. Meekes, Explanation for the supersaturation-dependent morphology of monoclinic paracetamol. *Crystal Growth & Design,* **2002**, *2*(5), 357-361.

[18] S. Bristow S, T, Shekunol BY, York P, Analysis of the supersaturation and precipitation process with supercritical CO_2. *Journal of Supercritical Fluids,* **2001**, *90*, 1570.

[19] P. DiMartino, P. Conflant, M. Drache, J. P. Huvenne, & A. M. GuyotHermann, Preparation and physical characterization of forms II and III of paracetamol. *Journal of Thermal Analysis,* **1997**, *48*(3), 447-458.

[20] G. Nichols, & C. S. Frampton, Physicochemical characterization of the orthorhombic polymorph of paracetamol crystallized from solution. *Journal of Pharmaceutical Sciences,* **1998**, *87*(6), 684-693.

[21] G. L. Perlovich, T. V. Volkova, & A. Bauer-Brandl, Polymorphism of paracetamol. *Journal of Thermal Analysis and Calorimetry,* **2007**, *89*(3), 767-774.

[22] P. DiMartino, A. M. GuyotHermann, P. Conflant, M. Drache, & J. C. Guyot, A new pure paracetamol for direct compression: The orthorhombic form. *International Journal of Pharmaceutics,* **1996**, *128*(1-2), 1-8.

[23] M. L. Peterson, S. L. Morissette, C. McNulty, A. Goldsweig, P. Shaw, M. LeQuesne, J. Monagle, N. Encina, J. Marchionna, A. Johnson, J. Gonzalez-Zugasti, A. V. Lemmo, S. J. Ellis, M. J. Cima, & O. Almarsson, Iterative high-throughput polymorphism studies on acetaminophen and an experimentally derived structure for form III. *Journal of the American Chemical Society,* **2002**, *124*(37), 10958-10959.

[24] B. Y. Shekunov, & D. J. W. Grant, In situ optical interferometric studies of the growth and dissolution behavior of paracetamol (acetaminophen) .1. Growth kinetics. *Journal of Physical Chemistry B,* **1997**, *101*(20), 3973-3979.

[25] B. Y. Shekunov, M. E. Aulton, R. W. AdamaAcquah, & D. J. W. Grant, Effect of temperature on crystal growth and crystal properties of paracetamol. *Journal of the Chemical Society-Faraday Transactions,* **1996**, *92*(3), 439-444.

[26] S. Finnie, R. I. Ristic, J. N. Sherwood, & A. M. Zikic, Characterization of growth behaviour of small paracetamol crystals growth from pure solution. *Chemical Engineering Research & Design,* **1996**, *74*(A7), 835-838.

[27] N. Rasenack, & B. W. Muller, Crystal habit and tableting behavior. *International Journal of Pharmaceutics,* **2002**, *244*(1-2), 45-57.

[28] K. V. R. Prasad, R. I. Ristic, D. B. Sheen, & J. N. Sherwood, Crystallization of paracetamol from solution in the presence and absence of impurity. *International Journal of Pharmaceutics,* **2001**, *215*(1-2), 29-44.

[29] M. N. Femioyewo, & M. S. Spring, Studies on paracetamol crystals produced by growth in aqueous solutions. *International Journal of Pharmaceutics,* **1994**, *112*(1), 17-28.

[30] T. Kumhom, P. L. Douglas, S. Douglas, S. Pongamphai, & W. Teppaitoon, Prediction of Solubilities of Solid Biomolecules in Modified Supercritical Fluids

Using Group Contribution Methods and Equations of State. *Industrial & Engineering Chemistry Research,* **2010**, *49*(5), 2433-2441.

[31] A. Ajchariyapagorn, T. Kumhom, S. Pongamphai, S. Douglas, P. L. Douglas, & W. Teppaitoon, Predicting the extraction yield of nimbin from neem seeds in supercritical CO2 using group contribution methods, equations of state and a shrinking core extraction model. *Journal of Supercritical Fluids,* **2009**, *51*(1), 36-42.

[32] W. B. Kay, Density of hydrocarbon gases and vapors at high temperature and pressure. *Industrial and Engineering Chemistry,* **1936**, *28*, 1014-1019.

[33] D. Suleiman, L. A. Estevez, J. C. Pulido, J. E. Garcia, & C. Mojica, Solubility of anti-inflammatory, anti-cancer, and anti-HIV drugs in supercritical carbon dioxide. *Journal of Chemical and Engineering Data,* **2005**, *50*(4), 1234-1241.

[34] J. M. Prausnitz, R.N. Lichtenthaler and E.G. de Azevedo, *Molecular Thermodynamics of Fluid Phase Equilibria*, Prentice-Hall, Englewoods Cliffs, **1998**.

[35] *Handbook of chemical property estimation methods. Environmental behavior of organic compounds*, McGraw-Hill, New York, **1982**.

[36] D. G. Miller, Estimating vapor pressures-comparison of equations. *Industrial and Engineering Chemistry,* **1964**, *56*(3), 46-57.

[37] W. J. Lyman, & W. F. R. Reehl, D.H., *Handbook of Chemical Property Estimation Methods: Environmental Behaviour of Organic Compounds*, McGraw-Hill, New York, **1982**.

[38] L. Constantinou, & R. Gani, New group-contribution method for estimating properties of pure compounds. *Aiche Journal,* **1994**, *40*(10), 1697-1710.

[39] R. C. Reid, J.M. Prausnitz, and T.K. Sherwood, *The Properties of Gases and Liquids*, McGraw-Hill, Montreal, **1987**.

[40] U. Plocker, H. Knapp, & J. Prausnitz, Calculation of high-pressure vapor-liquid equilibria from a corresponding-states correlation with emphasis on asymmetric mistures. *Industrial & Engineering Chemistry Process Design and Development,* **1978**, *17*(3), 324-332.

[41] F. Trachsel, C. Hutter, & P. R. von Rohr, Transparent silicon/glass microreactor for high-pressure and high-temperature reactions. *Chemical Engineering Journal,* **2008**, *135*, S309-S316.

[42] H. V. Ehrfeld W, Lowe H, *Microreactors: New Technology for Modern Chemistry*, Wiley-VCH, Weinheim, **2000**.

[43] O. Geschke, H. Klank, & P. Telleman, *Microsystem Engineering of Lab-on-a-Chip Devices*, Wiley-VCH, Weinheim, **2004**.

[44] A. Ajchariyapagorn, P. L. Douglas, S. Douglas, S. Pongamphai, & W. Teppaitoon, Prediction of solubility of solid biomolecules in supercritical solvents using group contribution methods and equation of state. *American Journal of Food Technology,* **2008**, *3*(5), 275-293.

[45] S. Bristow, B. Y. Shekunov, & P. York, Solubility analysis of drug compounds in supercritical carbon dioxide using static and dynamic extraction systems. *Industrial & Engineering Chemistry Research,* **2001**, *40*(7), 1732-1739.

[46] T. Lee, C. S. Kuo, & Y. H. Chen, Solubility, polymorphism, crystallinity, and crystal habit of acetaminophen and ibuprofen by initial solvent screening. *PharmaTech,* **2006**, *30*(10), 72-92.

[47] J. I. Langford, & A. J. C. Wilson, Scherrer after 60 years - survey and some new results in determination of crystallite size. *Journal of Applied Crystallography,* **1978**, *11*(APR), 102-113.

[48] J. Zhao, H. Lui, D. I. McLean, & H. Zeng, Automated autofluorescence background subtraction algorithm for biomedical Raman spectroscopy. *Applied Spectroscopy,* **2007**, *61*(11), 1225-1232.

[49] J. F. Kauffman, L. M. Batykefer, & D. D. Tuschel, Raman detected differential scanning calorimetry of polymorphic transformations in acetaminophen. *Journal of Pharmaceutical and Biomedical Analysis,* **2008**, *48*(5), 1310-1315.

[50] W. M. L. Wood, A bad (crystal) habit - and how it was overcome. *Powder Technology,* **2001**, *121*(1), 53-59.

[51] H. Nishiumi, M. Fujita, & K. Agou, Diffusion of acetone in supercritical carbon dioxide. *Fluid Phase Equilibria,* **1996**, *117*(1-2), 356-363.

[52] C. C. Lai, & C. S. Tan, Measurement of molecular-diffusion coefficients in supercritical carbon-dioxide using a coated capillary column. *Industrial & Engineering Chemistry Research,* **1995**, *34*(2), 674-680.

[53] S. D. Finnie, R. I. Ristic, J. N. Sherwood, & A. M. Zikic, Morphological and growth rate distributions of small self-nucleated paracetamol crystals grown from pure aqueous solutions. *Journal of Crystal Growth,* **1999**, *207*(4), 308-318.

[54] T. Adrian, & G. Maurer, Solubility of carbon dioxide in acetone and propionic acid at temperatures between 298 K and 333 K. *Journal of Chemical and Engineering Data,* **1997**, *42*(4), 668-672.

[55] J. M. Ha, B. D. Hamilton, M. A. Hillmyer, & M. D. Ward, Phase Behavior and Polymorphism of Organic Crystals Confined within Nanoscale Chambers. *Crystal Growth & Design,* **2009**, *9*(11), 4766-4777.

[56] J. Jinno, N. Kamada, M. Miyake, K. Yamada, T. Mukai, M. Odomi, H. Toguchi, G. G. Liversidge, K. Higaki, & T. Kimura, Effect of particle size reduction on dissolution and oral absorption of a poorly water-soluble drug, cilostazol, in beagle dogs. *Journal of Controlled Release,* **2006**, *111*(1-2), 56-64.

6 Summary and Outlook

6.1 Principal Thesis Contributions

The major contribution of this thesis has been to the field of continuous crystallization and microfluidics. This thesis is one of the first ones to take up the challenges of continuous crystallization in microchannels. It explores the microfluidics realm for the possibility of continuous crystallization. It provides an understanding of the issues related to spontaneous nucleation and discusses the challenges that have hindered continuous crystallization in microchannels from being widely successful. This thesis may serve as a guideline for achieving continuous crystallization in microfluidic systems, as well as for handling solids in microchannels. The technology developed in this thesis can be used to obtain insights into the fundamentals of complex crystallization processes, which can subsequently be applied to industrial processes. The main contributions of this thesis are developing a continuous microfluidic platform by appropriately addressing issues of crystallization; achieving continuous seeded crystallization by utilizing reaction engineering principles; demonstrating the use of continuous seeded crystallization device for obtaining fundamental insights into growth and habit modification mechanism; developing a microfluidic platform for continuous supercritical crystallization; and demonstrating the use of a continuous supercritical crystallization device for producing micron-sized crystals, as well as for screening the effects of process variables on product characteristics.

There has been a paradigm shift in the industrial crystallization. Contributions to industrial crystallization up to the 1970s have been mostly related to productivity and reproducibility issues. At present, the focus has shifted quite a bit to improving the monitoring and control of industrial crystallization, in order to make the manufacturing process more efficient and obtain better control of the properties of solid APIs. For advanced process design, optimization and control, the kinetic behavior of crystallization processes, namely kinetic data on nucleation, growth and agglomeration, are of greatest importance. Yet, the kinetic behavior is usually not available due to the complexity, cost

and duration of the experimental work required. This is where microfluidics can play a significant role by providing an inexpensive, automated platform to quickly obtain kinetics information.

However, microfluidics has its own challenges for solid synthesis and solid handling. One of the main challenges of continuous crystallization in microchannels is channel clogging. Many factors contribute to channel plugging, including uncontrolled nucleation of organic molecules, uncontrolled growth, interactions of solids with channel walls, agglomeration, and sedimentation. We developed an understanding of this clogging mechanism and address each of these factors in this thesis. We achieved control over the nucleation and growth process by decoupling them using reactor design principles, as well as an understanding of the individual steps of crystallization. Surface interactions were minimized by controlling the surface properties of the microchannels. Finally, agglomeration and sedimentation were controlled with appropriate process design that achieved desired supersaturation, and the dynamics of desupersaturation in the reactor channels.

We developed a microfluidic platform and demonstrated continuous seeded crystallization for the first time in this thesis. We demonstrated the use of our developed technology for three polymorphs of glycine: α-, β- and γ-form, each with different properties and habits. We used *in situ* characterization tools to successfully determine the crystal growth rates of all the three forms. We also showed how fundamental insights into the crystallization process can be obtained by determining the growth mechanism of gamma glycine for the first time and extracting thermodynamic data of glycine nuclei. Moreover, we illustrated how microfluidic devices could be used as an elegant tool to accurately measure the growth rates of high aspect ratio crystals by exerting shear on them and causing them to self-align.

The developed technology can be used to look into impurity effects on crystal growth and thus, crystal habit. The high spatiotemporal resolution of microfluidic devices provides an interesting tool to study habit evolution of crystals due to the presence of impurities, as well as solvents. Using the centrosymmetric habit of alpha glycine, this thesis illustrated the extraction of the kinetics of habit modification, and provided new insights into the habit modification mechanism of alpha glycine. The technique

developed in this thesis can be used to screen impurities for the efficacy of habit modification and develop an understanding of the habit modification mechanism. This information can subsequently be used to engineer additives that can be intentionally added to modify the habit of a given crystal system so as to facilitate industrial processing.

Furthermore, this thesis demonstrated continuous supercritical crystallization and spontaneous nucleation of small organic molecules in microfluidic devices for the first time. We demonstrated that the developed technology can be used to produce micron and submicron-sized crystals, which may be useful for increasing the bioavailability of poorly water soluble drugs, inhalable aerosols or highly potent drugs such as cancer drugs. The enhanced mixing in the presented device, as well as control over the contacting mode of supercritical antisolvent and crystallizing solution, provides a tool to produce crystals with narrower size distribution than can be achieved in batch supercritical crystallization processes. Also, the advantage of this device over a traditional continuous crystallization tool such as an impinging jet is that fast mixing can be achieved without the use of high energy. Using high energy for mixing can impart energy into the products, and thereby make amorphous materials that are highly unstable.

In addition to presenting one of the first examples of producing (sub) micron-sized organic crystals, we illustrated the use of the developed tool for easily screening process parameters such as temperature, pressure and solvent. Using acetaminophen as an example of poorly water soluble drugs, we screened the effects of pressure, solvents and supercritical condition on the crystal characteristics, namely the size, habit, aspect ratio, and the polymorphic form. The information obtained from such screening process can subsequently be used to optimize industrial processes. The screening ability of our device also provides a tool for safely searching for new polymorphs in the new domain of supercritical fluids, which is of great significance to the pharmaceutical industry. Finally, this thesis provides a small, but an important first step, towards continuous manufacturing of pharmaceuticals, by providing insights into the challenges of continuous solid processing.

6.2 Future Work

This thesis provides the basis for several high-impact research opportunities in continuous crystallization, as well as in microfluidics. Molecular crystallization is not a very well understood process, and needs well-controlled environment, such as those found in microfluidic devices. Nucleation, in particular, has been known as an elusive process in the crystallization community. This thesis has dealt extensively with the challenges of solid handling and come up with solutions for addressing many of them. This thesis has also dealt with crystal growth and nucleation of organic systems in microfluidic channels. Thus, it provides the perfect background required to go to the next step and obtain fundamental insights into the nucleation process. In order to gain an understanding of the nucleation fundamentals, we have to use high resolution *in situ* characterization tools that can be integrated with the microchannels. The laminar flow, controlled contact of reagents, and integration with *in situ* detection tools enable microfluidics to play a key role in understanding the nucleation process.

We demonstrated in this thesis that the continuous laminar flow device provides accurate information on the size, and thus kinetics of high aspect ratio crystal systems due to self-alignment. This work can be extended by integrating an automated imaging tool to the microfluidic devices that can be used for automated kinetic extraction. In addition, the developed platform can be used as a high throughput tool to screen effects of process parameters on crystal growth, which can subsequently be used to optimize the process. The presented tool can also be used to study complex growth processes and derive useful information about the growth mechanism.

However, one of the limitations of the continuous seeded crystallization device is the material used. PDMS, used in this thesis, is not compatible with many organic solvents, which limits the choice of solvent and antisolvent. Other optically transparent materials do not have well developed fabrication schemes. The options for materials with controllable surface properties, which are of utmost importance in crystallization and solid handling, are also limited. This presents another opportunity for future work that can broaden the scope of microfluidic crystallization. Coming up with a material that is optically transparent, can be as easily fabricated, yet is not limited by compatibility issues can potentially be very useful for crystallization of organic materials.

Finally, the supercritical crystallization work can be extended to higher pressures and more aggressive conditions. In this thesis, we were limited to approximately 100 bar by the failure point of the reactor. However, higher pressures can be reached with smaller channel dimensions. The properties of supercritical carbon dioxide changes rapidly at pressure higher than 100 bar, and hence, a change in pressure in that regime may significantly affect the crystal properties. At higher pressures, however, the properties will be closer to that of liquid phase, which may or may not reduce the crystallite size, depending on the solubility of individual organic systems in the operating supercritical fluid. The fluid dynamics and mass transfer of the three species, solute, solvent and antisolvent, in supercritical regime with dynamic properties (e.g. density and viscosity), represents a complex process. This presents an opportunity for modeling work in these supercritical systems.

Appendix A

Process sequence for SU-8 masters

In this section, we describe the details of the fabrication process for making SU-8 based masters used to mould PDMS microchannels for our reactors. The equipment names in the parentheses refer to machines in the Technology Research Laboratory (TRL) in MIT's Microsystems Technology Laboratories (MTL). The starting substrate is a 4" Silicon wafer (SSP, Test grade). The entire process is code purple. A two layer coating process is used to ensure uniform layer thickness over the entire wafer.

Process steps

1. Dehydration Bake: Bake the wafers on a hotplate at 200 °C for 20 min. This step removes any adsorbed moisture on the silicon wafer.
2. Spin coating of first SU-8(2050) layer: Transfer the wafers immediately from the dehydration bake hotplate to the spin coater (SU-8 spinner/ TRL) using a metallic wafer carrier. The wafer cools rapidly when placed on the metallic spin coater chuck. Use a nitrogen gun to blow away any dust particles on the wafer. Dispense a small amount (~20 mm diameter circle) of SU-8(2050) (Microchem Corp., MA) onto the wafer and start spinning immediately. SU-8(2050) has a quick evaporating solvent base, therefore immediate spinning is necessary. Spin at 650 rpm for 15s and 1100 rpm for 35s. This yields a layer of thickness ~100-150 μm.
3. Soft-bake of first SU-8(2050) layer: Transfer the freshly coated wafer to a hot plate. Heat at 65 °C for 10 minutes, ramp up to 95 °C and hold for 45 minutes. Cool to at least 65 °C before transferring to the spin coater for the next step.
4. Spin coating of second SU-8(2050) layer: Same sequence of steps as 2.
5. Soft-bake of second SU-8(2050) layer: Same sequence of steps as 3.
6. Photolithography to define microchannel pattern: Interval exposure (5s x 17, 4s interval) (EV1/TRL).

7. Post-exposure bake: Place the freshly exposed wafer to a hot plate. Heat at 65 °C for 10 minutes, ramp up to 95 °C and hold for 30 minutes. Cool to at least 50 °C before transferring for development.
8. Development: Develop in poly(glycol)mono ether acetate (PGMEA, Microchem.) for 45 min, replace with fresh solution every 15 min.
9. Rinse with Isopropyl alcohol and dry under a stream of nitrogen.

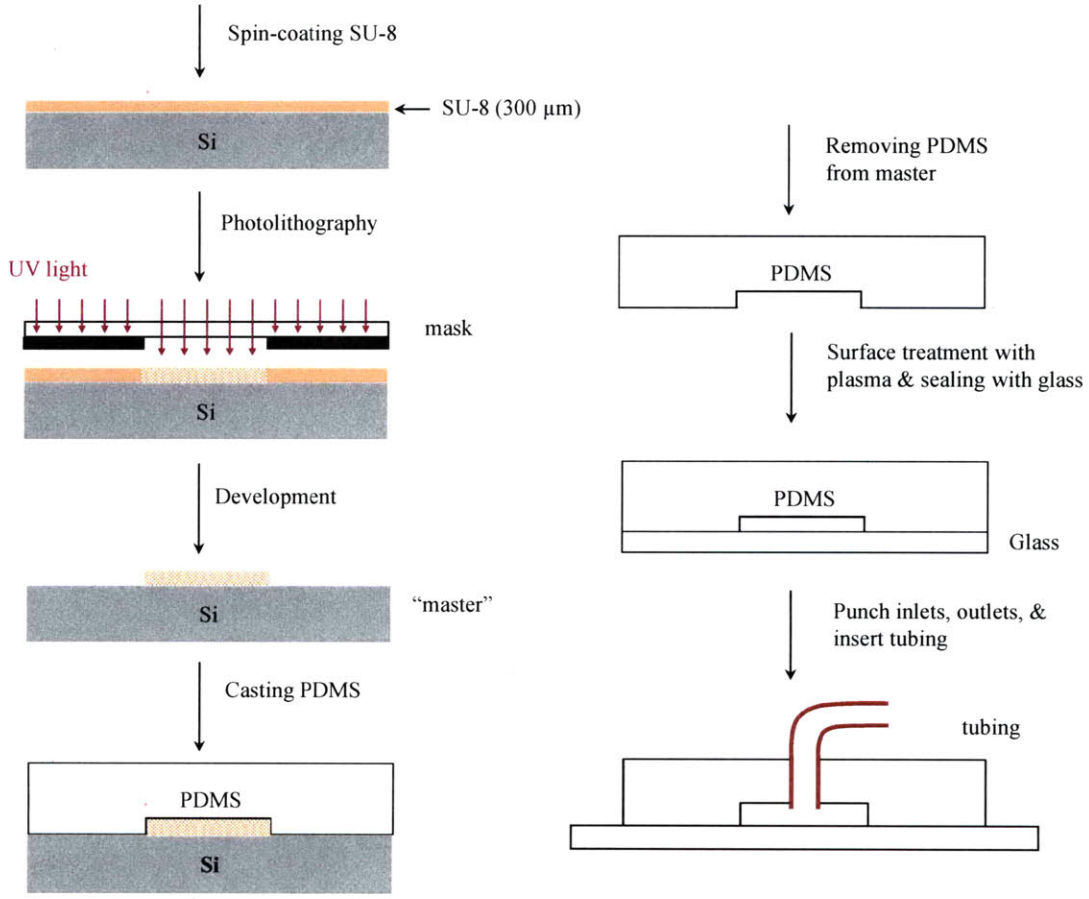

Figure A-1: SU-8 fabrication sequence.

Appendix B

The front (a) and back (b) mask used for high pressure silicon/pyrex devices.

a)

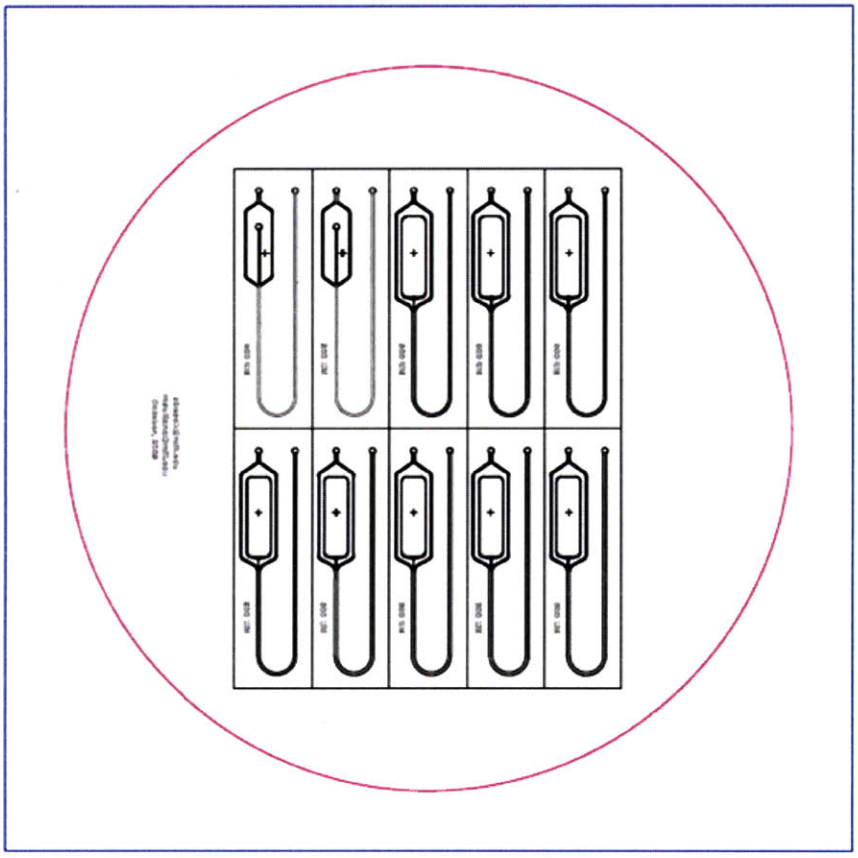

b)

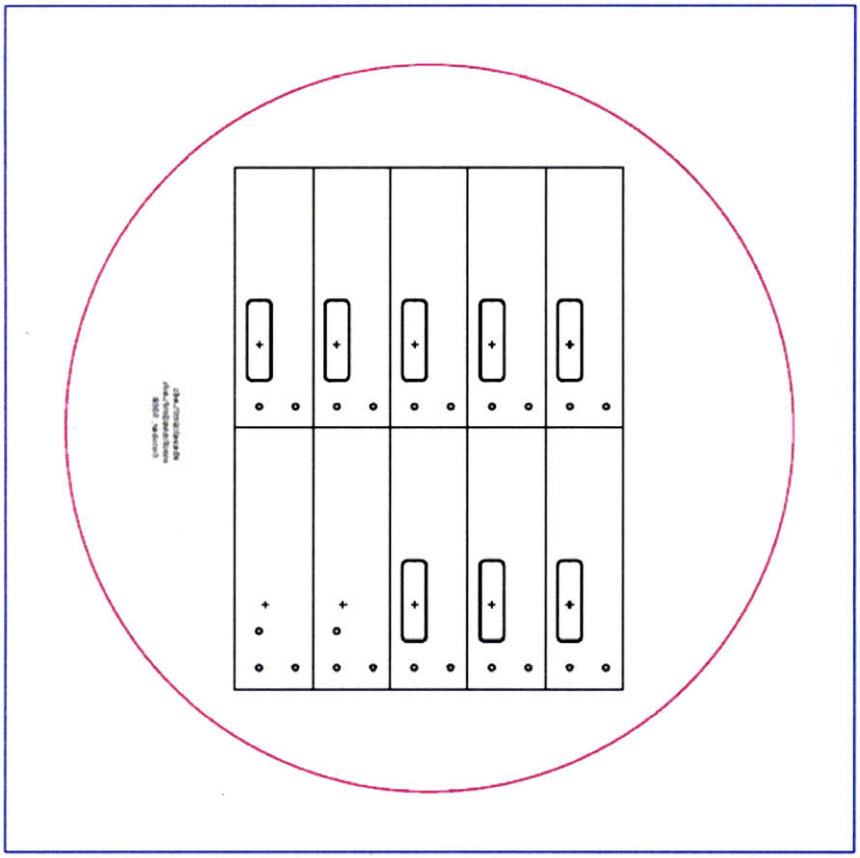

Appendix C

Process sequence for silicon/pyrex devices

In this section, we describe the details off fabrication process for making silicon/pyrex devices for supercritical crystallization. The equipment names in the parentheses refer to machines in the Technology Research Laboratory (TRL) in MIT's Microsystems Technology Laboratories (MTL).

Process steps

Clean silicon wafer and deposit thermal oxide, 1 μm to protect the top side during the etch. Etch port holes to a specified depth 400 μm on the bottom-side of the silicon wafer. Etch channels on the top side, aligned with port holes. Passivate the silicon channels by growing a thermal oxide. Bond the pyrex wafer to the top side of the silicon wafer, thereby sealing the flow channels.

1. Wafer cleaning and thermal oxide growth: Clean the wafers with RCA and grow 1 μm thermal oxide in furnace tubeA2.
2. Pattern bottom-side silicon wafer: Coat HMDS in HMDS coater, followed by spin coating of 10 μm new thick resist (AZ9260). Prebake at 95°C for 30 min and expose resist for 3x14s to UV. Develop the pattern for 1-2 minutes. Then, postbake the wafers at 95 °C for 30 min. Spin coat 1 μm thin resist on the topside and bake at 90°C for 60 min.
3. Pattern the bottom layer oxide: Pattern the oxide layer with BOE etch for 15 min. Use STS to pattern the bottom-side of the water to 300 μm. Remove resist using piranha clean.
4. Remove the oxide and resist: Remove the oxide layer with BOE etch for 15 min and then remove the resist with a piranha clean.
5. Thermal oxide growth: Use RCA station to perform an RCA clean on the wafers. Use furnace tubeA2 to grow thermal oxide of 5000A.
6. Pattern the topside silicon wafer: Follow steps 2-5 for patterning the topside of the wafer.

7. Anodic bonding with a pyrex wafer: Clean both the silicon and pyrex wafers with piranha wash. Contact and bond the wafers at 350°C (600-800V).
8. Die saw the dies in ICL.

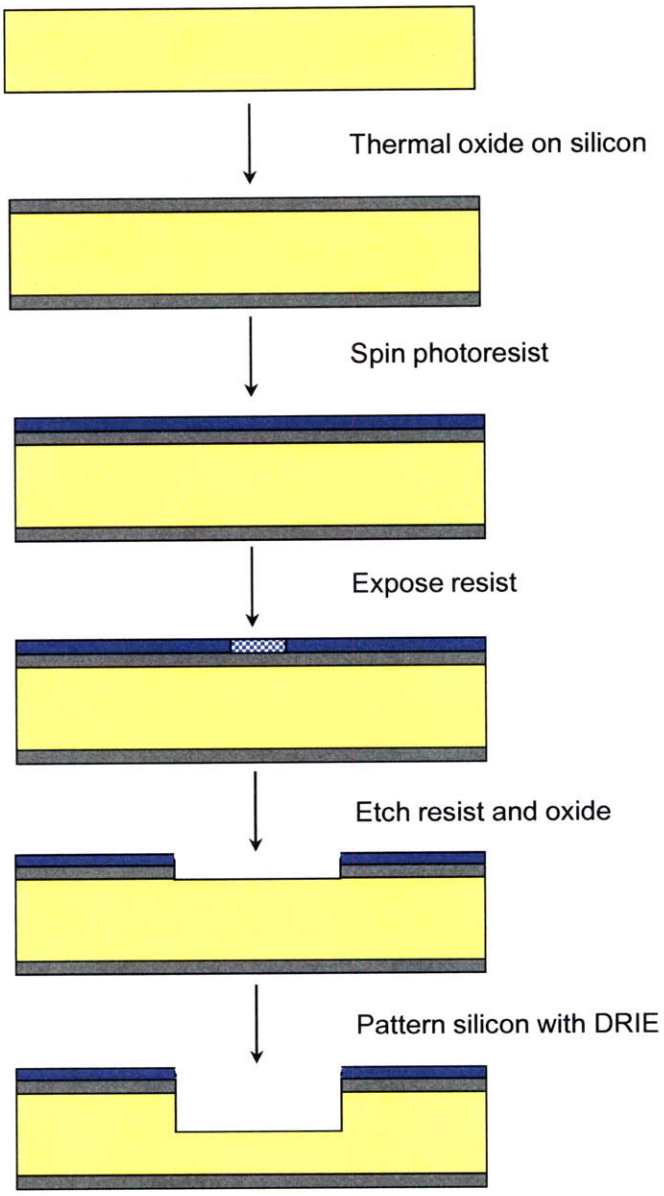

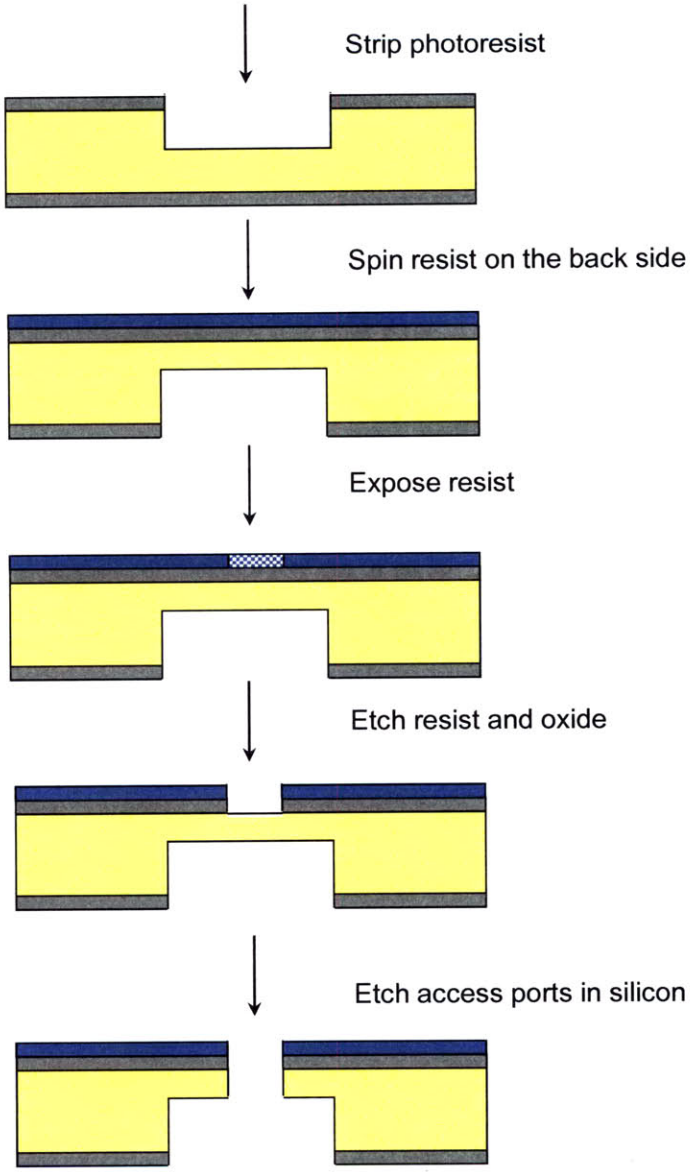
Strip photoresist
Spin resist on the back side
Expose resist
Etch resist and oxide
Etch access ports in silicon

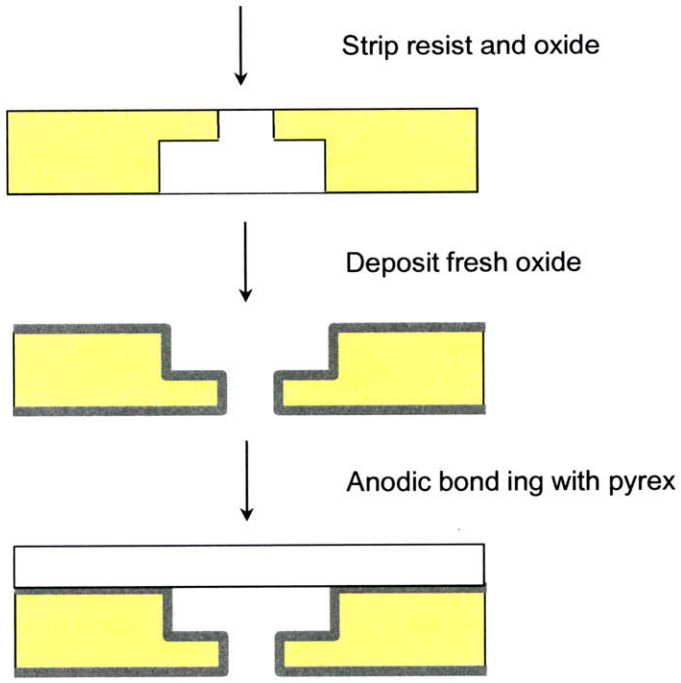
Strip resist and oxide
Deposit fresh oxide
Anodic bond ing with pyrex

Appendix D

Table E-1. Acetaminophen crystals produced from ethanol at 50 °C

P (bar)	*Count*	D_1	*Aspect Ratio*
81	301	2.25±0.86	1.83±0.79
85	197	1.59±0.52	1.57±0.38
90	195	1.37±0.65	1.57±0.50
95	195	1.58±0.70	1.53±0.34

Table E-2. Acetaminophen crystals produced from acetone at 50 °C

P (bar)	*Count*	D_1	*Aspect Ratio*
81	238	3.96±1.33	2.35±0.71
88	231	4.72±1.52	2.29±0.55
95	230	4.46±1.11	2.09±0.45
Subcritical	52	15.26±5.72	4.78±2.08

Table E-3. Acetaminophen crystals produced from ethyl acetate at 50 °C

P (bar)	*Count*	D_1	*Aspect Ratio*
81	180	2.05±1.12	1.52±0.49
85	157	1.07±0.30	1.49±0.25
95	177	2.25±0.85	1.43±0.32

Table E-4. Acetaminophen crystals produced from isopropanol at 50 °C

P (bar)	*Count*	D_1	*Aspect Ratio*
81	113	24.7±8.3	8.4±3.4
95	116	17.8±12.0	12.0±6.6

Table E-5. Acetaminophen crystals produced from n-butanol at 50 °C

P (bar)	*Count*	D_1	*Aspect Ratio*
81	111	15.6±6.7	15.4±7.9
95	127	21.1±11.8	9.1±4.9

Appendix E

Matlab code for solubility prediction

```
%-------------------------------------------------------------------------
%This program calculates the predicted solubility of solutes in supercritical fluid
%from only structural properties using Lee Kesler correlation----------
%written by Mahmooda Sultana-------------------------------------------
%-------------------------------------------------------------------------

function solubility_prediction
iflag_main=0;
clear all;

%Define state

T = 323;        %Temperature of the system in Kelvin
P_range=linspace(8,15,15);


% Enter component properties

Tc_s = 743.0775;    %critical temperature of solute in Kelvin
Pc_s = 3.229686;    %critical pressure of solute in MegaPascal
Vc_s = .41273;     %critical volume of solute in m3/kmol
Tb_s = 561.5971;    %normal boiling point of the solute in Kelvin

Kf = 1.15;  %Fishtine constant for the solute (looked up from tables)

theta_s=Tb_s/Tc_s;
omega_s =3*theta_s/(7*(1-theta_s))*log10(Pc_s*10)-1;  %acentric factor of the solute

%-------------------------------------------------------------------------
% Enter solvent properties

Tc_f1 = 304.2;    %critical temperature of solvent 1 (SCCO2 in this case) in Kelvin
Pc_f1 = 7.37;    %critical pressure of solvent 1 (SCCO2) in MegaPascal
Vc_f1 = 0.09;     %critical volume of solvent1 (SCCO2) in m3/kmol

omega_f1 = 0.23;    %acentric factor of the solvent

% Enter additional solvent properties here

 %the series are as ethanol, acetone, IPA, ethyl acetate and n-butanol
```

```
Tc_all=[489.2836, 490.11, 508.6977, 526.2081, 558.911];
Pc_all=[5.540048, 4.88, 4.752561, 4.162463, 4.185702];
Vc_all=[0.16542, 0.21, 0.22023, 0.28413, 0.27694];
Tb_all=[330.0078, 330, 347.6958, 349.8578, 393.8958];
yf_all=[0.09, 0.03, 0.14, 0.017, 0.2];

for p=1:5
   Tc_f2=Tc_all(p);
   Pc_f2=Pc_all(p);
   Vc_f2=Vc_all(p);
   Tb_f2=Tb_all(p);
   yf2=yf_all(p);

theta_f2=Tb_f2/Tc_f2;
omega_f2=3*theta_f2/(7*(1-theta_f2))*log10(Pc_f2*10)-1;

Vc_f_inter=0.5*(Vc_f1+Vc_f2);
Vc_f=Vc_f2*yf2^2+2*yf2*(1-yf2)*Vc_f_inter+Vc_f1*(1-yf2)^2;

Tc_f=Tc_f1*(1-yf2)+Tc_f2*yf2;   %using Kay's mixing rule
Pc_f=((yf2*Pc_f2*Vc_f2/Tc_f2)+((1-yf2)*Pc_f1*Vc_f1/Tc_f1))*Tc_f/Vc_f;

omega_f=omega_f1*(1-yf2)+omega_f2*yf2;  %using Kay's mixing rule

TciVci_TcjVcj=Tc_s*Vc_s/(Tc_f1*Vc_f1);

% calculate solute properties
R = 8.314;      %Gas constant J/(mol*K) OR m3*Pa/(mol*K) OR cm3*MPa/(mol*K)
del_Zb = 0.97;  %constant
eta = 0.251;

for k=1:length(P_range)

P = P_range(k);  %Pressure of the system in Megapascal

Tr_s = T/Tc_s;   %Reduced Temperature for solute
Tpb_s = T/Tb_s;

if Tpb_s>=0.6
   m_s=0.36;
elseif 0.5>Tpb_s
   m_s=1.19;
else
   m_s=0.8;
end
```

```
Del_Hvb_s = Tb_s*Kf*(8.75+1.987*log(Tb_s)); %enthalpy in cal/molK at the boiling
point
ln_Ps2 = Del_Hvb_s/(del_Zb*1.987*Tb_s)*(1-((3-2*Tpb_s)^m_s)/(Tpb_s)-2*m_s*(3-
2*Tpb_s)^(m_s-1)*log(Tpb_s));
% calculates the sublimation pressure of solid using Watson correlation

Ps2=exp(ln_Ps2)*0.101325;    %in MPa
V2s=119.691;% solid molar volume in cm3/mol
Pr_s=Ps2/Pc_s;

%-------------------------------------------------------------------------

% Use equation of state (Lee Kesler) to calculate properties of pure solid

b10=0.1181193; b20=0.265728; b30=0.154790; b40=0.030323; c10=0.0236744;
c20=0.0186984; c30=0.0; c40=0.042724; d10=0.155428E-4; d20=0.623689E-4;
beta0=0.65392; gamma0= 0.060167; %properties of the simple fluid, argon

b1r=0.2026579; b2r=0.331511; b3r=0.027655; b4r=0.203488; c1r=0.0313385;
c2r=0.0503618; c3r=0.016901; c4r=0.041577; d1r=0.48736E-4; d2r=0.0740336E-4;
betar=1.226; gammar= 0.03754; %properties of the reference fluid
omega_r=0.3978; %acentric factor of the reference fluid

B0s=b10-(b20/Tr_s)-(b30/Tr_s^2)-(b40/Tr_s^3);
C0s=c10-(c20/Tr_s)+(c30/Tr_s^3);
D0s=d10+(d20/Tr_s);

Vr0s_guess=Tr_s/Pr_s;

Vr0s = fzero(@solve_Vr,Vr0s_guess,[],Tr_s,Pr_s,B0s,C0s,D0s,c40, beta0,gamma0);
E0s=(c40/(2*gamma0*Tr_s^3))*(beta0+1-(beta0+1+gamma0/Vr0s^2)*exp(-
gamma0/Vr0s^2));
z0s=1+(B0s/Vr0s)+(C0s/Vr0s^2)+(D0s/Vr0s^5)+(c40/((Tr_s^3)*Vr0s^2))*(beta0+gamm
a0/Vr0s^2)*exp(-gamma0/Vr0s^2);
lnphi_0_s=z0s-1-log(z0s)+(B0s/Vr0s)+(C0s/(2*Vr0s^2))+(D0s/(5*Vr0s^5))+E0s;

Brs=b1r-(b2r/Tr_s)-(b3r/Tr_s^2)-(b4r/Tr_s^3);
Crs=c1r-(c2r/Tr_s)+(c3r/Tr_s^3);
Drs=d1r+(d2r/Tr_s);

Vrrs = fzero(@solve_Vr, Vr0s_guess,[],Tr_s,Pr_s,Brs,Crs,Drs,c4r, betar,gammar);
Ers=(c4r/(2*gammar*Tr_s^3))*(betar+1-(betar+1+gammar/Vrrs^2)*exp(-
gammar/Vrrs^2));
zrs=1+(Brs/Vrrs)+(Crs/Vrrs^2)+(Drs/Vrrs^5)+(c4r/((Tr_s^3)*Vrrs^2))*(betar+gammar/
Vrrs^2)*exp(-gammar/Vrrs^2);
```

```
lnphi_r_s=zrs-1-log(zrs)+(Brs/Vrrs)+(Crs/(2*Vrrs^2))+(Drs/(5*Vrrs^5))+Ers;

lnphi_s=lnphi_0_s+((lnphi_r_s-lnphi_0_s)*omega_s/omega_r);

phi_s=exp(lnphi_s);
z_s=z0s+((zrs-z0s)*omega_s/omega_r);

%-------------------------------------------------------------------------
%Mixture property calculation

ysolute=1.0068E-6;

Pr_s = P/Pc_s;

   Vc_s_f=(((Vc_f^(1/3))+(Vc_s^(1/3)))^3)/8;    %critical volume of the interaction
   Tc_s_f=((Tc_s*Tc_f)^(1/2))*kij;
   omega_m=(1-ysolute)*omega_f+ysolute*omega_s;

   Vc_m=((1-ysolute)^2)*Vc_f+2*(1-ysolute)*ysolute*Vc_s_f;
   Tc_m=((((1-ysolute)^2)*(Vc_f^eta)*Tc_f)+(2*(1-
ysolute)*ysolute*(Vc_s_f^eta)*Tc_s_f))/(Vc_m^eta);
   Pc_m=(0.2905-0.085*omega_m)*0.008314*Tc_m/Vc_m; % here R is in units of MPa
cm3/kmolK

   Tr_m=T/Tc_m;
   Pr_m=P/Pc_m;

   Vr0m_guess=Tr_m/Pr_m;

   B0m=b10-(b20/Tr_m)-(b30/Tr_m^2)-(b40/Tr_m^3);
   C0m=c10-(c20/Tr_m)+(c30/Tr_m^3);
   D0m=d10+(d20/Tr_m);

   Vr0m = fzero(@solve_Vr,Vr0m_guess,[],Tr_m,Pr_m,B0m,C0m,D0m,c40,
beta0,gamma0);
   E0m=(c40/(2*gamma0*Tr_m^3))*(beta0+1-(beta0+1+gamma0/Vr0m^2)*exp(-
gamma0/Vr0m^2));

z0m=1+(B0m/Vr0m)+(C0m/Vr0m^2)+(D0m/Vr0m^5)+(c40/((Tr_m^3)*Vr0m^2))*(beta
0+gamma0/Vr0m^2)*exp(-gamma0/Vr0m^2);
   lnphi_0_m=z0m-1-
log(z0m)+(B0m/Vr0m)+(C0m/(2*Vr0m^2))+(D0m/(5*Vr0m^5))+E0m;
   delH_RTc_0_m=Tr_m*(z0m-1-
((b20+(2*b30/Tr_m)+(3*b40/Tr_m^2))/(Tr_m*Vr0m))-((c20-
(3*c30/Tr_m^2))/(2*Tr_m*Vr0m^2))+(d20/(5*Tr_m*Vr0m^5))+3*E0m);
```

```
   Brm=b1r-(b2r/Tr_m)-(b3r/Tr_m^2)-(b4r/Tr_m^3);
   Crm=c1r-(c2r/Tr_m)+(c3r/Tr_m^3);
   Drm=d1r+(d2r/Tr_m);

   Vrrm = fzero(@solve_Vr,Vr0m_guess,[],Tr_m,Pr_m,Brm,Crm,Drm,c4r,
betar,gammar);
   Erm=(c4r/(2*gammar*Tr_m^3))*(betar+1-(betar+1+gammar/Vrrm^2)*exp(-
gammar/Vrrm^2));

zrm=1+(Brm/Vrrm)+(Crm/Vrrm^2)+(Drm/Vrrm^5)+(c4r/((Tr_m^3)*Vrrm^2))*(betar+g
ammar/Vrrm^2)*exp(-gammar/Vrrm^2);
   lnphi_r_m=zrm-1-
log(zrm)+(Brm/Vrrm)+(Crm/(2*Vrrm^2))+(Drm/(5*Vrrm^5))+Erm;
   delH_RTc_r_m=Tr_m*(zrm-1-((b2r+(2*b3r/Tr_m)+(3*b4r/Tr_m^2))/(Tr_m*Vrrm))-
((c2r-(3*c3r/Tr_m^2))/(2*Tr_m*Vrrm^2))+(d2r/(5*Tr_m*Vrrm^5))+3*Erm);

   lnphi_m=lnphi_0_m+((lnphi_r_m-lnphi_0_m)*omega_m/omega_r);
   zm=z0m+((zrm-z0m)*omega_m/omega_r);
   delH_TRc_r_m=delH_RTc_0_m+((delH_RTc_r_m-
delH_RTc_0_m)*omega_m/omega_r);

   domega_m_dZ=omega_f-omega_s;
   dz_cm_dZ=-0.085*domega_m_dZ;

   dVcm_dZ=2*((1-ysolute)*(Vc_f-Vc_s_f)+(ysolute*(Vc_s_f-Vc_s)));

   dTcm_dZ=((2*((1-ysolute)*(((Vc_f^eta)*Tc_f)-
((Vc_s_f^eta)*Tc_s_f))+(ysolute*((Vc_s_f^eta)*Tc_s_f-(Vc_s^eta)*Tc_s))))-
(eta*Vc_m^(eta-1))*Tc_m*dVcm_dZ)/(Vc_m^eta);

   zc_m=.291-0.08*omega_m;

   dPcm_dZ=Pc_m*((dz_cm_dZ/zc_m)+(dTcm_dZ/Tc_m)-(dVcm_dZ/Vc_m));

   dlnphim_domegam=(lnphi_r_m-lnphi_0_m)/omega_r;

   lnphi_solute_in_mix=lnphi_m-((delH_TRc_r_m/T)*dTcm_dZ)+(((zm-1)/Pc_m)*(1-
ysolute)*dPcm_dZ)-(dlnphim_domegam*(1-ysolute)*domega_m_dZ);
   phi_solute_in_mix=exp(lnphi_solute_in_mix);
   ysolute=(Ps2*phi_s/(P*phi_solute_in_mix))*exp(((P-Ps2)*V2s)/(8.314*T));

  P

if p==1
   y_in_etoh(k)=ysolute
elseif p==2
```

```
   y_in_acetone(k)=ysolute
elseif p==3
   y_in_IPA(k)=ysolute
elseif p==4
   y_in_ethylacetate(k)=ysolute
else
   y_in_nbutanol(k)=ysolute
end

end

end

%-------------------------------------------------------------------------

P_range=P_range*10;

%figure;
hold on;
plot(P_range,y_in_etoh,'k', P_range,y_in_acetone, 'r',P_range,y_in_IPA, 'b',
P_range,y_in_ethylacetate, 'g',P_range,y_in_nbutanol, 'y')

xlabel('Pressure(bar)'); ylabel('yi*'); title('Solubility of acetaminophen');
legend('ethanol','acetone','isopropanol','ehtyl acetate', 'n-butanol');

%hold off
return

%-------------------------------------------------------------------------
%-------------------------------------------------------------------------
%Solve for Vr
function n=solve_Vr(Vr0, Tr,Pr,B,C,D,c4,beta,gamma)

n=1+(B/Vr0)+(C/Vr0^2)+(D/Vr0^5)+(c4/(Tr^3)/Vr0^2)*(beta+gamma/Vr0^2)*exp(-
gamma/Vr0^2)-(Pr*Vr0/Tr);

return
```

Appendix F

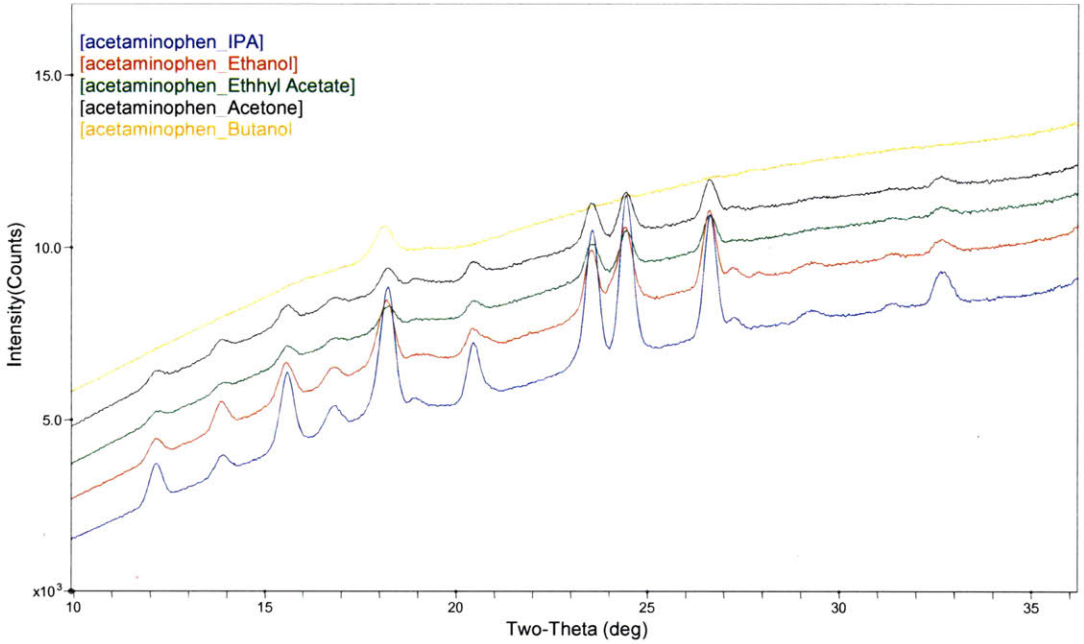

Figure G-1: Unprocessed X-ray diffraction pattern obtained for acetaminophen produced from various solvents.

Appendix G

Matlab code for fluorescence rejection

```
%-------------------------------------------------------------------------
%This program subtracts fluorescence background
%written by Mahmooda Sultana----------------------------------------------
%-------------------------------------------------------------------------

clear all;
clc;

load aspirin.txt;

iterations=200; %number of iterations to run

%Assigning data
shift_full=aspirin(:,1);
intensity_full=aspirin(:,2);
size_full=size(aspirin);

%Chop off the fist 100 cm-1
shift=shift_full(300:6120);
intensity=intensity_full(300:6120);
size_reduced=size(shift);

%Polynomial fitting
[p,s,MU]=polyfit(shift, intensity, 6);
shift_hat=(shift-MU(1))/MU(2);
generated=polyval(p, shift_hat);

for k=1:iterations

for i=1:size_reduced(1)
   if (generated(i)>intensity(i))
      generated(i)=intensity(i);
   end
end

[p,s,MU]=polyfit(shift, generated,6);
shift_hat=(shift-MU(1))/MU(2);
generated=polyval(p, shift_hat);
end
```

```
residual=intensity-generated;

figure;
plot(shift, intensity,'-',shift, generated, 'r--', shift, residual, '-.')

Data=[shift, residual];
save aspirin_fluorescence_free.txt Data -ascii
```